OXY-FUEL COMBUSTION ANALYSES OF POROUS AND ITM REACTORS FOR BOILER AND OTHER APPLICATIONS

BY

IBRAHIM BALARABE MANSIR

A Dissertation Presented to the

DEANSHIP OF GRADUATE STUDIES

KING FAHD UNIVERSITY OF PETROLEUM & MINERALS

DHAHRAN, SAUDI ARABIA

In Partial Fulfillment of the
Requirements for the Degree of

DOCTOR OF PHILOSOPHY

In

MECHANICAL ENGINEERING

MAY 2018

KING FAHD UNIVERSITY OF PETROLEUM & MINERALS
DHAHRAN- 31261, SAUDI ARABIA

DEANSHIP OF GRADUATE STUDIES

This thesis, written by **IBRAHIM BALARABE MANSIR** under the direction of his thesis advisor and approved by his thesis committee, has been presented and accepted by the Dean of Graduate Studies, in partial fulfillment of the requirements for the degree of **DOCTOR OF PHILOSOPHY IN MECHANICAL ENGINEERING.**

Med Habib May 31, 2018

Dr. Mohamed A. Habib
(Advisor)

R. B. Mansour

Dr. Rached Ben-Mansour
(Member)

A. Khalifa

Dr. Atia Khalifa
(Member)

Esmail

Dr. Esmail M. A. Mokheimer
(Member)

Dr. Mohamed El-Gebeily
(Member)

Dr. Zuhair M. Gasem
Department Chairman

Dr. Salam A. Zummo
Dean of Graduate Studies

02-07-2018

Date

Dedicated to my extended family

ACKNOWLEDGMENTS

Praise be to Almighty ALLAH (S.W.T.) for His blessings and mercy bestowed upon me and for giving me a healthy life to complete this dissertation work successfully. May HE continue to guide us on to the right path.

I wish to, first of all, deeply acknowledged the King Fahd University of Petroleum and Minerals for giving me the scholarship as well as virtuous academic platform throughout my PhD program. I will also like to acknowledge the chance and support given to me by the management of ABU and CERT, Zaria to pursue this PhD.

My profound gratitude goes to my able advisor, Dr. Mohamed A. Habib for his immense contributions towards the success of this work. I have benefited from his guidance, motivations, constructive criticisms, edifyingly swift response, resources, as well as morale boosting when the going gets tough. I wish to also appreciate the contribution of Dr. Atia Khalifa for his support during my experimental work. I have gained a lot from his guidance through his treasure of experiences during this work. The enormous contributions of Dr. Rached Ben-Mansour are strongly appreciated. His unceasing support and guidance during CFD modeling made this work a success. I wish to warmly recognize the endless contribution of Dr. Medhat Nemitallah towards successful completion of this work. His assiduous mentorship was all I needed to reach this point. My utmost appreciation goes to the graduate coordinator as well as my dissertation committee member, Dr. Esmail Mokhiemer for his fatherly advice, guidance and contribution to the betterment of this work. My sincere gratitude goes to my dissertation committee member, Dr. Mohamed El-

Gebeily for his contribution towards successful completion of this work. A very special appreciation goes to my colleagues working in combustion group for their support, openness for discussions and constructive criticisms, especially Mr. Zubairu Abubakar. It was my pleasure working with them. Many thanks to Mr. Karam, the former lab. technician of the heat engines laboratory, for his support throughout the experimental work. I would also like to acknowledge all the faculty members with whom I took courses or assisted me throughout this program. I would like to thank anybody that contributed in this work by any means.

My utmost appreciation goes to my extended family, parents, brothers and sisters for their love, prayers, support and guidance. A special thanks to my lovely wife and my children for their interminable love, support, prayers and endurance. Many thanks go to all my colleagues at the Centre for Energy Research and Training, for their prayers, and motivations

TABLE OF CONTENTS

ACKNOWLEDGMENTS ..... **V**

TABLE OF CONTENTS ..... **VII**

LIST OF TABLES ..... **XI**

LIST OF FIGURES ..... **XII**

LIST OF APPENDICES ..... **XVI**

LIST OF ABBREVIATIONS, NOMENCLATURE AND SYMBOLS ..... **XVII**

ABSTRACT ..... **XXII**

ملخص الرسالة ..... **XXIV**

CHAPTER 1 INTRODUCTION **1**

1.1 Global Warming and CO_2 Emissions **1**

1.2 Carbon Capture Technologies **2**

1.3 Oxy-fuel Combustion Technology **4**

1.4 Research Objectives **9**

CHAPTER 2 LITERATURE REVIEW **11**

2.1 Carbon Capture and Storage Technologies **11**

2.1.1 Pre-combustion carbon capture **12**

2.1.2 Post-combustion carbon capture **15**

2.1.3 Oxy-fuel combustion carbon capture **16**

2.1.4 CO_2 Transport and storage **17**

2.2 Characteristics of Oxy-fuel Combustion **19**

2.2.1 Lean blow-out limit **26**

2.3 Modeling of Oxy-fuel Combustion **27**

2.3.1 Reduced reaction mechanism for oxy-fuel combustion **27**

2.3.2 General Conservation Equations **30**

2.3.3 Radiation Modeling....33
2.4 Membranes for Oxygen Separation....35
2.4.1 Mixed Ionic and Electronic Conducting (MIEC) membranes for oxygen separation....37
2.4.2 Oxygen transport mechanism in MIEC membranes....39
2.4.3 Configurations of ITM for reactor applications....41
2.4.4 ITM oxygen flux fundamentals....43
2.4.5 Oxygen permeation flux through BSCF membranes....46
2.5 Oxygen Transport Membrane Performance....48
3 CHAPTER 3 METHODOLOGY....52
3.1 Introduction....52
3.2 Experimental Setup of Porous Combustor....52
3.2.1 Non-reacting experimental setup....53
3.2.2 Combustion Experimental Setup (Reacting)....63
3.3 Numerical Modeling of Porous Plate Combustor....69
3.3.1 2D Non-reactive modeling....69
3.3.2 2D Reactive modeling....71
3.3.3 3D Reacting modeling....71
3.4 ITM Numerical Modeling....72
3.4.1 Geometry description and boundary conditions....76
3.4.2 Geometry description and boundary conditions....81
4 CHAPTER 4 RESULTS AND DISCUSSIONS FOR THE POROUS COMBUSTOR....83
4.1 Non-Reactive Experiments....84
4.1.1 Averaged axial velocities....90
4.1.2 Local distributions of mixture fraction and equivalence ratio....92
4.2 Numerical Simulations of Oxy-combustion Characteristics....98
4.3 Oxy-combustion Experiments (Reactive)....108
4.3.1 Flame shapes/structures....108

4.3.2 Horizontal temperature distributions at the exhaust 114

4.3.3 Vertical temperature distributions at the exhaust 116

4.3.4 Longitudinal temperature distributions near the exhaust 118

4.3.5 Averaged exhaust temperatures 120

4.3.6 Lean flammability limits 121

4.4 3D Combustion Modeling (Reactive) 124

4.4.1 Flame description 125

4.4.2 Flame shapes comparison with experiments 126

4.4.3 Temperature comparisons with experiments 131

4.4.4 Numerical temperature distributions 137

4.4.5 Exhaust gas concentration 143

5 CHAPTER 5 RESULTS AND DISCUSSIONS FOR THE OTM REACTOR MODELING 148

5.1 2D Model Validation 149

5.1.1 Mesh size independence 149

5.1.2 Model Validation 151

5.2 OTR Geometry Development 153

5.3 Oxygen Permeation Flux 154

5.3.1 Effect of gases inlet temperature on O_2 permeation flux 155

5.3.2 Effect of gases inlet mass flow rate on O_2 permeation flux 160

5.3.3 Effect of OTM thickness on O_2 permeation flux 166

5.4 OTR Heat Transfer Characteristics 168

5.4.1 Effect of gas inlet temperature on heat transfer 168

5.4.2 Effect of gas inlet temperature on combustion heat transfer 171

5.4.3 Effect of gas inlet mass flow rate on heat transfer 174

5.4.4 Effect of gas inlet mass flow rate on combustion heat transfer 177

5.4.5 Effect of outer-pipe surface condition on heat transfer 180

5.4.6 Effect of outer-pipe surface condition on combustion heat transfer 181

5.4.7 Effect of inner-pipe emissivity on heat transfer 183

5.4.8 Effect of inner-pipe emissivity on combustion heat transfer 184

5.4.9 Effect of outer-pipe emissivity on heat transfer 186

5.4.10 Effect of outer-pipe emissivity on combustion heat transfer 187

5.5 Number of OTR Units for Fire-Tube Boiler Application 188

6 CHAPTER 6 CONCLUSIONS AND RECOMMENDATIONS 189

6.1 Conclusions 191

6.2 Recommendations 195

REFERENCES 196

APPENDICES 218

VITAE 247

LIST OF TABLES

Table 3.1. Properties of Porous Alumina Cover Plate 42520 55
Table 3.2. Laser Specifications 57
Table 3.3. Camera Specifications 58
Table 3.4. Lens Specifications 58
Table 3.5. Non-Reactive Experimental Plan at Reactor Power of 1.36 kW 59
Table 3.6: Experimental plan for the combustion at different concentrations of CO_2 and a fixed fuel firing rate of 1.5 kW for a range of equivalence ratio 67
Table 3.7: Effect of equivalence ratios at fixed fuel firing rate of 1.5 kW. 68
Table 3.8: Effect of fuel firing rates at different equivalence ratios. 68
Table 3.9: Effect of fuel firing rates at different stoichiometric equivalence ratio 68
Table 3.10. Sets of numerical cases for the analysis of oxy-combustion characteristics within the porous-plate reactor at various equivalence ratios 72
Table 3.11: Effect of feed and sweep streams inlet temperatures 78
Table 3.12. Effect of feed and sweep streams inlet mass flow rates 78
Table 3.13. Effect of steam saturation temperature at the outer pipe surface 78
Table 3.14: Effect of diluent (CO_2) inlet mass flow rates 79
Table 3.15: Effect of OTM thickness 79
Table 3.16: Effect of inner-pipe thermal conductivity 80
Table 3.17: Effect of inner-pipe emissivity 80

LIST OF FIGURES

Figure 1.1: CO_2 Capture Technologies 6

Figure 1.2: CO_2 Capture Options..... 7

Figure 2.1: World natural gas consumption from 2012 to 2040 12

Figure 2.2: Three CO_2 capture processes 13

Figure 2.3: Schematic diagram of pre-combustion capture for power generation…….15

Figure 2.4: Principle of pre-combustion CO_2 capture 15

Figure 2.5: Principle of post combustion CO_2 capture 16

Figure 2.6: Principle of oxy-fuel combustion CO_2 capture 17

Figure 2.7: Layout showing typical injection of CO_2 into depleted hydrocarbon reservoir 19

Figure 2.8: Four concepts of conduction mechanism for dense ceramic membranes: (i) solid electrolyte,(ii) dual phase, (iii) MIEC, (iv) asymmetric porous with graded porosity 37

Figure 2.9: Ideal ABO_3 perovskite crystal structure 39

Figure 2.10: Schematic representation of O_2 transport in dense ceramic MIEC membranes 40

Figure 2.11: Configurations of ITMs 42

Figure 3.1. Schematic diagram of the overall experimental setup of the reactor:. 55

Figure 3.2: PIV setup of the reactor. 56

Figure 3.3: PIV analysis sequence. 62

Figure 3.4: The combustor geometry. 65

Figure 3.5: Outlet Nodalization of Horizontal and Vertical temperature measuring points. 66

Figure 3.6: Nodalization of longitudinal temperature measurement. 66

Figure 3.7: (a) Schematic diagram of the OTR, (b) 2D representations of the OTR..... 75

Figure 4.1: Velocity vectors at different equivalence ratios. 86

Figure 4.2: Streamlines at different equivalence ratios. 88

Figure 4.3: Experimental velocity profiles at the three different sections (a, b and c) within the porous-plate reactor for different equivalence ratios 90
Figure 4.4: Comparison of experimental and numerical values of average velocities along the combustor at the three equivalence ratios. 91
Figure 4.5: Variation of fuel mixture fraction along the test section. 93
Figure 4.6: Variation of the average local equivalence ratio along the test section. 94
Figure 4.7. Position of average equivalence ratio along the porous flow domain. 95
Figure 4.8: Traverse variation of fuel mixture fraction downstream of porous plates. 96
Figure 4.9: Traverse variation of equivalence ratios downstream of the porous plates. .. 97
Figure 4.10: Effect of equivalence ratio on the outlet temperature at 3 kW. 101
Figure 4.11: Effect of equivalence ratio on the averaged outlet temperature at 3 kW. .. 103
Figure 4.12: Contour plots of temperature over a range of equivalence ratio at reactor power of 3 kW. 104
Figure 4.13: Contour plots of mass fractions of CH_4 over a range of equivalence ratio at reactor power of 3 kW. 105
Figure 4.14: Effect of equivalence ratio on the average mass fractions of the species . 107
Figure 4.15: Effects of operating conditions on the flame structure at 1.5kW. 111
Figure 4.16: Effect of operating conditions on the normalized flame length. 113
Figure 4.17b: Normalized horizontal temperature variation at the outlet, for fuel firing rate of 1.5kW 115
Figure 4.18: Normalized vertical temperature variation at the outlet, for fuel firing rate of 1.5kW 117
Figure 4.19: Normalized longitudinal temperature variation towards the exhaust at fuel firing rate of 1.5kW. 119
Figure 4.20: Normalized outlet temperature variation at fuel firing rate of 1.5kW 120
Figure 4.21: Effect of operating equivalence ratio on blowout limits at fixed fuel firing rate of 1.5 kW 122
Figure 4.22: Effect of fuel firing rate on blowout limits over a range of operating equivalence ratio. 123
Figure 4.23: Effect of fuel firing rate on blowout limits at stoichiometric operating equivalence ratio. 123

Figure 4.24: Three-dimensional flame shapes at stoichiometric equivalence ratio. 127
Figure 4.25: Comparison between experimental and numerical flame shapes at different equivalence ratio for % of CO_2 in the oxidizer mixture. 130
Figure 4.26: Comparison between vertical numerical and experimental gas temperatures at outlet for different operating conditions. 132
Figure 4.27: Comparison between horizontal numerical and experimental gas temperatures at outlet for different operating conditions. 134
Figure 4.28: Comparison between longitudinal numerical and experimental temperatures at the combustor centerline. 136
Figure 4.29: Effect of equivalence ratio and percentage of CO_2 addition on the normalized vertical temperature distribution at the exhaust. 138
Figure 4.30: Effect of equivalence ratios and percentage of CO_2 addition on the normalized horizontal temperature distribution at the exhaust. 140
Figure 4.31: Effect of equivalence ratios and percentage of CO_2 addition on the normalized longitudinal temperature distribution at the centerline. 142
Figure 4.32: Effect of percentage of CO_2 addition on the averaged exhaust gas species concentrations. 145
Figure 5.1: Mesh independence analysis 150
Figure 5.2: Comparison of O_2 permeation flux between numerical and experimental data (solid lines - this numerical model and symbols - experimental work of Behrouzifar et al., [182]) 152
Figure 5.3: Comparison of O_2 permeation flux between numerical and experimental data (circular symbols from this numerical model and triangular symbols from experimental work of Mezghani and Hamza [197]) 152
Figure 5.4: Effect of gas inlet temperature on the rate of O2 permeation flux across the OTM at an inlet gases flow rate of 5E-4 kg/s. 158
Figure 5.5: Effect of gases inlet temperature on the rate of O_2 permeation across the OTM at inlet gases flow rate of 5E-4 kg/s. 160
Figure 5.6: Effect of gas inlet mass flow rate on the rate of O_2 permeation flux across the OTM at an inlet gases temperature of 900 ^oC. 164
Figure 5.7: Effect of gases inlet mass flow rate on the rate of O_2 permeation across

the OTM at inlet gases temperature of 900°C. 165
Figure 5.8: Effect of OTM thickness on oxygen permeation at fixed gases inlet temperature and mass flow rates of 900°C and 5E-4 kg/s, respectively. 167
Figure 5.9: Effect of gas inlet temperatures on heat transfer to the outer-pipe at inlet gases mass flow rate of 5E-4 kg/s. 170
Figure 5.10: Effect of gas inlet temperatures on combustion heat transfer to the outer-pipe at inlet gases mass flow rate of 5E-4 kg/s. 173
Figure 5.11: Effect of gas inlet mass flow rates on heat transfer to the outer-pipe at inlet gases temperature of 900 °C. 176
Figure 5.12: Effect of gas inlet mass flow rates on combustion heat transfer to the load at inlet gases temperature of 900 °C. 179
Figure 5.13: Effect of outer-pipe surface condition (saturation temperature and pressure of steam) on heat transfer at base case condition. 181
Figure 5.14: Effect of outer-pipe surface condition on combustion heat transfer at base case condition. 182
Figure 5.15: Effect of inner-pipe surface emissivity on heat transfer at base case condition. 184
Figure 5.16: Effect of inner-pipe surface emissivity on combustion heat transfer at base case condition. 185
Figure 5.17: Effect of outer-pipe surface condition on heat transfer at base case. 187
Figure 5.18: Effect of outer-pipe surface condition on combustion heat transfer at base case condition. 188

LIST OF APPENDICES

APPENDIX A: The original WD reduced mechanism with kinetic rate data; with..... 218

APPENDIX B: The modified Westbrook-Dryer reduced mechanism for oxyfuel reaction with kinetic rate data. 218

APPENDIX C: Global Multi-Steps Combustion Mechanism for Methane by Westbrook and Dryer with Kinetic Rate Data 218

APPENDIX D: Jones Lindstedt Global Multi-Steps Combustion Mechanism for Methane with the Kinetic Rate Data 219

APPENDIX E: Modified Multi Steps Combustion Mechanisms for Methane with Kinetic Rate Data 219

APPENDIX F: JL 6-steps reaction mechanism for oxy-combustion 219

APPENDIX G: Optimize JL parameters for oxycombustion application 220

APPENDIX H: The refined JL combustion mechanisms for the MILD oxy-combustion of natural gas 220

APPENDIX I: Comparison between calculated and numerical simulation of average Velocity of the fuel side before the porous plates..... 221

APPENDIX J: Comparison between experimental and numerical simulation of average velocity of the reaction zone within the porous plates. 221

APPENDIX K: Flame Images..... 222

APPENDIX L: Experimental and Numerical Comparison of Flame Shapes 233

APPENDIX M: Maximum Percentage Difference between Experimental and Numerical Combustor Temperatures..... 234

APPENDIX N: OTR Base Case Parameters 235

APPENDIX O: OTR Oxygen Permeation Flux 236

APPENDIX P: OTR Heat Transfer Characteristics 239

APPENDIX Q: Effect of outer-pipe surface condition on OTR temperature contours 241

APPENDIX R: User Defined Function using C++ for O_2 permeation across OTM 242

LIST OF ABBREVIATIONS, NOMENCLATURE AND SYMBOLS

$\boldsymbol{A}$	:	Area
$\boldsymbol{a}$	:	Absorption Coefficient
$\boldsymbol{a_{\varepsilon,i}}$	:	Emissivity Weighting Factor for Specie *i*
AMG	:	Advanced Multi-Grid
CCS	:	Carbon Capture and Sequestration
CFD	:	Computational Fluid Dynamics
Da	:	Damköhler
$\boldsymbol{D_m}$	:	Mass Diffusion Coefficient
DO	:	Discrete Ordinate
$\boldsymbol{D_v}$	:	Volumetric Diffusion Coefficient
$\boldsymbol{E}$	:	Energy
FDS	:	Fire Dynamics Simulator
$\boldsymbol{g}$	:	Gravitational Acceleration
GHG	:	Green House Gases
HTMR	:	High Temperature Membrane Reactor
$\dot{\boldsymbol{h}}$	:	Positive Electron Hole

$\boldsymbol{I}$	:	Radiation Intensity
IA	:	Interrogation Area
IEO	:	International Energy Outlook
IGCC	:	Integrated Gasification Combined Cycle
IPCC	:	International Panel for Climate Change
IPL	:	Image Processing Library
ITM	:	Ion Transport Membrane
JL	:	Jones and Lindstedt
$\boldsymbol{Jo_2}$	:	Oxygen Permeation Flux
$\boldsymbol{K}$	:	Thermal Conductivity
$\boldsymbol{K_f}$	:	Reaction Rate - Forward
$\boldsymbol{K_r}$	:	Reaction Rate - Reverse
LBO	:	Lean Blow-Out
$\boldsymbol{L_c}$	:	Characteristic Thickness of Membrane
$\boldsymbol{l_f}$	:	Flame Length
$\boldsymbol{l_{f,n}}$	:	Flame Length - Non-dimensional
$\boldsymbol{M}$	:	Molecular Mass

$\dot{m}$	:	Mass Flow rate
MIEC	:	Mixed Ionic-Electronic Conducting
NGCC	:	Natural Gas-fired Combined Cycle
NIST	:	National Institute of Standards and Technology
No_2	:	Oxygen Molar Flow rate
OECD	:	Organization for Economic Co-operation and Development
O_o	:	Lattice Oxygen
OTM	:	Oxygen Transport Membrane
OTMR	:	Oxygen Transport Membrane Reactor
OTR	:	Oxygen Transport Reactor
P	:	Pressure
PCC	:	Phantom Camera Control
P_f	:	Fuel Firing Rate
PIV	:	Particle Imaging Velocimetry
PM	:	Polymeric Membrane
Po_2'	:	Partial Pressure of Oxygen (Higher side)
Po_2''	:	Partial Pressure of Oxygen (Lower side)

$\dot{Q}$	:	Volume Flow rate
R	:	Gas Constant
RANS	:	Reynolds Averaged Navier Stokes
RTE	:	Radiative Transfer Equation
∇	:	Divergence Operator
$\nabla \vec{v}^T$	:	Effect of Volume Dilation
S2S	:	Surface-to-Surface
S_h	:	Energy Source Term
S_i	:	Mass Source Term
SIMPLE	:	Semi-Implicit Method for Pressure Linked Equations
SPP	:	Steam Power Plant
T	:	Temperature
t	:	Time
T_{norm}	:	Normalized Temperature
UDF	:	User Defined Function
UNFCCC	:	United Nations Framework Convention on Climate Change
V	:	Volume

v	:	Velocity
$V_{ö}$	:	Oxygen Vacancy
w	:	Width
WD	:	Westbrook and Dryer
$WSGGM$	:	Weighted Sum of Gray Gases Model
Y_i	:	Specie Mass Fraction
Z	:	Mixture Fraction
Z_{st}	:	Stoichiometric Mixture Fraction
σ_i	:	Partial Ionic Conductivity
σ_e	:	Partial Electronic Conductivity
σ_s	:	Scattering Coefficient
ε	:	Emissivity
μ	:	Dynamic Viscosity
ρ	:	Density
$\bar{\bar{\tau}}$	:	Stress Tensor
φ	:	Equivalence Ratio
Ω'	:	Solid Angle
χ	:	Longitudinal Distance

ABSTRACT

Full Name : **Ibrahim Balarabe Mansir**

Thesis Title : **Oxy-Fuel Combustion Analyses of Porous and ITM Reactors for Boiler and other Applications**

Degree : **Doctor of Philosophy**

Major Field : **Mechanical Engineering**

Date of Degree : **May 2018**

Carbon dioxide is considered as the major greenhouse gas responsible for the current global climate change. There exist several technologies for reducing the emission of CO_2 by capturing it in the utility industries. Oxy-fuel combustion carbon capture technology offers a brighter future for emission-free society. The key concept of oxy-fuel combustion technology is the use of pure oxygen, obtained via air separation technologies, for combustion instead of air. Currently, the membrane separation technology is gaining high momentum due to its flexibility for different applications. In this study, two approaches were employed for the application of the oxy-methane combustion in gas turbine and fire-tube boiler applications. In the first approach, a face-to-face two-porous-plates reactor was developed to mimic the processes of oxygen permeation and oxy-fuel combustion in high-temperature membrane reactors (HTMR). In the second approach, numerical modeling of oxygen transport membrane (OTM) reactor for application in a two-pass fire tube boiler was conducted. It involved the analyses of oxygen permeation and oxy-fuel combustion characteristics to replace the existing fire-tube burner with bundles of OTM reactors that can supply power in the range from 1 to 5 MWe. In both approaches, methane was supplied, as a fuel, after being mixed in a sample stream with CO_2, as a diluent, while pure oxygen was supplied across the porous plates (in the first approach) and across the membrane feed

side (in the second approach). In both approaches, flow and oxy-fuel combustion characteristics were studied over wide ranges of oxidizer/diluent and equivalent ratios as well as gases inlet conditions. The combustion characteristics of the porous plate reactor were investigated experimentally and numerically. The results indicated enhanced mixing zone created beside the trailing edge of the porous plate and the flame located downstream of the porous plates. The temperature at the trailing edge of the porous plate ranges from 1130 K (at Φ=0.4) to 1240 K (Φ=1.0), which lies within the operating limit of operation of the ceramic membranes when the results are projected on HTMR operation. The minimum limit of $\%O_2$ to allow for a visible flame was found to be about 21% (79% CO_2) at stoichiometric condition. The combustor stability in terms of lean blow-out limit is affected by the fuel firing rate, equivalence ratio and the percentage of CO_2 addition. The numerical modeling of the two-pass OTM reactor revealed that, for the non-reactive conditions, the effects of gases inlet temperature and mass flow rates on oxygen permeation along the length of the membrane were meager within the scope of this study. The gases inlet conditions dictate the rate of oxygen permeation under reactive conditions. The relationship between membrane thickness and O_2 permeation was inversely proportional under both reactive and non-reactive conditions. The gases inlet temperature and mass flow rates control the amount of heat transfer to the load (Outer pipe). The sweep gas inlet condition was more critical to the stability of the combustion reaction. The boiler operating condition modeled based on the thermal load has insignificant effect on the heat transfer at fixed fuel firing rate. The radiative properties of the OTM reactor materials plays a major role in the total heat transfer to the load. The current design of the proposed OTM reactor can deliver power output in the range from 1 to 5 MWe.

ملخص الرسالة

الاسم الكامل: **إبراهيم بالاربي مانسير**

عنوان الرسالة: **تحليل حرق الوقود بالأكسجين لمفاعلات الأغشية المسامية وأغشية نقل الأكسجين المستخدمة في الغلايات والتطبيقات الاخرى**

التخصص: **الهندسه الميكانيكية**

تاريخ الدرجة العلمية: **مايو 2018**

يعتبر ثاني أكسيد الكربون هو العنصر الرئيسى فى الغازات الدفيئة المسؤولة عن التغير الحالى للمناخ العالمى. توجد عدة تقنيات للحد من انبعاث ثاني أكسيد الكربون في صناعات المرافق. توفر تكنولوجيا الحرق بالأكسجين لإحتجاز الكربون مستقبلاً أكثر إشراقًا من أجل مجتمع خالي من إنبعاثات الكربون. إن المفهوم الأساسي لتكنولوجيا حرق الوقود بالأكسجين هو استخدام الأكسجين النقي، الذي يتم الحصول عليه عبر تقنيات فصل الهواء، فى عملية الاحتراق بدلاً من الهواء. حاليا، تكتسب تقنية الفصل بالغشاء زخما عاليا بسبب مرونتها للتطبيقات المختلفة. في هذه الدراسة، تم استخدام طريقتين لتطبيق احتراق الميثان بالأكسجين تشمل تطبيقات التوربينات الغازية وغلايات أنابيب الحريق. في النهج الأول ، تم تطوير مفاعل ثنائى الألواح المسامية والمتقابلة وجهاً لوجه لمحاكاة عمليات فصل الأكسجين وحرق الوقود بالأكسجين في مفاعلات الأغشية عالية الحرارة. في النهج الثاني، تم إجراء النمذجة العددية لمفاعل غشاء نقل الأكسجين للتطبيق في غلاية أنبوب الحريق ثنائية المسار. وقد اشتملت الدراسة على تحليلات فصل الأكسجين وخصائص حرق الوقود بالأكسجين من أجل استبدال الموقد الموجود في غلاية أنبوب الحريق بمجموعة من مفاعلات غشاء نقل الأكسجين التي يمكن أن تزود الطاقة في نطاق يتراوح من 1 إلى 5 ميجاوات كهرباء. في كلا النهجين، تم تزويد الميثان، كوقود، بعد خلطه فى سريان واحد مع ثاني أكسيد الكربون، كمخفف، في حين تم تزويد الأكسجين النقي عبر الألواح المسامية (في النهج الأول) وعبر جانب التغذية للغشاء (في النهج الثاني). في كلا النهجين، تم دراسة خصائص السريان وحرق الوقود بالأكسجين على مدى نطاقات واسعة من المؤكسد/المخفف والنسب المتكافئة وكذلك ظروف دخول الغازات. تم دراسة خصائص الاحتراق للمفاعل ثنائى الألواح المسامية تجريبيا وعدديا. أشارت النتائج إلى تكون منطقة خلط محسنة بجانب الحافة الخلفية للوحة المسامية حيث استقر عندها اللهب. تراوحت درجة الحرارة عند الحافة الخلفية للوحة المسامية بين 1130 كلفن (عند نسبة تكافؤ 0.4) إلى 1240 كلفن (عند نسبة تكافؤ 1) والتي تقع ضمن

الحد التشغيلي لتشغيل الأغشية السيراميكية عند اسقاط النتائج على حالة استخدام مفاعلات الأغشية عالية الحرارة. تم العثور على الحد الأدنى المسموح من تركيز الأكسجين من أجل الحصول على لهب مرئي حوالى 21% (79% ثانى أكسيد كربون) عند الحالة المتكافئة. يتأثر استقرار اللهب من حيث حد انطفاء اللهب عند الخلط الهزيل بمعدل إحتراق الوقود ونسبة التكافؤ والنسبة المئوية لإضافة ثانى أكسيد الكربون. كشفت النمذجة العددية لمفاعل غشاء فصل الأكسجين ثنائي الممرات، بالنسبة للظروف غير التفاعلية، أن تأثيرات درجة حرارة مدخل الغازات والكتلة المتدفقة على معدل نفاذ الأكسجين على طول الغشاء كانت ضئيلة في نطاق هذه الدراسة. تحدد ظروف دخول الغازات للمفاعل معدل نفاذ الأوكسجين في ظل ظروف التفاعل. العلاقة بين سماكة الغشاء ومعدل نفاذ الأكسجين كانت متناسبة عكسيا تحت كل من الظروف التفاعلية وغير التفاعلية. تتحكم درجة حرارة دخول الغازات وتدفق الكتلة في كمية نقل الحرارة إلى الحمل. كانت حالة دخول غاز الكسح هي أكثر أهمية لاستقرار لهب الاحتراق. وجد أن حالة تشغيل الغلاية المصممة على أساس الحمل الحراري لها تأثير ضئيل على نقل الحرارة عند معدل حرق ثابت للوقود. تلعب الخواص الإشعاعية لمواد مفاعل غشاء فصل الأكسجين دورًا رئيسيًا في نقل الحرارة الكلي إلى الحمل. التصميم الحالي لمفاعل غشاء فصل الأكسجين المقترح يمكن أن يولد ناتج طاقة في المدى من 1 إلى 5 ميجاوات كهرباء.

CHAPTER 1

INTRODUCTION

1.1 Global Warming and CO_2 Emissions

Even though there have been different views about the causes of global climate change, there has been also unanimity in its occurrence and numerous climate experts are of the believe that greenhouse gases (GHG) anthropogenic emission in the atmosphere has been the ultimate cause of the current climatic change [1]. Among the main sources of anthropogenic greenhouse gases emissions, burning of fossil fuels has been identified as the main concern in the current century [2]. As reported by the International Energy Agency [3], the global energy consumption based on fossil fuel amounts to about 80% of the total global energy demand. This results in the emission of 32.3 Gt of CO_2 to the atmosphere in the year 2014 [3]. Recent findings indicated that about 40% of the global CO_2 emission is a result of electricity generation, with more than 30% coming from fossil fuels [3]. The current and future energy policy will be shaped by the fight against climate change, by committing to the emission reductions pledged by countries under the United Nations Framework Convention on Climate Change (UNFCCC) to achieve the 2^oC temperature rise by 2035 as agreed in Paris, 2015. Several routes for lowering CO_2 emissions can be applied including increasing of plant efficiency (provides reduction of CO_2 emission by 2-3% for increase of plant efficiency of 1%); decreasing of carbon content

in the fuel by utilizing less carbon fuels; reducing unnecessary fuel consumption and employing carbon capture and sequestration technologies (CCS) [2, 4]. A lot of efforts are being put to curtail the CO_2 emission by exploiting the latter option in the utility industries via research and development. In order to achieve the targeted 2oC temperature rise limit by 2050, one-sixth of the planned reduction in GHG emissions, is anticipated to be achieved through the application of CCS technologies [5].

1.2 Carbon Capture Technologies

CCS is the process of capturing, purifying, compressing, transporting and storing of unwanted CO_2 emitted from the above-mentioned sources. These technologies prevent the release of CO_2 into the atmosphere by storing it in underground geological formations or in depleted oil and gas fields [6]. The CCS technologies, as summarized in Figure 1.1, have been categorized as post-combustion, pre-combustion and oxyfuel combustion [7-10]. In pre-combustion process, the fuel carbon is converted into syngas at initial stage before the combustion process. This can convert up to 90% of the carbon contained in the fuel into a synthetic gas via reforming or gasification processes. The pre-combustion is still a premature technology that requires major modifications to the current fossil power plants and huge investment if is to be applied to new fossil fuel power plants [8]. In post-combustion technology, carbon dioxide emission is mitigated by separation and removal of CO_2 from the flue gases via absorption using solvents (basically amines), adsorption using metal organic framework, as well as CO_2 selective membrane separation. This technology is yet to be available in commercial scale due to the challenges in large scale

amine processes, high purity of flue gas requirements by most sorbents, extraction of steam to regenerate solvents and additional water consumption. This technology requires additional energy (25 to 30%) for plant operation as well as high capital and recovery costs [11]. In oxy-fuel combustion technology, pure oxygen is being used for the combustion of fuel resulting in only H_2O and CO_2 as by-products of combustion. Oxy-fuel combustion process results in high combustion temperature and hence part of the flue gas is recycled into the combustion zone to lower the combustion temperatures to within allowable limits to maintain material integrity. The flue gas of high CO_2 concentration is usually dried, purified, and compressed for further storage as mentioned.

Among the fossil fuel sources of CO_2 emissions, combustions of natural gas (usually containing about 95% methane) has been an important contributor globally. The United States Energy Information Administration projected that the contribution of the CO_2 emission from natural gas combustion may reach about 8.6%, exceeding the 2007 contribution of 5.93% of the world's energy-related CO_2 emissions [12]. Although coal-fired steam power plants (SPP) have been the focal point of most studies on CCS technologies due to its higher CO_2 emissions, the natural gas-fired combined cycle (NGCC) power plants are also being considered. The current 350g CO_2/kWhel specific emissions of natural-gas in NGCC power plants can be reduced to below 100g CO_2/kWhel by the application of the CCS technologies [13].

1.3 Oxy-fuel Combustion Technology

CCS Oxy-combustion technology is among the foremost technologies that are being considered recently for CO_2 capture from power plants. Oxy-fuel combustion is the process of combusting/burning fuels with pure O_2 rather than air. It is characterized by high flame temperatures which necessitate the recycling of some part of the flue-gases back in to the combustor in order to control the flame temperature. There has been significant progress in the development of oxyfuel combustion technology after the International Panel for Climate Change (IPCC, 2005) publication of its special report on CO_2 capture and storage [14]. Most of the existing power plants utilize air as the oxidizer for combustion, meanwhile oxyfuel combustion concept requires the use of pure oxygen. This necessitates the oxygen separation from air using various techniques in order to fit into the conventional as well as the future power plants. As shown in Figure 1.2, the three main air separation processes are cryogenic, membrane and solid sorbent processes [15, 16]. The most established technology among the three is the cryogenic distillation which allows for large scale production of O_2 at very high purities (up to 99%) at low temperature [16, 17]. Despite the production of high purity of O_2 by this technique, the design complexity, high energy demand as well as low exergetic efficiencies (15-24%) necessitate the investigation of alternative air separation concepts [18, 19]. The solid sorbent (adsorption) process, despite having O_2 purity of up to 95%, has not been fully mutualized due to excessive capital requirements of the solvent [17, 20]. The most recent separation technology is the membrane separation which includes the use of polymeric membranes (PM) and high temperature ion transport ceramic membrane (ITM). The polymer-based membrane can provide O_2-enriched air at higher concentrations (60–80%) with low energy consumption

in comparison with the cryogenic and adsorption techniques [16, 21]. Whereas, the PM can enrich the oxygen content in air up to 80% and ion transport membranes can achieve near 100% oxygen purity, even though both types of membranes are still under developmental [16, 21]. The use of ITMs for O_2 separation has been given significant attention much research due to its potential of reduction in cost of energy requirement for the production of O_2 by about 35%. This can be ascertained by assessing the file of patents and research publications on the matter over the last decade [20]. There are some proposals to combine the above membrane technologies to produce high purity O_2, however the ideas have not been yet fully exploited [16].

Recently, many researchers, with interest in the study of oxy-fuel combustion using membranes for air separation, dwell more on the use of mixed ionic and electronic conducting ceramic membranes. This can be seen from the current effort by many industries in the development and optimization of these membrane technologies for combustion as well as synthetic gas (syngas) production via methane partial oxidation [22-26]. Among the membrane materials for O_2 permeation that are currently under extensive studies, are basically the perovskite type ceramic membranes with some recent modifications [22, 26, 27]. Successful implementation of oxy-fuel combustion on mixed ionic-electronic conducting (MIEC) membranes is the ultimate goal that will allow conventional combustors to be replaced with oxygen transport membrane reactors (OTMRs), where oxygen separation and oxy-combustion are co-located at the membrane instead of being performed separately.

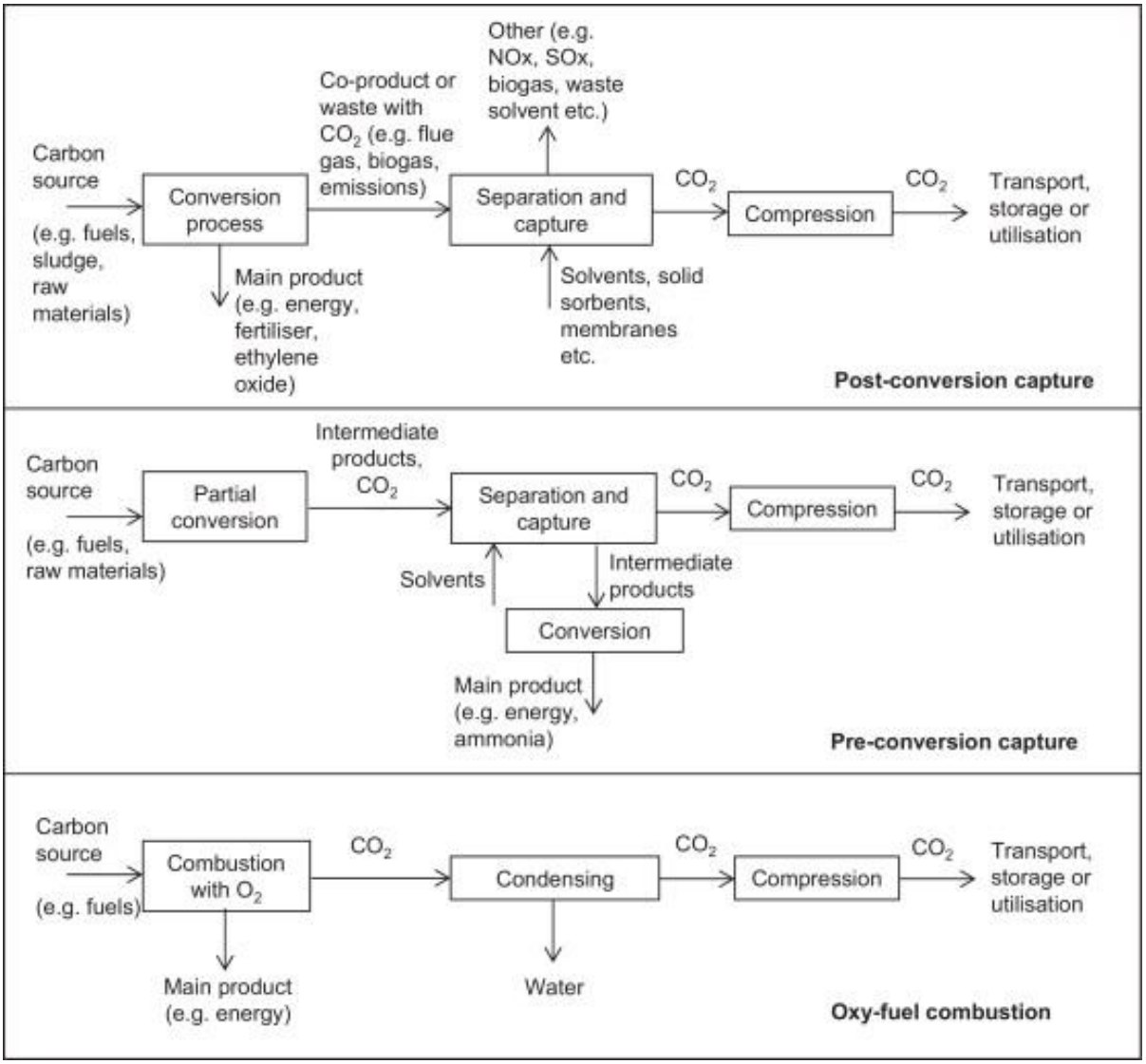

Figure 1.1: CO_2 Capture Technologies [9, 10].

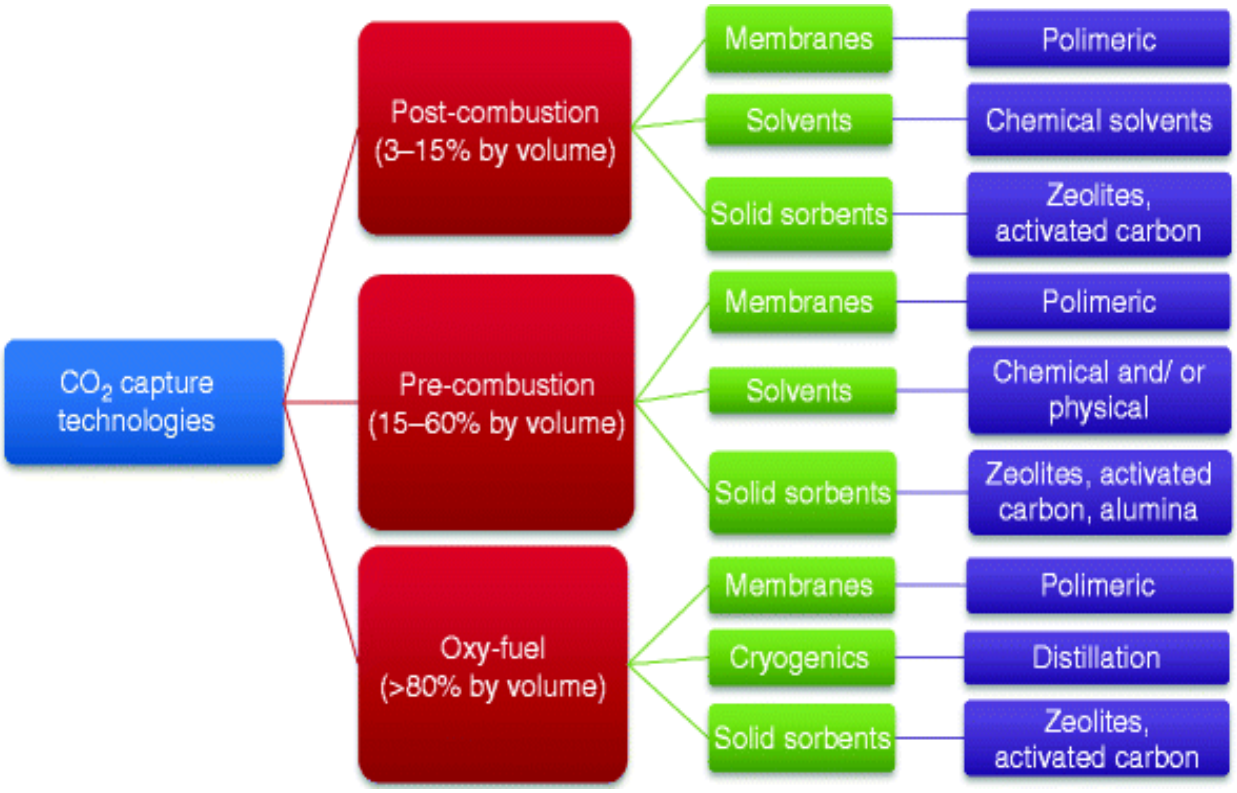

Figure 1.2: CO_2 Capture Options [15].

The present research study is focused on experimental testing and numerical simulations of oxy-fuel combustion characteristics in a face-to-face two porous-plates reactor. Also, numerical simulations of oxygen transport membrane reactor for application in fire tube boilers were performed. All numerical simulations involved validation of the different numerical models with the currently available experimental data in available literature and with the experimental data collected from the present studies. Combining the process of oxygen separation using ceramic membrane with the oxy-fuel combustion of fuel in the sweep side of the membrane using the separated oxygen results in a compact unit for power production that is called as high-temperature membrane reactor (HTMR). One of the goals

of the present study is to mimic the process of oxygen separation and oxy-combustion inside HTMR using the porous-plate reactor.

In the porous-plates reactor studies, both the flow field and oxy-methane combustion characteristics were investigated experimentally and numerically over wide ranges of mixing conditions and equivalent ratio. This reactor mimics the process of oxygen permeation and oxy-fuel combustion inside the HTMR. The process of oxy-combustion inside the HTMRs is difficult to be achieved at normal lab conditions and the oxygen permeation flux across the membrane still not enough for complete fuel combustion. Because of that, porous plates are used in the present study instead of membranes to investigate the flame characteristics and location with respect to the porous plate that should help in the development of HTMRs. Firstly, the non-reactive flow characteristics were investigated experimentally and numerically to predict the flow mixing behavior and the location of the flame zone. Particle Imaging Velocimetry (PIV) technique was used to visualize the non-reactive flow in the main channel under oxygen permeation in terms of average axial velocity of the main stream flow, velocity vectors and streamlines. Secondly, flow field and oxy-combustion characteristics of methane were investigated numerically over ranges of operating conditions. Experimental investigation of the combustion characteristics and lean blow-out (LBO) limits of non-premixed oxy-methane diffusion flames in a porous-plate reactor were performed over wide ranges of operating conditions.

1.4 Research Objectives

The present research study is focused on experimental testing and numerical simulations of oxy-fuel combustion characteristics in a porous-plate reactor. Also, numerical simulations of ion transport membrane reactor for application in fire tube boilers are performed. All numerical simulations will involve validation of the different numerical models with the currently available experimental data in the open literature and with the experimental data collected from the present experiments. The following are the specific objectives:

1. To investigate the flow and combustion characteristics in a porous plate reactor for oxy-fuel combustion applications.

a. To experimentally determine the non-reactive flow-field characteristics at fuel-lean equivalence ratios:

   i. Velocity vectors
   ii. Streamlines
   iii. Velocity profiles
   iv. Average velocities

b. To experimentally determine the combustion characteristics at different equivalence ratios and diluent/oxidizer ratios on:

   i. Flame structure
   ii. Exhaust temperature
   iii. Lean flammability limits (Lean Blowout, LBO)

c. To develop and validate numerical models of non-reactive flow and oxy-combustion to determine the influence of the following parameters on the flame structure, combustion temperature and exhaust compositions:

i. Mixture fractions
ii. Effects of equivalence ratio
iii. Effects of diluent addition

2. To develop and validate numerical models for oxygen separation and oxy-combustion in a two-pass oxygen transport reactors (OTR).

a. To develop the geometry of the two-pass OTR for fire-tube boiler applications.

b. To investigate numerically the characteristics of oxy-combustion of methane in the two-pass OTR in terms of:

i. Effects of inlet temperatures of feed and sweep gas on O_2 permeation flux.
ii. Effects of feed and sweep gas inlet mass flow rates on O_2 permeation flux.
iii. Effects of diluent flow rates on O_2 permeation flux.
iv. Thickness of the oxygen transport membrane (OTR) on O_2 permeation flux.

c. To study the effects of the following parameters on heat transfer to the water jacket along the OTR.

i. Gas streams inlet temperatures.
ii. Gas streams inlet mass flow rates.
iii. Diluent mass flow rates.
iv. Operating temperature of the boiler.
v. Emissivity of the inner and outer pipes.

CHAPTER 2

LITERATURE REVIEW

2.1 Carbon Capture and Storage Technologies

The major GHG contributor to the recent climate change has been the carbon dioxide gas from combustion of fossil fuels and other industrial processes. For a decade estimate (from 2000 to 2010), out of about 78% of the total increase in GHG emissions throughout the period resulted from the emissions of CO_2 via combustion of fossil fuels as well as other industrial practices [28]. Among the fossil fuel sources of CO_2 emissions, combustion of natural gas (usually containing about 95% methane) has been an important contributor globally. The main reason of natural gas being a strong competitor in CO_2 emission amid other resources is its profusion and vigorous production. Its fuel efficiency and cleaner combustion made it more salient for new power plants among other fuels such as other petroleum products or coal [29]. As projected by the International Energy Outlook 2016 (IEO2016), the worldwide natural gas consumption will upsurge from 120 to 203 trillion cubic feet (Tft3) in the period from 2012 to 2040 as shown in Figure 2.1 [29]. As reported by the IEO2016 [29], the natural gas industrial consumption increases by about 1.7% annually, while the consumption will increase by about 2.2% annually for electricity generation purposes within the period from 2012 to 2040 as shown in Figure 2.1. Although the coal-fired steam power plants (SPP) have been the focal point of most studies on CCS technologies due to its higher CO_2 emissions, the power plants based on natural gas-fired

combined cycle (NGCC) are also being considered. The current and future energy policy will be shaped by the fight against climate change by committing to the emission reductions pledged by countries under the United Nations Framework Convention on Climate Change (UNFCCC) to achieve the 2^{o}C temperature rise by 2035 as agreed in Paris, 2015. The CCS technologies, as summarized in Figure 2.2, has been classified as pre-combustion, post-combustion, and oxy-fuel combustion [7-10].

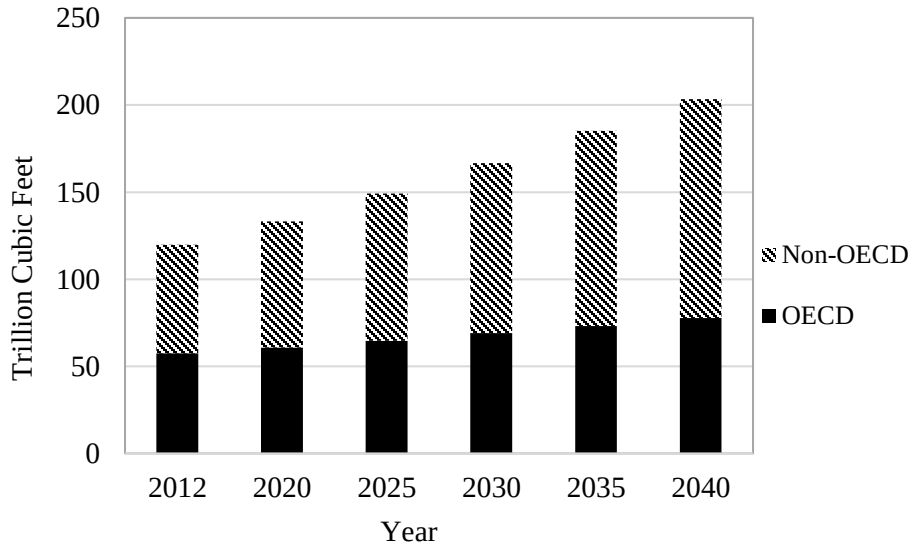

Figure 2.1: World natural gas consumption from 2012 to 2040 [29].

2.1.1 Pre-combustion carbon capture

Pre-combustion carbon capture entails the reaction of fuel with air or O_2 and/or steam thereby producing a fuel gas (synthetic gas or syngas), consisting primarily a mixture of carbon-monoxide (CO) and hydrogen (H_2). The CO is then reacted with the steam using catalyst to produce more H_2 and CO_2 and a process called shift conversion. This can convert

up to 90% of the carbon contained in the fuel into a synthetic gas via reforming or gasification processes [11]. In the steam reforming process, steam is reacted with fuel to generate syngas (Reaction I). When O_2 is added to liquid or gaseous fuels in a process refers to as "partial oxidation reaction", the syngas is as well formed, and the process is called "gasification" when solid fuel is used for the oxidation (Reaction II). The final conversion of the syngas into CO_2 and H_2O by steam addition is termed as "water-gas shift reaction as shown in Reaction III [11, 29, 31].

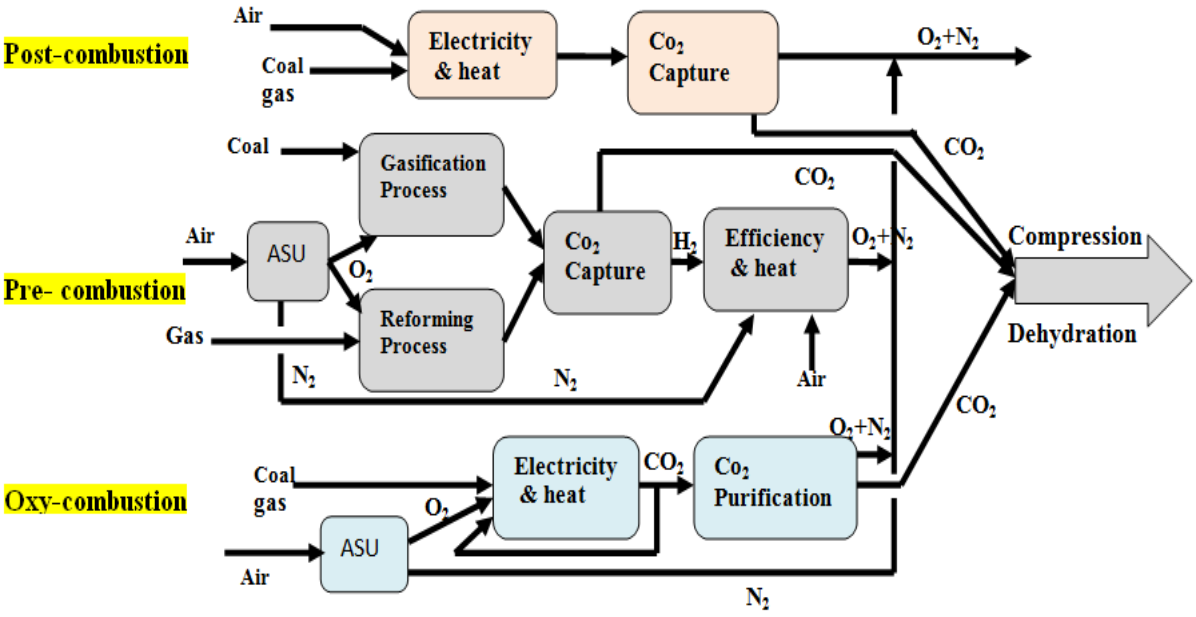

Figure 2.2: Three CO_2 capture processes [30].

The schematic diagram of pre-combustion capture for power generation as well as its' principles of operations are shown in Figures 2.3 and 2.4, respectively.

Steam reforming:

$$C_aH_b + aH_2O \leftrightarrow aCO + (a + b/2)\ H_2 \qquad \text{REACTION I}$$

Partial oxidation:

$$C_aH_b + a/2\ O_2 \leftrightarrow aCO + (b/2)\ H_2 \qquad \text{REACTION II}$$

Water-gas shift:

$$CO + H_2O \leftrightarrow CO_2 + H_2 \qquad \text{REACTION III}$$

The CO_2 generated is separated through a physical or chemical absorption process and further purified for compression and storage, while providing H_2-rich fuel that can be utilized for various applications, like in furnaces, fuel cells, gas turbines, boilers, etc. [11]. The pre-combustion path to CO_2 capture in the existing power plants has been applied to Integrated Gasification Combined Cycles (IGCC) as well as Natural Gas Combined Cycles (NGCC). Currently only about four power plants operating on IGCC are in operation worldwide but without CO_2 capture implementation. The US Kemper County-Mississippi Power has been the only known IGCC plant equipped with CO_2 capture technology even though it is not yet operational at full scale [11]. The additional cost for the generation of syngas made NGCC less economically palatable in comparison to other carbon capture options [32, 33]. The pre-combustion technologies which is still premature require major modifications to the current fossil power plants and require huge investment if is to be applied to new fossil fuel power plants [8].

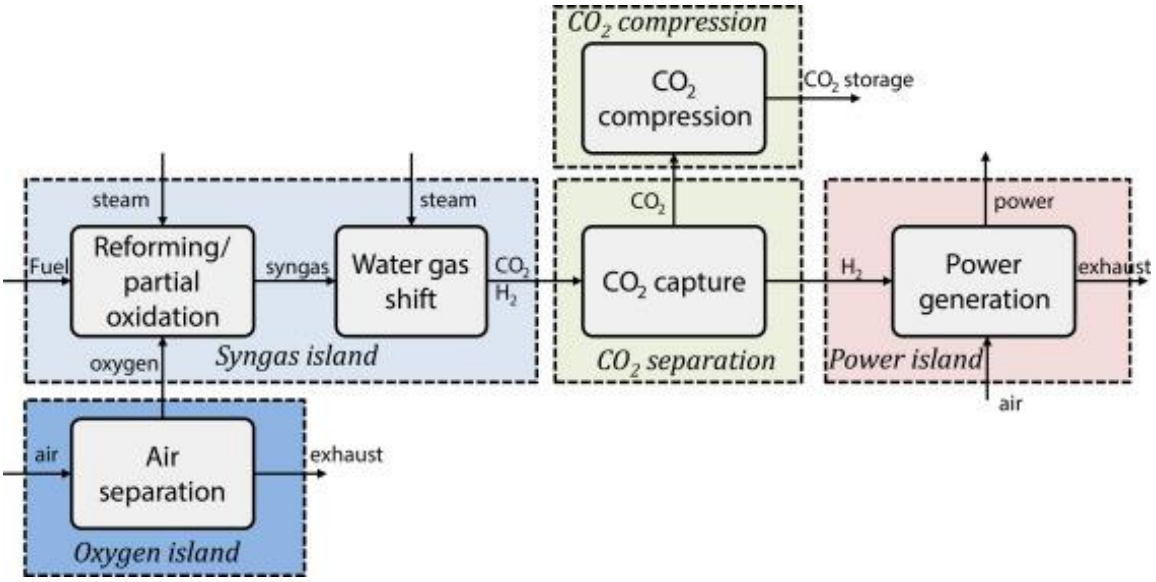

Figure 2.3: Schematic diagram of pre-combustion capture for power generation [11].

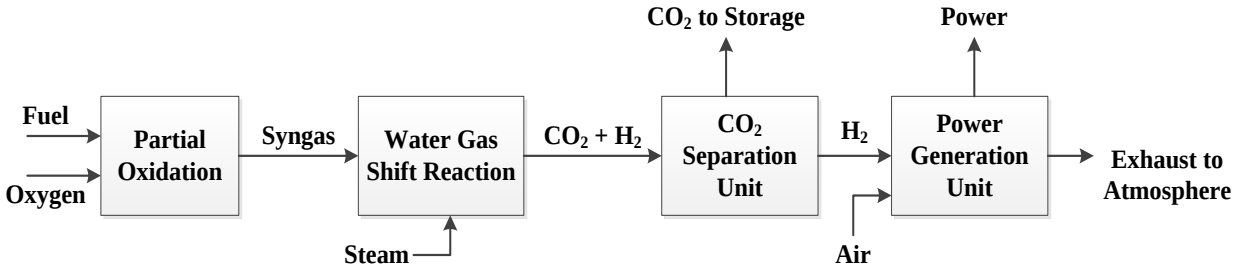

Figure 2.4: Principle of pre-combustion CO_2 capture [34].

2.1.2 Post-combustion carbon capture

In post-combustion technologies, the carbon dioxide emission is mitigated by separation and removal of CO_2 from the flue gases via absorption using solvents (basically amines), adsorption using metal organic framework, as well as CO_2 selective membrane separation, as shown in Figure 2.5. The use of liquid solvents (amine based) has been the most established technology for the post-combustion CO_2 capture [35-37]. The solid sorbents

adsorption concept has also been considered as promising alternative technologies [36, 38]. The adsorption technology has been extensively studied for the gas separation in industrial based processes such as purification of H_2 [39], air separation and drying [40, 41], separation of hydrocarbons [42], etc. This technology is yet to be available in commercial scale due to the challenges in large scale amine processes, high purity of flue gas requirements by most sorbents, extraction of steam to regenerate solvents, additional water consumption etc., requiring additional energy (25 to 30%) for plant operation as well as high capital and recovery costs [11, 43].

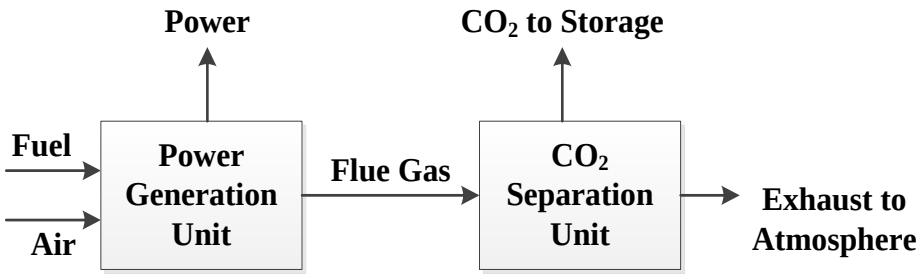

Figure 2.5: Principle of post combustion CO_2 capture [34].

2.1.3 Oxy-fuel combustion carbon capture

In oxy-fuel combustion process, mainly pure O_2 is being utilized for the fuel combustion resulting in only H_2O and CO_2 as the by-products of the combustion. Oxy-fuel combustion process produces very high temperature and hence part of the flue gas is usually recycled into the combustion zone to lower the exhaust temperatures to within allowable limits to maintain material integrity. The flue gas containing mostly CO_2 is usually dried purified and compressed for further storage as mentioned. The schematic diagram of oxy-combustion capture process is shown in Figure 2.6.

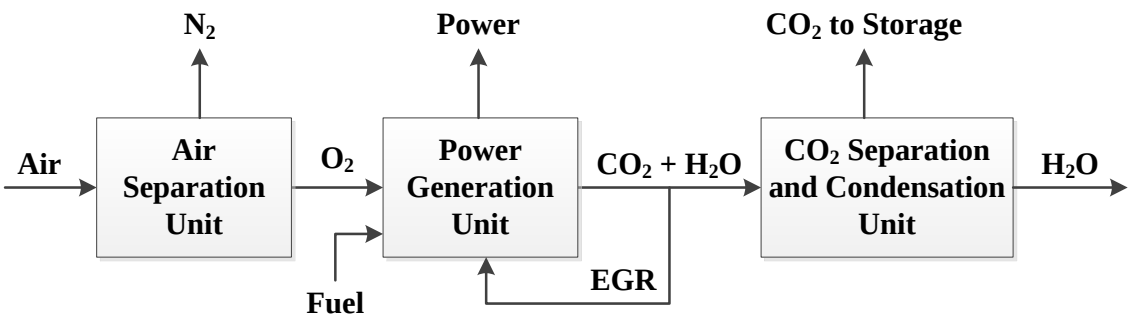

Figure 2.6: Principle of oxy-fuel combustion CO_2 capture [34].

2.1.4 CO_2 Transport and storage

There have been plenteous ways of transporting gaseous CO_2 captured based on the above capture technologies in a safe, economical and reliable fashion. These include surface or underground pipeline transportation, across sea or oceans on ships, road tankers [44]. The transport technology is speedily being developed based on the adoption of progress made in the natural gas transportation in the recent history. The captured CO_2 can either be utilized or stored in underground geological reservoirs [45, 46]. The CO_2 can be utilized by recycling it for reuse in food industries, agriculture, as fire extinguishers, refrigeration systems, energy productions, mineralization process, methane and methanol production via photo-catalysis of CO_2 etc. [45-49].

The major factors that need to be considered in CO_2 storage is the ability of the storage sites to possess; little environmental influence, high level of safety characteristics and

capability to conform to technical and geological standards [50-52]. On these bases, there are three major ways through which storage of the captured CO_2 may be achieved: geological storage, ocean storage and calcination process. Out of the three methods of CO_2 storage outlined above, geological storage happened to the highly considered one since it is also used by petroleum industries for decades to improve their rates of production and to ensure total productivity lifespan of the field [53]. Geological storage consists of three key options which include injection into: coal bed, deep saline aquifers or depleted hydrocarbon reservoirs [54, 55]. CO_2 storage in a deep saline aquifers and depleted hydrocarbon reservoirs normally achieved at a depth of 800 m and lower where it is believed that the conditions (i.e. temperature and pressure) will enable the CO_2 to be stored in a supercritical state (31.1 ^{o}C and 7.38 MPa). At this situation, there will be no distinction between vapor and liquid phase and the CO_2 will possess both gas-like property (i.e. compressible fluid) and liquid-like property (i.e. density in the rage of that of crude oil) [50, 51] which eventually make it suitable for replacement. Figure 2.7 shows typical injection of CO_2 into depleted hydrocarbon reservoir. In case of ocean storage, CO_2 is injected to ocean at a depth below 1000 m where the pressure, temperature and salinity are good enough to maintain both the stability and long-time storage of the CO_2. The calcination process involves the conversion of CO_2 to inorganic solid carbonates by using alkaline oxides. Though, the process may be natural, but it occurs very slowly.

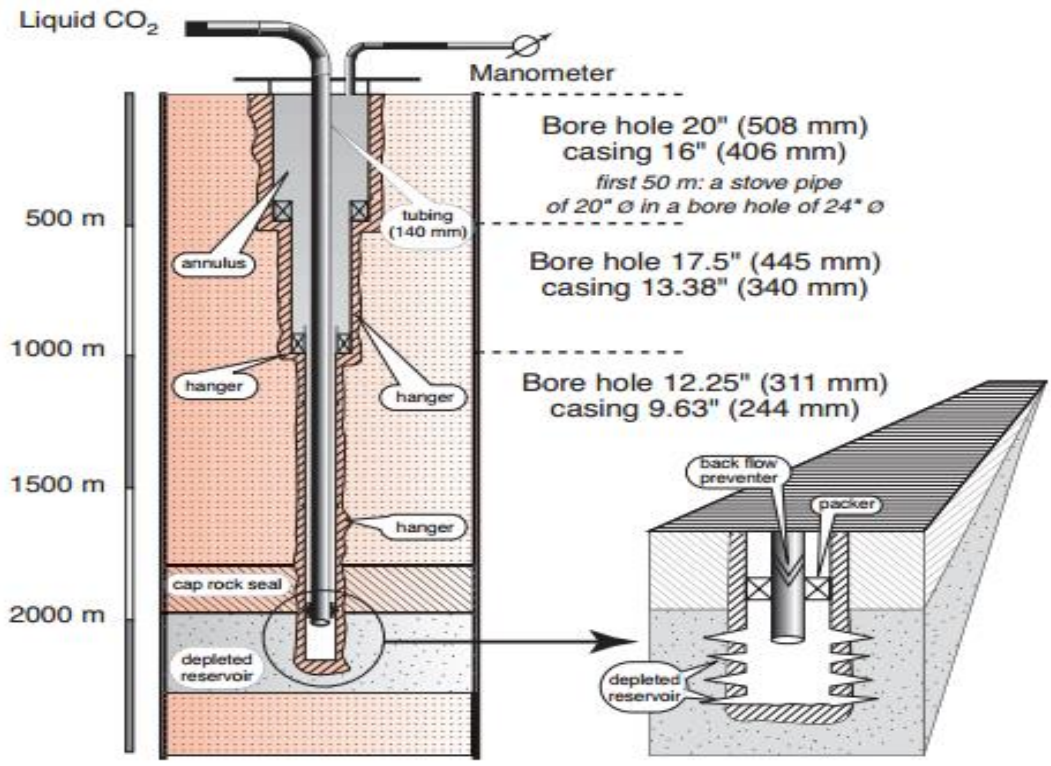

Figure 2.7: Layout showing typical injection of CO2 into depleted hydrocarbon reservoir [50].

2.2 Characteristics of Oxy-fuel Combustion

Oxy-fuel combustion technology is among the proposed CO_2 capture technology with promising prospect for power generation and carbon free society. Since technology involve combustion of fuel with pure O_2 rather than air, the exhaust flue gas mostly comprises of CO_2 and H_2O. The water can be condensed, and other possible contaminants also removed from the exhaust stream leaving only stream of pure CO_2 that can be reused or compressed and stored. One of the main characteristics of this combustion is relatively high temperatures in the combustion zone. Nitrogen has been providing dilution in the reaction

zone, but that effect is no longer available since only pure O_2 is being reacted. Hence portion of the exhaust flue gas is being recirculated back in to the combustion zone to provide the required temperature moderation as well as compensate for the dilution lost in the combustion process [56].

There has been extensive research on oxy-fuel combustion as reported in many literatures. Currently, the mainstream of the oxycombustion research are focused on the combustion of pulverized coal [57]. The main items of interest as reviewed by [57-61] focused mainly on fundamentals of oxy coal combustion, with keen interest in combustion emissions, heat transfer, flame stability, issues related to ash, CFD modelling as well as techno-economic evaluation of pulverized fuel combustors. They recognized the need for more research to further understand the fundamental changes that occurs when applying the oxy-coal combustion technology to the conventional air-fired combustors and the new plants. These include the effect of feed oxygen concentration as well as the recycled CO_2 ratio, heat transfer, ignition delay, emissions, burn-out, retrofitting cost and the overall CO2 capture cost. Similarly, the following conclusions were made with regards to the application of oxyfuel technology to pulverized fuel combustion as reported by [62-77]: (1) the aerodynamics of pulverized fuel particles and turbulent flows of air-fired coal combustion can easily be modified and applied to oxyfuel combustion. (2) Refinement of models for gaseous radiative heat transfer as well as soot formation in oxycombustion applications. (3) Refinement of the global turbulence–chemistry interaction to a more robust one due to the high-concentration CO_2 and H_2O in the oxycombustion process which has effect on the combustion at gas phase. (4) About 70-80% reduction in NOx emission in oxyfuel

combustion with similar fuel bound NOx to air-fired combustion. (5) Modification to the WSGGMs currently being implemented to eliminate the discontinuity problem and improvement of particle radiation which overwhelms gas radiation in pulverized fuel combustors. (6) Requirement of more experimental and numeral data with regards to ignition and burnout under precise oxy-fuel conditions. (7) The need to study the effect of oxycombustion conditions on the amount of inorganic elements released and their corrosive effect as well as formation of aerosols, aggravate pollution, and fly ash emissions. (8) Investigation into the fundamental basics of advanced oxy-fuel technologies like flameless and mild oxycombustion as well as biomass oxycombustion. (9) Need for more research and developments for low energy penalty, low capital costs, higher efficiency in form of design, modeling and optimization of CCS systems.

To obtain the same mass fraction of O_2 in atmospheric air in a CO_2-O_2 mixture, the volume fractions of CO_2 and O_2 has to be 70 and 30% respectively [56]. Also, the increase in CO_2 and H_2O from the recycling process in oxycombustion results in higher emissivity and heat capacity of the exhaust mixture which enhances both convection and radiation heat transfer [56]. The main factor for sizing an oxy-combustor has been found to be the higher radiation heat release [19]. This due to the increased CO_2 and H_2O concentrations in the exhaust stream. Recently, Martin et al., [78] studied the radiative heat release from oxy-methane as well as oxy-syngas in a laboratory scale premixed combustor. They assess the effects of equivalence ratio, diluent (CO_2) addition, firing input as well as H_2 addition on the radiation heat released. They found that for the syngas flames, the higher the firing inputs the lower the radiative heat release factor. Whereas the same trend was also observed due to increase

CO_2 recirculation ratios on the radiative heat release factor, the opposite was the case when H_2 content was increased.

Gas turbine model combustor was used to study the oxyfuel flames at atmospheric pressure. The flame structure and stability of partially premixed and swirl stabilized combustor, with equivalence ratio range of 0.5 – 1.0, O_2 mole fractions of 20 – 40%, and power of 10 – 30 kW were studied by [79] by using OH- chemiluminescence imaging. Their results showed that the lower limit of O_2 mole fraction was 22% below which instability as well as blow-out were observed, even at stoichiometric and higher power operation. Similar range of equivalence rations were investigated by [80], for the flame structure and stability at various O_2/CO_2 ratios, ranging from 100/0 to 25/75, in a model gas turbine combustor. They also reported 21% O_2 as the lower stable and blow-out limit. They also achieved lower exhaust gas temperature with increase in equivalence ratio. The stability of the oxyfuel flame is usually affected if the percentage O_2 in the oxidizer mixture is less than 25% with extinction at condition below 21% as reported by [81]. Under premixed oxyfuel laminar combustion conditions, the effect of adding CO_2 and H_2O on the laminar burning velocity of $CH_4/O_2/N_2/H_2Og$ as well as $CH_4/O_2/CO_2/H_2Og$ in a combustor at atmospheric pressure and 100^oC reactants inlet temperature, for the range of equivalence ratio of 0.5 to 1.5 showed a quasilinear drop in flame speed in both diluted cases [82]. The decrease in flame speed was also reported by [83] when CO_2 replaces N_2 in the oxidizer there by decreasing the performance of the combustor in terms of the species and temperature distributions.

On the study of the chemical effects of CO_2 recirculation on the heat release rates and the flame speed, several works have been reported [83-86]. As reported by [85], the burning velocity of methane combustion is significantly reduced because of CO_2 chemical effect. When compared with air-fired combustion, the chemical effects of CO_2 in oxyfuel combustion reduce the combustion temperature in a manner analogous to the physical effects of CO_2 in an atmosphere containing 36% O_2 and 64% CO_2 [84]. Whereas for the mole fractions between 20 to 28%, the heat release rates due to the reactions $OH + CO \Leftrightarrow CO_2 + H$ and $CO_2 + CH_2(S) \Leftrightarrow CO + CH_2O$ are usually the most profoundly impacted by the addition of CO_2, the effect of the CO_2 on the basic reactions when the O_2 mole fraction was increased from 28 to 32% counterbalance each other [84].For the range of O_2 mole fractions from 32 to 36%, the most impacted reactions heat release rates are that of $H_2 + OH \Leftrightarrow H_2O + H$ and $O_2 + H \Leftrightarrow OH + O$, and for the range of 36 to 50%, the reaction $OH + HO_2 \Leftrightarrow O_2 + H_2O$ is the most highly influenced by CO_2 addition [84].

In order to maintain stable flame under oxy-combustion conditions, there should be certain minimum amount of oxygen concentration in the oxidizer to enable sufficient temperature levels within the combustor to sustain the combustion reactions. The premixing of O_2 and CO_2 as oxidizer at certain ratios reported to exhibit poor burnout and flame instability [87]. Heil et al. [88] also reported flames lift-off and poor burnout when the O_2 molar concentration in the oxidizer mixture (CO_2+O_2) was set to 21% and stable flame and full fuel burnout were obtained while increasing this ratio above 27%. While increasing O_2 concentration in the oxidizer mixture, the temperature of the combustion exhaust gases was increased as well as excess O_2 in the exhaust stream was reported. Liu et al. [89] reported

24%/76% molar ratio of O_2/CO_2 as the minimum oxidizer lower stability limits for gas turbine combustion applications. Peter Kutne et al. [79] studied the stability of swirl stabilized flames based on oxy-methane combustion for the range of equivalence ratio from 0.5 to 1 and thermal power from 10 to 30 kW for O_2 mole fraction in the inlet oxidizer mixture from 20% to 40%. They reported unsuccessful combustion when the O_2 mole fraction was below 22% for all considered ranges of power and equivalence ratio due to blowout and flame instabilities. Carbon dioxide addition, as a diluent, affects the oxy-combustion characteristics of natural gas flames in terms of variations in the following parameters within the combustor [82-86, 90-96] (a) adiabatic flame temperature of the mixture, (b) radiative heat transfer, (c) transport properties-viscosity, mass diffusivity, thermal conductivity, (d) specific heat of the mixture, (e) chemical kinetic, and (f) flame structure. Therefore, oxy-methane combustion in an environment of high CO_2 concentrations provides fresh combustion challenges and opportunities for the study of the above parameters.

The use of porous plate reactors has been increased significantly due to its flexibility of introducing the oxidizer mixture through the whole combustion chamber. This is of immense importance in case of oxy-fuel combustion to uniformly distribute O_2 through the whole combustion chamber and, accordingly, reduce the creation of elevated temperature spots within the flame zone. Habib et. al., [97] studied the characteristics of oxy-fuel combustion in a porous plate reactor experimentally and numerically for the reactive and non-reactive cases. The results showed uniform temperature distribution through the porous plates due to the uniformity of oxygen distribution through the combustion zone.

The effect of oxy-fuel mixing is significant especially for porous plate reactors as it affects directly the combustion chemistry within the combustor. Mixture fraction is defined as the fraction of the fluid mass that originates as fuel. Mass fractions for all other species can be derived based on state relationships from the mixture fraction [98].

Combustion models based on the mixture fraction concept has been commonly used to simulate and evaluate the combustion characteristics in combustors and fire models, including the Fire Dynamics Simulator (FDS) developed at the National Institute of Standards and Technology (NIST) [99]. Numerical simulations, using the Commercial CFD software, CFX-11, were performed by Dharavath et al. [100] to investigate the effect of equivalence-ratio on the combustion behavior and air-fuel mixing on the full-scale scramjet combustor of a hypersonic air-breathing vehicle with ethylene fuel at ground test conditions by solving species transport equations, k-ω turbulence model as well as the three-dimensional RANS equations. They validated the computational results against an experimental data available in the literature and then performed parametric study of the full-scale combustor performance parameters, namely: total pressure loss, combustion efficiency, and thrust [100]. A similar work was conducted by Han et al. [101] to investigate the effects of air–fuel mixing quality on combustion parameters for two low temperature diesel combustion regimes using conventional diesel combustors. They found that the intake and injection pressures are the most crucial factors influencing the air–fuel mixing process. To achieve the different combustion regimes, they varied the concentration of intake oxygen. The improvement of air–fuel mixing with enhanced combustion process in the two cases was studied [101].

2.2.1 Lean blow-out limit

Flame blowout occurs when the flame is incapable of sustaining combustion at locations downstream from the exit of the combustor [102, 103]. Karbasi and Wierzba [104] studied the effect of dilution of fuel jet for a co-flow arrangement in order to determine the velocities at the flame blowout. The diluents used were Nitrogen, Helium, and carbon dioxide. It was found that the addition of the diluent in the co-flow has a greater influence on the blowout limit in comparison to the case when the diluent was premixed within the fuel jet. The diluents, in descending order of their influence, are CO_2, N_2 and He. Several models were developed based on flow exit velocity and fuel properties to estimate the blowout limits. The method relies heavily on how the fuel velocity and diluent, or co-flow are measured. Mostly, the blowout limit is found to decrease with increase in the flow velocity [102]. The LBO has been theoretically characterized using two different approaches [105-107]. The first approach is based on the Damköhler (Da) number concept, defined as the ratio of characteristic mixing time to the characteristic chemical reaction time. It is based on the postulation that lean blowout occurs when the residence time is not sufficient time enough to allow for the chemical reactions to occur. The second method considers the ratio of the flame speed to the flow speed based on the assumption of flamelet-like combustion, in that, the lean blowout occurs when the flow speed exceeds the flame speed at critical positions within the combustor [108]. In both the approaches, lean blowout is influenced by heat content, fuel kinetic characteristics, diffusivity, and the flow field of the combustor [109].

2.3 Modeling of Oxy-fuel Combustion

Computational fluid dynamics (CFD) refers to the analysis of systems involving heat transfer, fluid flow, as well as the other related phenomena using computer-based simulation [110]. The CFD has become a very important tool with many areas of application spanning across many fields such as: power plants, combustion systems, ships hydrodynamics, vehicles and aircraft aerodynamics, turbomachinery, electrical and electronic, chemical processes, marine engineering, oceanography and hydrology, meteorology, biomedical engineering, heating-ventilation and air-conditioning, etc, [110-115]. There have been enormous applications of CFD in design optimizations, troubleshooting and analysis in various engineering and non-engineering fields.

2.3.1 Reduced reaction mechanism for oxy-fuel combustion

Combustion related applications of CFD technique has also been reported in many literatures employing detailed and reduced reaction mechanisms. The application of the CFD in industries is usually computationally demanding [116]. This necessitate the use of reaction mechanisms that are simplified to minimize the computing task. Despite the recent use of detailed reaction mechanism in combustion as the result of the current upsurge in computational capabilities and more accuracy, the reduces or global mechanisms are still preferred due to economic considerations [117]. Some of the most recent applications of the reduced mechanism in CFD combustion simulations available in the literature are reported by [117-128]. It is widely accepted that, in order to simulate complex geometries

as well as complex geometry, simplified kinetic mechanisms are essential. Among the well-known applicants of the reduced schemes are Westbrook and Dryer (WD) and Jones and Lindstedt (JL) [129, 130].

The higher temperature associated with oxy-fuel combustion make application of the reduced mechanisms less valid. Most of the reduced mechanisms do not include dissociation reactions as well as radicals. Thus, in order to implement the schemes for oxycombustion systems, the mechanisms are being re-modified and validated against available experimental data [117-128]. In the case of combustion of methane with air, when temperature or CO concentration are of interest the reaction rate parameters need to also be modified, the frequently used simplified global reaction mechanisms are those developed and offered by Westbrook and Dryer as well as Jones and Lindstedt, as shown in the Appendices A - H.

Two-Step Westbrook and Dryer Mechanism

The WD mechanism consists of two reactions with the last reaction being reversible. The mechanism is listed in the form of three irreversible steps as follows:

$CH_4 + 3/2\ O_2 \rightarrow CO + 2\ H_2O$ REACTION IV

$CO + 1/2\ O_2 \rightarrow CO_2$ REACTION V

$CO_2 \rightarrow CO + 1/2\ O_2$ REACTION VI

Appendix A shows the 2-steps Mechanism and their kinetic data, consisting of two reactions of CH_4 and CO with O_2, where the reaction of CO with O_2 is a reversible reaction

for CO_2 decomposition making the third reaction [131]. The modified WD reaction mechanism for oxy-fuel conditions that was validated with a detailed chemical kinetic mechanism by retaining the first CH_4 and O_2 reaction, while refining the second CO-CO_2 reactions so as to improve the computation of the concentrations of major species and to account for the pressure dependence as well as the appropriate heat of reaction for the [CO]/[CO_2] equilibrium [116, 131]. The modified WD reaction mechanism is shown in Appendix B. Similar reaction rates parameters for the original and refined WD mechanism were reported by [116] as shown in Appendices C and E respectively.

Four-Step Jones and Lindstedt Mechanism

The four-step global reaction mechanism developed by Jones and Lindstedt [132] for methane combustion with air in premixed diffusion flames are given by Reactions VII-X below:

$CH_4 + 1/2\ O_2 \rightarrow CO + 2\ H_2$ REACTION VII

$CH_4 + H_2O \rightarrow CO + 3\ H_2$ REACTION VIII

$H_2 + 1/2\ O_2 \leftrightarrow H_2O$ REACTION IX

$CO + H_2O \leftrightarrow CO_2 + H_2$ REACTION X

The mechanism comprises of the first two irreversible contending reactions for the fuel breakdown, and the last two reversible reactions, controlling the reaction rates for H_2 and CO. The reaction rate parameters/expressions were initially estimated based on equilibrium assumptions [128-132]. Appendices D and H shows the four-step JL reaction mechanism with the kinetic rate data for methane combustion based on different units of conversion.

Similar approach was employed for the modifications and validation of the rate parameters to account for the oxy-fuel combustion characteristics. Some of such modified and validated parameters are shown in Appendices E, G, H based on different applications and variations in unit conversions [116, 128-132].

2.3.2 General Conservation Equations

The general mathematical equations for modeling combustion process are the conservation of mass, momentum, and energy as well as equation of species transport. These governing equations are elliptic as well as three-dimensional that are suitable for modeling combustion phenomena. These equation as provided by [133, 134] are given below.

2.3.2.1 Continuity equation

The general form of continuity equation or mass conservation equation is given by Equation (2.1).

$$\frac{\partial \rho}{\partial t} + \nabla \cdot (\rho \vec{v}) = S_i \tag{2.1}$$

where S_i is the external addition mass source term. When there is no external mass source addition and the system operates at steady state, the Equation 2.1 reduces to Equation 2.2

$$\nabla \cdot (\rho \vec{v}) = 0 \tag{2.2}$$

2.3.2.2 Momentum Equation

The general form of continuity or mass conservation equation for both compressible and incompressible flows can be written as (Equation 2.3)

$$\frac{\partial}{\partial t}(\rho\vec{v}) + \nabla\cdot(\rho\vec{v}\vec{v}) = -\nabla p + \rho\vec{g} + \nabla\cdot(\bar{\bar{\tau}}) \tag{2.3}$$

Where the stress tensor, $\bar{\bar{\tau}} = \mu\left[(\nabla\vec{v} + \nabla\vec{v}^T) - \frac{2}{3}\nabla\cdot\vec{v}I\right]$

μ is the viscosity; the term $\nabla\vec{v}^T$ is the effect of volume dilation; *I* is the unit tensor. The Equation 2.3 can also be reduced to Equation 2.4 for a Newtonian fluid

$$\nabla\cdot(\rho\vec{v}\vec{v}) = -\nabla p + \mu\nabla^2\vec{v} \tag{2.4}$$

2.3.2.3 Energy Equations

The energy equation in its steady form, as shown in Equation 2.5, accounts for energy transfer due to conduction, viscous dissipation, species diffusion, as well as energy source terms [135] [136]

$$\frac{\partial}{\partial t}(\rho E) + \frac{\partial}{\partial x_j}((\rho E + P)\cdot\vec{v}) = \frac{\partial}{\partial x_j}\left(K_{eff}\left(\frac{\partial T}{\partial x_j}\right) - \sum_j h_j J_j + \bar{\bar{\tau}}_{eff}\cdot\vec{v}\right) + S_h \tag{2.5}$$

Where $E = h - \frac{P}{\rho} + \frac{v^2}{2}$; $K_{eff} = k + k_t$, and S_h which is the energy source term comprises of the heat of chemical reaction and radiation heat exchange. The Equation 2.5 can as well be reduced to Equation 2.6.

$$(\rho C_P)\vec{v}\cdot\nabla\vec{v} = \nabla\cdot(\mathrm{k}\nabla T) + S_h \tag{2.6}$$

2.3.2.4 Species transport equation

The species transport equation provides the mass fraction or concentration of each species Y_i, by solving the coupled convection–diffusion equation for the i^{th} species.

$$\frac{\partial}{\partial x_i}(\rho \vec{v} Y_i) = -\frac{\partial}{\partial x_i} Y_{m,i} + R_i + S_i \tag{2.7}$$

where $Y_{m,i} = -\rho D_{m,i} \frac{\partial Y_i}{\partial x_i}$; and $D_{\mathrm{m,i}} = \frac{1-X_{\mathrm{i}}}{\sum_{j,j\neq 1}\left(\frac{X_{\mathrm{i}}}{D_{\mathrm{i,j}}}\right)}$

2.3.2.5 Mixture fractions

The mixture fraction is a non-dimensional conserved quantity that indicate the local fuel-oxygen ratio in non-premixed mixture as given by Equation (2.8) and the stoichiometric mixture fraction as given by Equation (2.9) [137-140]. Equivalence ratio of oxy-fuel combustion is defined as the ratio of stoichiometric oxidizer to fuel ratio divided to the actual oxidizer to fuel ratio. A unique relation between the equivalence ratio and the mixture fraction has been developed by [137, 139] as shown in Equation (2.10).

$$Z = \frac{\nu Y_f - Y_O + Y_{O,2}}{\nu Y_{f,1} + Y_{O,2}} \tag{2.8}$$

$$Z_{st} = \frac{Y_{O,2}}{\nu Y_{f,1} + Y_{O,2}} \tag{2.9}$$

$$\phi = \frac{Z(1-Z_{st})}{Z_{st}\,(1-Z)} \tag{2.10}$$

For $Z < Z_{st}$ (fuel lean); $Z > Z_{st}$ (fuel rich); $Z = Z_{st}$ (stoichiometric mixture)

2.3.3 Radiation Modeling

The Radiative heat transfer is one of the most important heat transfer mechanism in which heat is transferred from a medium by virtue of its temperature without a need for a material medium for the transfer. Heat transfer by radiation can be categorized into only surface-to surface effect (wall radiations) and the volumetric (participating media) effect in which both the walls and the fluid medium it confines participate in the radiations. The second case of participating gas is more prominent in combustion researches and applications [141]. The analysis of radiative heat transfer must involve the knowledge of spectral or total radiative properties of surfaces and/or media through which the radiative energy transfer occurs. These properties are basically emissivity, absorptivity, and reflectivity which define the ultimate magnitude of radiative energy exchange in any process involving heat transfer and vary for different materials and media [142]. For an absorbing, emitting, and scattering medium, radiative transfer equation (RTE) must be solved to establish radiation contribution in the overall heat transfer. The RTE is then coupled to the energy equation for total heat transfer analysis of the system.

$$\frac{dI(r,s)}{ds} = kI_b - (k + \sigma_s)I(r,s) \tag{2.11}$$

Due to the complexity of radiation and its coupling with the other modes of heat transfer in turbulent reacting flows, several models were proposed aimed at some simplification. The choice of any model will depend on the problem at hand as well as the application among other things. In the commercial ANSYS Fluent version 16.0 code, the available radiation models are:

a) Discrete Transfer Model

b) P-1 Model

c) Rosseland Model

d) Surface-to-Surface (S2S) Model

e) Discrete Ordinates (DO) Model

2.3.3.1 Discrete Ordinate (DO) Radiation Model

The DO radiation model solves radiative heat transfer problems that include both surface-to-surface and participating medium. The surfaces in question could be a semi-transparent wall among other surfaces. Also, the model can be used for gray and non-gray radiation using a gray-band model. The Weighted-Sum-of-Gray-Gases (WSGGM) Model is employed for the determination of absorption coefficient (a property dependent on the gas composition and temperature). While the WGSSM holds under some assumptions, it is more accurate than the oversimplified gray gas model as it takes into account particular absorption bands. Ultimately, the models are adequate to predict the thermal radiation exchange between the combustion gases and the combustion chamber walls.

The RTE depicted as a field equation in direction $\vec{s}$ is used in the DO model [143]. The equation is given as;

$$\nabla \cdot (I(\vec{r},\vec{s})\,\vec{s}) + (\mathrm{a} + \sigma_s) I(\vec{r},\vec{s}) = an^2 \frac{\sigma T^4}{\pi} + \frac{\sigma_s}{4\pi}\int_0^{4\pi} I(\vec{r},\vec{s}) \Phi(\vec{s},\vec{s}')\, d\Omega' \qquad (2.12)$$

Based on the WSGGM, the total emissivity over the distance *s* can be computed using;

$$\varepsilon = \sum_{i=0}^{I} a_{\varepsilon,i}(T)(1 - e^{-\kappa_i p s}) \qquad (2.13)$$

The absorption coefficient for i = 0 is assigned a value of zero to account for windows in the spectrum between spectral regions of high absorption ($\sum_{i=1}^{I} a_{\varepsilon,i} < 1$) and the corresponding weighting factor can be obtained using;

$$a_{\varepsilon,0} = 1 - \sum_{i=1}^{I} a_{\varepsilon,i} \tag{2.14}$$

The temperature dependence of $a_{\varepsilon,i}$ is evaluated using;

$$a_{\varepsilon,i} = 1 - \sum_{j=1}^{J} b_{\varepsilon,i,j} T^{j-1} \tag{2.15}$$

Where $b_{\varepsilon,i,j}$ are the polynomial coefficients for emissivity.

2.4 Membranes for Oxygen Separation

The ceramic-based membranes for oxygen separation are layers of material(s) that allows a gas to permeate through it by applying driving force. The partial pressure gradient of the gas to be permeated and/or an electric potential difference across the material acts as the driving force. Four among the most common concepts of the permeable membranes as shown in Figure 4.2.1 are [144, 145]: (i) solid electrolyte membrane, (ii) dual phase membrane, (iii) mixed ionic–electronic conducting (MIEC) membrane, and (iv) asymmetric porous membrane with graded porosity. The solid electrolytes-based membranes are pure O_2 conducting membranes that provides O_2 permeation in a controlled manner based on the amount of external electric current supplied, as shown in Figure 2.8(i). The membrane configuration shown in Figure 2.8(ii), is referred to as the dual phase type. It the metallic phase dispersal in the matrix of O_2 ion-conducting oxide/material. Despite the report of increase in the electronic conductivity of dual phase membranes as the result of increase in the concentration of the doping material, the solubility of the solid

multivalent material limits the level of increase in the conductivity. They are strong evidence of damage of the dual phase membranes as the result of incessant electronic conduction with accompanying O_2 permeation in oxygen sensors and fuel cells [146].

Figure 2.8(iii) shows the schematic configuration of the MIEC membrane. The electronic conductivity of the MIEC membranes provides the necessary internal short-circuit and maintain neutrality of the total charge by concomitant electron – ion (O^{2-}) fluxes balance. These are densely impermeable to gas molecules, but only permit oxygen ions (O^{2-}) and the electrons (e) exchange across them based on pressure gradients. This involves the dissociation and ionization of the oxygen molecule (O_2) which allows the O^{2-} permeation from the side that has higher partial pressure to the side with lower oxygen partial pressure. The MIEC membranes produces higher pure O_2 than the other conducting counterparts. The MIEC membrane proven to be practically attractive due to their conduction of both electrons and oxygen ions without application of external circuitry. The schematic configuration of the porous membrane with graded porosity is shown Figure 2.8(iv). These types of membranes have better mechanical support as well as greater surface area to volume ratio. They are typically made from materials like γ-Al $_2O_3$, α-Al $_2O_3$, SiO_2 and TiO_2. MIEC membranes are known to offers higher electronic conductivity at higher temperatures (700-1000^oC). Despite the higher O_2 permeation characterized by the perovskites-type membranes than the non-perovskites, the oxygen generation cost is higher in the case of perovskites-type due the requirement of the temperature elevation higher than that of the non-perovskite [147].

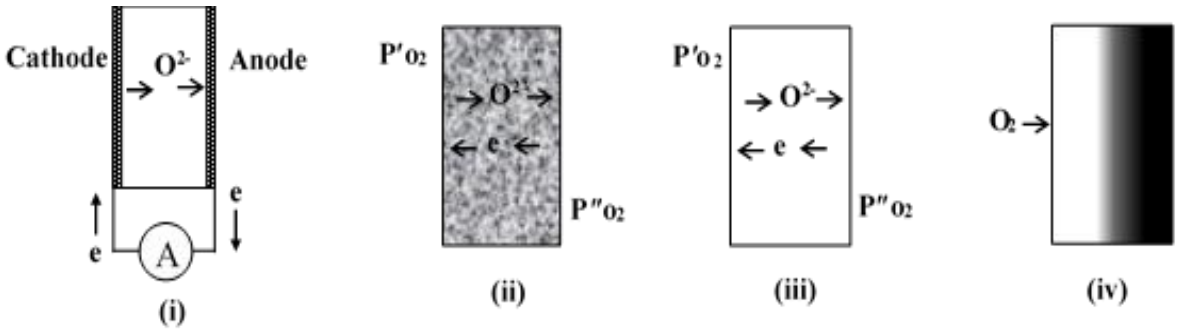

Figure 2.8: Four concepts of conduction mechanism for dense ceramic membranes: (i) solid electrolyte, (ii) dual phase, (iii) MIEC, and (iv) asymmetric porous with graded porosity [145].

2.4.1 Mixed Ionic and Electronic Conducting (MIEC) membranes for oxygen separation

The MIEC membranes that are being used for O_2 separation has been giving significant attention by many researchers due to their potentials of reduction in cost of energy requirement for the production of O_2. They are made up of mostly dense ceramic membranes that usually works at elevated temperatures (80-100^oC). They are given different acronyms like: MIEC, OTM (Oxygen Transport Membranes), ITM (Ion Transport Membranes) [26, 144, 148-150]. The MIEC materials, also known as perovskite materials, are ceramic materials that possesses crystal structure similar to that of calcium-titanium oxide ($CaTiO_3$) having a general chemical formula of ABO_3 [144]. Whereas the **A**-site cation can be an alkali, rare earth, or an alkaline earth ion, e.g. Ba, Ca, La, Na, Sr etc., the *B*-site is mostly transition metal, e.g. Co, Cu, Ni, Fe, Ti, Zr, etc., and *O* is oxygen atom [151].

The phase structures of an ideal ceramic-based membrane are shown in Figure 2.9. The **A**-atoms are situated at the center of the crystal and each atom is surrounded by 12 equidistant oxygen atoms. The six **B**-atoms are positioned at the corners of the cube and the oxygen atoms are at the centers of the edges of the cube. An ideal structure of ABO_3 does not have ionic conductance capacity until there is partial replacement of the cations at the **A**-site and *B*-site which will provide the necessary oxygen vacancies that can be used for the conduction of the oxygen ions. The general formula representing thr doped perovskite membrane by partial substitution of the cations is given as $A_xA'_{1-x}B_yB'_{1-y}O_{3-\delta}$, where *x* and *y* vary from 0 to 1 and δ is the oxygen vacancies concentration in the structure. Many *A*-site and *B*-site cations partial substitution strategies have been developed to provide economically viable oxygen fluxes as shown by many researchers [20, 144, 152-154]. The most currently studied MIEC membranes are the $La_{1-x}Sr_xCo_{1-y}Fe_yO_{3-\delta}$ (LSCF) and $Ba_{1-x}Sr_xCo_{1-y}Fe_yO_{3-\delta}$ (BSCF). $SrFe_{0.9}Ta_{0.1}O_{3-\delta}$, $Sr_{0.7}Ba_{0.3}Fe_{0.9}Mo_{0.1}O_{3-\delta}$, $Pr_{0.4}Sr_{0.6}Co_xFe_{1-x}O_{3-\delta}$ ($0 \leq x \leq 1$), $Ba_{0.95}La_{0.05}FeO_{3-\delta}$, and $SrCo_{1-y}Nb_yO_{3-\delta}$ ($0.025 \leq y \leq 0.4$). Other types of perovskite O_2 semi-permeable membranes include structured ceramic (e.g. $Sr_{1.4}La_{0.6}GaFeO_{3-\delta}$), modified ceramics (e.g. $SrFeCo_{0.5}O_x$), dual-phase ceramic–metal (e.g. $Sr_{0.2}La_{0.8}Fe_{0.69}Co_{0.1}Cr_{0.2}Mg_{0.01}O_3$ + 50Ag/50Pd), thin dual phase with chemically stable lead and yttria-stabilized zirconia, $BaBi_{0.4}Co_{0.2}Fe_{0.4}O_{3-\delta}$ (BBCF), $BaTi_{0.2}Co_{0.5}Fe_{0.3}O_{3-\delta}$ (BTCF), $La_{0.4}Ca_{0.6}FeO_{3-\delta}$ (LCF), $La_{0.5}Sr_{0.5}CoO_{3-\delta}$ (LSC), $La_2NiO_{4+\delta}$ (LNO), $SrCo_{0.8}Fe_{0.2}O_{3-\delta}$ (SCF), etc, [24-27, 155-159].

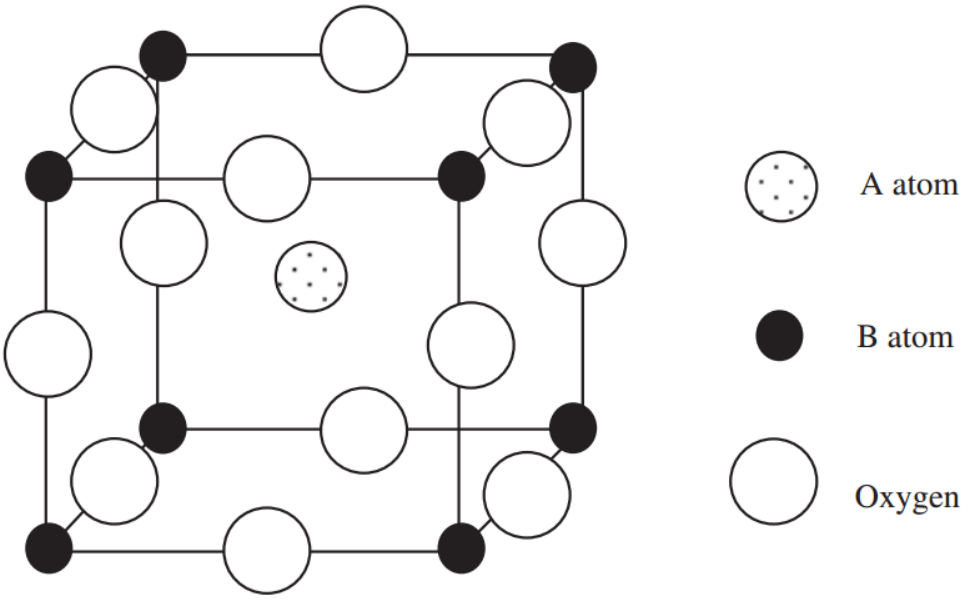

Figure 2.9: Ideal ABO_3 perovskite crystal structure [144, 147].

2.4.2 Oxygen transport mechanism in MIEC membranes

The O_2 transport requires a driving force for its migration across the membrane. This is usually the partial pressure gradient between the permeate and the feed side of the membrane. The transport will occur from high O_2 partial pressure side (feed side), to the lower O_2 partial pressure side (sweep or permeate side), by using the gradient of O_2 chemical potential based on the temperature of the membrane. The bulk diffusion and/or the surface exchange resistance limits the oxygen permeability of ITMs. Figure 2.10 present the schematic diagram of the oxygen transport mechanism in an ITM based of the following stages [153, 160, 161].

(i) O_2 mass transfer from the higher oxygen partial pressure feed stream to the surface of the membrane surface.

(ii) O_2 adsorption and dissociation into ions at the surface layer of the membrane.

(iii) Bulk ionic diffusion in the membrane lattice structure.

(iv) Oxygen ionic recombination at the opposite interface

(v) O_2 mass transfer from the surface to the lower oxygen partial pressure sweep stream.

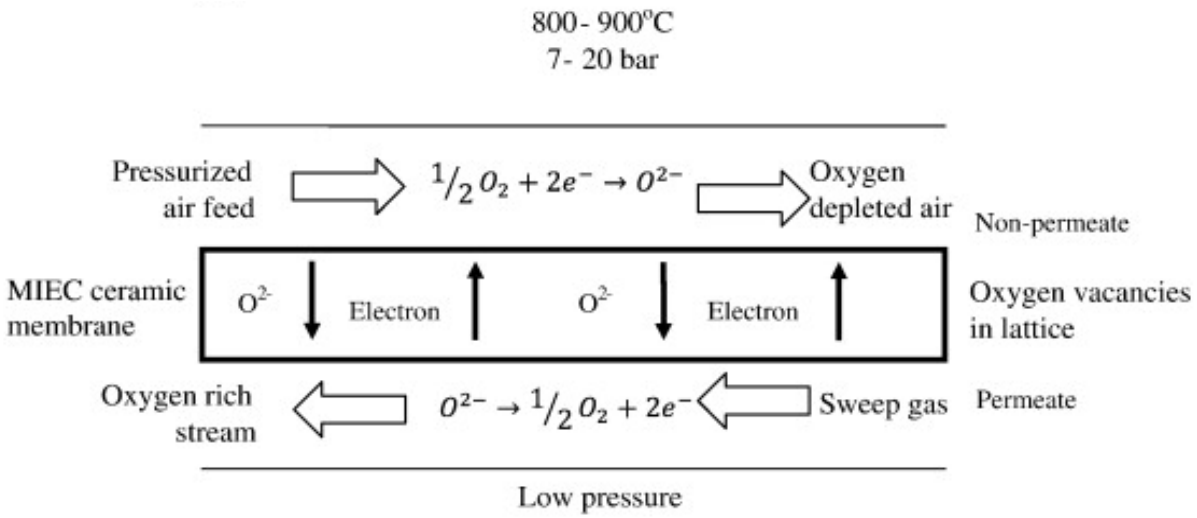

(a)

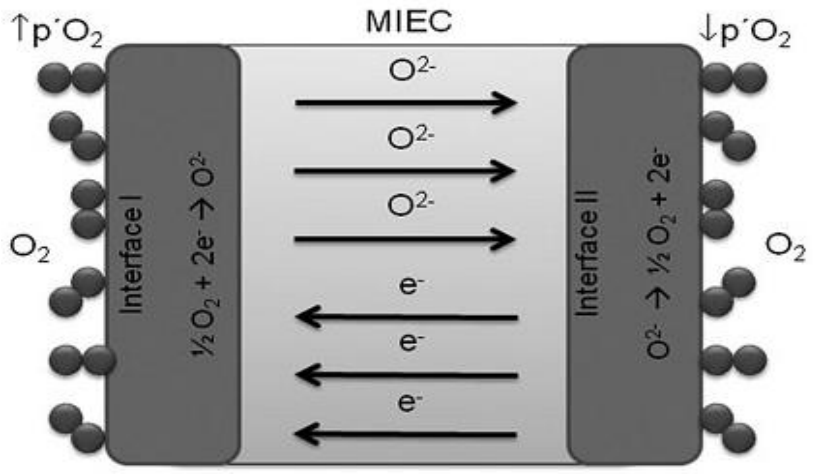

(b)

Figure 2.10: Schematic representation of O_2 transport in dense ceramic MIEC membranes [20, 152, 153].

The kinetics surface exchange reactions govern the two interfaces reactions at stages (ii) and (iv) while the bulk diffusion occurs at the stage (iii). The material properties of the membrane dictate the resistance levels at the two interfaces I and II. These include the perovskite composition, the total surface area exposed to the transport as well as the thickness [153, 160].

2.4.3 Configurations of ITM for reactor applications

The three most studied geometric configurations of ITM are: disk or planar, hollow fiber and tubular as shown in figure tubular, and hollow fiber, as shown in Figure 2.11. The planar as well as the tubular configurations have been utilized for large scale commercial applications [26, 162]. The larger surface area of the hollow fiber membranes is making them popular nowadays due to it relatively higher surface area to volume ratio than that of the disk, planar or the tubular counterparts. Conversely, the lower thickness of the hollow fiber membranes due to their lesser thickness lower their mechanical strength in comparison to other configurations making their assembling in the reactor very difficult [163].

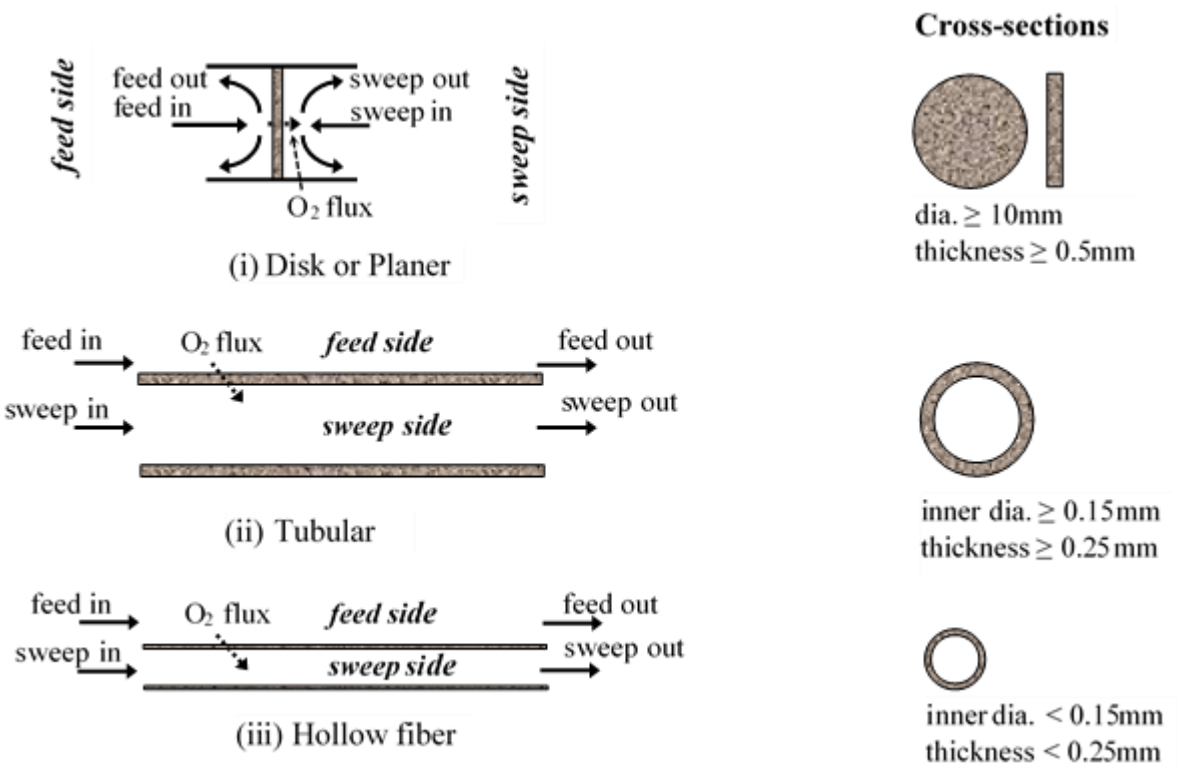

Figure 2.11: Configurations of ITMs [164].

The flow configuration of the ITM reactor could be either co-current or counter current flows. Whereas in co-current configuration the feed and sweep gases are passed in the same axial direction, the opposite direction of the flow of the two gases made the flow to be counter-current. The ITM membrane are being modified to include various forms of porous layers as well as asymmetric configurations [165]. The addition of the porous layers, metallic reinforcement or catalysts to the membranes tends to increase their mechanical strength as well as the surface reactions in order to improve desired reaction or oxygen permeation [166, 167]. This can permit the use of much thinner membranes for the oxygen exchange reaction.

2.4.4 ITM oxygen flux fundamentals

Separation of oxygen from a gaseous stream such as air has been primary objective of ITMs. In order to develop or utilize an improved membrane for optimum performance, there is need for proper understanding of the permeation processes across the ITM. The oxygen transport across an ITM involves the concomitant exchange of the oxygen ions with electrons. The maximum amount of oxygen at a given total conductivity occur when the electronic and ionic *transference numbers* are equal. As defined by [145], the electronic or ionic *transference number* refers to the fraction of the total current carried by that electron or the ion when passing through a solid or an electrolyte. The schematic representation of O_2 transport in an ITM has been shown in Figure 2.10.

The resistances between the membrane and the gas phase are customarily neglected since they are mostly very small and hence the surface exchanges of stages (ii) and (iv) and the bulk diffusion of stage (iii), as described in section 2.4.2, are mostly being considered when developing the oxygen transport equations [22, 168, 169]. There are many sub series involved in the surface exchange processes as properly explained by [170]. The oxygen bulk diffusion which is usually influenced by the oxygen vacancy, electron holes as well as the electrons has been commonly depicted using the prominent Wagner theory for a fairly thick membrane with the oxygen flux as shown in Equation 2.16, based on the following assumptions [145, 152]:

1. The diffusion of oxygen ions determines the overall rate of oxygen permeation across the membrane lattice or the electronic charge transport across the bulk oxide [145];

2. The electrons and oxygen ions are in local equilibrium with oxygen molecules [152].

$$J_{O_2} = \frac{RT}{16LF^2}\int_{p''_{O_2}}^{p'_{O_2}} \frac{\sigma_e\sigma_i}{\sigma_e+\sigma_i} d\ln p_{O_2} \tag{2.16}$$

Where J_{O_2} is the flux of oxygen permeated (mol/m^2-s)

The surface exchange reactions occurring at the two interfaces of the membrane surfaces are shown in Equation 2.17 and 2.18 for the feed and sweep sides, respectively. While the oxygen ion vacancies to generate electron holes and oxygen ions in the feed side, the reverse is the case in the sweep side where the electron holes and oxygen ions combine to generate molecular oxygen thereby creating other oxygen ion vacancies.

$$0.5\, O_2 + V_{\ddot{O}} \overset{k_f/k_r}{\longleftrightarrow} O_{\mathrm{o}} + 2\,\dot{h} \tag{2.17}$$

$$O_{\mathrm{o}} + 2\,\dot{h} \overset{k_f/k_r}{\longleftrightarrow} 0.5\, O_2 + V_{\ddot{O}} \tag{2.18}$$

The bulk diffusion as well as the surface exchange kinetics were incorporated in to a single equation (Equation 2.19) by some researcher based on the following sets of assumptions in addition to those taken for the derivation of Equation 2.16 [144, 171, 172]:

1. Neglecting the gas radial diffusion.
2. The gas phase is assumed to be ideal.
3. The same oxygen partial pressures at both the shell and the tube sides of the surface of the membrane.

The Equation 2.19 was derived in details by [173-175] for tubular configuration of ITMs and it was reported to work successfully in *LSCF* and *BSCF* hollow fiber membranes [169, 176].

$$\frac{dNo_2}{dl} = \frac{K_f\left(\sqrt{Po_2^{'}} - \sqrt{Po_2^{''}}\right)}{\frac{K_f \ln(r_2/r_1)}{\pi D_v}\sqrt{Po_2^{'} Po_2^{''}} + \frac{\sqrt{Po_2^{'}}}{2\pi r_1} + \frac{\sqrt{Po_2^{''}}}{2\pi r_2}} \tag{2.19}$$

Where No_2 is the oxygen molar flowrate, K_f is the forward reaction rate constant, l is the variable length of the membrane, $p'o_2$ and $p''o_2$ are partial pressures of oxygen at the feed and sweep sides, respectively.

The characteristic thickness of the membrane (*Lc*) is the thickness at which the surface exchange reactions equate the permeation resistance by bulk diffusion of oxygen. It is given by:

$$L_c = \frac{D_v}{2K_f}\left(\frac{1}{\sqrt{Po_2^{'}}} + \frac{1}{\sqrt{Po_2^{''}}}\right) \tag{2.20}$$

The characteristic thickness is a function of oxygen partial pressures as well as the temperature. It is also inversely proportional to the amount of oxygen flux that can permeate across the membrane. Hence, the smaller the thickness of the membrane the higher the oxygen permeation in the case where the bulk diffusion remains predominant. For thicker membranes, the Wagner theory (Equation 2.16) can predicts the bulk oxygen diffusion with reasonable accuracy [22, 177].

According to many researchers [123, 160, 168, 169, 178, 179], the oxygen permeation flux relationships for disk/planar and tubular perovskites type membranes are expressed in Equations 2.21 and 2.22 respectively.

$$Jo_2 = \frac{D_V K_r \left(\sqrt{Po_2^{'}} - \sqrt{Po_2^{''}}\right)}{2K_f L\sqrt{Po_2^{'} Po_2^{''}} + D_V\left(\sqrt{Po_2^{'}} + \sqrt{Po_2^{''}}\right)} \tag{2.21}$$

$$Jo_2 = \frac{D_V K_r \left(\sqrt{Po_2^{'}} - \sqrt{Po_2^{''}}\right)}{2K_f (r_o - r_i)\sqrt{Po_2^{'} Po_2^{''}} + \frac{D_V r_m}{r_i}\sqrt{Po_2^{'}} + \frac{D_V r_m}{r_o}\sqrt{Po_2^{''}}} \tag{2.22}$$

where $r_m = (r_o - r_i)/\ln(r_o - r_i)$. The coefficients K_f, K_r and D_v, are temperature dependent, that can be obtained by using Arrhenius law as shown in Equations 2.23 to 2.25, respectively. The activation energy and pre-exponential coefficients are usually obtained experimentally [160, 180, 181].

$$K_f = K_{f_o} e^{\left(-E_{K_f}/RT\right)} \tag{2.23}$$

$$K_r = K_{r_o} e^{\left(-E_{K_r}/RT\right)} \tag{2.24}$$

$$D_V = D_{V_o} e^{\left(-E_{D_V}/RT\right)} \tag{2.25}$$

2.4.5 Oxygen permeation flux through BSCF membranes

Separation The mathematical model for predicting oxygen permeation through a BSCF membrane has recently been developed as given in Equation 2.28 [182] by modifying the generalized (D_v, K_f, K_r) DKK model suggested by Xu *et al.*, (Equation 2.27) [169]. The model incorporated the effect of the feed and sweep gas flow rates. The permeation flux is

dependent on the membrane temperature (T), membrane thickness (t) and the oxygen partial pressure difference between the feed and permeate sides. The mass flow rate of oxygen permeated across the membrane is computed from Equation 2.26:

$$\dot{m}_{O_2} = J_{O_2}.M_{O_2}.A \tag{2.26}$$

The general DKK model is given as:

$$J_{O_2} = \frac{D_v K_r\left(P_{\mathrm{O2-f}}^{n} - P_{\mathrm{O2-s}}^{n}\right)}{2tK_f P_{\mathrm{O2-f}}^{n}.P_{\mathrm{O2-s}}^{n} + D_v\left(P_{O2-f}^{n} + P_{\mathrm{O2-s}}^{n}\right)} \tag{2.27}$$

Where the coefficients K_f, K_r and D_v, are given in Equations 2.23 – 2.25, respectively.

The oxygen flux through the BSCF membrane can be computed from Equation 2.28 using the K_f, K_r and D_v, coefficients given in Equations 2.29 – 2.31 [182]:

$$J_{O_2} = \frac{D_v K_r\left(P_{\mathrm{O2-f}}^{0.25} - P_{\mathrm{O2-s}}^{0.25}\right)}{2tK_f P_{\mathrm{O2-f}}^{0.25}.P_{\mathrm{O2-s}}^{0.25} + D_v\left(P_{\mathrm{O2-f}}^{0.25} + P_{\mathrm{O2-s}}^{0.25}\right)} \tag{2.28}$$

Where $$D_{\mathrm{v}} = 5.9807\,.\,10^{-5}.\exp\left(-\frac{92709}{8.314\,T}\right) \tag{2.29}$$

$$K_{\mathrm{f}} = 41.688\,.\exp\left(-\frac{146680}{8.314\,T}\right) \tag{2.30}$$

$$K_{\mathrm{r}} = 1.166\,.\,10^{4}.\exp\left(-\frac{102910}{8.314\,T}\right) \tag{2.31}$$

$P_{\mathrm{O2\text{-}f}}$ and $P_{\mathrm{O2\text{-}s}}$ are the oxygen partial pressures at feed and sweep side, respectively, K_{r}, K_{f} and D_{v} are the surface exchange reverse and forward reaction rate constants and the bulk diffusion coefficient, respectively.

2.5 Oxygen Transport Membrane Performance

The The largest source of carbon dioxide (CO_2) emission in to the atmosphere is believed to come from the combustion of fossil-based fuels in power plants. The CO_2 emission is considered as the major greenhouse gas responsible for the current global climate change. There exist several technologies aiming at reducing the emission of greenhouse gas by capturing the CO_2 in the utility industries. These include pre-, post- and oxy-fuel combustion carbon capture technologies. Oxy-fuel combustion technology has the potential of zero emission due to the use of oxygen only instead of air in which near stoichiometry, the end products of the combustion are mainly CO_2 and H_2O. The water vapor can easily be condensed, and the CO_2 stored. But the oxy-fuel combustion process is associated with high temperatures and hence recirculating the flue gas (mainly CO_2) or other inert gas lowers the combustion temperatures[1, 183]. Application of oxy-fuel combustion technology to power plants is currently getting special attention. As reported by Buhre *at al.,* [58], there was one-third reduction in NOx emissions and decrease in CO from a conventional coal-fired boiler as the result of integrating oxy-fuel combustion technology. Replacing N_2 from air with CO_2 as diluent in oxy-fuel combustion resulted in lesser fuel consumption as well as lower combustion temperatures [184, 185]. The cost of the conventional cryogenic air separation process as well as its thermodynamic inefficiency has been the driving force for the quest of Ion Transport Membranes (ITM) as alternatives [56]. They are mostly dense, mixed conducting and nonporous ceramics materials that permit electrons and oxygen ions transport from the higher to the lower oxygen partial pressure sides at higher temperatures [186]. The factors influencing the permeation flux of oxygen depends on the type of materials and thickness of membrane along with the

conditions of the oxygen permeation such as temperature and pressure, as well as sweep gas flow rate [187]. Axisymmetric geometry has been the most widely adopted design for the ITM reactors [24].

There are several literatures investigating the oxygen permeation performance across perovskite membranes. The prominent ones that studied the permeation performance at higher pressures were reported by [150, 188, 189]. The oxygen permeation flux was found to increase linearly with increase in the logarithmic value of p'_{O2}/p''_{O2}, where p'_{O2} and p''_{O2} are the feed and permeate sides oxygen partial pressures, respectively. Therefore, high oxygen permeation flux can be achieved by supplying high pressure air. The effect of membrane thickness on oxygen permeation flux on has been observed by many researchers [182, 190-192]. They concluded that increase in membrane thickness reduces the oxygen permeation flux due to the effect of bulk diffusion. The critical membrane thickness was obtained to be approximately 1.0 mm for the membrane operating temperature range of 700–1000 ^{o}C [193]. Temperature has been among the most sensitive factors influencing oxygen permeation flux of membranes. Among the countless literatures that reported increase in O_2 permeation due to temperature increase include [138, 190, 194-196]. The oxygen permeation flux was insignificant at temperatures below 600 °C. While, when the temperature was increased to 650 °C, there were significant oxygen permeation flux with sharp increase when the temperature was above 800 °C as the result of improved surface reaction rate and/or oxygen ionic diffusion.

Fairly recently, Mezghani and Hamza [197] reported that $Ba_{0.5}Sr_{0.5}Co_{0.8}Fe_{0.2}O_{3-\delta}$ is the most promising material for ion transport membranes due to its higher oxygen permeation flux. However, the main problem associated with the use of BSCF was inadequate chemical stability in the vicinity of higher CO_2 concentrations. They use methane gas to evaluate the performance of BSCF membranes for oxy-fuel combustion applications at optimized methane flow rates of 0.65 ml/min at 920 °C. They reported that the BSCF membrane was more stable when operating at fuel lean mixture. The rate of oxygen permeation of the membrane reduces when all the oxygen generated is instantly consumed during the combustion reaction without excess oxygen. The more the excess oxygen in the combustor the higher the long-time stability of the BSCF membrane. The performance investigation of $Ba_{0.5}Sr_{0.5}Co_{0.8}Fe_{0.2}O_{3\delta}$ oxygen transport membrane was conducted numerically in a botton-cell reactor model for oxygen separation from air and instantaneous combustion with methane by Ahmed *et al.,* [195]. They considered both reactive and non-reactive cases for the study of O_2 permeation and the effect of percentage of methane on reactivity. The reactivity as well as oxygen permeation were proportional to the percentage of CH_4 due to increase in volumetric flow rates. Similar findings were reported by Nemitallah [178] using oxygen permeation model for reacting flows in a modified design of the button-cell reactor to study oxy-methane combustion characteristics. An initial performance analysis of a single pass carbon-free fire-tube boiler integrated with ITM has been conducted by Ben-Mansour *et al.,* [194] at elevated temperatures. They studied the effects of the reactor wall temperature on oxygen permeation, reaction rate as well as heat flux. Their findings indicated optimum improvement of both combustion characteristics and heat transfer at temperature of 1100 ^{o}C and 6% methane mass fraction, while the variation in fuel flow

rates did not show substantial effect on the performance of the reactor due to low flow rates. In order to obtain sufficiently higher heat fluxes, they recommended scaling-up of the ITM reactor. A four-channels two-crossing membranes ITM rector geometry was utilized in the design of an ITM reactor for possible fire tube boiler applications at elevated pressure [150]. They considered a reactor length of 1.8 m and 20 bar operating pressure to determine the effects of percentage of CH_4 in the sweep side and the flow configurations on the boiler performance in the power range of 5-8 MWe. About 12,500 units of ITM reactors, 5 m high, with total volume of 45.5 m^3 was calculated. When using ITM reactors under reactive conditions with CO_2 as the diluent, the flame thickness is maximum near the surface of the membrane and the diffusion flame temperature decreases due to the influx of the cold oxygen [198]. The focus of most of the application of ITM reactors is more on to the gas turbine combustors with only few available researches on to fire tube boilers despite its eminent potentials of curving CO_2 emissions in large scale industrial boilers [199].

CHAPTER 3

METHODOLOGY

3.1 Introduction

This section describes the procedures followed for the purpose of achieving the objectives of this work. It consisted of three sections: firstly, the experimental methodologies for the investigation of the flow and combustion characteristics in the porous reactors; secondly, the numerically modeling of the flow and combustion analyses of the porous reactors and thirdly, numerical modeling of a two-pass oxygen transport reactor (OTR) for fire-tube boilers application.

3.2 Experimental Setup of Porous Combustor

In order to investigate the flow as well as the combustion characteristics in a porous plate combustor for oxy-fuel combustion applications as the first objective, two experimental setups were manufactured. The first setup was meant to study the non-reacting flow-field characteristics at fuel-lean equivalence ratios using PIV system for flow visualization and velocity and flow characterization in terms of velocity vectors, streamlines, velocity profiles as well as average velocities. The second setup is meant for the determination of the combustion characteristics at different equivalence ratios and diluent/oxygen ratios.

3.2.1 Non-reacting experimental setup

A porous plate reactor with rectangular cross-sectional area was constructed for oxy-fuel combustion to mimic ITM reactor. As shown in Figure 3.1b, the porous plate reactor comprises three sections; the central combustion chamber where fuel feed and oxygen are being mixed, the upper and lower chambers where oxygen is being supplied. The oxygen chambers are made of stainless steel with a ceramic porous plate attached to permit oxygen supply. Pure oxygen is supplied in the two oxygen chambers from a pressurized oxygen gas cylinder while the fuel (methane), together with the diluent (carbon-dioxide) were also supplied in their pure form from their respect pressurized cylinders, as shown in Figure 3.1a. Each pressurized cylinder was connected to a mass flow controller which regulates the gas flow rate entering into the sections. The fuel and diluent are mixed upstream of the reactor in a mixing chamber. The length of the mixing chamber was 80 cm. In reaction zone (central zone), the fuel supplied, and diluent mix with the incoming oxygen permeating through the porous plate from both the upper and the lower oxygen chambers. The oxygen permeates through the two porous plates with specifications as provided in Table 3.1. The plates provide uniform oxygen distribution due to its uniformity of porosity of the two plates.

The porous plate used are ‘porous alumina cover plate (ELS 42520-X) made by ESL Electro-Science, USA, having the properties shown in Table 3.1. The upper and lower oxygen chambers are closed, hence all the pressurized oxygen supply passed through the porous plate in to the central combustion zone. The combustion zone is made up of the two oxygen zones and two quartz glass plates from opposite sides for flow/combustion

visualization. The nominal height of the two oxygen sections is 30mm each, while the reaction zone is 25mm with length of 400mm, and width of 55mm, as shown in Figure 3.1c. The quartz glass plates have a thickness of 2mm each.

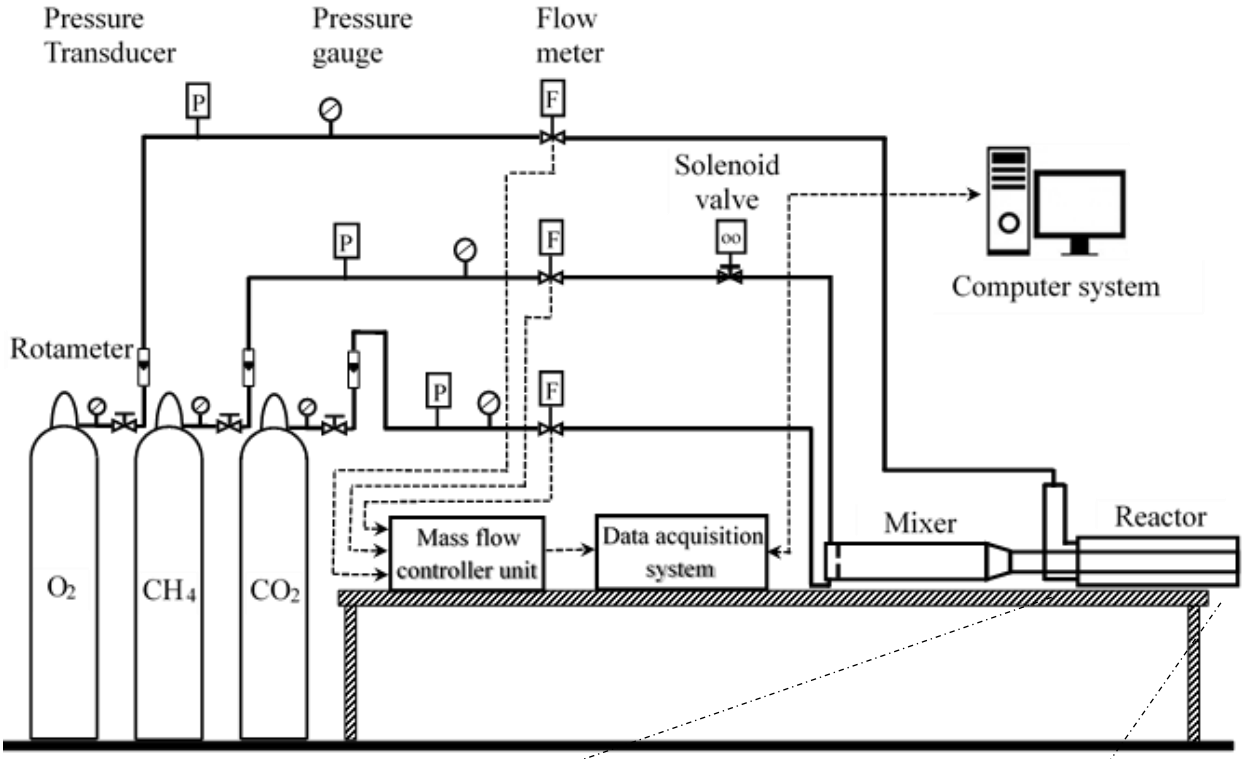

(a)

(b)

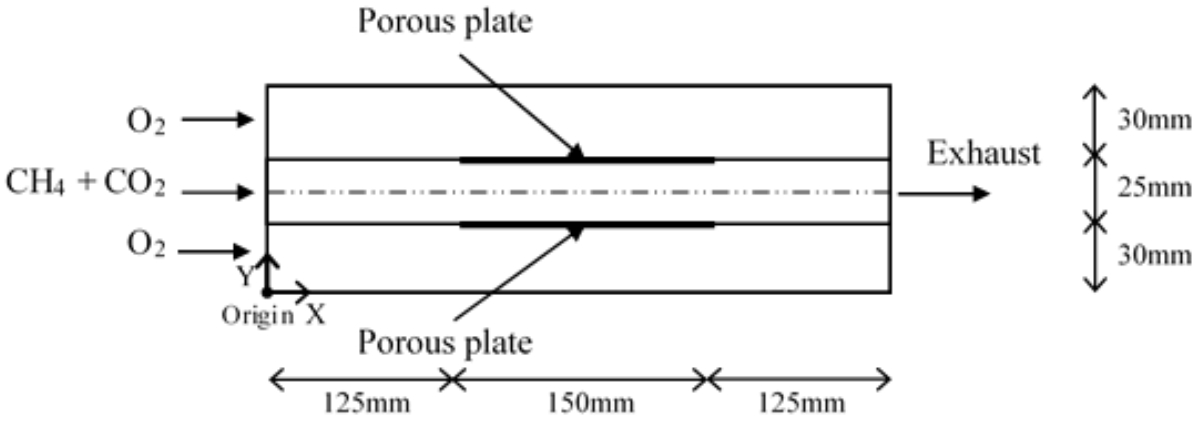

(c)

Figure 3.1. Schematic diagram of the overall experimental setup of the reactor: (a) overall flow configuration, (b) descriptive view of the reactor, (c) 2-D representation of the reactor.

Table 3.1. Properties of Porous Alumina Cover Plate 42520

Material	**Length**	**Width**	**Thickness**	**Porosity**	**Maximum Temperature**	**Recommended Temperature**
Fired alumina ceramic plates	150*mm*	5*mm*	1*mm*	40%	1550 ^{o}C	1450 ^{o}C

In order to study the non-reacting flow-field characteristics, a PIV system was setup for flow visualization, velocity and flow characterization. The set up involves the use of tracer particles as flow seeding and a laser light sheet to illuminate the particles. A high speed digital camera was used to capture the images of the flow of the illuminated particles due to the reflection of the laser light at very small time-intervals (micro-seconds) as shown in Figure 3.2. The images are pre-processed and analyzed using different correlation analysis methods depending on the nature of the fluid flow in question. The velocity distribution and other related parameters were obtained by post-processing the analyzed flow images as outline by [200, 201].

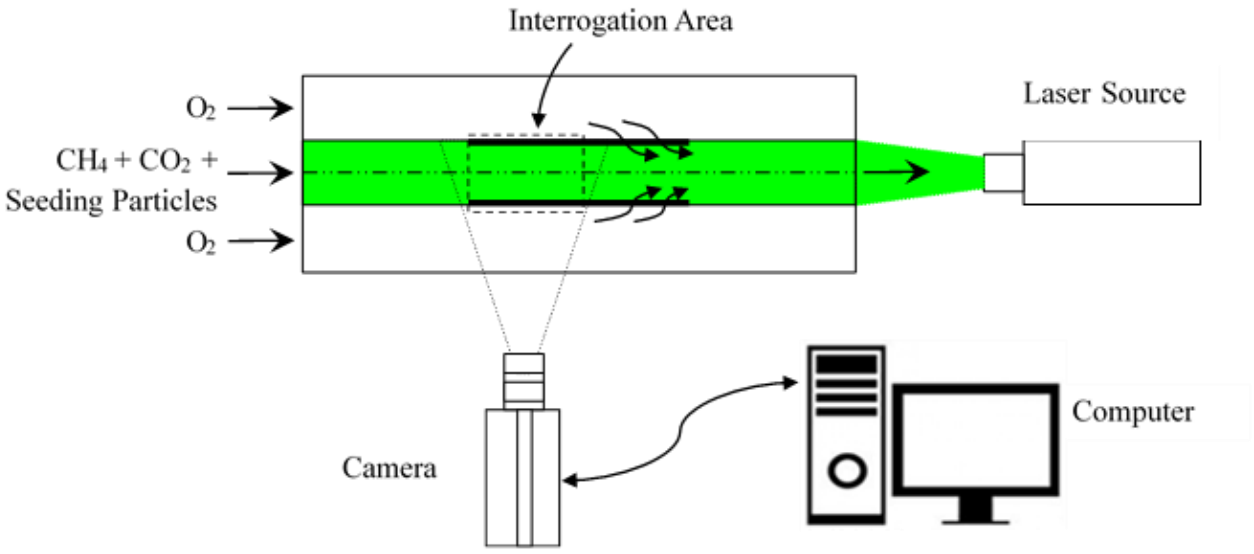

Figure 3.2: PIV setup of the reactor.

A manual RayPower 2000 Laser from DANTEC Dynamics [202], was used to supply the laser light sheet of about 45mm from the base plate with a wave length of 532nm and output power of about 2000mW. This light beam illuminates the seeding particles (Al_2O_3, 0.9 g/mol weight) supplied with the fuel (CH_4). Phantom high-speed camera, SpeedSense 9040 series, from Vision Research - AMETEK Material Analysis Division, with maximum resolution of 1632 x 1200 pixels was calibrated and used to acquire stream of images at a trigger rate of 600 f/s. Detailed specifications of the Laser, Camera and the Lens are shown in Tables 3.2 – 3.4, respectively.

Table 3.2. Laser Specifications

Specification	Raypower 2000
Lasing medium	Gas
Wavelength	532 ± 1 nm
Output power	> 2000 mW
Beam diameter at the aperture	3.0 nm
Polarization ratio	> 100:1
Operating temperature	10 – 35 ^oC
Mains supply	100 – 240 V AC, 3 A max, 50 – 60 Hz
TTL modulation frequency	max 10 kHz

Table 3.3. Camera Specifications

Specifications	Speedsense Camera 9040
Sensor type	CCD progressive scan monochrome
Chip size	18.77 × 13.8 *mm*
Resolution	1632 × 1200 *pixels*
Pixel size	11.5 μm
Bit depth	8, 12, 14
Maximum exposure time	2 μs
Fps (full frame)	1016/508 *f/s*

Table 3.4. Lens Specifications

Specifications	Nikon AF Micro Nikkor 60 *mm* f/2.8 *D*
Focal length	60 *mm*
f-number	2.8 - 32
Distance scale	0.219 - ∞ *m*

3.2.1.1 Experimental runs

The detailed procedure of the PIV experiments runs started with setting up of the required gas flows for an equivalence ratio from the experimental plan for the reactor at 1.36 kW power (Table 3.5) using the overall flow setup shown in Figure 3.1. As suggested by [203, 204], the camera intensity calibration was conducted by keeping the cap on the camera assembly in order to obtain a reference of the intensity. Also, the optimization of the laser repetition rates and current follow the technique enlisted by [203]. The laser was receiving continuous trigger signal matching the set-frequency before it was switched to external mode. The camera mode was set to continuous grab and the particle images were well

focused. The camera was being controlled by a computer program Phantom Camera Control (PCC). Steady state videos were recorded in cine format and then converted into 1000 images and saved. The same procedure was repeated for all the three runs of the experimental plan.

Table 3.5. Non-Reactive Experimental Plan at Reactor Power of 1.36 kW

Experiment No.	Volume Flow rate (lit/min)			O_2/CO_2	φ
	CH_4	CO_2	O_2		
Case 1	2.5	8.3	8.3	1.0	0.6
Case 2	2.5	10.0	10.0	1.0	0.5
Case 3	2.5	12.5	12.5	1.0	0.4

The flow images were acquired as single frames with the camera using the PCC studio. Proceeding to the PIV analysis, the images were exported to Dantec Dynamic Studio and stored in the database. The software was designed to acquire, analyze and post-process data. The field of view method of calibration was used to inspect and modify origin and scale factor used in converting image plane (pixels) to object plane (metric units) by specifying the height which is equivalent to the height of the reaction zone. An analysis sequence for the gas flow was build-up as shown in Figure 3.3 and utilized to obtain the velocity vectors, velocity profiles, and the streamlines from the images. The following steps shows the details of the analysis sequences:

1. Making Double Frame; this process is applied to the raw images to convert them from single frames to double frames by combining them in twos. This was done by specifying N/2 double images in the option.

2. Image Min and Max; this method is a subset of Image Processing category and it is used to determine the field of minima/maxima over a series of images. Here, the method was used to extract the field of minima from the paired raw images obtained from the previous conversion and returns one image.
3. Image Arithmetic; this method allows performing arithmetic (addition, subtraction, multiplication and division) on pixel values of the image. It was used to subtract the minimum image from step (2) from the raw images in step (1). This is a form of background subtraction technique to remove background noises from the raw images.
4. Image Mean; this calculates the average intensity of corresponding pixels (pixels with identical coordinates) in all selected images. The images must be compatible in terms of dimensions and grayscales. The inputs for this step are images from step (3) and the output is a single map.
5. Image Processing Library (IPL)-Blur; this module contains filters like low-pass and high-pass filters, Morphology, signal processing, utility and threshold that can be used to smooth images, detect edges, enhance image contrast, carryout non-linear calculations. The image from step (4) was processed to reduce the particle image intensity by blurring.
6. Image Arithmetic; this is used to subtract output image of step (5) from the raw images obtained in step (3). The aim is to reduce the intensity of each image in the ensemble.
7. Image Processing Library (IPL); here Gaussian filters (5×5) was applied twice to images from step (6) to smooth the images. This step makes the images of particles more visible. The Gaussian filter is a linear low-pass filter like mean filters but differs

in the sense that it weighs grayscale at the center of kernels higher than those at the edges.

8. Image Min and Max; this step selects the minimum field form images from the output of step (7).
9. Image Arithmetic; this is used to subtract output image of step (8) from the raw images obtained in step (7). The aim is to check the numeric diffusion that may have been introduced by applying filters.
10. Adaptive Correlation; Correlation algorithm was applied to the output images from step (9) to generate vector maps. Adaptive correlation is a form cross-correlation with additional post-processing algorithms like local validation. Additionally, processes like local validation to detect bad vectors, the overlap of IA to compensate for the loss of vector field resolution, high accuracy module, and window deformation were applied to the images using this correlation type. Local validation was achieved through Peak Validation and Local Neighborhood Validation. The overlap of IA was achieved with 50% overlap between IA pairs in both horizontal and vertical directions. The velocity vectors were obtained from displacement vectors and time interval using the Central Difference Scheme which was the most accurate methodology suitable for PIV measurement. The high accuracy sub-pixel interpolation is part of the adaptive correlation algorithm that is used to determine correlation peak.
11. Vector Statistics: this calculates statistics from multiple vector maps and presents the results of mean velocity vectors in a vector map. Other parameters obtained were the streamlines and the velocity profiles.

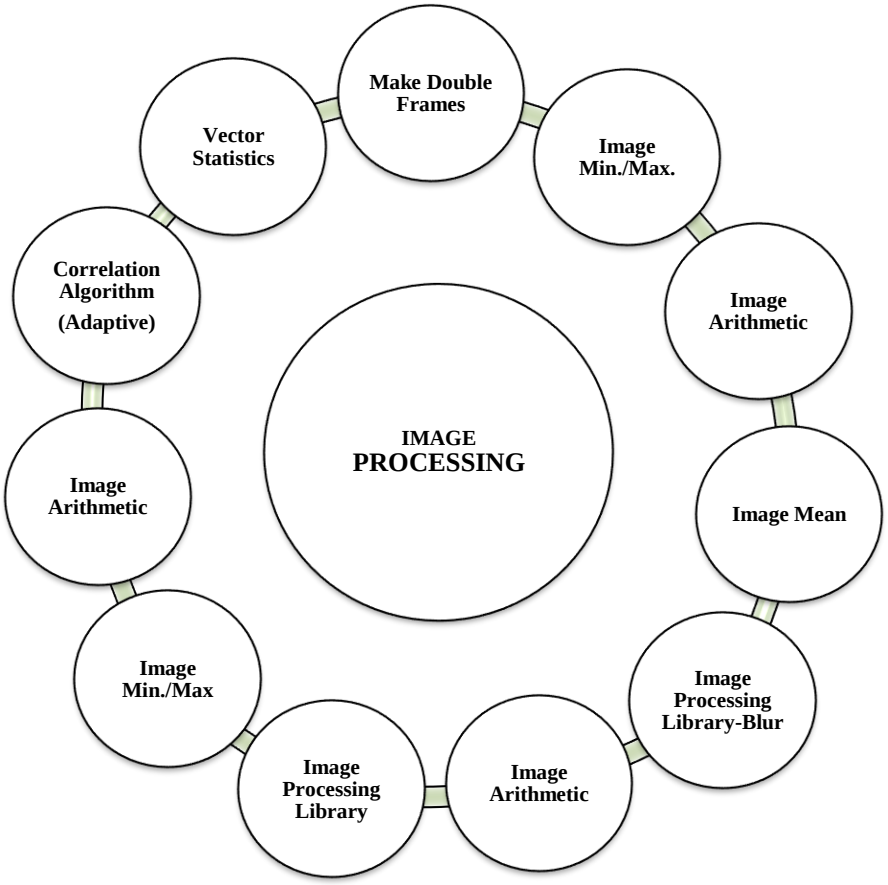

Figure 3.3: PIV analysis sequence.

3.2.1.2 Measuring equipment for non-reacting flows

a. PIV Setup: This includes; (1) A manual RayPower 2000 Laser from DANTEC Dynamics [202], (2) Phantom high-speed camera, SpeedSense 9040 series, from Vision Research - AMETEK Material Analysis Division; (3) Camera precision focus Lens. Details of each equipment can be found in Tables 3.2 – 3.4.

b. Mass flow controllers: Controls the species mass flow rates, Bronkhorst 'D' type flow controllers 'In-flow' with an uncertainty of ± 0.5% were used. The capacity of the flow controllers is ranging from 10 *L/min* to 70 *L/min*. The flow controllers are

connected to data acquisition system via a computer system which controls the gases mass flow rate.

c. Rotameters: The species flow rate can be controlled either using the mass flow controllers or manually. For manual operation, flow rate can be set by opening or closing of the valve and the flow rate can be measured by means of rotameters that are installed in lines of different species.

d. Pressure gauges and regulators: To measure the oxygen supply pressures, *Keller Leo 1* type digital pressure gauges were used having an uncertainty of ± 0.2%. All the gas cylinders are equipped with pressure gauges and regulators for the control of the line pressures.

3.2.2 Combustion Experimental Setup (Reacting)

The aims of this experiment are to determine the combustion characteristics of the porous reactor at different equivalence ratios and diluent/oxidizer ratios. The major parameters to be determined includes the flame structures, the lean blowout limits, the exhaust gas temperature distribution, and the flue gas compositions. The same setup shown in Figure 3.1 was used for the combustion measurements with slight reduction in cross-sectional area of the fuel-diluent mixture inlet section of the reactor and high temperature porous material with pressure drop of up to 1.7 bar (absolute), as shown in Figure 3.4(a). The dimensions of the reactor were 240mm in x-direction from the fuel-diluent inlet of the combustor, 25mm in y-direction, and 45mm in z-direction. The cross-section of the fuel-diluent inlet (y-z) was 1mm x 2mm, while the porous oxygen inlet cross-section (x-z) was 120mm x 25mm.

3.2.1.2 Combustion experimental conditions

The fuel (CH_4) and the diluent (CO_2) were premixed in the mixing chamber prior to the reaction zone and mixed with the oxygen permeate from the porous oxygen zone. The same procedure for the flow settings of the non-reacting flow experiments were adopted based on the experimental plan shown in Tables 3.6 - 3.9. In Tables 3.6 and 3.7, the fuel flow rate was fixed at 2.76 *l/min* (equivalent to 1.5 *kW* calorific value of the fuel) while varying the percentage of CO_2 in the oxidizer at a fixed equivalence ratio and varying the oxygen flow rates to achieve different equivalence ratios.

The temperature and pressure of the inlet gases were 21 ^oC and 1 atm, respectively. The exhaust gas temperatures as well as steady state flame visual images were measured/recorded at each set of the experiments. The fuel lean flammability limits were studied at different fuel power and different equivalence ratios by varying percentage of CO_2 in the oxidizer mixture. Tables 3.8 and 3.9 show the detailed experimental plans for studying the effect of fuel firing rates on the blowout limit at different equivalence ratios. The lean stability limits were determined by starting stable flames at a fixed equivalence ratio (fixed mass flow rates of fuel and oxygen) while increasing the diluent (CO_2) flow rate up to the blow out limits. The flame was ignited, manually, at very low flow rates of O_2 and CH_4 (2 and 1 *L/min*, respectively) before increasing the flow rates and supplying the diluent as well to the required plan.

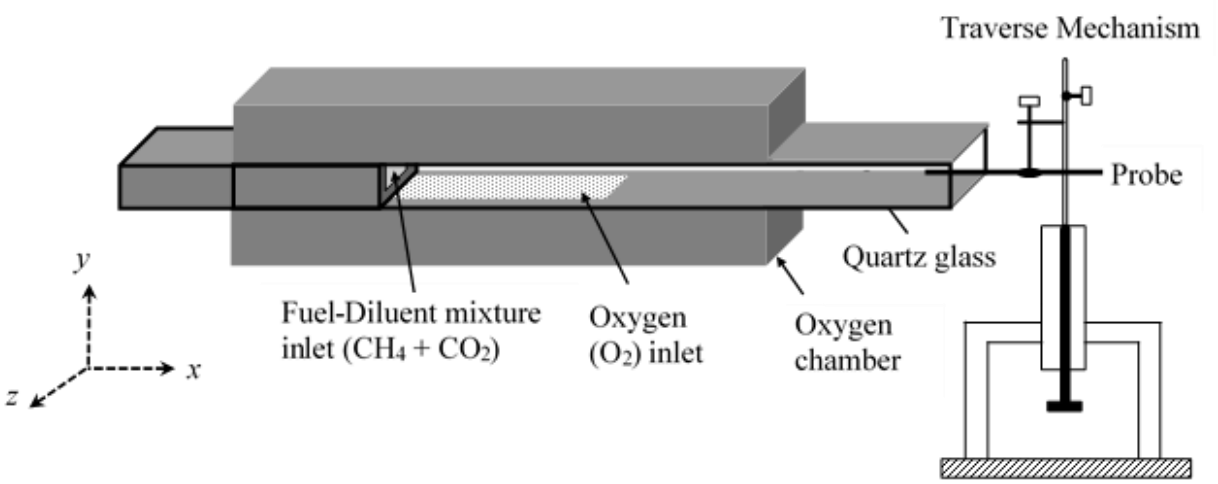

(a) Schematic diagram of the combustor geometry

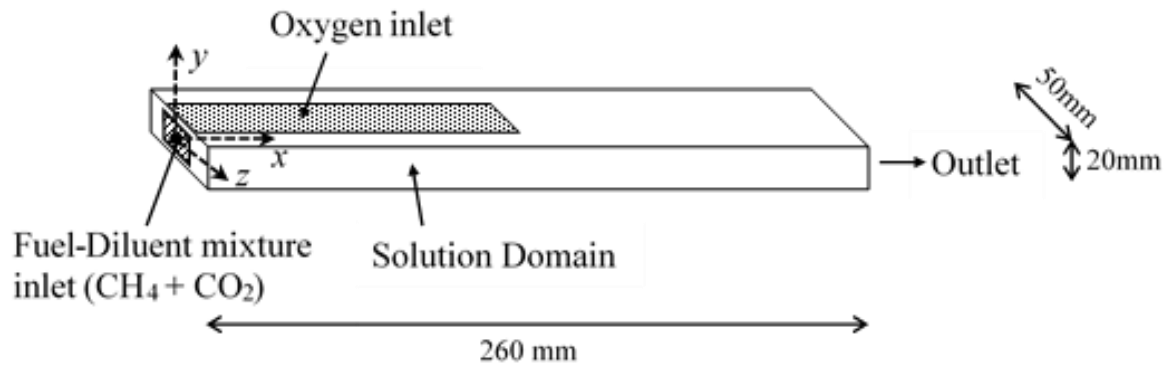

(b) 3D representation of the solution domain of the reactor

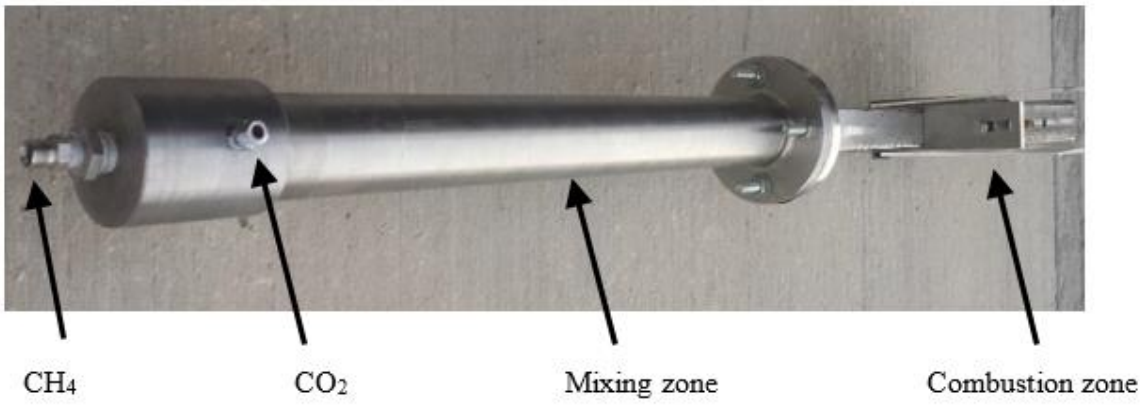

(c) Fuel-Diluent mixer

Figure 3.4: The combustor geometry.

The temperature distributions in the combustor were measured using an R-type thermocouple with temperature range of up to 1480 ± 1.5 ^{o}C. Three-dimensional temperature measurements were conducted near the outlet of the combustion chamber by inserting the thermocouple probe from the exhaust of the combustion chamber, as illustrated in Figure 3.4. The temperatures were measured horizontally, vertically and longitudinally at scheduled locations shown in Figure 3.5 and Figure 3.6. The temperatures were measured for a constant fuel firing rate of 1.5 kW.

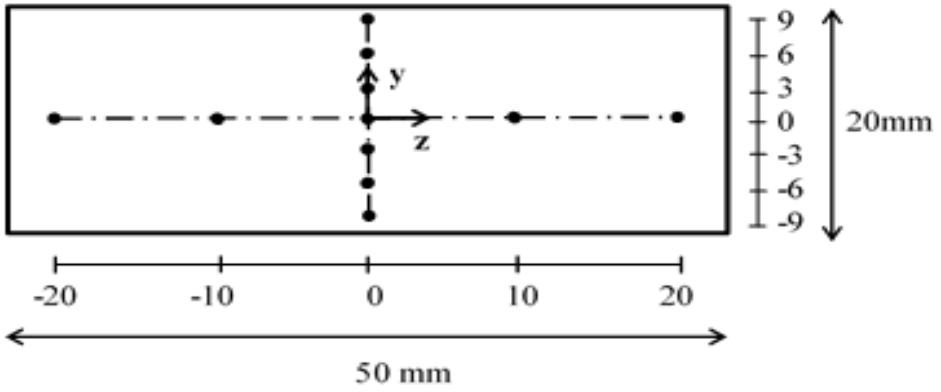

Figure 3.5: Outlet Nodalization of Horizontal and Vertical temperature measuring points.

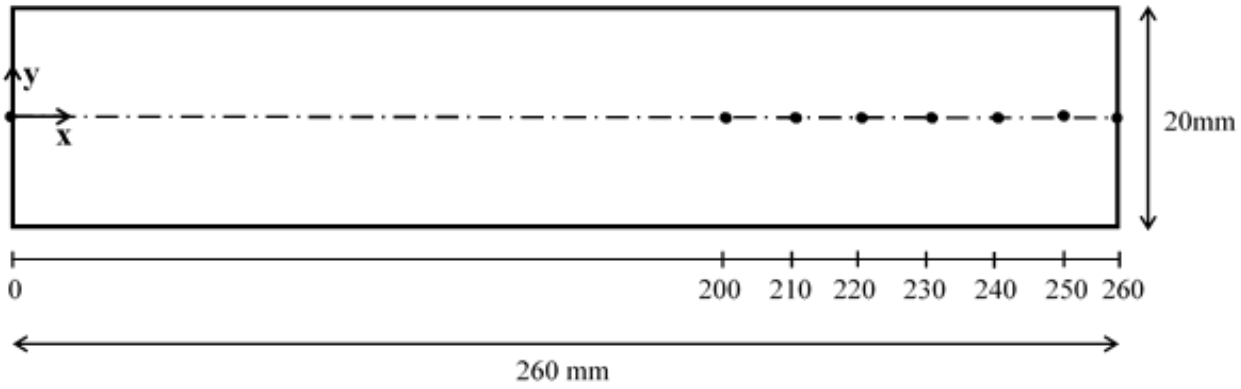

Figure 3.6: Nodalization of longitudinal temperature measurement.

3.2.2.1 Measuring equipment for combustion experiment

The equipment listed in section 3.2.1.2 were also used for the combustion experiments except the PIV setup (*a*). Other equipment utilized are:

a. High Resolution Camera: *Canon OS-80D* with precision focus camera for flame structure imaging.

b. Thermocouple: The Rhodium type (*R*-type) thermocouple with grade wire temperature range of -50 to 1480^{o}C, for exhaust temperature distribution measurements. It has an uncertainty of ± 1.5 ^{o}C or ± 0.25% (whichever is greater).

Table 3.6: Experimental plan for the combustion at different concentrations of CO_2 and a fixed fuel firing rate of 1.5 kW for a range of equivalence ratio

% $CO_2\|_{oxidizer}$	$\dot{Q}_{CH_4}$ (L/min)	ϕ = 1.0		ϕ = 0.7		ϕ = 0.5	
		$\dot{Q}_{O_2}$ (L/min)	$\dot{Q}_{CO_2}$ (L/min)	$\dot{Q}_{O_2}$ (L/min)	$\dot{Q}_{CO_2}$ (L/min)	$\dot{Q}_{O_2}$ (L/min)	$\dot{Q}_{CO_2}$ (L/min)
70	2.76	5.52	12.87	7.88	18.39	11.03	25.75
55	2.76	5.52	6.74	7.88	9.63	11.03	13.49
45	2.76	5.52	4.51	7.88	6.45	11.03	9.03
35	2.76	5.52	2.97	7.88	4.24	11.03	5.94
27	2.76	5.52	2.04	7.88	2.92	11.03	4.08
0	2.76	5.52	0.00	7.88	0.00	11.03	0.00

Table 3.7: Effect of equivalence ratios at fixed fuel firing rate of 1.5 kW.

ϕ	$\dot{Q}_{CH_4}$ (L/min)	$\dot{Q}_{O_2}$ (L/min)
1.0	2.76	5.52
0.9	2.76	6.13
0.8	2.76	6.90
0.7	2.76	7.88
0.6	2.76	9.20
0.5	2.76	11.03

Table 3.8: Effect of fuel firing rates at different equivalence ratios.

ϕ	1.5 kW		1.0 kW		0.75 kW		0.5 kW	
	$\dot{Q}_{CH_4}$ (L/min)	$\dot{Q}_{O_2}$ (L/min)	$\dot{Q}_{CH_4}$ (L/min)	$\dot{Q}_{O_2}$ (L/min)	$\dot{Q}_{CH_4}$ (L/min)	$\dot{Q}_{O_2}$ (L/min)	$\dot{Q}_{CH_4}$ (L/min)	$\dot{Q}_{O_2}$ (L/min)
1.0	2.76	5.52	1.84	3.68	1.38	2.76	0.92	1.84
0.9	2.76	6.13	1.84	4.09	1.38	3.07	0.92	2.04
0.8	2.76	6.90	1.84	4.60	1.38	3.45	0.92	2.30
0.5	2.76	11.03	1.84	7.36	1.38	5.52	0.92	3.68

Table 3.9: Effect of fuel firing rates at different stoichiometric equivalence ratio

Fuel firing rate (kW)	$\dot{Q}_{CH_4}$ (L/min)	$\dot{Q}_{O_2}$ (L/min)
0.75	1.38	2.76
1.00	1.84	3.68
1.50	2.76	5.52
2.00	3.68	7.36
2.50	4.60	9.20
3.00	5.52	11.03

3.3 Numerical Modeling of Porous Plate Combustor

The numerical simulations of the combustion were of two folds, first, 2D modeling of the non-reactive flow and oxy-methane combustion in the porous plate combustor and secondly, 3D oxy-methane combustion modeling of porous combustor to determine the combustion characteristics at different equivalence ratios and diluent/oxygen ratios as stipulated in the objectives of this research. In all the cases, mesh grid independence tests were conducted to avoid the effects of mesh size on the accuracy of the numerical results. The mesh sizes with least effects on the results of the parameters of interest were applied for the simulations. Details of one of the grid independence test will be discussed in Chapter 5. Also, the models were validated with the experimental data from this work and other available experimental data from the literature.

3.3.1 2D Non-reactive modeling

A finite volume approach of computational fluid dynamics (CFD) was employed to simulate the effect of oxygen permeation on the fuel feed velocity profile of a porous plate reactor, based on the CFD method devised by Habib et al., (2015) [97]. The flow geometry considered for the simulation of the porous plate reactor was a 2-D flow domain as shown in Figure 3.1(c). The commercial ANSYS 15.0 Workbench software was used to build the 2-D geometry, mesh the geometry into 144,000 cells, having 289,980 faces and 145,977 nodes with maximum aspect ratio of 1.7. The total volume was 0.036 m3. Finer mesh grids were considered at the relevant boundaries and the combustion zone were higher gradients

are expected. These mesh details were adopted after conducting mesh grid independence test. The general conservation equations (continuity, momentum and specie conservation) used by the software for the computations of the velocity, pressure, and concentration of the species were given in Section 2.2.2 of this report.

ANSYS 15.0 Fluent software based on finite volume approach was employed for the discretization of the conservation equations used for the numerical simulation. Pressure-Velocity coupling was achieved using an inbuilt 2D double precision solver semi-implicitly. Second-order upwind schemes was used for the species and momentum discretization while standard scheme was applied for the pressure. Advanced Multi Grid solver (AMG) was used to ensure convergence using the following under-relaxation factors: pressure = 0.3; density = 1; momentum = 0.7; body force = 1; energy = 0.8 and species = 1. Recursive 'f-cycle' process was set, and gradient stabilized bi-conjugate method was used to prevent convergence irregularities. Absolute convergence check criteria were set at 10-6 for all the residuals which implies convergence after all the residuals falls below the set criteria. Three cases (as shown in Table 3.5) were run and the average velocities were obtained at three sections of the IA for the purpose of model's validation. The species mass fractions were also obtained and utilized for the calculations of the mixture fractions, as well as average local equivalence ratios across the combustor.

3.3.2 2D Reactive modeling

The same CFD approach for the non-reactive flow simulation was employed for the combustion of both the 2D and 3D representations of the combustors via solving the same governing equations with additional energy and radiation heat transfer models described in Sections 2.3.2.3 and 2.3.3.2, respectively. In addition, Discrete Ordinate (DO) radiation model was used for computing radiative heat transfer for both the exhaust gases which are mostly participating media and surface-to-surface radiation. In order to determine the absorption coefficient of the exhaust gas mixture, ANSYS Fluent that Weighted-Sum-of-Gray-Gases (WSGG) Model was used. The model predicts the thermal radiation heat transfer between the flue gases, the walls of the combustor and the surrounding. The modified Westbrook-Dryer reduced methane chemical oxidation reaction mechanism for oxyfuel reaction with kinetic rate data provided by Andersen et al., [116] (Appendix B) was adapted for the chemical kinetics of the oxy-methane reactions. The scope of the experimental plan shown in Tables 3.10 were considered for the numerical simulations of the 2D combustor shown in Figure 3.1.

3.3.3 3D Reacting modeling

The combustor setup shown in Figure 3.4 that was used for the combustion experiments was modeled using 3D representation of the geometry. The same CFD approach for the 2D simulation described in Sections 3.3.2 was employed for the 3D modeling of the combustor shown in Figure 3.4 (b) by solving the same governing equations using the 3D double-

precision ‘SIMPLE’ solver. The scope of the experimental plan shown in Tables 3.6 were also considered for the numerical simulations in the 3D combustor.

Table 3.10. Sets of numerical cases for the analysis of oxy-combustion characteristics within the porous-plate reactor at various equivalence ratios

Case No.	Mass Flow rates x10^{-4} (kg/s)			Equivalence ratio (ϕ)
	CH_4	O_2	CO_2	
1	0.60	2.41	7.71	1.0
2		2.67	8.56	0.9
3		3.01	9.63	0.8
4		3.44	11.0	0.7
5		4.01	12.8	0.6
6		4.81	15.4	0.5
7		6.02	19.3	0.4

3.4 ITM Numerical Modeling

Application of oxy-fuel combustion in a two-pass Oxygen Transport Reactor (OTR) was intended for application in fire-tube boilers. Two-pass fire tube boiler design was considered with the schematic diagram of the geometry shown in Figures 3.7. In this design, several OTR units are used in lieu of the fire tubes available in conventional fire tube boilers. The OTR will be applied to a typical fire tube boiler for the generation of power in the range from 1 to 5 MWe to be fueled by natural gas (methane). This will

involve the replacement of the fire box (burner) with bundles of tubular OTM combustors that will supply the required power range. The fuel (Methane) pre-mixed with the sweep/diluent gas (CO_2) was burnt with pure oxygen selected by the ITM. Among the two types of the ITMs discussed in Section 2.4.1 BSCF-type was used for the oxygen permeation modeling due to its highest oxygen permeation flux. The geometry of the oxygen transport reactor was optimized to achieve the required boiler specifications. The membranes thickness was also optimized to provide the required amount of oxygen for the near stoichiometric combustion of the fuel.

The geometry was modeled using 2D representation of the OTR due to its axisymmetric nature as shown in Figures 3.7(b). The commercial ANSYS 17.1 Workbench software was used in developing the 2D mesh file of the geometry. The CFD approach that was developed for the combustion numerical modeling of section 3.3.2 was applied for the simulation of the OTR. A source/sink term (S_i) that is responsible for accounting for the transport of the O_2 across the OTM was included in the general equations shown in Section 2.3.2. The modified continuity and transport equations that takes care of the O_2 movement from the feed side to the permeate side as suggested by [205, 206] are given by Equations 3.1 and 3.2 respectively.

$$\nabla \cdot (\rho \vec{v}) = S_i \tag{3.1}$$

$$\nabla \cdot (\rho \vec{v} Y_i) = -\nabla \cdot \left(\rho D_{i,m} \nabla Y_i\right) + R_i + S_i \tag{3.2}$$

Where ρ is density, $\vec{v}$ is velocity vector, S_i is mass source term, Y_i is mass fraction of i-th specie (local), $D_{i,m}$ is diffusion coefficient of species in the mixture and R_i is the rate of production of i-th specie due to chemical reaction. The diffusion coefficient of the mixture, $D_{\mathrm{i,m}}$ for specie transport, can be computed as (Equation 3.3) [196]:

$$D_{\mathrm{i,m}} = \frac{1-X_{\mathrm{i}}}{\sum_{j,j\neq 1}\left(\frac{X_{\mathrm{i}}}{D_{\mathrm{i,j}}}\right)} \tag{3.3}$$

Where $D_{i,j}$ is binary mass diffusion coefficient which can be evaluated using Chapman-Enskog equation by utilizing kinetic theory [207].

In oxygen transport membrane the mass source term S_i, accounts for the oxygen mass influx into the reaction zone via permeation as well as the mass deficit (sink) of the feed zone as shown in Equation 3.4:

$$S_i = \begin{cases} -\frac{Jo_2 \cdot A_{cell} \cdot Mo_2}{V_{cell}} & feed\ side \\ +\frac{Jo_2 \cdot A_{cell} \cdot Mo_2}{V_{cell}} & sweep\ zone \end{cases} \tag{3.4}$$

Where Jo_2 is oxygen permeation flux, A_{cell} and V_{cell} are the cells' area and volume, respectively, Mo_2 is the oxygen molecular weight.

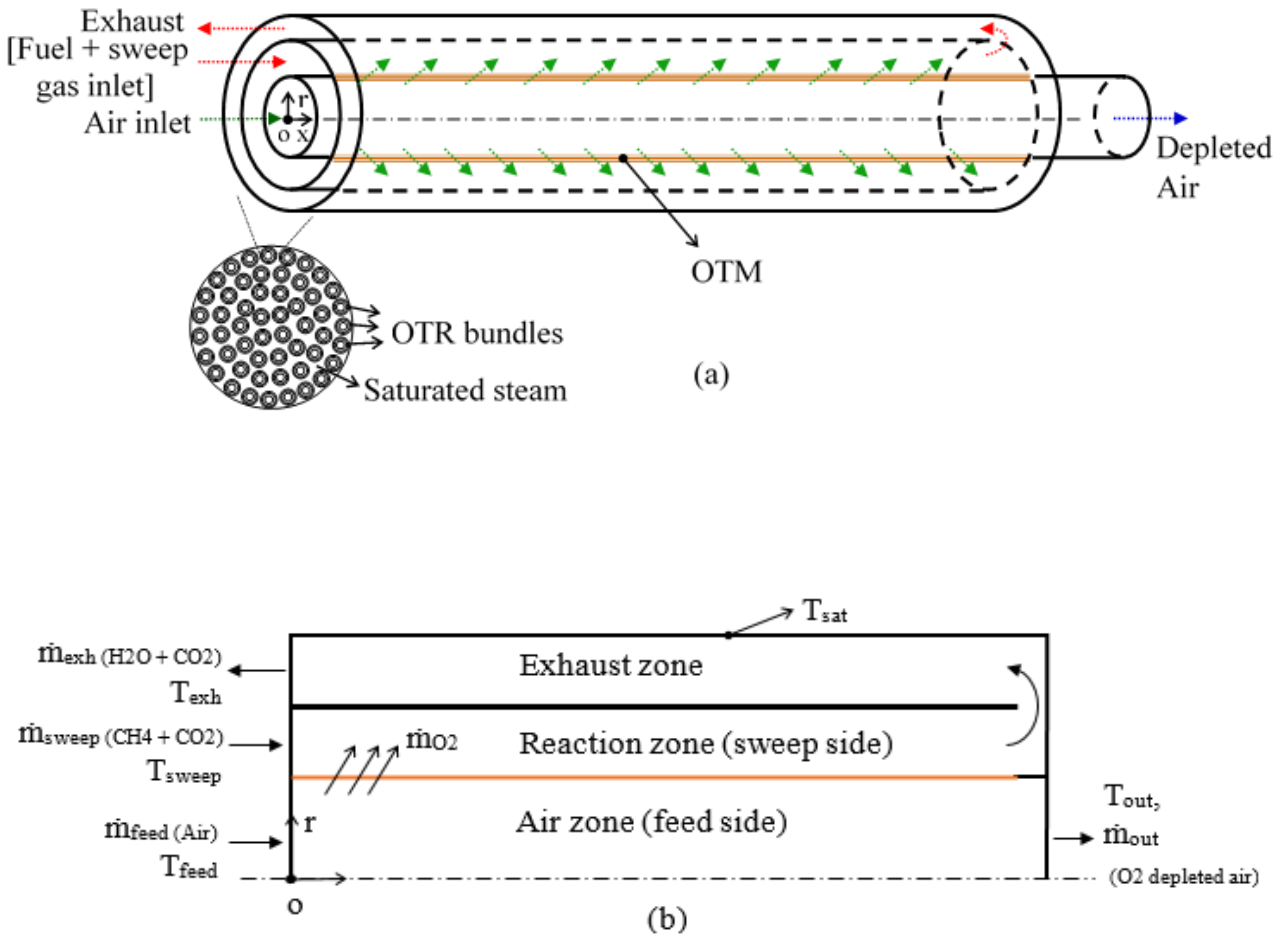

Figure 3.7: (a) Schematic diagram of the OTR, (b) 2D representations of the OTR.

3.4.1 Geometry description and boundary conditions

The geometry consisted of concentric tubes with inner-most pipe made of OTM (1 mm thick, 20 mm internal diameter and 500 mm long). Despite the potential of increase in O_2 flux at lower OTM thickness, there is a critical thickness beyond which its structural integrity will be affected by the pressure difference across it, hence 1 mm was considered [208]. The second pipe is made of low thermal conductivity material (0.1 [W/m-K], 0.95 outer surface emissivity) with a thickness of 3 mm and outer diameter of 40 mm. The outer pipe, which is in contact with the saturated steam at constant boundary temperature (corresponding the saturation condition) is made of aluminum having internal diameter of 50 mm. Air at elevated temperature is supplied through the central pipe (feed side) while a mixture of methane and sweep gas (carbon dioxide) were supplied through the annulus between the second inner pipe and the central OTM tube. The outer annulus conveyed the exhaust gases after combustion and transferred the exhaust gas heat to the saturated steam at the outer surface of the outer pipe. Mass flow inlet boundary conditions were specified at both the sweep and feed inlet sections while pressure outlet was specified for the two exit sections. Mass source boundary condition at the membrane interface were specified via the UDF. The OTM permeates oxygen ions from the feed side into the sweep side where it reacts with the CH_4 in the sweep side. The 1 mm thick BSCF membrane used has a density of 3000 kg/m^3, specific heat capacity of 0.871 kJ/kg-K and thermal conductivity of 20 W/m-k.

Due to significantly large power range of the proposed boiler as well as the current state of the art in the OTM development, the fuel, diluent as well as the air flow rates must be explored to achieve the overall goal of carbon emission free boiler. Also, the current dependence of oxygen transport membrane on temperature elevation necessitate the temperature optimization for sufficient oxygen permeation. Hence Tables 3.11, which show the set of boundary conditions for the parametric studies of the effects of inlet temperature of the gases on the combustion as well as heat transfer to the saturated steam has been considered in this work. It involves three sets of boundary conditions whereby the effect feed inlet temperature cases considered were shown in the second block of Table 3.11, the effect of sweep gases inlet temperature cases in the third block and the combine effect of both feed and sweep temperatures shown in the last block, while keeping the mass flow rates of both the feed and sweep gases constant at 0.0005 kg/s. In a similar fashion, the effect of change in mass flow rates of the gases were considered in Table 3.12 while keeping the inlet temperatures of both the feed and sweep gas streams at 900 ^{o}C. Furthermore, the operating conditions of the intended boiler will also affect the combustion performance. This effect has been evaluated by considering six sets of parametric boundary conditions as shown in Table 3.13. In each case, the temperature and mass flow rates of the gas streams were kept at 900 ^{o}C. and 0.0005 kg/s, respectively, while varying the outer-pipe surface temperatures corresponding to the saturation temperature and pressure of steam from 10 – 50 bars.

Table 3.11: Effect of feed and sweep streams inlet temperatures

		Feed inlet temp.		Sweep inlet temp.		Feed and Sweep temp.	
$\dot{m}_{feed}$ [kg/s]	$\dot{m}_{sweep}$ [kg/s]	T_{feed} [^oC]	T_{sweep} [^oC]	T_{feed} [^oC]	T_{sweep} [^oC]	T_{feed} [^oC]	T_{sweep} [^oC]
5.0E-04	5.0E-04	800	900	900	800	800	800
5.0E-04	5.0E-04	850	900	900	850	850	850
5.0E-04	5.0E-04	900	900	900	900	900	900
5.0E-04	5.0E-04	950	900	900	950	950	950
5.0E-04	5.0E-04	1000	900	900	1000	1000	1000

Table 3.12. Effect of feed and sweep streams inlet mass flow rates

		Feed inlet flow rate		Sweep inlet flow rate		Feed and Sweep flow rate	
T_{feed} [^oC]	T_{sweep} [^oC]	$\dot{m}_{feed}$ [kg/s]	$\dot{m}_{sweep}$ [kg/s]	$\dot{m}_{feed}$ [kg/s]	$\dot{m}_{sweep}$ [kg/s]	$\dot{m}_{feed}$ [kg/s]	$\dot{m}_{sweep}$ [kg/s]
900	900	1.0E-05	5.0E-04	5.0E-04	1.0E-05	1.0E-05	1.0E-05
900	900	5.0E-05	5.0E-04	5.0E-04	5.0E-05	5.0E-05	5.0E-05
900	900	1.0E-04	5.0E-04	5.0E-04	1.0E-04	1.0E-04	1.0E-04
900	900	5.0E-04	5.0E-04	5.0E-04	5.0E-04	5.0E-04	5.0E-04
900	900	1.0E-03	5.0E-04	5.0E-04	1.0E-03	1.0E-03	1.0E-03

Table 3.13. Effect of steam saturation temperature at the outer pipe surface

$\dot{m}_{feed}$ [kg/s]	$\dot{m}_{sweep}$ [kg/s]	T_{feed} [^oC]	T_{sweep} [^oC]	P_{sat} [bar]	T_{sat} [^oC]
5.0E-04	5.0E-04	900	900	10	180
5.0E-04	5.0E-04	900	900	15	199
5.0E-04	5.0E-04	900	900	20	212
5.0E-04	5.0E-04	900	900	25	224
5.0E-04	5.0E-04	900	900	30	234
5.0E-04	5.0E-04	900	900	50	264

The diluent (CO_2) mass flow rates were varied from 0.000225 to 0.00123 kg/s in order to study its effect on O_2 permeation flux. The six cases considered were enumerated in Table 3.14. In all the cases, the inlet temperatures of both the feed and sweep gas streams were kept at 900 ^oC while the mass flow rate of the feed gas stream was maintained at 0.0005 kg/s. The effect of OTM thickness on the oxygen permeation flux was consider as shown in Table 3.15 while keeping the inlet temperatures and mass flow rates of both the feed and sweep gas streams at 900 ^oC and 0.0005 kg/s, respectively.

Table 3.14: Effect of diluent (CO_2) inlet mass flow rates

%CH_4	%CO_2	$\dot{m}_{CH4}$ [kg/s]	$\dot{m}_{CO2}$ [kg/s]	$\dot{m}_{sweep}$ [kg/s]	$\dot{m}_{feed}$ [kg/s]	T_{sweep} [^oC]	T_{feed} [^oC]
0.10	0.90	2.5E-05	2.25E-04	2.50E-04	5.0E-04	900	900
0.08	0.92	2.5E-05	2.88E-04	3.13E-04	5.0E-04	900	900
0.06	0.94	2.5E-05	3.92E-04	4.17E-04	5.0E-04	900	900
0.05	0.95	2.5E-05	4.75E-04	5.00E-04	5.0E-04	900	900
0.04	0.96	2.5E-05	6.00E-04	6.25E-04	5.0E-04	900	900
0.02	0.98	2.5E-05	1.23E-03	1.25E-03	5.0E-04	900	900

Table 3.15: Effect of OTM thickness

OTM thickness [mm]	T_{feed} [^oC]	T_{sweep} [^oC]	$\dot{m}_{feed}$ [kg/s]	$\dot{m}_{sweep}$ [kg/s]
0.8	900	900	5.0E-04	5.0E-04
1.0	900	900	5.0E-04	5.0E-04
1.2	900	900	5.0E-04	5.0E-04

To evaluate the influence of thermal properties of the OTR materials on the combustion characteristics as well as the heat transfer, the emissivities of the inner and outer pipes are critical to the radiation heat transfer within the OTR. Hence, Tables 3.16 and 3.17 were used for the analyses of their effects on the radiation heat transfer while keeping other boundary conditions constant.

Table 3.16: Effect of inner-pipe thermal conductivity

$k_{\text{inner-pipe}}$ [W/m-K]	T_{feed} [^{o}C]	T_{sweep} [^{o}C]	$\dot{m}_{\text{feed}}$ [kg/s]	$\dot{m}_{\text{sweep}}$ [kg/s]
0.05	900	900	5.0E-04	5.0E-04
0.10	900	900	5.0E-04	5.0E-04
0.30	900	900	5.0E-04	5.0E-04
0.50	900	900	5.0E-04	5.0E-04
0.70	900	900	5.0E-04	5.0E-04
0.90	900	900	5.0E-04	5.0E-04
0.95	900	900	5.0E-04	5.0E-04
1.00	900	900	5.0E-04	5.0E-04

Table 3.17: Effect of inner-pipe emissivity

Inner-pipe emissivity	T_{feed} [^{o}C]	T_{sweep} [^{o}C]	$\dot{m}_{\text{feed}}$ [kg/s]	$\dot{m}_{\text{sweep}}$ [kg/s]
0.05	900	900	5.0E-04	5.0E-04
0.10	900	900	5.0E-04	5.0E-04
0.30	900	900	5.0E-04	5.0E-04
0.50	900	900	5.0E-04	5.0E-04
0.70	900	900	5.0E-04	5.0E-04
0.90	900	900	5.0E-04	5.0E-04
0.95	900	900	5.0E-04	5.0E-04
1.00	900	900	5.0E-04	5.0E-04

3.4.2 Geometry description and boundary conditions

Due to axisymmetric nature of the considered geometry, the oxy-fuel combustion was modeled in a single, two-dimensional OTR unit that was presented in Figure 3.7. The CFD code ANSYS Fluent Release: 17.1.0 was used in double-precision for the combustion modelling. The solver type used for computing the solution was pressure-based, which enables the pressure-based Navier-Stokes solution algorithm. This was choosing due to the very low flow rates and its higher convergence speed. The pressure-based solver uses a coupled algorithm. This solves the pressure-based continuity equation and the momentum equations in a coupled manner. A relative velocity formulation was used since the domain was moving. Steady state, Laminar flow was considered due to the low flow rates with maximum Reynolds number of 1914 at the feed side. Energy model was used to solve the energy equations. Discrete Ordinate Model was considered for the two non-reacting species that participate in the radiation. Species transport was enabled for the mixture of the combustion exhaust gases with inlet diffusion. The set of oxygen permeation Equations 2.28 – 2.31 provided in Section 2.4.5 were used for the modeling the oxygen permeation flux across the tubular OTM. The generalized finite-rate chemical kinetics model was used to simulate the chemical kinetics of the volumetric reactions. This required importing a chemical kinetic (CHEMKIN) file containing the reaction mechanisms in to the FLUENT solver. The oxygen permeation flux equation was defined in the FLUENT 17.1.0 via a User Defined Function (UDF) written in C++ language. The code was, then, compiled and hooked to the ANSYS FLUENT software. The possible problem of hydraulic jump across the membrane was fixed by patching the cells of the permeate as well as the sweep sides with the mass fractions of the species which determines the partial pressures of species.

The SIMPLE Pressure-Velocity coupling scheme was chosen. The discretization scheme for Pressure, Density, Momentum, Energy and Species and the Discrete Ordinate were all set to Second Order Upwind. Enhancement of the solution convergence was ensured by employing the aggressive advanced multi-grid (AMG) scheme. For the coupled equations consisting of continuity, momentum, energy, and species, AMG ‘f-cycle’ was set as a recursive method. To evade irregular convergence, the available bi-conjugate gradient stabilized scheme was used. The solution convergence criteria were set as below 10-9 for the continuity and energy residuals. Also, in order to confirm the convergence, mass fractions of carbon dioxide and water, outer-pipe surface heat flux and exhaust gas temperatures were monitored until their values became constant. Mesh grid dependency test was performed to ensure mesh size independency for accurate solutions and the model was validated with available experimental data.

CHAPTER 4

RESULTS AND DISCUSSIONS FOR THE POROUS COMBUSTOR

This section contained the results of both experimental and numerical modeling studies of the flow field and oxy-fuel combustion characteristics inside the porous-plates reactor. The results are presented under four sub-sections: non-reactive flow-field experimental analysis, 2D numerical modeling of the flow and combustion characteristics, experimental testing of oxy-fuel combustion, and 3D numerical modeling of oxy-fuel combustion. The non-reactive flow characteristics were investigated experimentally and numerically to predict the flow mixing behavior and the location of the flame zone. Among the non-reactive flow-field characteristics studied, the investigation includes the velocity vectors, flow streamlines, velocity profiles, and average velocities at some chosen locations within the mixing zone using PIV technique. Then, flow field and oxy-combustion characteristics of methane were investigated numerically over ranges of operating conditions. The non-reactive flow model was used for further analyses of the flow-field as well as methane combustion studies. The non-reactive flow setup was adjusted based on the previous results to cater for hot oxy-methane combustion. The temperature distributions downstream of the combustor were measured and the flames shape were captured and analyzed. A 3D model was developed for the reactor and the results from the combustion experiments were used for the model validation. The flame structure, stability, temperature distributions as well

exhaust emissions were investigated using both the experimental studies and the numerical model. Methane was used as fuel and premixed with the diluent (CO_2) prior to the combustion zone inlet while pure O_2 was supplied to the combustion zone through the two face-to-face porous plates.

4.1 Non-Reactive Experiments

The three sets of experiments planned in Table 3.5 were conducted to determine the effect of oxygen permeation across the two porous plates on the velocity profile within the central (mixing) zone of the reactor under non-reactive flow conditions. In all the three cases, a constant fuel volume flow rate of 2.5 lit/min and fixed volumetric flow rate ratio of CO_2/O_2 of 1.0 were considered. This low fuel flow rate was considered to mimic the operation of High-Temperature Membrane Reactors (HTMRs) combining both oxygen separation and oxy-combustion of the fuel using the permeated oxygen in the permeate side of the membrane. Still oxygen separation membranes are under development to produce higher oxygen permeation flux for complete combustion of the fuel for HTMR applications. In this study, two face-to-face porous-plates are used instead of membranes to allow ease control of oxygen supply enabling the study of flow field and oxy-combustion characteristics of HTMRs. The experiments were conducted at different O_2 flow rates. Case 1 represent oxygen flow rate 8.3 l/min at equivalence ratio of 0.6, Case 2 represent oxygen flow rate 10 l/min at equivalence ratio of 0.5, 10.0 while Case 3 was conducted at 12.5 l/min of oxygen for equivalence ratio of 0.4.

From the PIV analyses, the averaged velocity vectors and the streamlines plots for the first apart of the IA (Figure 3.2) are presented for the three considered cases shown in Figures 4.1 and 4.2 respectively. Near the walls (porous plates), the velocity vectors were scarce, shorter in length indicating low velocity in the mixing boundary layer and deflected as the result of the oxygen gas permeation from the oxygen zone into the central zone seeded with particles. As shown in Figure 4.1, the level of mixing increases with the decrease of equivalence ratios. This can be attributed to the increase in oxygen flow rate associated with the increase in equivalence ratio. This behavior can be seen more evidently from the contours of streamlines presented in Figure 4.2. The third case, having the highest oxygen flow rate, showed increased fluctuation near the porous plates due to enhanced flow mixing. If the results are projected on HTMR operation, this enhanced flow mixing should help reducing oxygen partial pressure at the permeate side of the membrane resulting in increased oxygen permeation flux. Also, this enhanced mixing zone beside the membrane protects the membrane against the flame elevated temperature and helps in flame anchoring and stabilization within the HTMR.

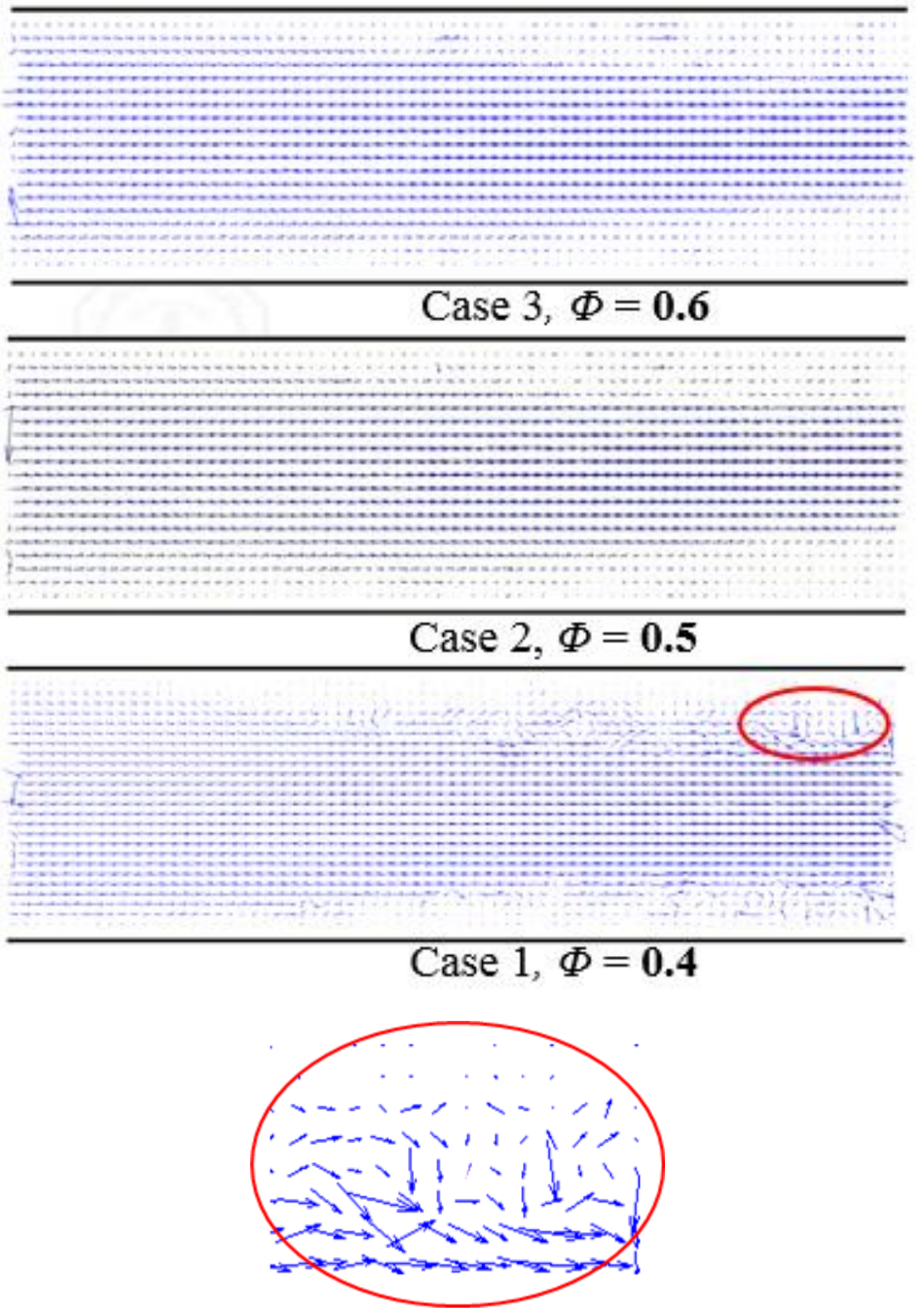

Figure 4.1: Velocity vectors at different equivalence ratios.

Figure 4.3 shows the traverse velocity profiles of the fuel-diluent and oxygen mixture obtained at three different sections of the IA for the considered range of experiments. Section *a, b* and *c* are located at 10 mm, 35 mm and 70 mm from the leading edge of the porous plate axially, as presented in Figure 4.3d. As per Figure 4.3, the velocity profiles tend to deviate from the known parabolic profile of internal flows along the length of the porous plate due to permeation of oxygen across the porous plates. At a given equivalence ratio, the total permeation flow rate of oxygen increases along the reactor in the axial direction, from section *a* to section *c*, resulting in an increase in flow velocity and more distortion of the profiles at the end of the IA, which corresponds to the middle zone of the porous plates. Whereas, the distortion of the velocity profiles due to oxygen mixing also increases with decrease in equivalence ratio. While decreasing the equivalence ratio, the maximum velocity increases due to the increase in compression of the fuel-diluent stream by the increase in the pressure of the oxygen cross-flow.

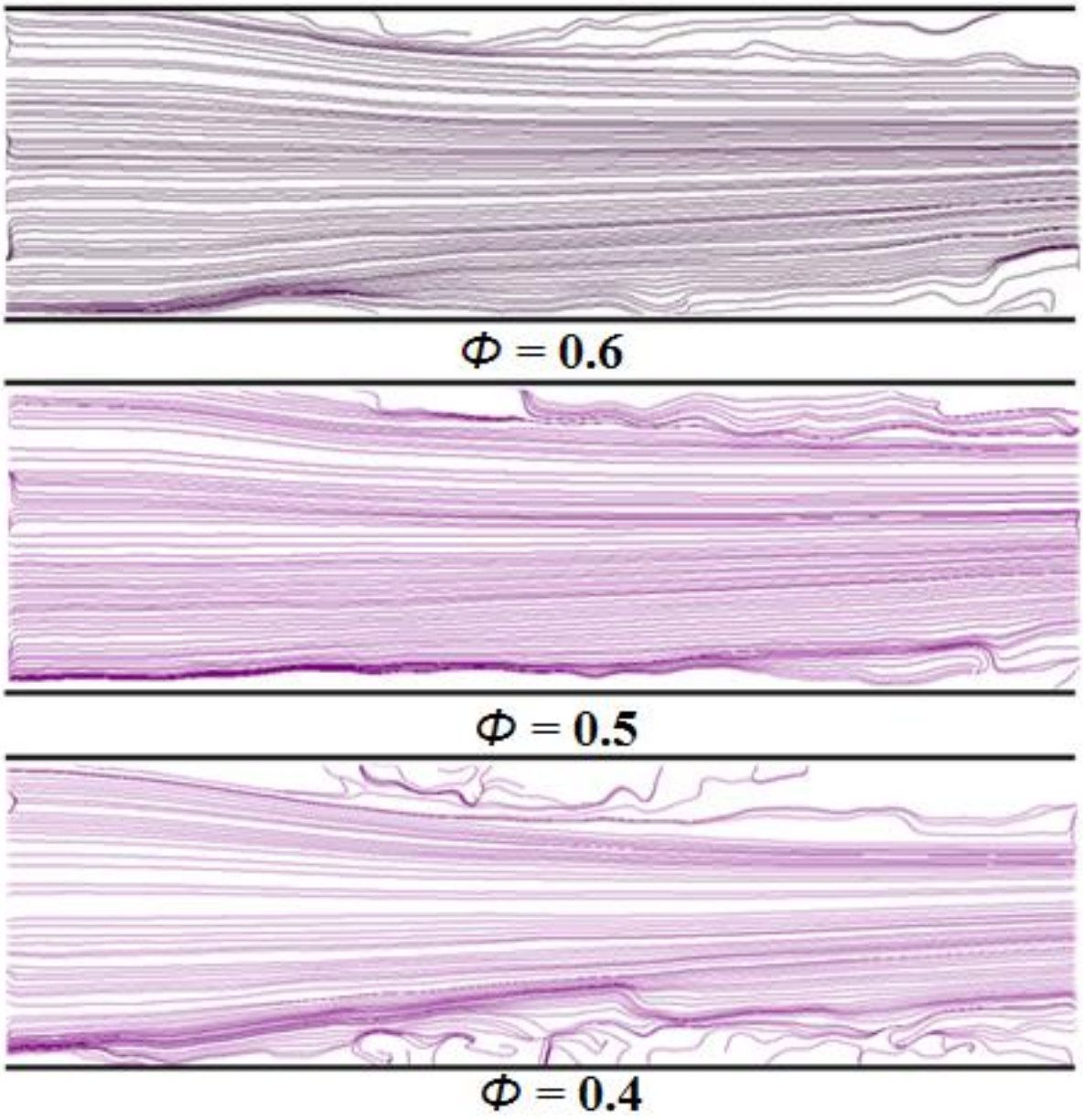

Figure 4.2: Streamlines at different equivalence ratios.

The mean velocities of the fuel and diluent mixture before the porous plates were calculated to be 0.100, 0.116 and 0.140 *m/s* ± 0.5% for equivalence ratios of 0.6, 0.5 and 0.5 respectively, as shown in APPENDIX I. The images from the flows were analyzed using the PIV system for the interrogation area (IA) of 25.3x750mm^2 (first half of the porous plate) for the two sets of experiments with φ of 0.5 and 0.6, and the overall length of the porous plate (Figure 4.3d, sections *a-f*) for the case of φ = 0.4. Average velocities were obtained at different axial locations in the central zone between the two porous plates for all the cases considered and tabulated in APPENDIX J.

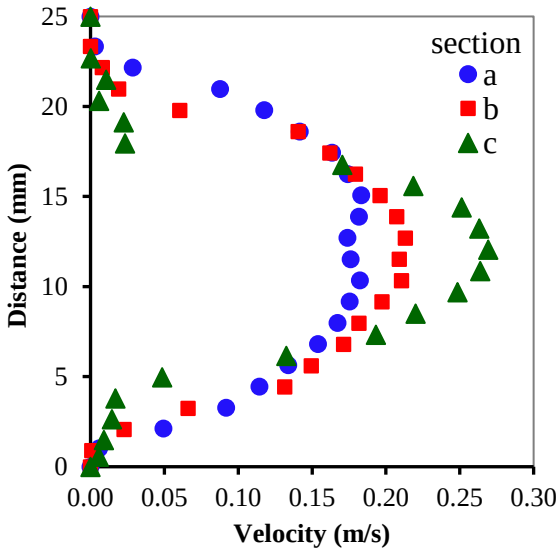

(a) Φ = 0.6

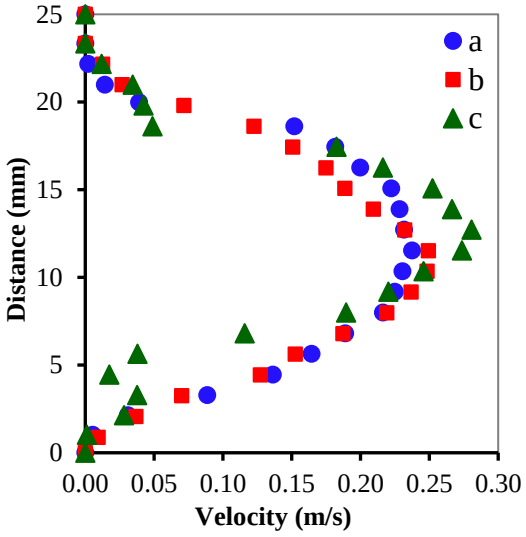

(b) Φ = 0.5

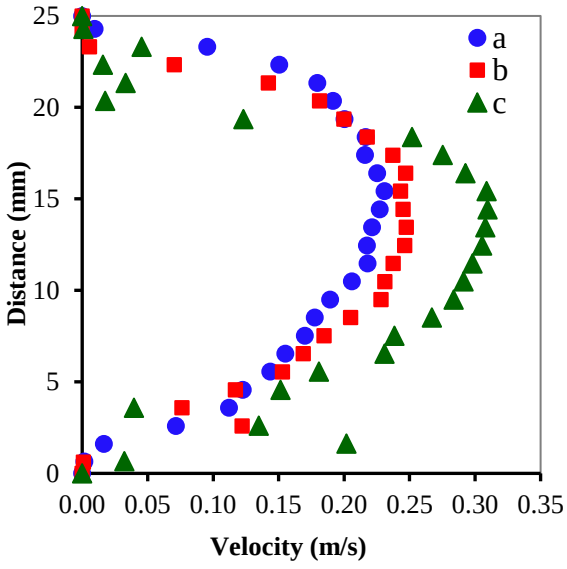

(c) Φ = 0.4

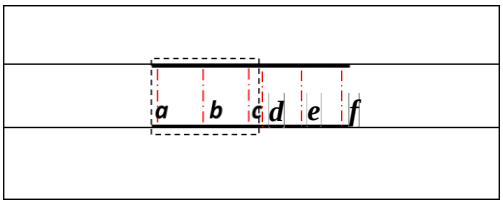

(d) Sectional descriptions of IA

Figure 4.3: Experimental velocity profiles at the three different sections (a, b and c) within the porous-plate reactor for different equivalence ratios

4.1.1 Averaged axial velocities

When the experimental conditions were simulated numerically using the present CFD model at the corresponding equivalence ratios, the corresponding average velocities of the flow in the central zone between the two porous plates at the six sections of the flow domain were extracted from the mass-weighted average surface integrals. These sections correspond to the same sections used during the PIV experiments to give room for comparison. Both experimental and numerical values of average velocities are compared as shown in Figure 4.4. The comparison of average velocities shows good agreement between the experimental and simulated results with absolute error of less than 4%. Due to continuous oxygen permeation across the porous plates to the central channel, the total volume flow rate is increased, resulting in increase in the average velocity in the axial

direction downstream of the porous plate. Projecting the analysis to the HTMR operation, the excess oxygen permeated from the end parts of the membranes in the axial direction cools down the flame temperature and protect the membrane against excessive temperature rise. Also, the enhanced velocity downstream of the membrane helps better flame anchoring and stabilization downstream of the membrane zone.

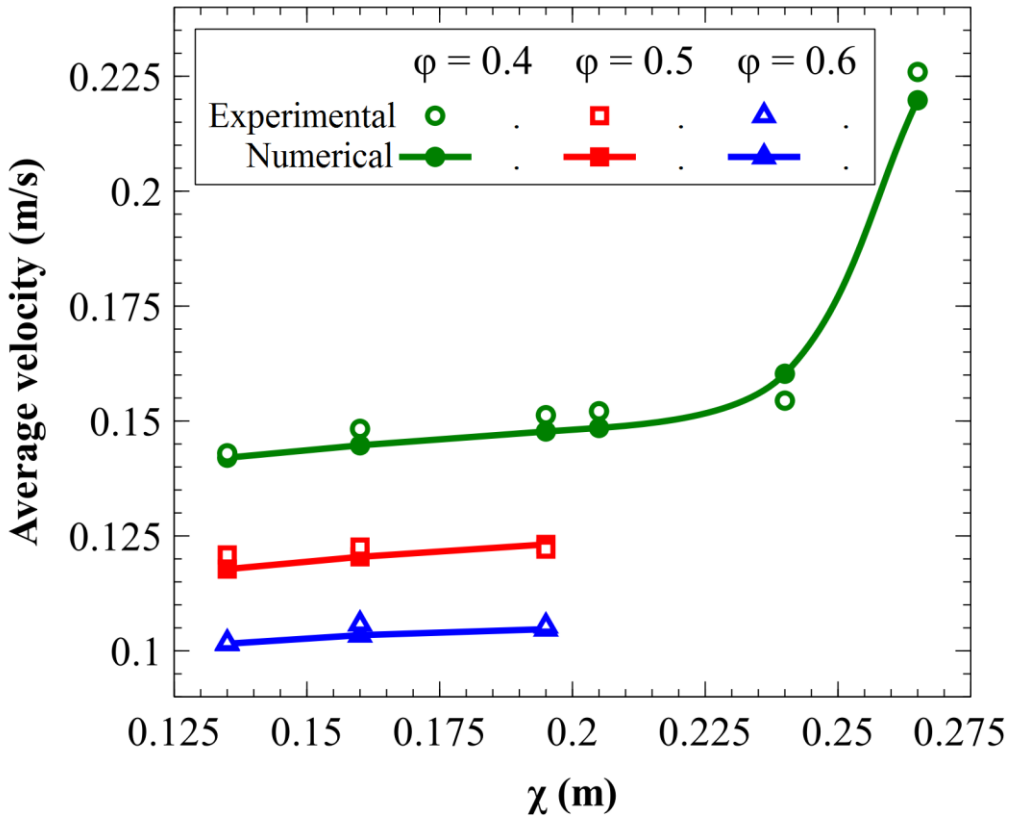

Figure 4.4: Comparison of experimental and numerical values of average velocities along the combustor at the three equivalence ratios.

4.1.2 Local distributions of mixture fraction and equivalence ratio

The mass fractions of CH_4, CO_2 and O_2 were obtained numerically at different axial positions, and Equations 2.8 through 2.10 were applied to compute the mixture fractions and the local equivalence ratios through the reactor as presented in Figures 4.5 and 4.6, respectively. From Figure 4.5, the mixture fraction decreases axially along the porous plate section and remain constant downstream of the porous plate at all operating equivalence ratios. The results show no oxygen at the beginning of the porous plate. The mass flux of the oxygen increases almost linearly up to about three-quarters of the porous section and then increases exponentially toward the end of the porous plate. The mixture fraction reaches its' lowest value at the end of the porous plate and remains constant up to the exit section of the reactor since there was no more oxygen inflow. These results coincide with the findings by Farooqui *et al.,* (2013)[209] for oxygen permeation inside a HTMR. The results show insignificant increase of mixture fraction with the increase in the overall operating equivalence ratio through the center of the reactor as the oxygen flow is introduced from top and bottom porous plates. Figure 4.6 shows the variation of average local equivalence ratio along the length of the porous plate reactor. Since there is little amount of oxygen at the beginning of the porous plate, the average equivalence ratio is the highest, and it decreases rapidly to the stoichiometric value towards the end of the porous plates due to oxygen permeation across the porous plates. Downstream of the porous plates, the local equivalence ratio decreases to the set value (global equivalence ratio) for the three cases. This shows that the reactor attains an averaged equivalence ratio equal to the set value, based on the inlet flow rates, just downstream of the porous plate. This gives an idea about the position in the reactor where the set equivalence ratio is achieved and,

accordingly, the location of the flame downstream of the porous plates. The interaction between the permeated oxygen and the main flow creates recirculation zone across the entire length of the reactor which helps stabilizing the flame and acts as flame anchoring point for the flame downstream of the porous plates. The location of the flame downstream of the membrane for the operation of HTMRs of similar design protects the membrane against high flame temperature and allows for complete fuel conversion.

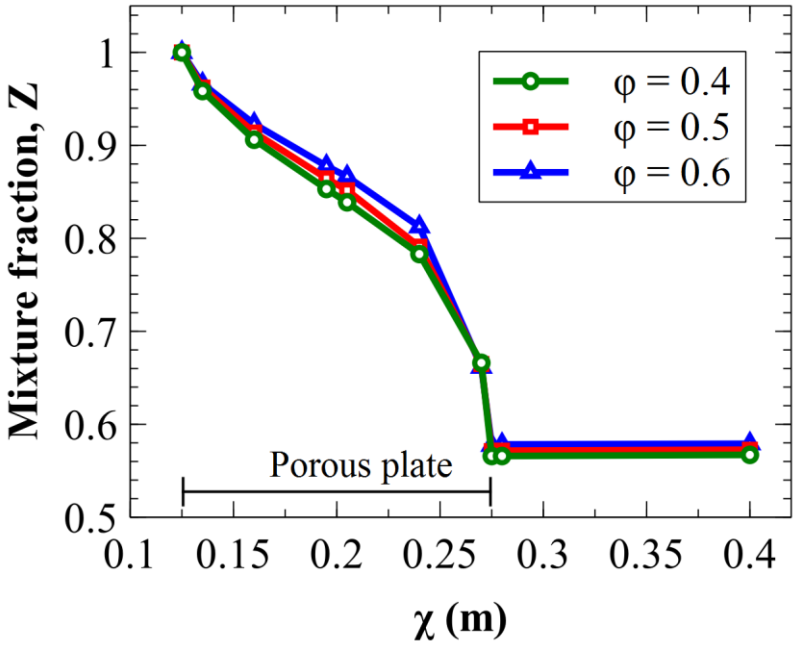

Figure 4.5: Variation of fuel mixture fraction along the test section.

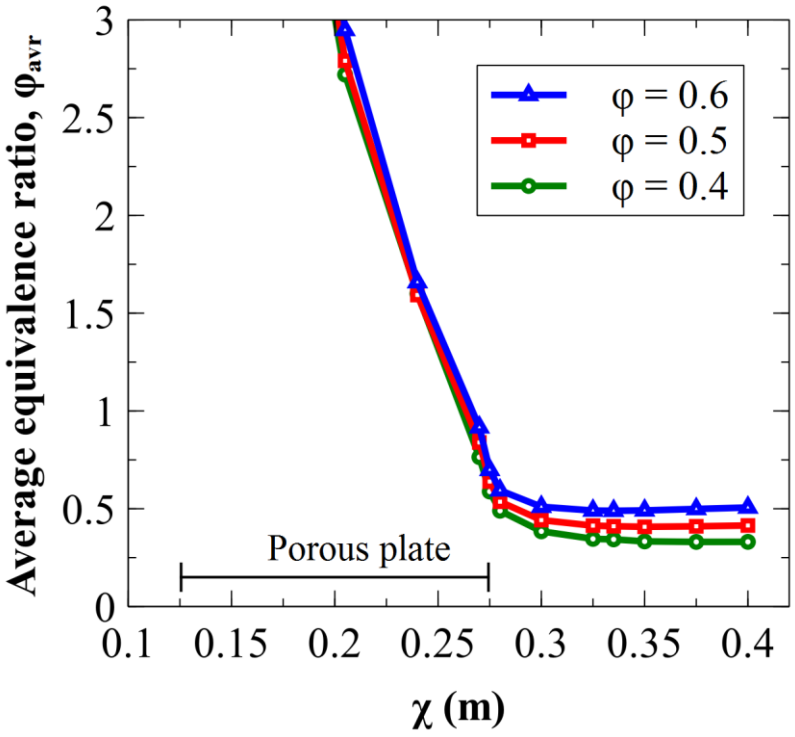

Figure 4.6: Variation of the average local equivalence ratio along the test section.

The analysis of the average equivalence ratio paved the way for establishing a general relationship between the inlet (global) equivalence ratio and the position within the reactor where this value is achieved. This has been depicted in Figure 4.7. A linear relationship between the global equivalence ratio and the axial position where it occurs was obtained as follows (Equation 4.1):

$$\phi_g = 4.1857 - 12.86\chi \tag{4.1}$$

where χ (m) is the position, from the origin. The plot shows that the higher the set (global) equivalence ratio, the lower the mixture fraction and the shorter the axial

distance at which it is achieved. This means that for operation toward stoichiometric combustion, the flame will be shifted upstream. This may be attributed to the reduced flow rate of O_2 and CO_2 and reduction in total axial flow velocity.

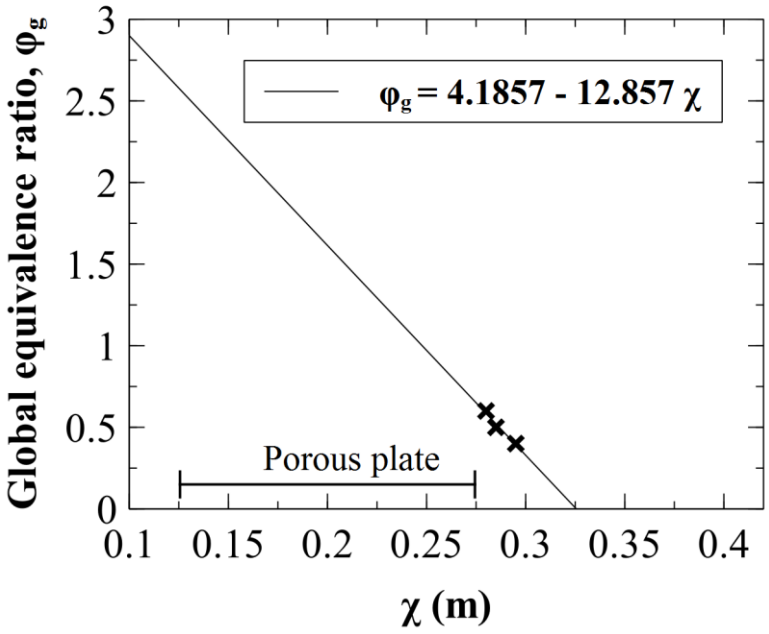

Figure 4.7. Position of average equivalence ratio along the porous flow domain.

For more insight, the traverse variations of mixture fraction and local equivalence ratio within the reactor, in the zone between the two porous plates, are presented in Figures 4.8 and 4.9 respectively. The results in Figures 4.8 indicate that higher oxygen mass fractions are obtained at the end of the porous plates, and the profile is sharper at the centerline of reactor with a steep decrease towards the porous plates. The variations in the profile of mixture fraction in the traverse direction are reduced downstream of the porous plates indicating better mixing. The improved mixing downstream of the porous plates is

assured by the distributions of local equivalence ratio as shown in Figure 4.9a at inlet equivalence ratio of 0.6 and Figure 4.9b for three cases studied. Note: Higher local equivalence ratios were truncated in Figure 4.9 due to their irrelevance. The values of mixture fraction and the equivalence ratio increases in the traverse direction, from the surface of the porous plates toward the center of the reactor where their maximum values are attained, for all operating set equivalence ratios. The higher the equivalence ratio the higher the mixture fraction and the local equivalence ratio.

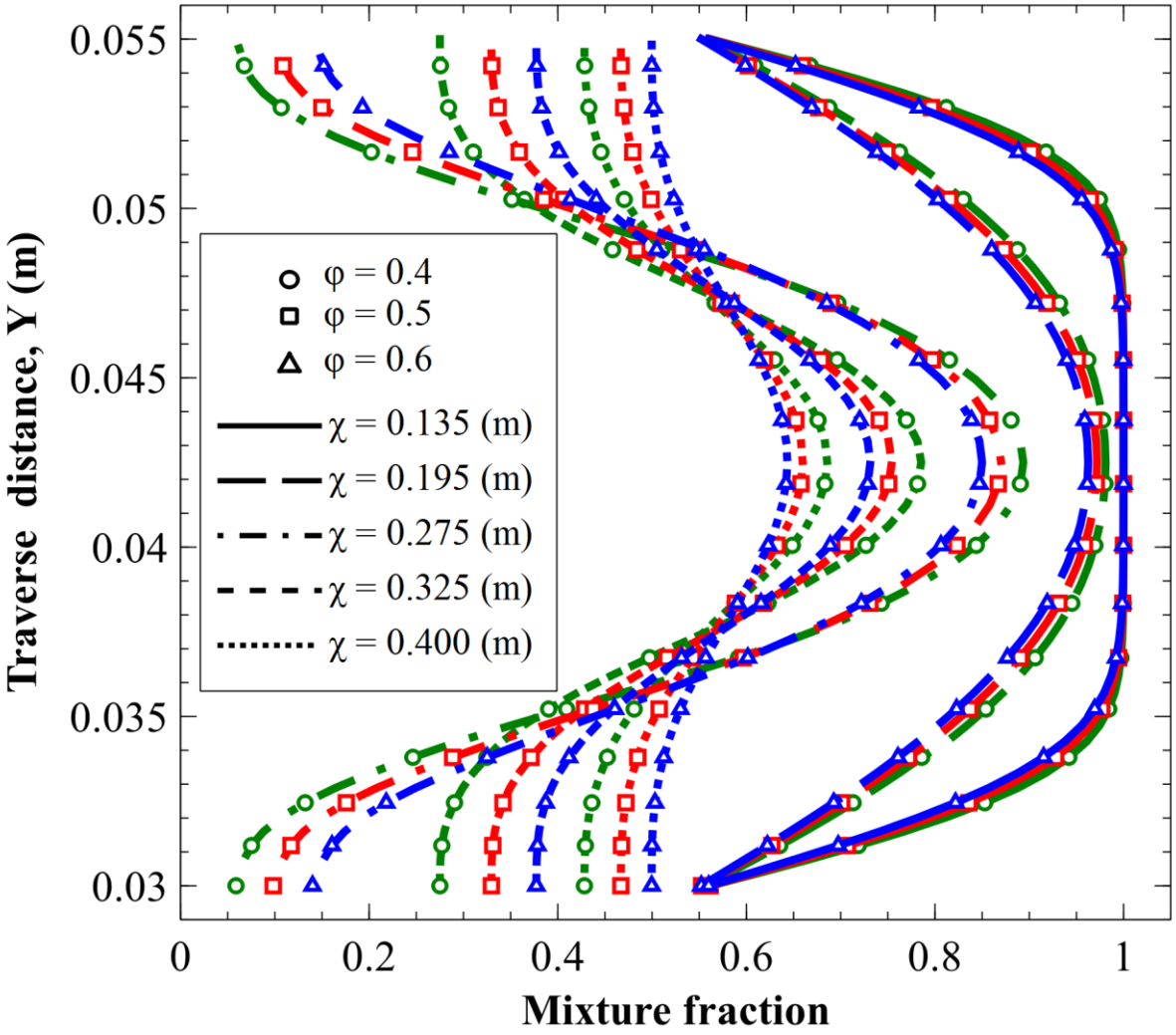

Figure 4.8: Traverse variation of fuel mixture fraction downstream of the porous plates.

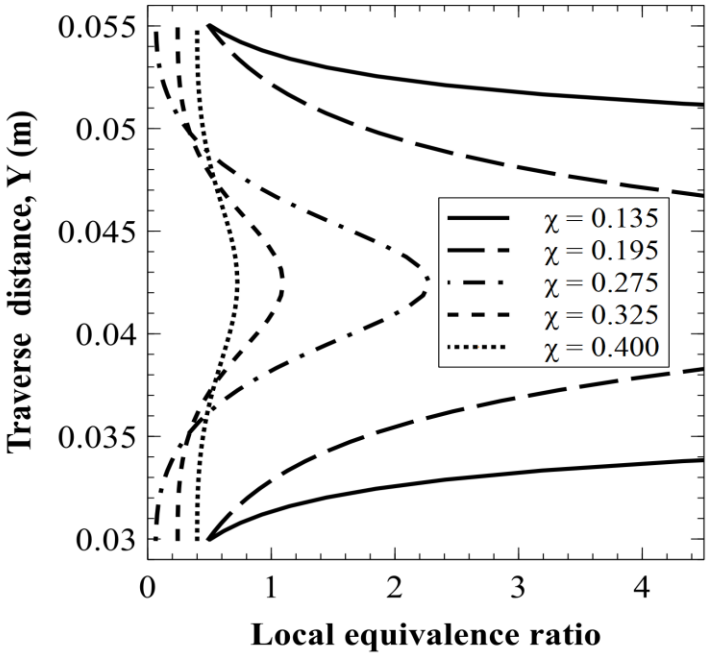

(a) $\Phi = 0.6$

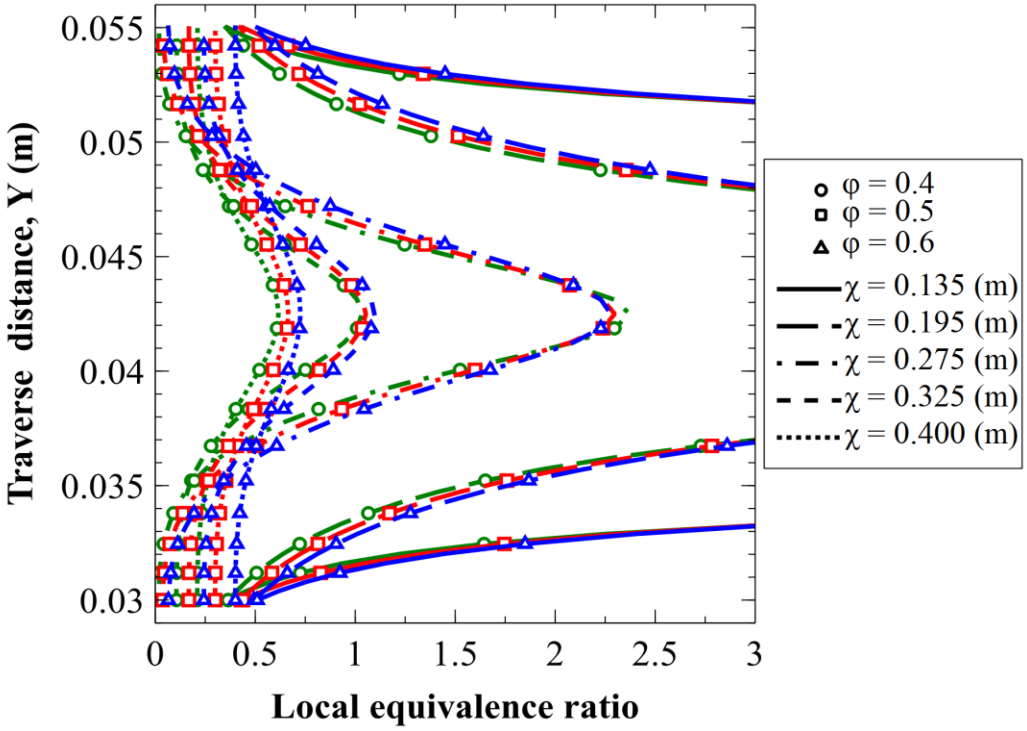

(b) three different equivalence ratios

Figure 4.9: Traverse variation of equivalence ratios downstream of the porous plates.

4.2 Numerical Simulations of Oxy-combustion Characteristics

This section investigates the characteristics of oxy-combustion with the porous plate reactor numerically to determine the location of the flame with respect to the porous plate and the distributions of temperature and species concentrations. This should give an idea about the generated flame when the case is projected on HTMR applications. Numerical calculations were performed considering the 2-D porous plate reactor geometry presented in Figure 3.1(c) at the reactor power of 3 kW. Grid independence study was performed, and it was found that there were no significant variations of the results (<1%) beyond the grid points of 29,520 which was used in the current simulations. The mass flow inlet boundary condition was selected for all gas flows with inlet temperature of 298 K, while pressure outlet boundary condition was set at the common exit section of the reactor. The thermal boundary conditions applied to the porous plates and the inner walls supporting them was 'coupled'. Under this condition the solver will directly compute the heat transfer from the adjacent cells solutions and hence, no additional thermal boundary conditions are required. For the other external walls 'mixed' thermal boundary condition was applied which accounts for both convective and radiative heat transfer to the ambient at temperature of 298K, external emissivity of 1 and heat transfer coefficient of 20 W/m^2K. All the walls were modeled as opaque while the quartz glass was modelled as semi-transparent. The outlet boundary condition was constant atmospheric pressure at temperature of 298 K. The energy, momentum and species transport as well as the radiative transfer equations were solved using steady pressure-based solver in the ANSYS Fluent 16.5 software. The energy and radiation models are implemented one after the other (uncoupled) sequentially, using the conservative finite-volume scheme [210]. The

pressure-velocity segregate algorithm used was the Semi-Implicit Method for Pressure Linked Equations (SIMPLE) with higher order of the relaxation terms. Table 3.10 showed the seven cases considered for the analysis of oxy-combustion characteristics inside the porous-plate reactor over a range of equivalence ratio from the stoichiometric condition down to very lean operation at equivalence ratio of 0.4.

In all cases, fuel mass flow rate is kept constant at 0.6 $x10^{-4}$ kg/s (reactor power of 3 kW), and the volumetric percentage of O_2 in the CO_2-O_2 oxidizer is kept fixed at 30%. in order to obtain similar adiabatic temperature for the case of normal air combustion [211]. The flow rates of fuel and oxidizer are kept within the low range to mimic the processes of oxygen permeation and oxy-combustion in side HTMRs for clean power production applications.

Figure 4.10 shows the effect of equivalence ratio, over a range from 0.4 up to 1.0, on the distributions of temperature in the traverse and axial directions for the all the cases considered in Table 3.10. As per Figure 4.10(a), the traverse distributions of temperature (at the trailing edge of the porous plate) show improvement in the temperature level within the reactor while increasing the equivalence ratio toward stoichiometry. This may be attributed to improved convective heat transfer within the rector at lower equivalence ratios due to the associated increase in the total oxidizer (O_2 plus CO_2) flow rate. The high flow of CO_2 at lower equivalence ratio slows down the reaction kinetic rates by absorbing part of the combustion energy released and, consequently, the combustion temperature is reduced. The excess amount of permeated oxygen from the trailing part of the porous plate

cools down the combustion products and reduces the combustion temperature at lower equivalence ratio. However, in HTMRs, oxygen is permeated through a membrane which consumed portion of the heat of combustion for oxygen separation. Based on that and from economic point of view, HTMRs are preferred to work under stoichiometric conditions (Φ=1.0). At Φ=0.9 in Figure 4.10(a), the main stream temperature at the center of the reactor is higher than the obtained temperature at Φ=1.0. This can be attributed to the reduced level of mixing between the permeated oxygen and the main flow stream containing the fuel due to the reduction of the amount of permeated oxygen at Φ =1.0. As per Figure 4.10(a), the temperature on the trailing edge of the porous plate ranges from 1130 K (at Φ=0.4) to 1280 K (Φ=0.9). This temperature range lies within the operating limit of operation of the ceramic membranes when the cased is projected on HTMR operation. At all equivalence ratios, the intense reactions are delayed in the main flow to the downstream region of the porous plate as per the temperature plots in Figure 4.10(b) and the temperature contours in Figure 4.11.

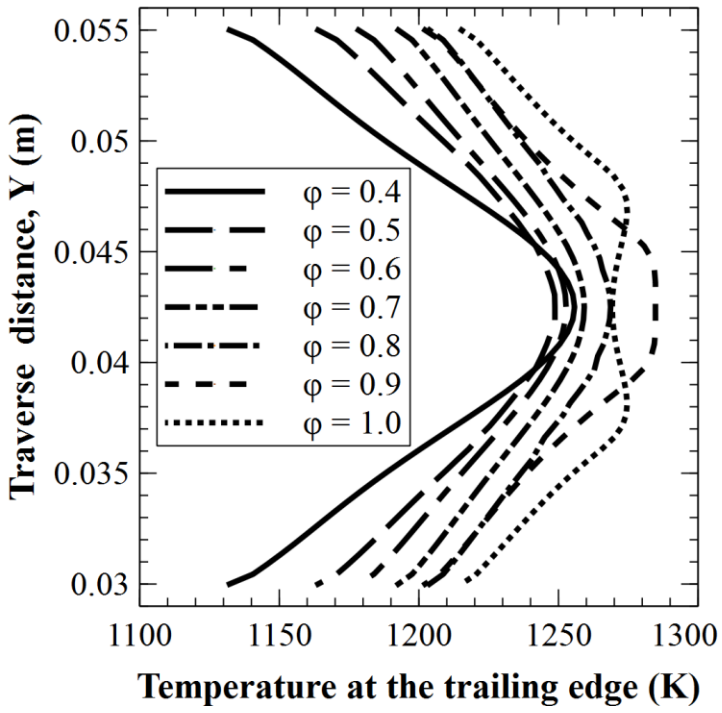

(a)

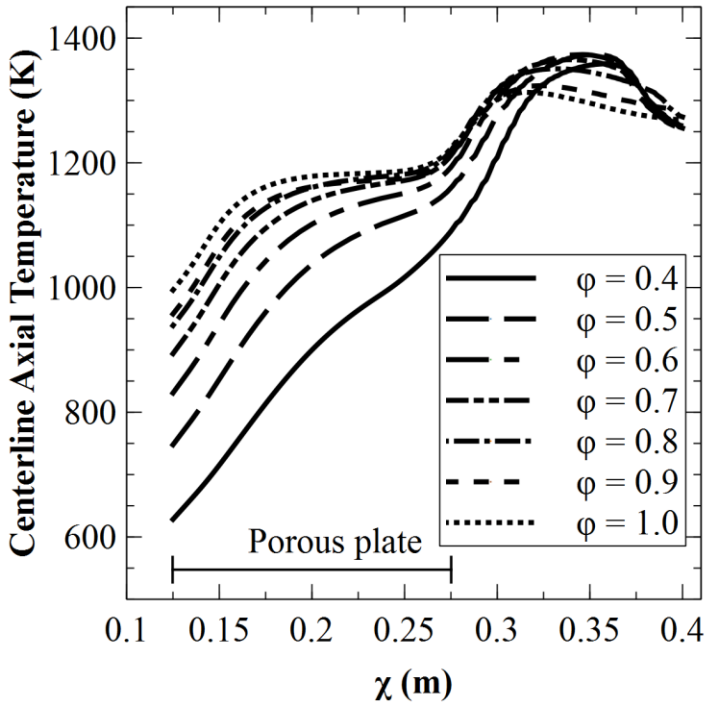

(b)

Figure 4.10: Effect of equivalence ratio on the outlet temperature at 3 kW. (a) Traverse variation, (b) Axial variation.

The improved mixing in the downstream region of the porous plate results in improvement in the combustion temperature as per Figures 4.10(b) and 4.12. The lean combustion operation resulted in better mixing and higher flame temperature as compared to stoichiometric combustion. However, the excess amount of oxidizer under lean operation cools the exhaust stream down to reach similar temperature as the stoichiometric combustion at the exit section of the reactor. These results support the operation of the reactor under stoichiometric condition from both economical and performance points of view, especially when the case is projected on the HTMR operation. As shown in Figure 4.12, the present reactor design keeps the zone beside the porous plate hot due to initiation of reactions once oxygen appears in the central zone. This feature of the present reactor design is very crucial for the operation when the porous plate is replaced by ceramic membrane for HTMR applications, as the membrane should be kept at elevated temperature to be activated for oxygen permeation. The lower amount of permeated oxygen and reduced level of mixing with the main stream results in elongated flame at stoichiometric condition when compared to lean operation as shown in Figure 4.12.

There was a linear relationship between the average outlet temperature and inlet equivalence ratio within the range under study and the range outside can be extrapolated using Equation 4.2, as shown in Figure 4.11.

$$\text{Average Temperature } (K) = 92\Phi + 1165 \qquad (4.2)$$

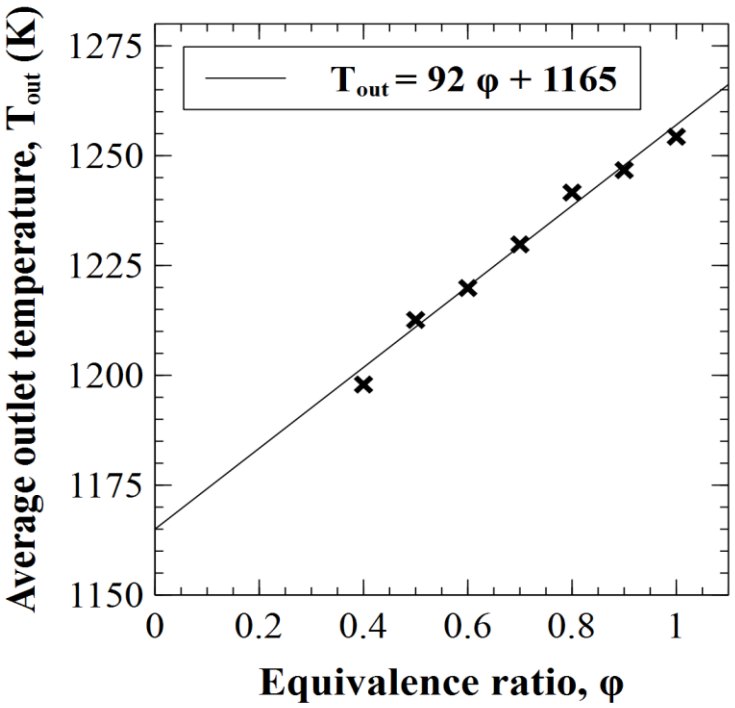

Figure 4.11: Effect of equivalence ratio on the averaged outlet temperature at 3 kW.

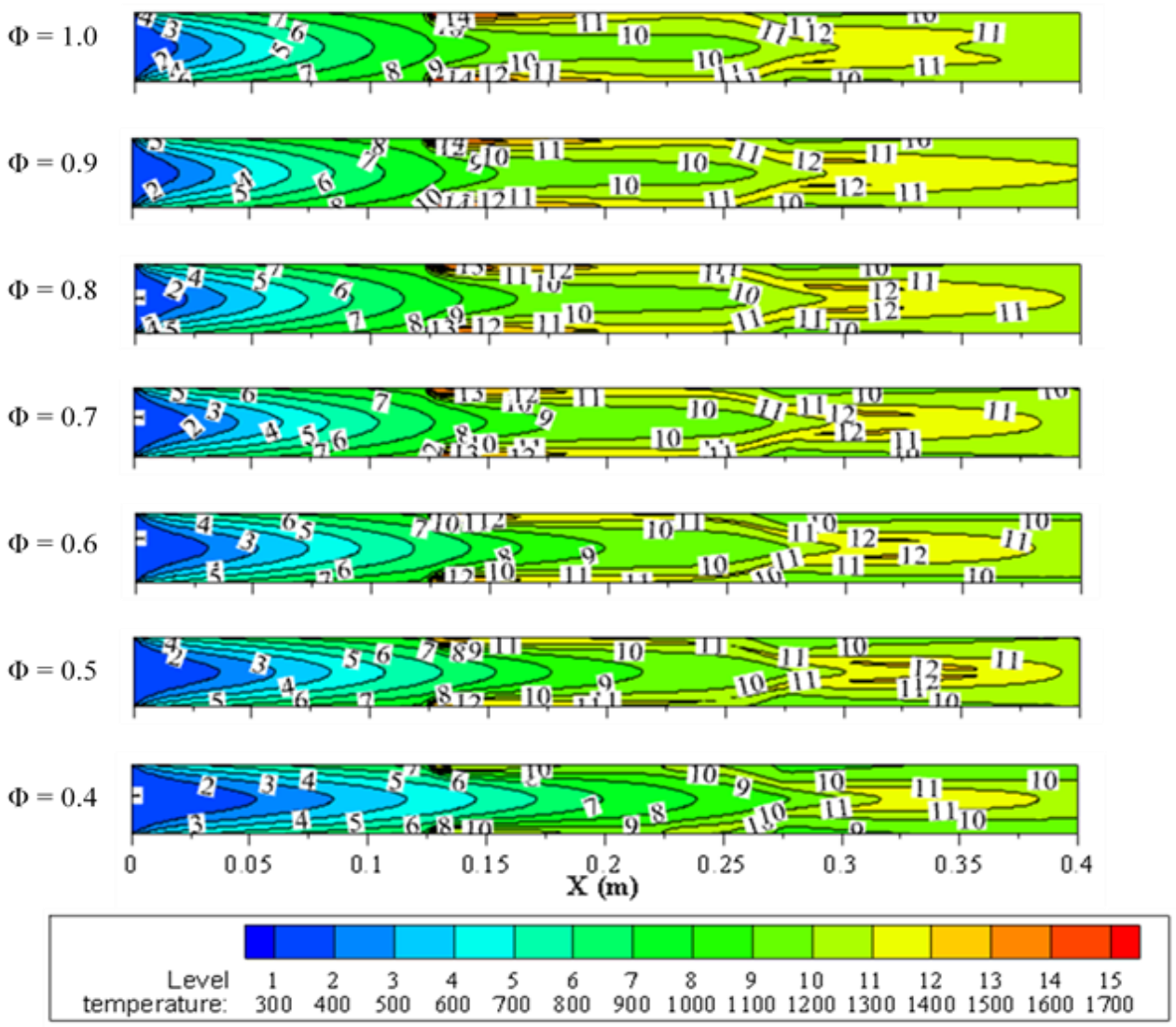

Figure 4.12: Contour plots of temperature (K) over a range of equivalence ratio at reactor power of 3 kW.

For the same reasons, methane depletion rate within the reactor was lower at stoichiometric condition compared to lean operation as shown from the contour plots of methane concentrations presented in Figure 4.13. Also, full conversion of the fuel is delayed in the downstream zone close to the exit section at higher equivalence ratios as shown in Figure 4.13.

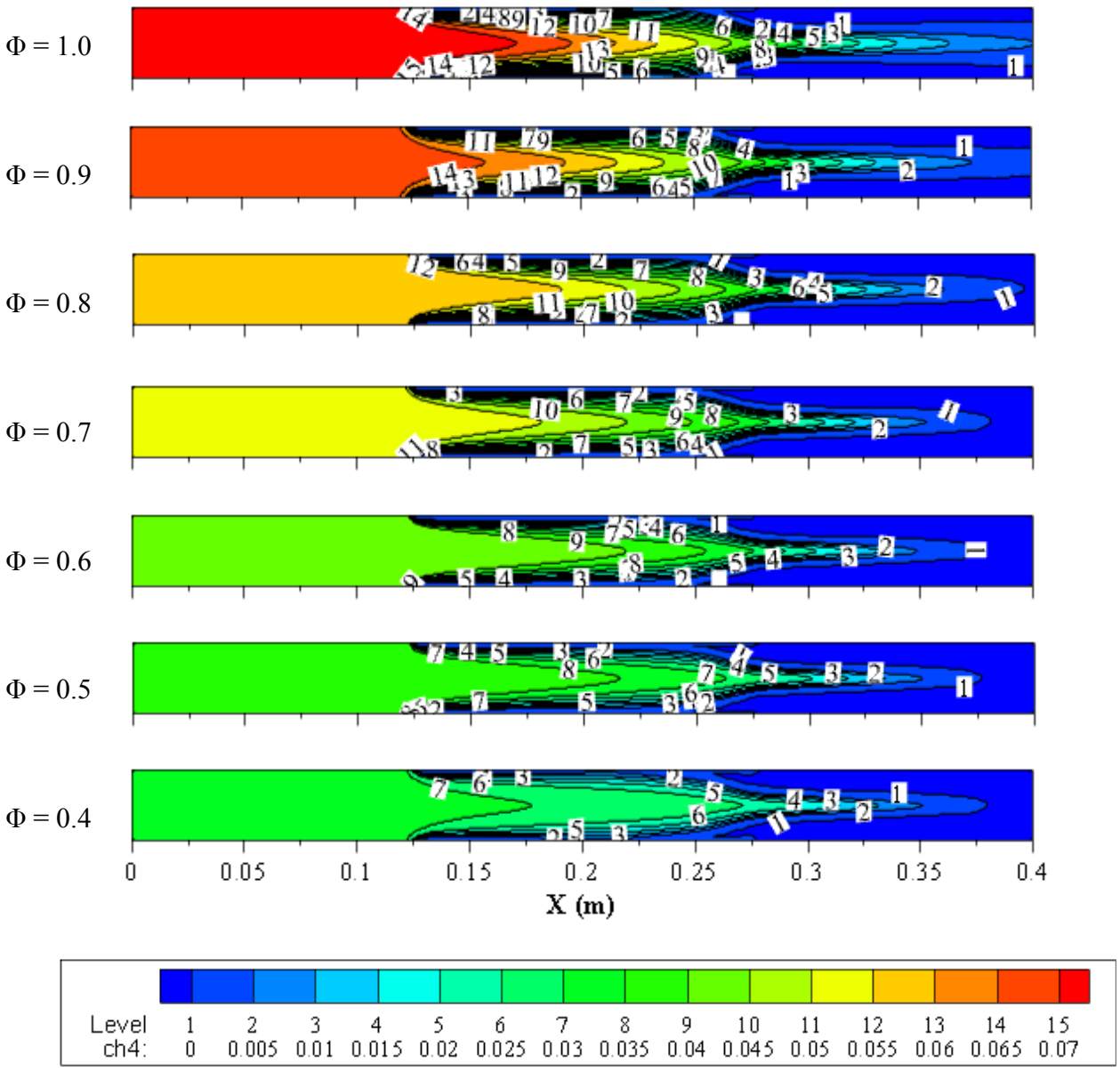

Figure 4.13: Contour plots of mass fractions of CH_4 over a range of equivalence ratio at reactor power of 3 kW.

The effect of the inlet equivalence ratio on the species consumption and production along the combustor at various equivalence ratios has been presented in Figure 4.14. The mass fractions of all the species remain constant before the (from 0 to $0.125m$). CH_4 mass fraction decreased from the beginning of the porous plate to the end of the combustor where it was fully consumed with the exception of the case with equivalence ratio of 1.0, where about 0.1% still remained at the outlet of the combustor as shown in Figures 13 and 4.14a. The oxygen mass fraction shown in Figure 4.14b increases from zero at the beginning of the porous plate but suddenly consumed due to mixing with the fuel and swiftly rise to maximum at the end of the porous plate, before further decreasing up to the outlet. The CO_2 mass fraction, contrary to that of the O_2, decreases and increase at the early portion of the porous plate due to O_2 permeation and consumption in the region, as shown in Figure 4.14c. The mass fraction also decreases drastically to its minimum due to higher O_2 concentration before increasing towards the outlet. There was a switch among the profiles of the CO_2 with respect to inlet equivalence ratios from cases with higher equivalence ratios having lower CO_2 mass fractions to the same cases having higher CO_2 mass fractions due to increased CO_2 production associated with the higher equivalence ratios during combustion. The water production shown in Figure 4.14d increases with increase in equivalence ratio and along the combustor due to CH_4 consumption.

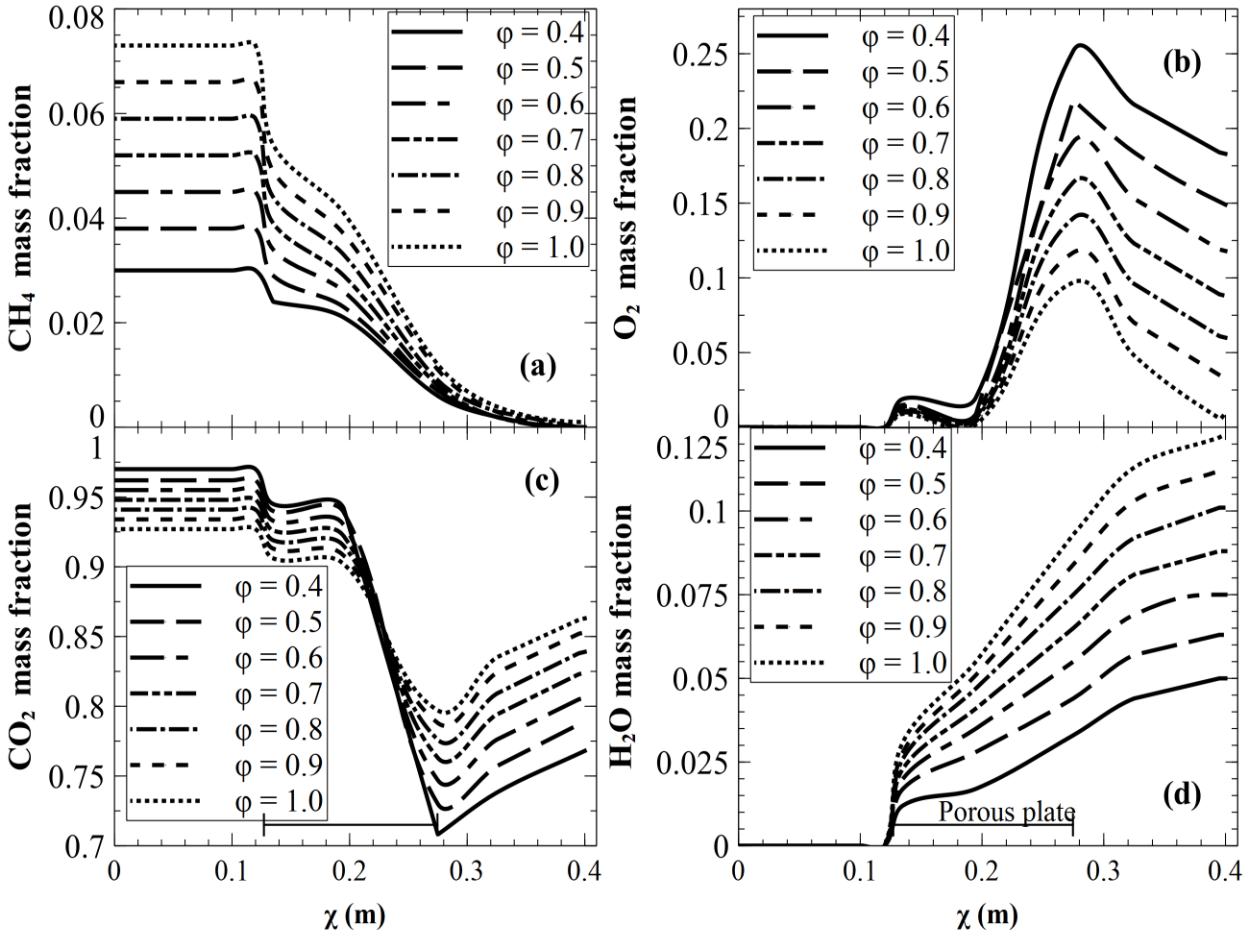

Figure 4.14: Effect of equivalence ratio on the average mass fractions of the species *(*CH_4, O_2, CO_2, H_2O*)*.

4.3 Oxy-combustion Experiments (Reactive)

This section focused on the results from experimental testing of oxy-fuel combustion characteristics in the porous plates reactor over wide ranges of mixing conditions and equivalent ratios. The experimental study aimed at investigating the combustion characteristics and lean blow-out limits of oxy-methane diffusion flames over wide ranges of operating conditions as described in section 3.2.2.

4.3.1 Flame shapes/structures

4.3.1.1 Effects of CO_2 addition

The experimental plan structured in Table 3.6 was followed using the set up and procedure described in section 3.2.2. The flame shapes were the visible flame images of the oxy-methane combustion captured at steady state combustion conditions for various percentages of CO_2 addition at equivalence ratios of 0.5, 0.7, 0 and 1.0 for the power of 1.5kW. Two flame-sheets were observed anchored to the upper and lower breadths of the fuel+CO_2 inlet section and elongated along the longitudinal axis of the combustor as shown in Figure 4.15. The dark regime is the portion where there was no visible flame in the combustor while the colored portion attached to the fuel+CO_2 inlet represented the flame regime. For the pure methane combustion case, without the CO_2 addition (0% CO_2), the flame remains highly whitish glow indicating the luminous intensity of the light at all the lean equivalence ratios under study.

At all the equivalence ratios studied in this laminar diffusion combustion, the flame length increases with increase in the percentage of CO_2 in the mixture contrary to the effect of CO_2 addition in a swirl stabilized turbulent flows [212, 213] where the flame length decreases and become more compact due to turbulent mixing with increase in percentage CO_2 in the mixture. The observed increase in length in this laminar combustion studies was as the result of CO_2 being supplied together within the fuel inlet. This increases the fuel side Reynolds number causing a jet behavior with higher momentum that extended the mixing zone. This has been visualized in all cases as shown in Figure 4.15 (a), with the case having highest percentage of CO_2 in the oxidizer mixture (70%) having the most elongated flame. Detailed flame images for other $\%CO_2$ additions and equivalence ratios can be found at Appendix K.

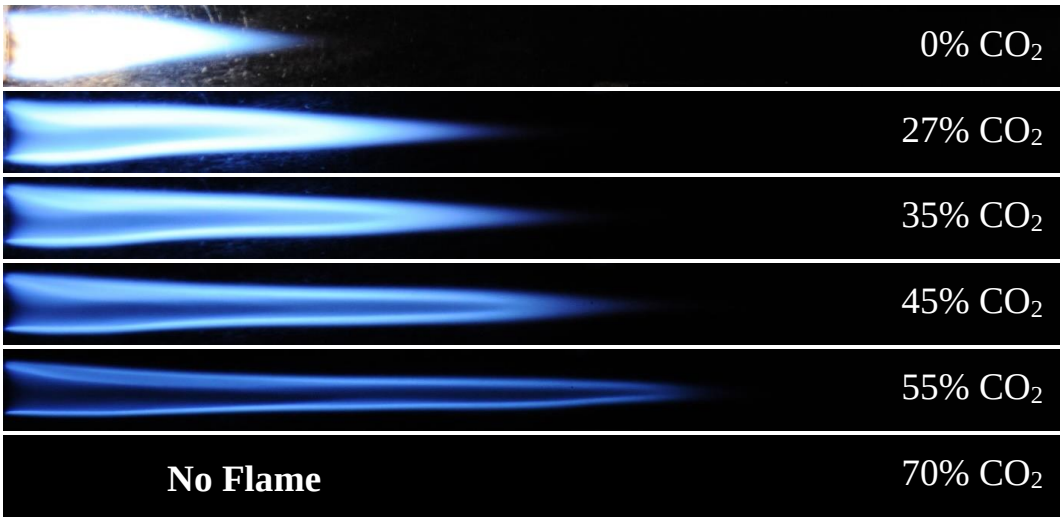

(i) $\Phi = 0.5$

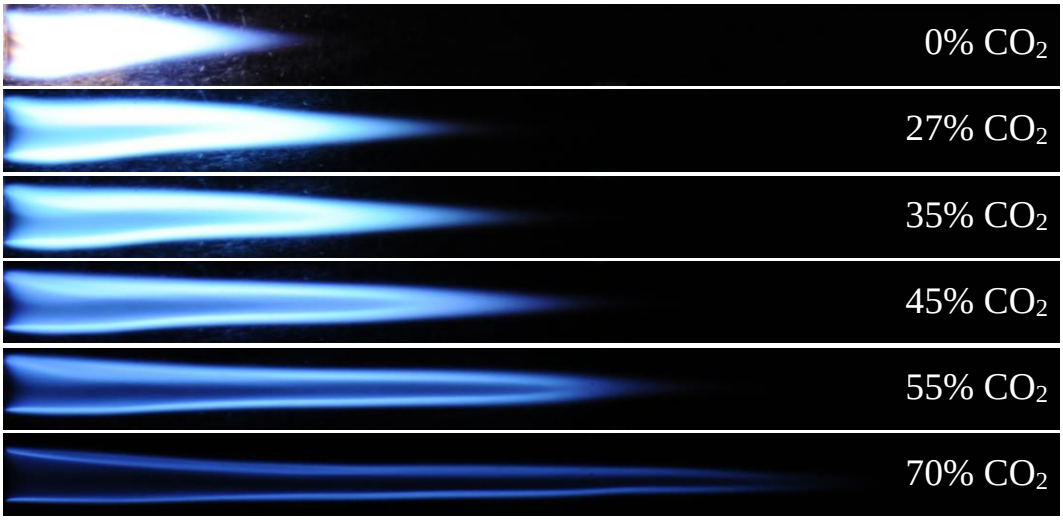

(ii) $\Phi = 0.7$

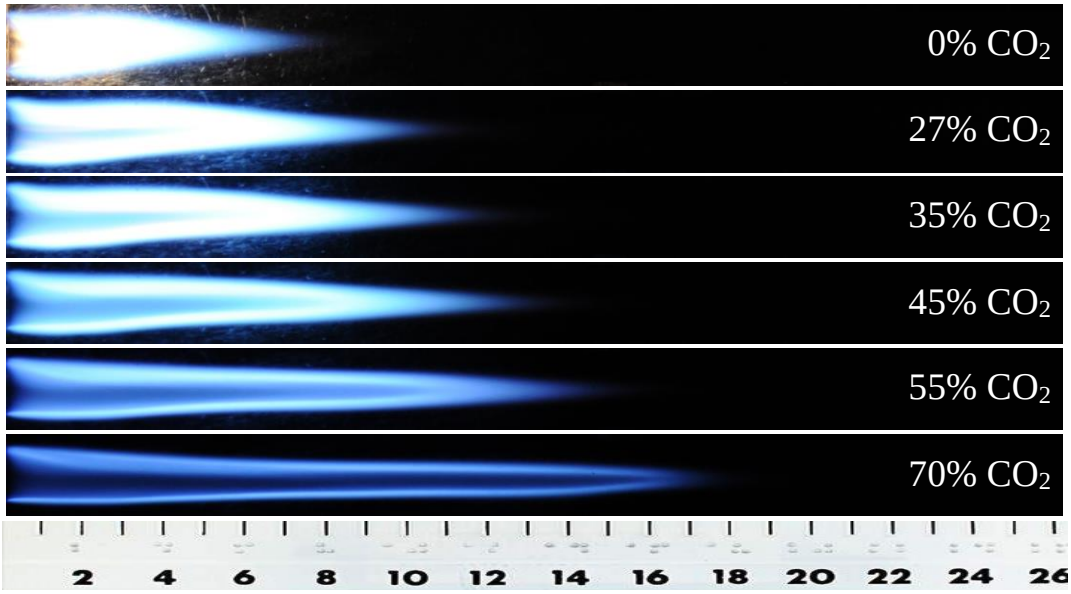

(iii) $\Phi = 1.0$

(a) Effect of $\%CO_2$ in the oxidizer mixture at three different equivalence ratios

(i) 0% CO_2

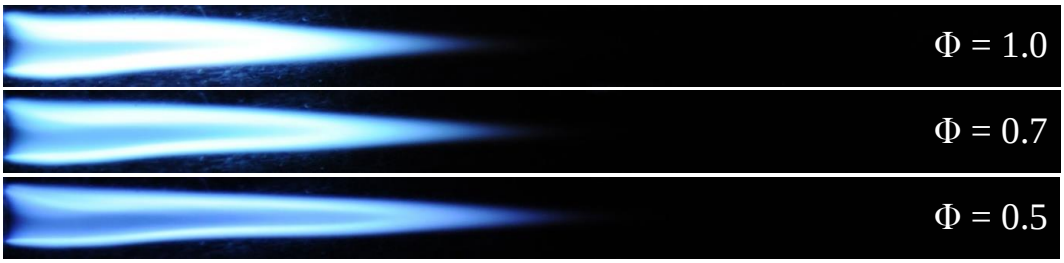

(ii) 35% CO_2

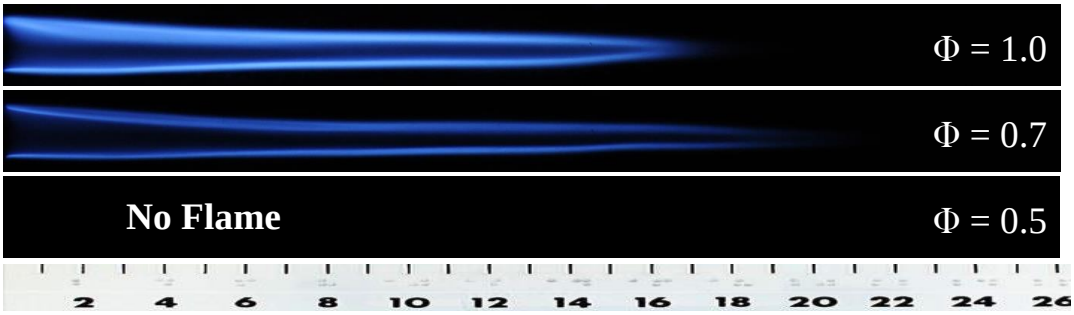

(iii) 70% CO_2

(b) Effect of equivalence ratio at different %CO_2 in the oxidizer mixture

Figure 4.15: Effects of operating conditions on the flame structure at 1.5kW.

Flame Nondimensionalization

Normalizing flame length with the effective diameter has been reported to be helpful in combustor and furnaces design. In physical meaning, this represent the characteristic length

of the flame that will conceptually allow the same mass and momentum flux as the actual length [214, 221]. In this work, the flame length has been nondimensionalized by the width of the rectangular cross-section of the fuel+CO_2 inlet section.

In Figure 4.16 (a), the effect of CO_2 addition elongates the normalized flame length to more than double of its length without the CO_2 addition at all the equivalence ratios studied. Whereas there was significant flame length increase due to CO_2 addition, the flame length slightly decreases with increase in equivalence ratio when CO_2 was added as shown in Figure 4.16 (b). This was likely due to the increase in mixing of the species as well as decrease in excess oxygen that lowers the flame temperature resulting in more compact flames as also seen in Figure 4.15 (b). Note: the flame extinguished at equivalence ratio of 0.5 with 70% CO_2 addition due to low fuel percentage in the mixture to support the flame. Visually, the flame luminous intensity decreases with increase in CO_2 percentage in the mixture as shown in Figure 3 at each equivalence ratio. The addition of CO_2 increases the convection and radiation heat loss from the reaction zone which entails lower flame temperatures. Since the flame luminosity is directly correlated to the flame temperature, the cases with higher % CO_2 had lower luminous intensities due to lower flame temperatures. Similar luminous behavior has been reported by other researchers [213]. Also, the higher the equivalence ratio the higher the luminous intensity at a constant %CO_2 due to the increase in flame temperatures as shown in Figure 4.16 (b). The raw flame length data can be found in Appendix K.

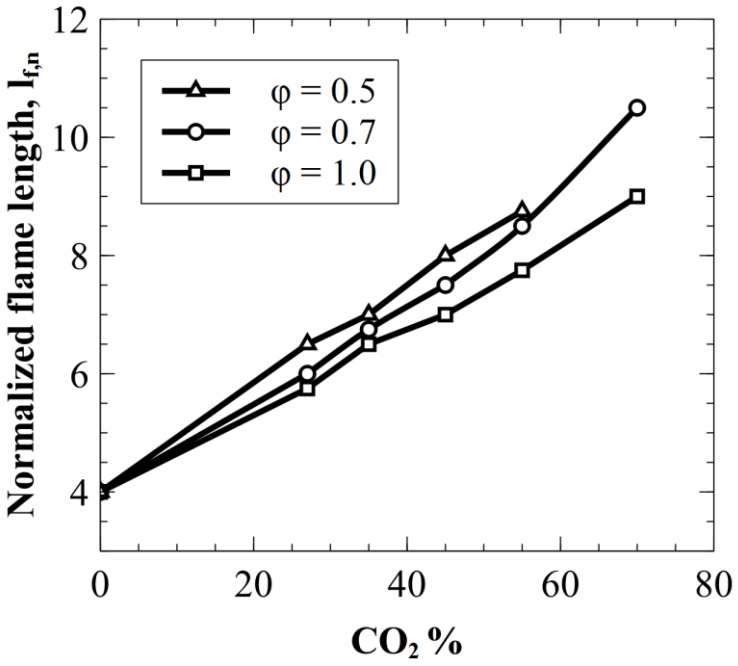

(a)

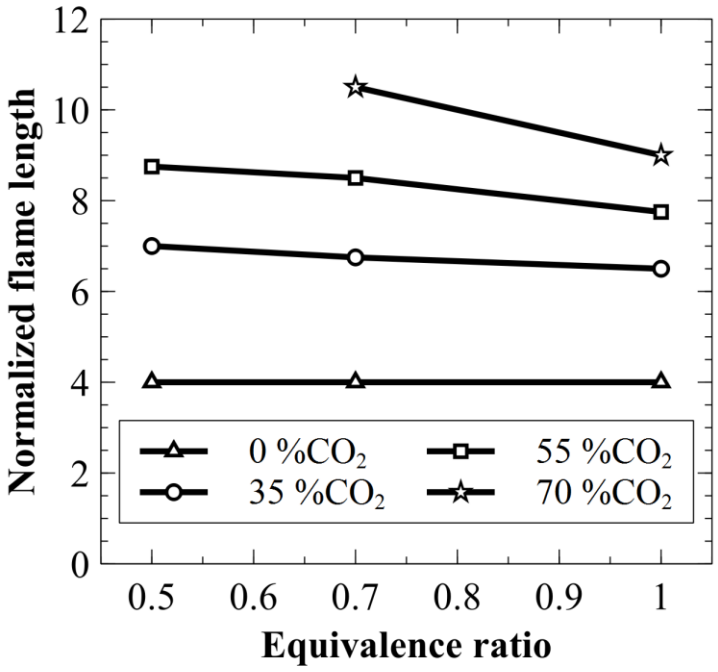

(b)

Figure 4.16: Effect of operating conditions on the normalized flame length. (a) % CO_2 in the oxidizer, (b) equivalence ratio ($l_{f,n} = l_f/w$).

4.3.2 Horizontal temperature distributions at the exhaust

The horizontal temperature distributions were measured across *z*-axis at five symmetric locations as shown in Figure 3.5. The results of the measurements were presented in Appendix K for three representative equivalence ratios at various percentages of CO_2 addition. The temperature decreases horizontally from the center of the combustor outlet to the walls, irrespective of the equivalence ratio and %CO_2 in the mixture, as shown in the figures. This was anticipated as the result of radiation heat loss via the quartz glass plates at the two sides of the combustor to the cold ambient at about 293 K. The variations were also symmetrical with the peak temperature at the center due to the symmetry of the inlets of the species. In order to capture the actual cooling effect of the CO_2 additions that was overshadowed by the flame radiation as the result of longer flames as discussed earlier, the exhaust temperatures were normalized by the non-dimensional flame length and the results were presented in Figures 4.17. As shown in Figure 4.17, the higher the percentage of CO_2 the lower the normalized temperatures in all the three cases. The pure oxy-combustion case (0% CO_2) was characterized by having the highest flame temperature as evident in the highest luminous intensity. The higher the equivalence ratio the higher the exhaust gas temperatures were observed in all the cases despite decrease in the flame length. The higher flame temperatures at higher equivalence ratio overwhelmed the radiation effect due the slight increase in the flame lengths. This was more vividly clear for the case without CO_2 addition, where the increase in flame length due to decrease in equivalence ratio, was insignificant, as shown in Figure 4.16 (b). Also, there was no flame at equivalence ratio of 0.5 with 70% CO_2 addition as shown in Figure 4.16 (c).

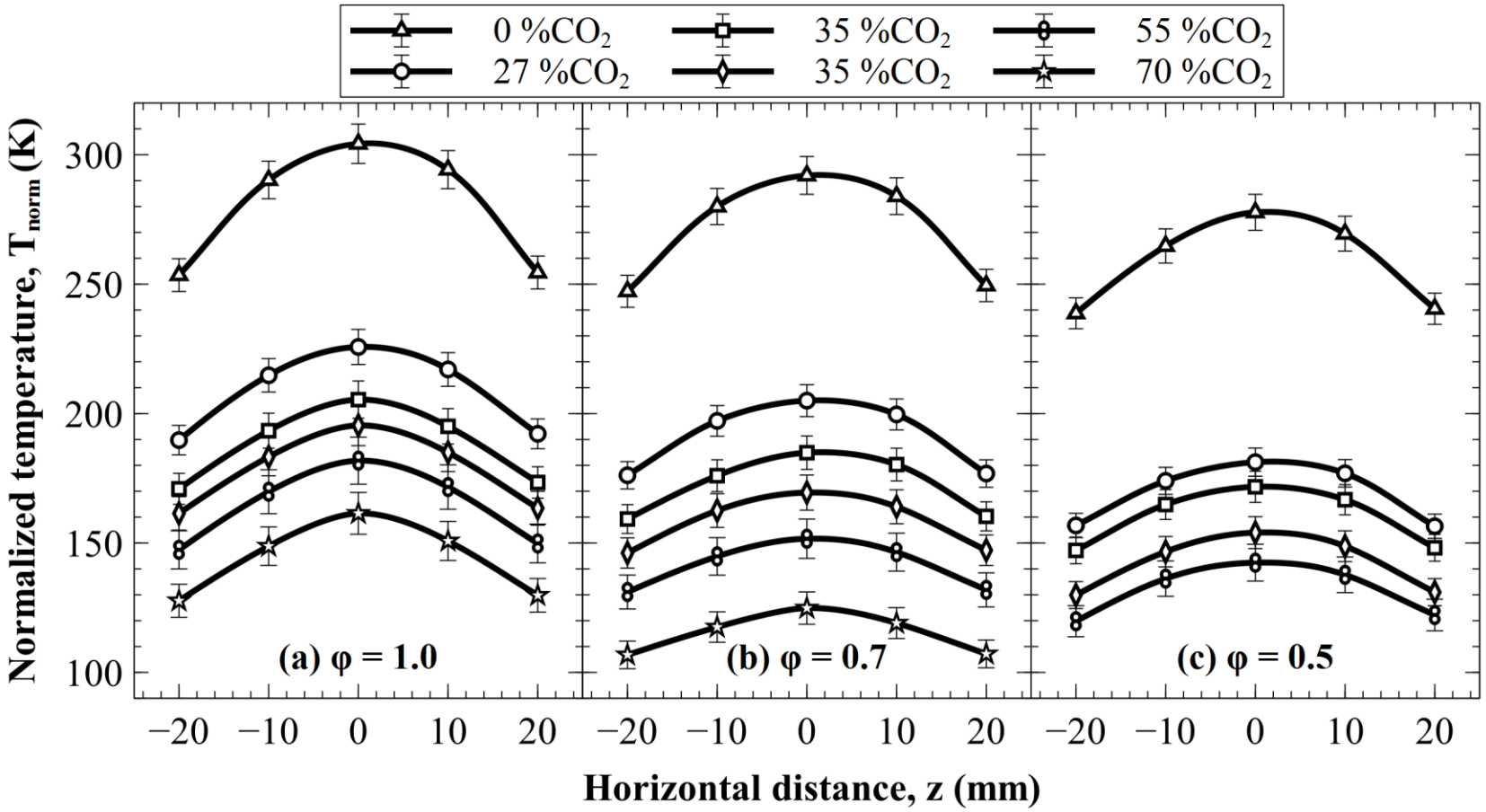

Figure 4.17: Normalized horizontal temperature variation at the outlet, for fuel firing rate of 1.5kW ***($T_{norm} = T/l_{f,n}$)*.**

4.3.3 Vertical temperature distributions at the exhaust

When the temperature distributions were measured vertically across *y*-axis at the seven symmetric nodal locations, the results were presented in Appendix K for the raw measurements and Figures 4.18 for the normalized data (Temperatures normalized by the nondimensional flame length). Parabolic profiles were obtained as in the case of horizontal measurements for the stoichiometric oxy-methane combustion case shown in Figure 4.17 (a). Whereas flat temperature distributions were observed vertically at the center of the combustor outlet when CO_2 was added for fuel lean cases, as shown in Figure 4.18 (b), (c), parabolic profiles were obtained at stoichiometric mixtures shown in Figure 4.18 (a). The maximum temperature occurred at the center irrespective of the percentage of CO_2 in the mixture. For the fuel lean conditions, the temperature profiles 'flattened' at the center when the $\%CO_2$ was $\geq 35\%$ (Figure 4.18 (b), (c)). This was due to upper and lower flame sheets being more distinctly separated at higher $\%\ CO_2$ addition and longer flames. The higher the equivalence ratio the higher the temperatures as stated earlier. The vertical temperature profiles were fully parabolic during pure oxy-methane combustion as well as stoichiometric mixtures with CO_2 addition at all the three equivalence ratios under study. When the oxygen content was increased (fuel lean cases) while the percentage of CO_2 also added the profiles becomes more uniformly distributed at the center.

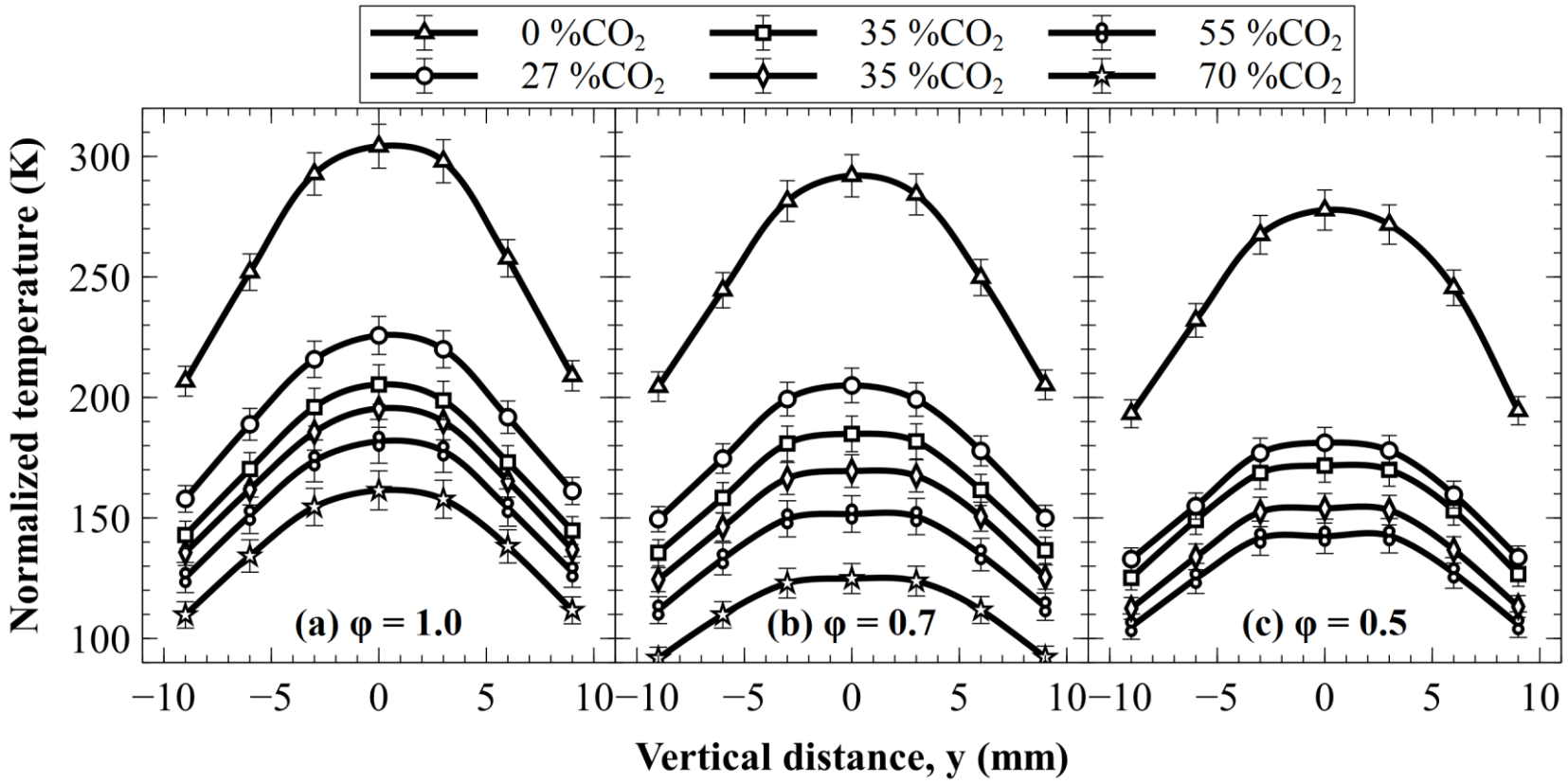

Figure 4.18: Normalized vertical temperature variation at the outlet, for fuel firing rate of 1.5kW.

4.3.4 Longitudinal temperature distributions near the exhaust

The longitudinal temperature measurements were taken from the outlet of the combustor upstream along *x*-axis for the seven nodal earmarked points illustrated in Appendix K for the raw measurements. The thermocouple's maximum temperature range limits the distance upstream of the flame. The measured temperatures were normalized by the non-dimensional flame length and plotted in Figure 4.19. All the results elucidated linear temperature drops downstream of the flame zone along the *x*-axis (Figure 4.19). The flame temperature behavior corroborates that of the luminous intensities of the flame images. The addition of CO_2 decreases the temperature due the decrease in flame temperatures as seen in the previous sections. The higher the percentage of CO_2 added to the fuel stream, the lower the temperature downstream of the combustor due to the thermal dilution effect of the CO_2. At the steady stoichiometric combustion (Figure 4.19 (a)) the temperature drops downstream of the combustor at an average slop of 2.4 K/mm irrespective of the % CO_2 in the mixture. As the amount of oxygen was increased to the two lean conditions the step temperature decrease reduces to 1.8 K/mm and 1.2 K/mm at equivalence ratios of 0.7 and 0.5 respectively, while still maintaining the fuel firing rate at 1.5 kW. These step decrease in temperature due to increase in oxygen (lean condition) can be use as design parameters for estimation of the combustion size with respect to the desired exhaust temperature requirements.

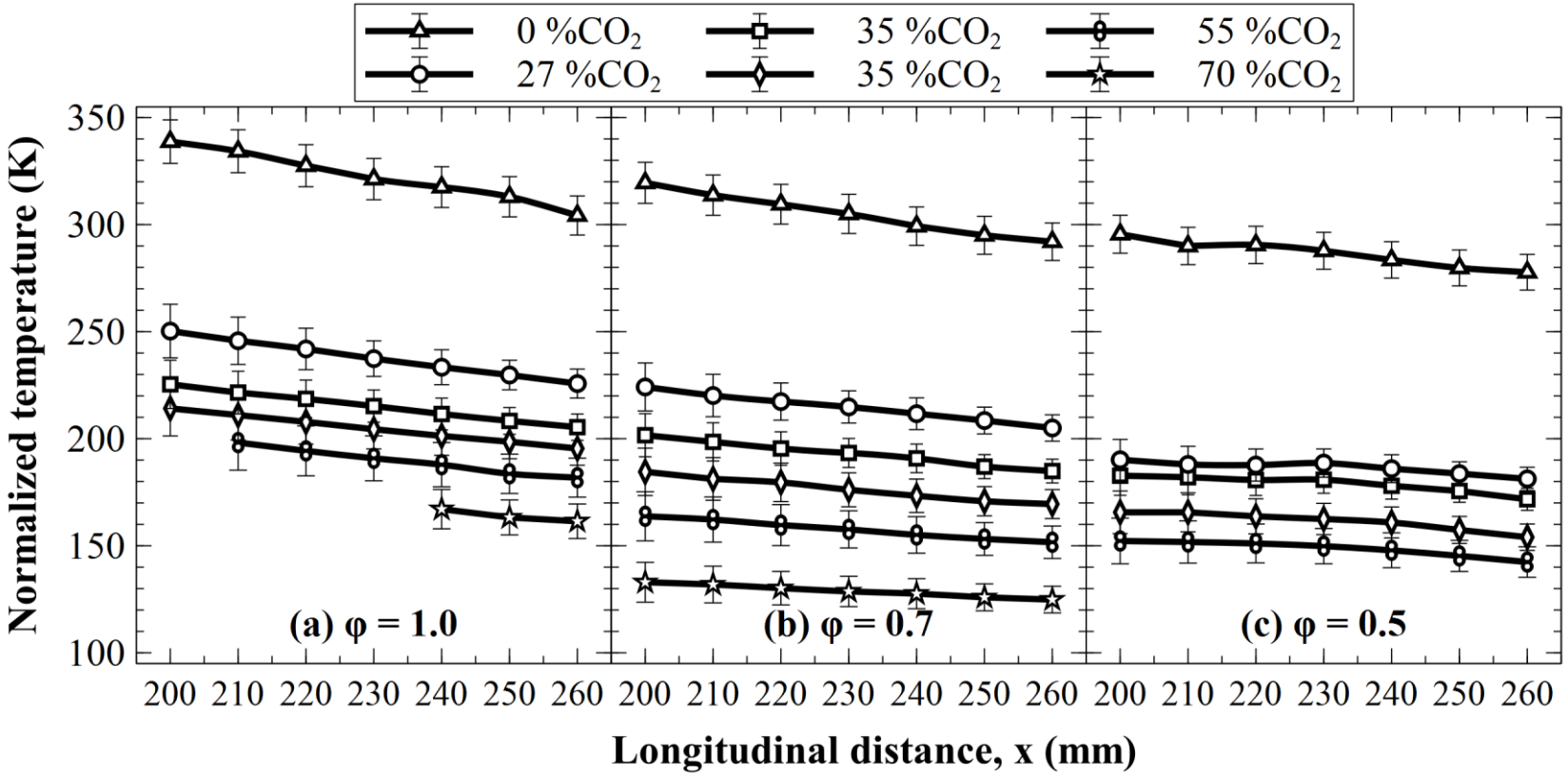

Figure 4.19: Normalized longitudinal temperature variation towards the exhaust at fuel firing rate of 1.5kW.

4.3.5 Averaged exhaust temperatures

The normalized horizontal and vertical temperature variations at the exit of the combustor as discussed in sections 4.3.2 and 4.3.3 were averaged for each % CO_2 addition to provide a more general overview of the effect of dilution and change in equivalence ratio on the flue gas temperatures as shown in Figure 4.20. At all the three equivalence ratios, the higher the percentage of CO_2 addition the lower the normalized temperatures due to CO_2 thermal dilution effect. The CO_2 was supplied at low energy level corresponding to less than 300 K (< 75 K, normalized) and exited with higher energy levels gained from the combustion heat release, and thus, lowering the overall combustor energy level. Fuel leaner equivalence ratio mixtures produces lower exhaust gas temperatures in comparison with its stoichiometric counterpart due to the presence of excess oxygen that acts as a heat sink. Hence at all the percentages of CO_2 considered the highest equivalent ratio mixture resulted in more flue gas temperatures.

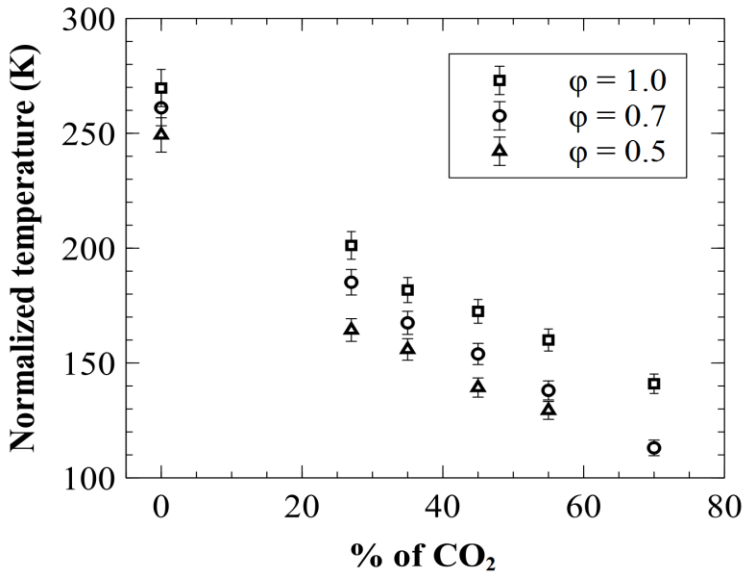

Figure 4.20: Normalized average outlet temperature variation at fuel firing rate of 1.5kW.

4.3.6 Lean flammability limits

The lean stability limits in terms of flame blow-out were determined by starting stable flames at a fixed equivalence ratio (fixed mass flow rates of fuel and oxygen) while increasing the diluent (CO_2) flow rate up to the blow out limits. The effect of equivalence ratio on the flame blowout limits at fixed fuel firing rate of 1.5 kW was shown in Figure 4.21 for a range of equivalence ratio, from 0.5 to 1.0. The results indicated increase in the LBO limit with the increase in the equivalence ratio. The flame blown out at about 65% CO_2 concentration in the oxidizer at the lowest operating equivalence ratio (φ=0.5). This increase to about 79% CO_2 at stoichiometric operating condition. A similar trend has been reported by Sayad et al. [215]. Decrease in equivalence ratio lowers the reaction temperatures and consequently reduces the capacity to overcome the activation energy for reactions to occur, and hence results in a decrease in flame speed. As reported by Kondo et al. [108], the flame blowout occurs when the flow speed exceeds the flame speed. Also, Chan et al. [216] concluded that for methane combustion, the laminar flame speed decreased with increasing CO_2 dilution as a result of decrease in the net rate of reaction due to low concentrations of reactants. Also, CO_2 addition acts as a heat sink, by lowering the combustion temperature and consequently decreasing the capacity to overcome the activation energy for reactions to occur [216]. Dirrenberger et al. [217] also reported that for methane-air combustion, the laminar flame velocity was directly proportional to the equivalence ratio up to stoichiometric equivalence ratio. Hence the leaner the mixture the lower the flame speed and the higher the flow speed, which causes flame blowout at the critical condition (residence time). The minimum obtained limit of

O_2 percentage in the oxidizer to allow for a visible flame was found to be about 21% (79% CO_2) at stoichiometric equivalence ratio as shown in Figure 4.21.

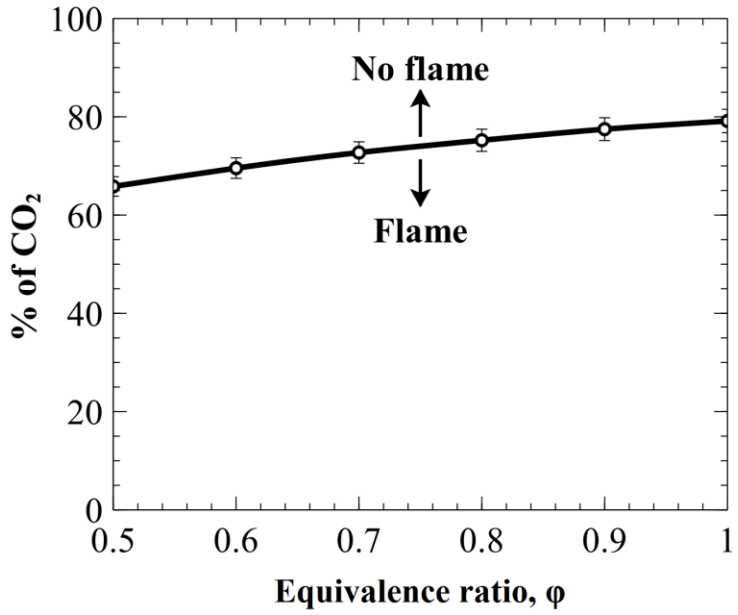

Figure 4.21: Effect of operating equivalence ratio on blowout limits at fixed fuel firing rate of 1.5 kW.

The combustor can be operated with visible flame within the flame zone. Similarly, the effect of fuel firing rates on blowout limits has been obtained at different equivalence ratios as shown in Figure 4.22. It was found that the percentage of CO_2 in the oxidizer at blowout limit decreases with the decrease in equivalence ratio irrespective of the fuel firing rate. The fuel firing rate was found to influence the concentration of CO_2 at the blowout limit at fixed equivalence ratio. The effect of fuel firing rate on blowout limits at stoichiometric operating equivalence ratio can be seen more vividly in Figure 4.23, where the increase in the fuel firing rate at stoichiometric equivalence ratio decreases the percentage of CO_2 in the oxidizer to cause flame blowout due to attainment of the required flow speed that overwhelmed the increase in the flame speed. An experimental

correlation between the effect of CO_2 % addition and fuel firing rate (P_f) was developed as shown in Equation 4.3, which can be used to extrapolate the blowout limit at any fuel firing rate.

$$\% CO_2 = 83 - 2.3 P_f \quad (4.3)$$

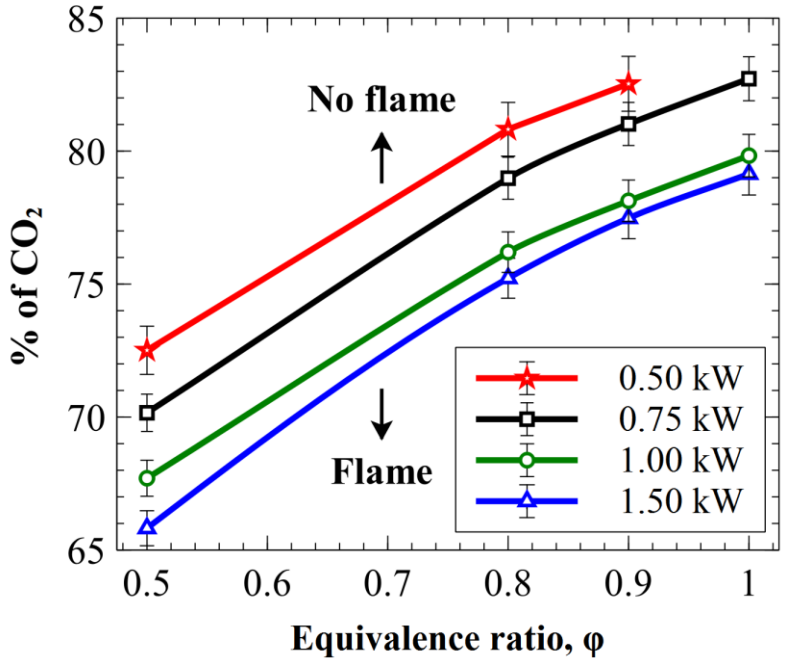

Figure 4.22: Effect of fuel firing rate on blowout limits over a range of operating equivalence ratio.

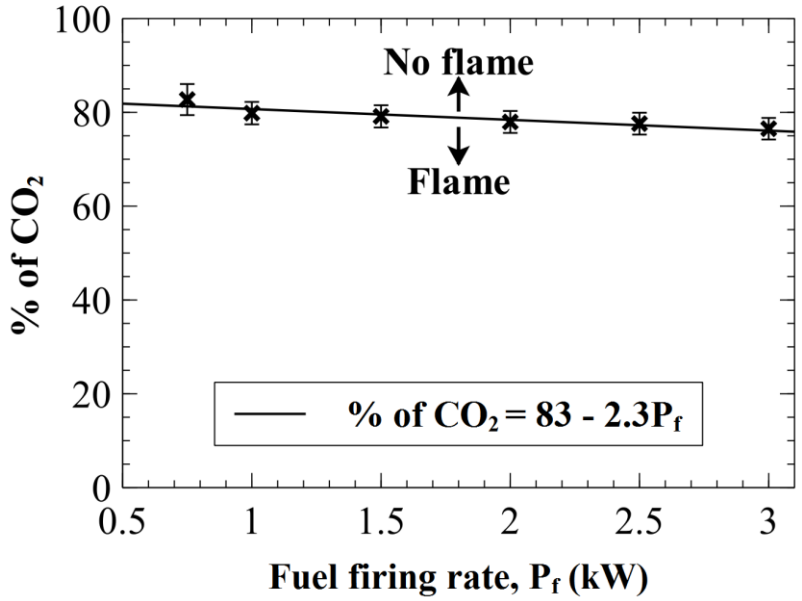

Figure 4.23: Effect of fuel firing rate on blowout limits at stoichiometric operating equivalence ratio.

4.4 3D Combustion Modeling (Reactive)

This section contains the numerical results of oxy-methane combustion modeling of atmospheric diffusion flame. A 3D model was developed for the reactor and the results from the combustion experiments were used for the model validation. The flame structure, temperature distributions as well as exhaust emissions were investigated using the numerical model and compared with the experimental results presented in section 4.3. Numerical calculations were performed considering the 3D porous plate reactor geometry presented in Figure 3.4(b) at the reactor power of 1.5 kW. Grid independence test was conducted, and it was found that there were no significant variations of the results (<1.2%) beyond the mesh having 301,623 nodes and 280,800 cells which was adopted for the 3D simulations. The mesh has a maximum orthogonal skew of 0.061 and maximum aspect ratio of 2.34. The mass flow inlet boundary condition was selected for all gas flows with inlet temperature of 298 K, while pressure outlet boundary condition was set at the common exit section of the reactor. The energy, momentum and species transport as well as the radiative transfer equations were solved using steady pressure-based solver in the ANSYS Fluent 17.1 software. The energy and radiation models are implemented one after the other (uncoupled) sequentially, using the conservative finite-volume approach. The SIMPLE pressure-velocity segregate algorithm was used with higher order of the relaxation terms. Table 3.6 showed the cases considered for the analysis of oxy-combustion characteristics for the three equivalence ratios from the stoichiometric condition down to lean operation at equivalence ratio of 0.5 with the exception of the first row at 70% CO_2. In all cases, fuel mass flow rate was kept constant at 2.76 L/min (corresponding to reactor power of 1.5 kW), with varying volumetric percentage of O_2 in the CO_2-O_2 oxidizer mixture. The flow

rates of fuel and oxidizer are kept within the laminar range to mimic the processes of oxygen permeation and oxy-combustion inside HTMRs for clean power production applications.

4.4.1 Flame description

The numerical results were used to characterize the flames in more details using the temperature contours generated at three dimensional planes which were not captured during the experiment. The steady state temperature contours from the combustion process modeled at stoichiometric condition are presented in Figure 4.24 for three different percentages of CO_2 addition as representative of the all conditions investigated. The red colored portions are the high temperature zones which indicated the reaction zone while blue portions represent the low temperature (colder) zones. In each case, the contours were extracted at the three different *xyz* planes to capture the overall flame shape. The temperature contours at the center of the combustor (*x-y* planes), as shown in Figures 4.24 (i's) for the three cases, depicted two flame sheets anchored to the upper and lower breadths of the CH_4+CO_2 inlet section and elongated along the longitudinal axis of the combustor forming 'an inverted V' shape. The flame sheets have an average thickness of about 2mm with their tips contacting each other at an angle of about 15^o. The *y-z* planes were captured at a longitudinal distance of 2cm from the origin (near the flame base) in order to view the horizontal configuration of the flames as shown in Figures 4.24 (ii's). The contours depicted that the flames were not perfectly rectangular, rather they were curved at the longitudinal edges due to the fuel and oxygen diffusions. Whereas flame from the case having 55% CO_2 curved inward thereby encircling the fuel stream due to higher Reynolds

number of the fuel stream that causes elongation of the reaction zone, the case without CO_2 addition, having lowest Reynolds number of the flue stream had their flames curved outwards while the flames remained relatively flat for the case of 35% CO_2 additions as seen in Figures 4.24 (ii's). The *x-z* planes shade more lights on the flame shapes based on the percentage of CO_2 added. The contours shown in Figure 4.24c (iii's) were extracted at inclined angles in line with the flame inclinations to capture the reaction zones. The case with no CO_2 addition showed a relatively rectangular flame while the elongation of the flame shape due to addition of the CO_2 causes the flames to thin at both the anchored position as well as the flame tips. This can also be explained by the geometrical difference between the breadth of the fuel stream inlet cross-section and that of the porous plate cross-section.

4.4.2 Flame shapes comparison with experiments

The comparison between the experimental visible flame images of the oxy-methane combustion captured at steady state conditions for various percentages of CO_2 addition at equivalence ratios of 0.5, 0.7, and 1.0 for the power of 1.5kW and numerical temperature contour plots are shown in Figure 4.25 and Appendix L. The images and the contour plots covered the field of view of the combustion zone of the reactor from the inlets to the outlet. The contour plots were extracted at the center of the combustor (*x-y* planes at z = 0), while the flame images were captured through the transparent quartz glass from a distance of about 100 cm using the high-speed camera rather than from the central plane. Also, the temperature contours give the general perspective about the high temperature regions which are synonymous with flame chemiluminescence.

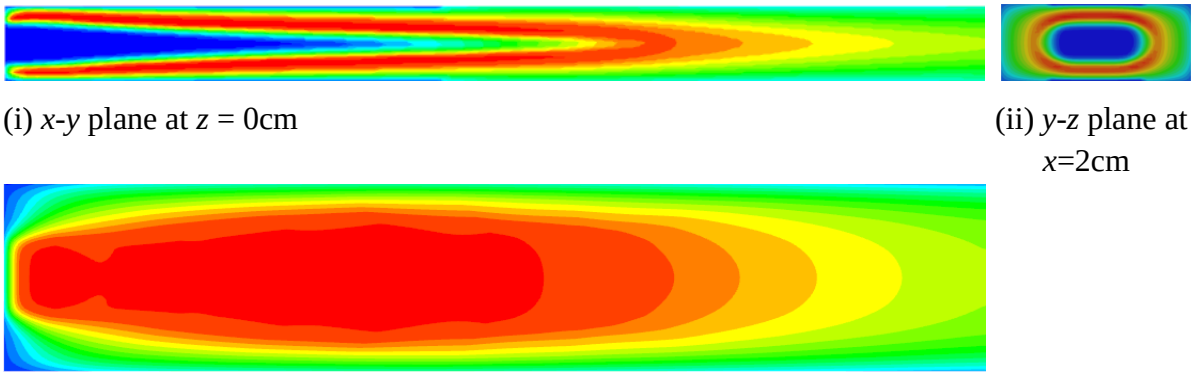

(i) *x*-*y* plane at *z* = 0cm (ii) *y*-*z* plane at *x*=2cm

(iii) *x*-*z* plane at *y* = (0.8, -0.2) cm

(a) 55% CO_2

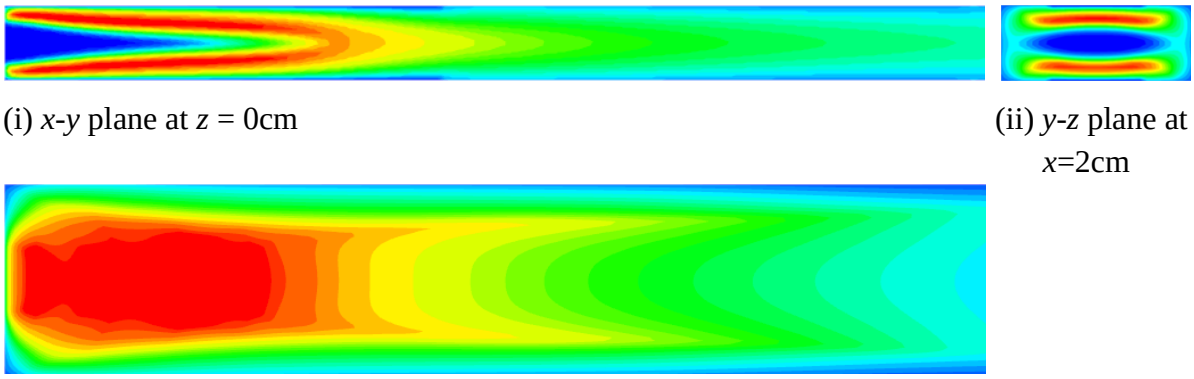

(i) *x*-*y* plane at *z* = 0cm (ii) *y*-*z* plane at *x*=2cm

(iii) *x*-*z* plane at *y* = (0.8, -0.7) cm

(b) 35% CO_2

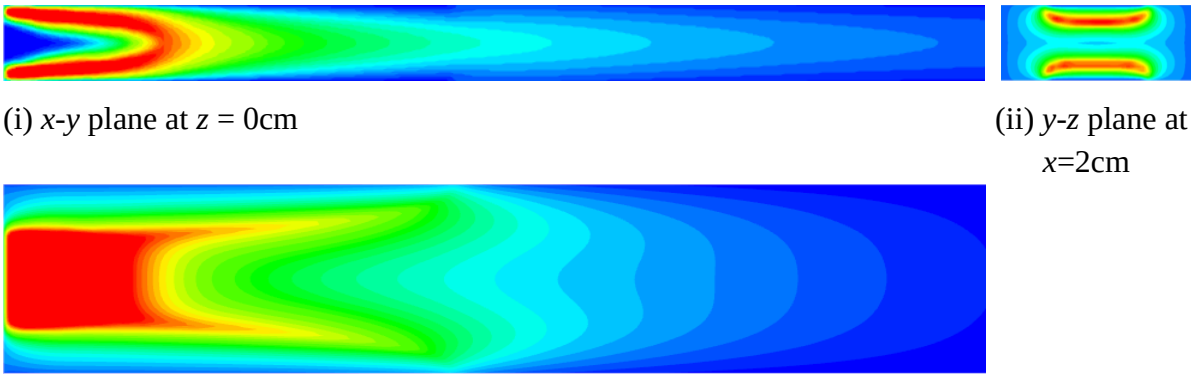

(i) *x*-*y* plane at *z* = 0cm (ii) *y*-*z* plane at *x*=2cm

(iii) *x*-*z* plane at *y* = (0.8, -1) cm

(c) 0% CO_2

Figure 4.24: Three-dimensional flame shapes at stoichiometric operating equivalence ratio.

The dark regime in the experimental images are the portion where there was no visible flame in the combustor while in the numerical contours, blue portion represent the lowest temperature regions with reddish regions being the highest temperature zones based on standard RGB color gradient. For the pure oxy-methane combustion case, without the CO_2 addition (0% CO_2) shown in Figure 4.25a, the highly whitish glow of the experimental flame that indicated the luminous intensity of the light showed similar trend compared to the numerical results at all the three equivalence ratios studied. This indicated very good agreement between the numerical contours and the experimental images despite fact that the experimental images do not show low temperature gradients regions. This good agreement has also been observed when CO_2 was added as shown in Figures 4.25 b-d, except for Figure 4.25e, when the percentage of CO_2 addition reaches 55%. At this higher percentage, the hot regions of the numerical plots were slightly longer than that of the experimental visible flames, especially at very leaner equivalence ratio of 0.5. This slight overprediction/increase in length was as the result of CO_2 being supplied together within the fuel inlet which resulted in increase in the fuel stream Reynolds number causing a jet behavior with higher momentum that extended the mixing zone. In all the cases compared, increase in equivalence ratio resulted in more compact flame with higher temperatures due to slight decrease in the fuel stream Reynolds number which was responsible for the elongation of the reaction zone. Also, the effect of CO_2 addition to the flame length was more pronounced due to significant change in the fuel stream Reynolds number which was responsible for the elongation of the reaction zone in comparison to that of equivalence ratio. More vivid comparisons between experimental and numerical flame shapes at different % of CO_2 in the oxidizer mixture for were presented in Appendix L.

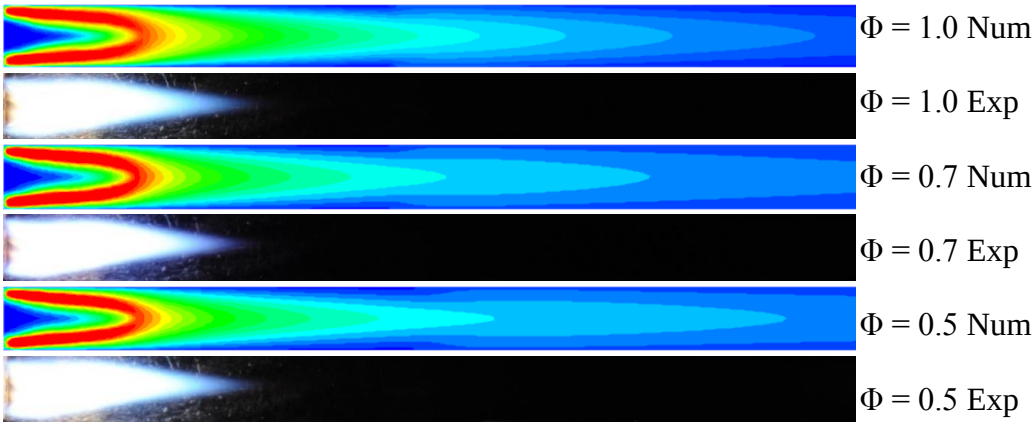

(a) 0% CO_2

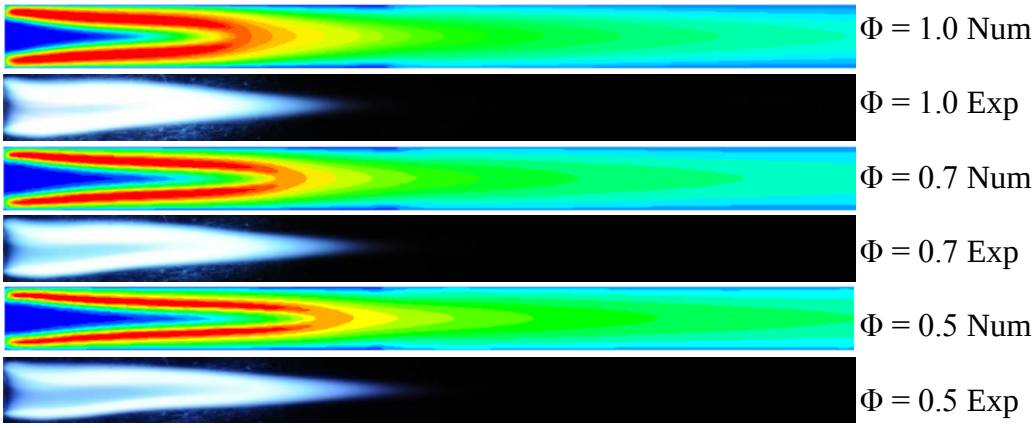

(b) 27% CO_2

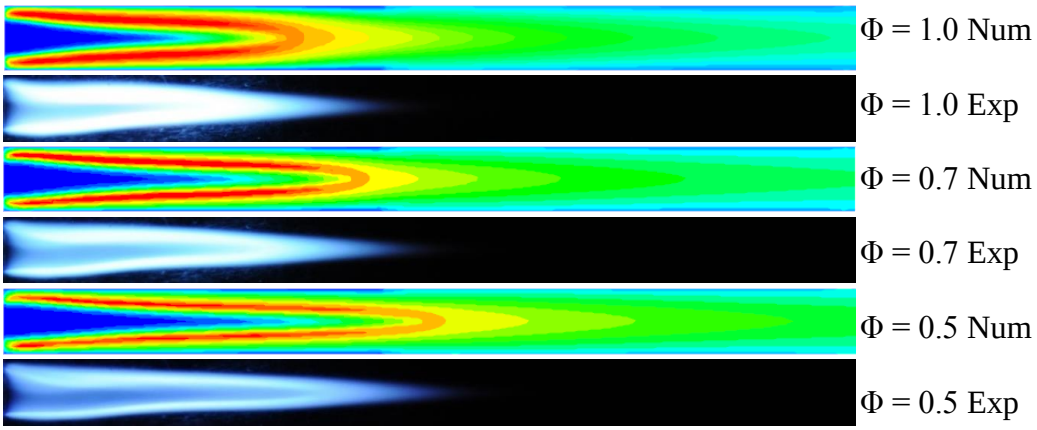

(c) 35% CO_2

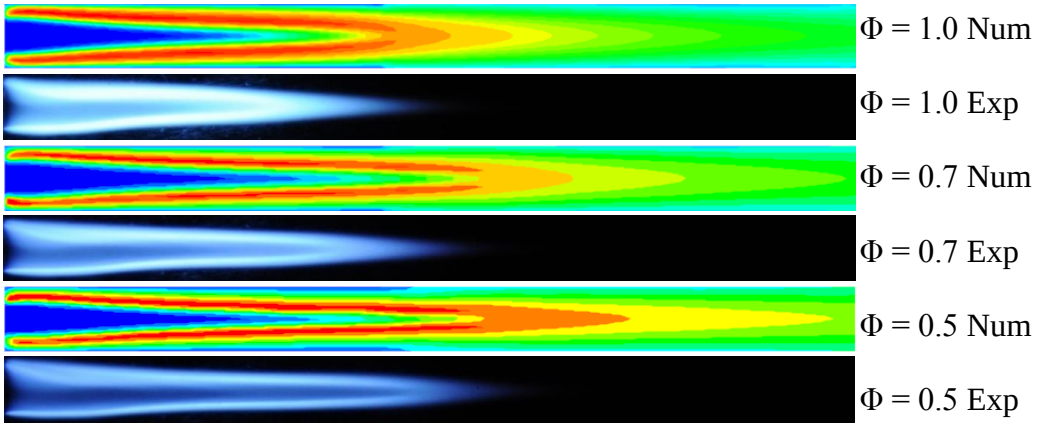

(d) 45% CO_2

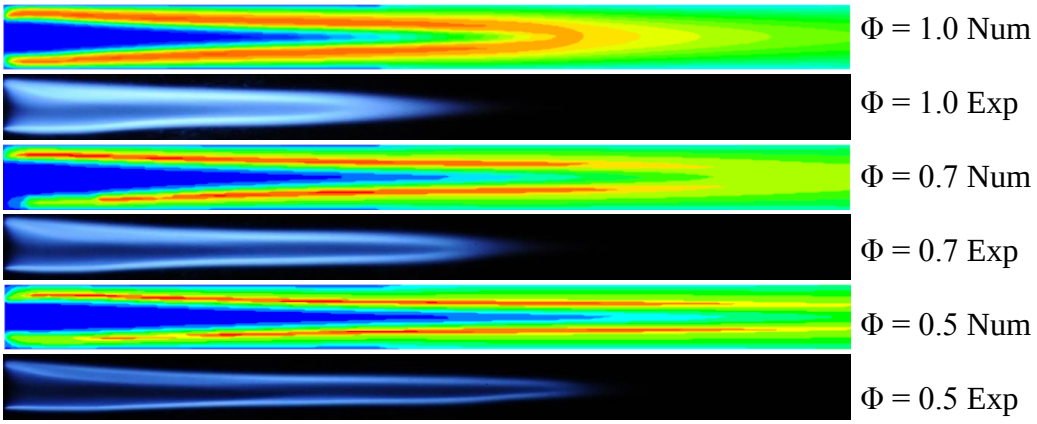

(e) 55% CO_2

Figure 4.25: Comparison between experimental and numerical flame shapes at different equivalence ratio for % of CO_2 in the oxidizer mixture.

(Note: Num = Numerical; Exp = Experimental)

4.4.3 Temperature comparisons with experiments

4.4.3.1 *Vertical temperature distributions comparison*

The vertical temperature distributions that were measured across *y*-axis at the seven symmetric nodal locations shown in Figure 3.5, are compared with the numerical results after being normalized with the non-dimensionless flame length, at different operating conditions, as presented in Figures 4.26. In general, there were good agreements between the experimental measurements and the numerical results at all the conditions with the numerical results slightly overpredicting the experimental measurements. The maximum percentage difference between the experimental and numerical results were at pure oxy-methane combustion (0% CO_2) in which it reached up to about 14% at stoichiometric equivalence ratio, 11% and 13% at equivalence ratios of 0.5 and 0.7 respectively. This deviation between the numerical results and the experimental data might be attributed to imperfection of the temperature probe positioning during the measurements and heat loses due to imperfect sealing between the quartz glass and the other combustor walls. The higher the percentage of CO_2 addition in the mixture the lower the percentage difference between the results due to lower combustion temperatures characterized by the thermal dilution effect of CO_2 as the result of its higher molar heat capacity. Detailed percentage difference between the experimental data and numerical results can be found in the Appendix M. The temperature profiles were parabolic with maximum values obtained at the center point except for the case of 55% CO_2 addition at equivalence ratio of 0.5, where there were two temperature peaks due to upper and lower flame sheets being more distinctly separated at the tips and longer flames.

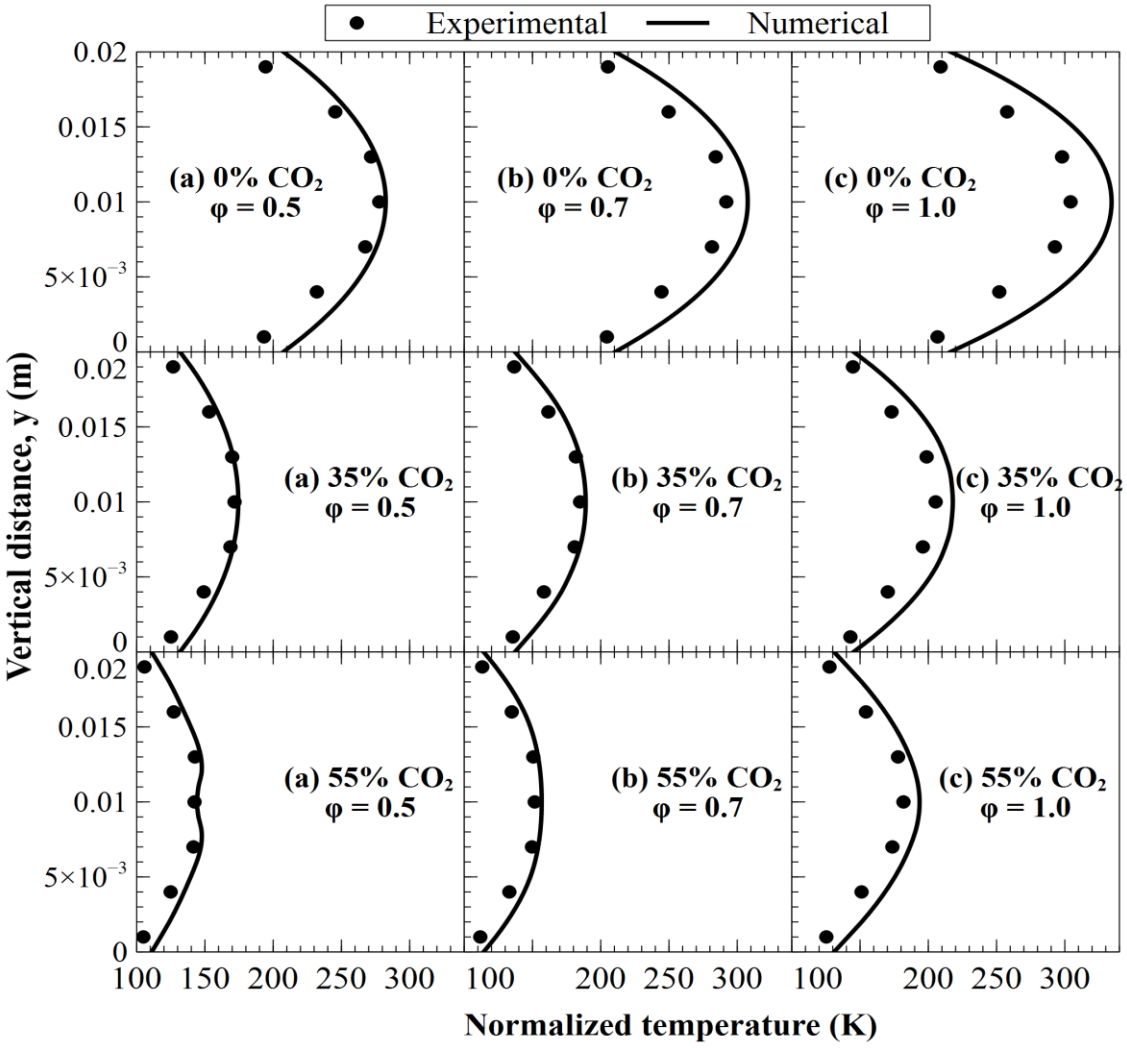

Figure 4.26: Comparison between vertical numerical and experimental gas temperatures at outlet for different operating conditions.

$(x = 0.26, -0.01 \leq y \leq 0.01, z = 0)$

4.4.3.2 Horizontal temperature distributions comparison

Figure 4.27 shows the comparison between numerical and experimental gas temperatures at the combustor outlet for different operating conditions. The temperature distributions were measured across the z-axis at the 5 symmetric nodal locations shown in Figure 3.5. The experimental data were compared with the numerical results in a similar fashion as discussed in section 4.3.3.1. The numerical results are well compared with the experimental data within a maximum of about 14% difference at stoichiometric equivalence ratio for all the cases considered. The percentage difference decreases to about 5% and below at equivalence ratios of 0.7 and 0.5 respectively. The percentage of CO_2 addition in the mixture decreases the percentage difference between the results in this case. The temperature distributions were also symmetrical with the peak temperature occurring at the center due to the symmetry of the inlets of the species at all the conditions. In all the three cases, the higher the percentage of CO_2 the lower the normalized temperatures. Increasing the equivalence ratio resulted in increase in the percentage difference between the results due to increase in combustion temperatures.

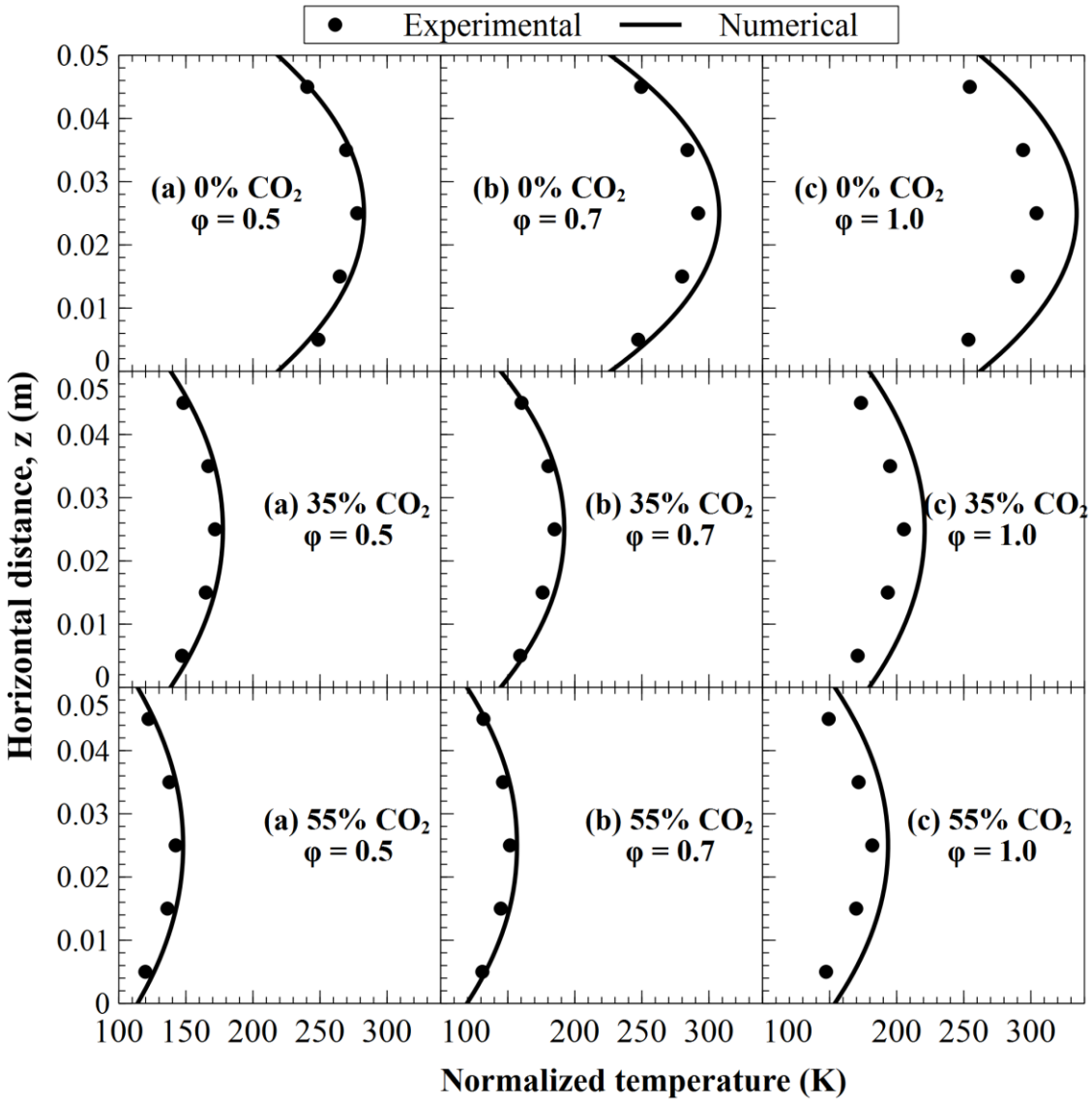

Figure 4.27: Comparison between horizontal numerical and experimental gas temperatures at outlet for different operating conditions.

($x = 0.26$, $y = 0$, $-0.025 \leq z \leq 0.025$)

4.4.3.3 Longitudinal temperature distributions comparison

The longitudinal temperature measurements were conducted downstream of the combustor due to the thermocouple range limitation. The measurements covered the seven nodal locations as stated in Figure 3.6. The numerical simulations under the same conditions provided the opportunity of understanding the overall longitudinal temperature variations starting from origin. For the sake of comparison, the numerical results were truncated to the range of the experimental data as shown in Figure 4.28 for different operating conditions. The agreement between the experimental data and the numerical results were within a maximum of below 10% difference at all the equivalence ratio for the cases of pure oxy-methane combustion. The percentage of CO_2 addition in the mixture increases the percentage difference between the results in almost all the cases except at 55% CO_2 at stoichiometry where the difference decreases to below 10%. The percentage differences were more prominent upstream of the combustor due to increase in temperature beyond the limit of the thermocouple at some instance.

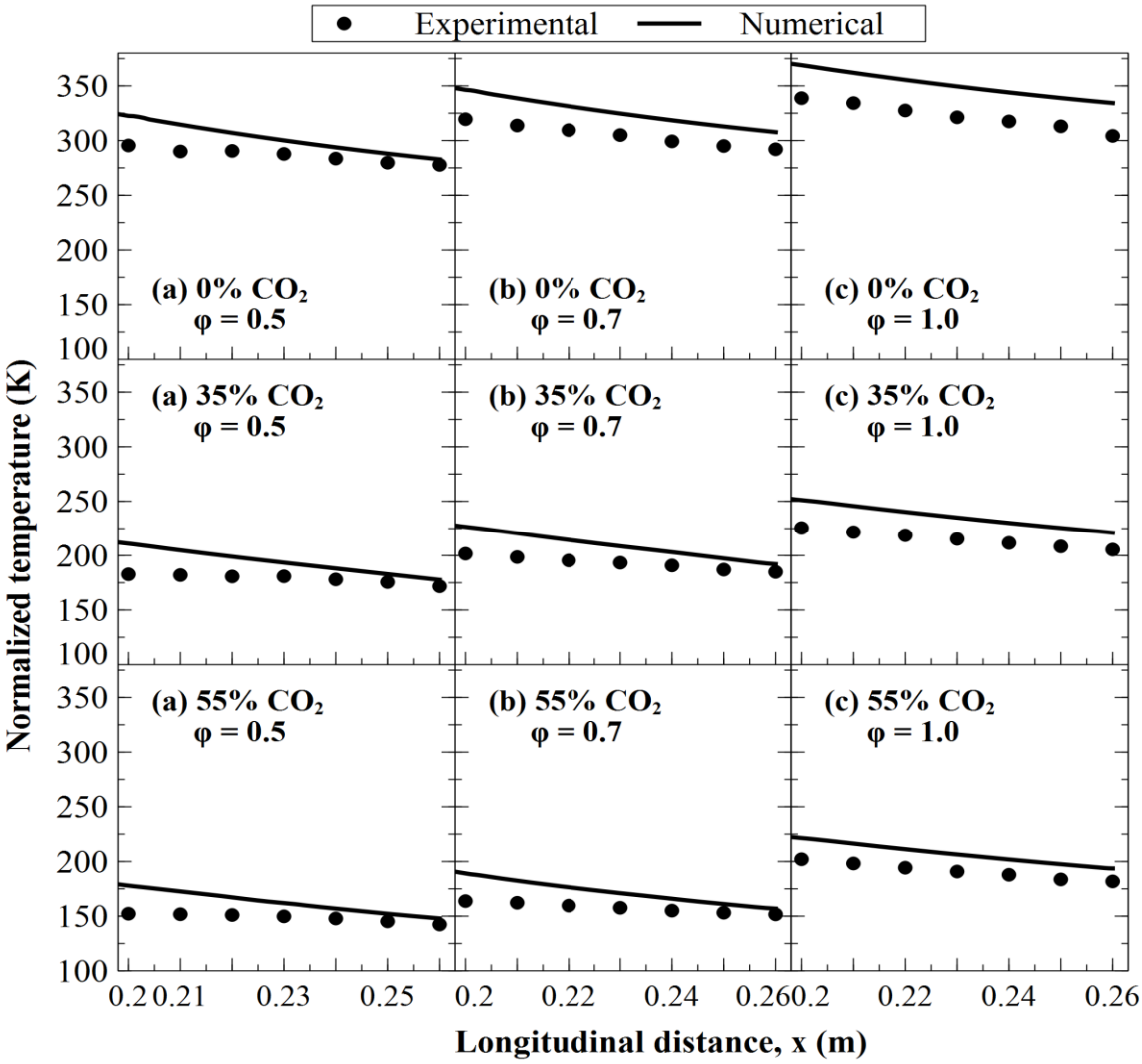

Figure 4.28: Comparison between longitudinal numerical and experimental temperatures at the combustor centerline for different operating conditions.

$(0 \leq x \leq 0.26, y = 0.26, z = 0)$

4.4.4 Numerical temperature distributions

4.4.4.1 Vertical temperature distributions

The vertical temperature distributions were obtained numerically at the combustor exhaust across *y*-axis at the center for different operating conditions as presented in Figures 4.29. Figures 4.29-a indicates the effect of equivalence ratio on the vertical temperature distribution normalized by the non-dimensional flame length, as discussed earlier, for three representative percentage of CO_2 additions. The temperature profiles are symmetric with maximum occurring at the center and decreased towards the upper and lower walls for all the %CO_2 additions except for the case of 55% where two maximum temperature peaks occurred between the center and the upper and lower walls due to the flame elongation to near the outlet, as shown in Figure 4.25-e for numerical results at equivalence ratio of 0.5 ($\varphi = 0.5$ num). For all percentages of CO_2 additions, the higher the equivalence ratio the higher the temperature due to increase in reactivity as the result of increase in fuel percentage in the combustor and decrease in excess oxygen which act as a heat sink.

For the case of 0% CO_2 addition, the exhaust gas temperature was much higher than the CO_2 added counterparts which was the characteristics of pure oxy-methane combustion. This was more clearly presented in Figure 4.29-b where addition of the CO_2 resulted in lowering the exhaust gas temperatures at all the equivalence ratios studied. Whereas uniform temperature distributions were observed vertically at the center of the combustor outlet at higher % CO_2, as shown in Figure 4.29-b, parabolic profiles were obtained at pure oxy-methane conditions. When the oxygen content was increased (fuel lean cases) while

the percentage of CO_2 addition also increased, the temperature profiles becomes more uniformly distributed at the center, with the variation being increase with decrease in the CO_2 addition. This is caused by the thermal dilution effect of CO_2 that resulted in the reduced flame temperatures and enhanced exhaust gas mixing.

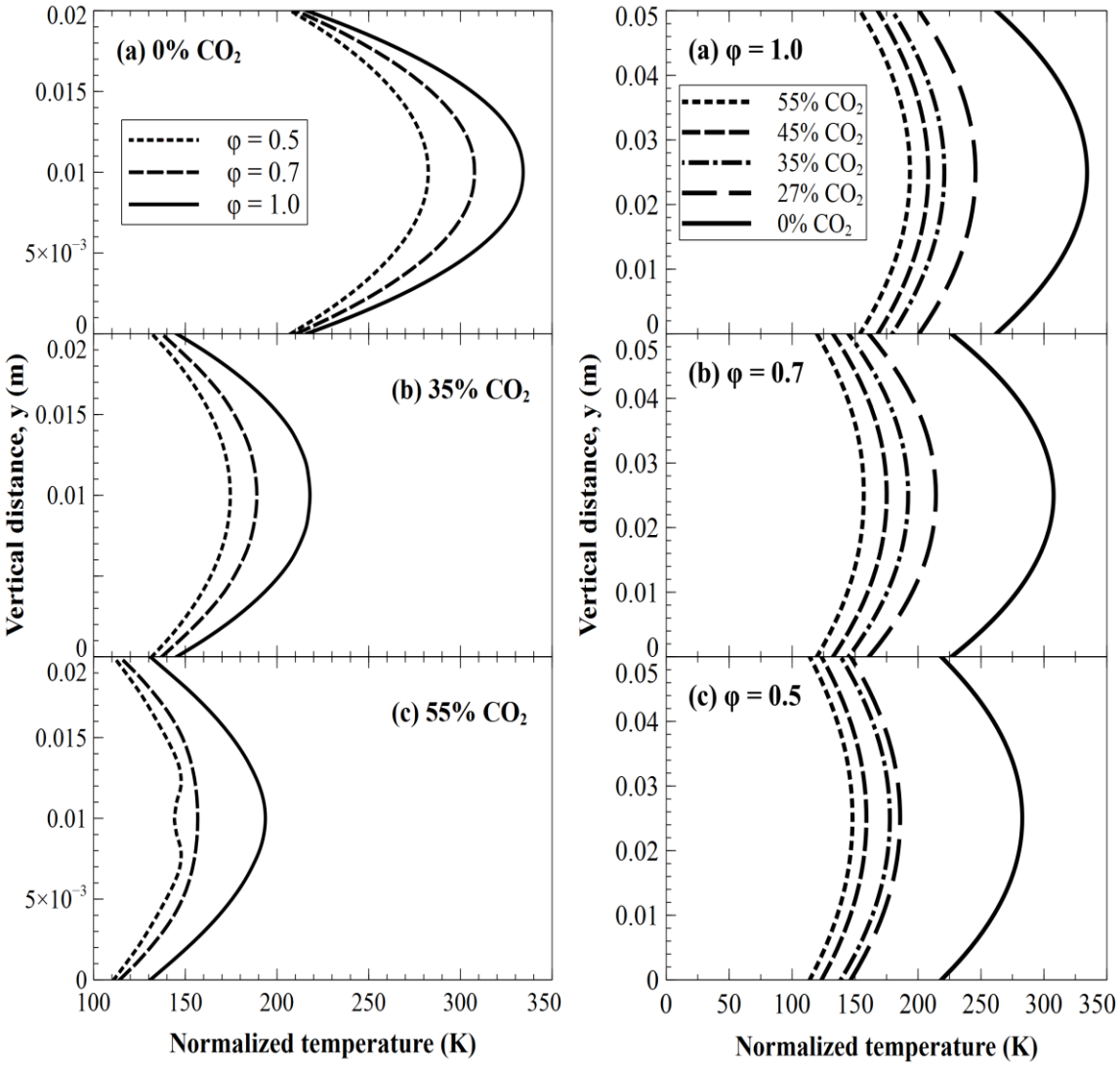

(a) Effect of equivalence ratios (b) Effect of % CO_2

Figure 4.29: Effect of equivalence ratio and percentage of CO_2 addition on the normalized vertical temperature distribution at the exhaust.

($x = 0.26, -0.01 \leq y \leq 0.01, z = 0$)

4.4.4.2 Horizontal temperature distributions

The horizontal temperature distributions across *z*-axis at the combustor exhaust obtained numerically for different operating conditions were presented in Figures 4.30. Figures 4.30-a shows the effect of equivalence ratio on the vertical temperature distribution normalized by the non-dimensional flame length, for three representative percentage of CO_2 additions. The temperature decreases with increase in horizontal distance from center of the combustor outlet irrespective of the equivalence ratio and $\%CO_2$ in the mixture, as shown in the Figures 4.30. This was expected as the result of radiation heat loss through the quartz glass plates at the two sides of the combustor to the cold ambient at about 293 K. The variations were also symmetrical with the peak temperature at the center due to the symmetry of the inlets of the species. For all percentages of CO_2 additions, increase in equivalence ratio resulted in the elevation of temperature due to increase in reactivity as the result of increase in fuel percentage in the combustor and decrease in excess oxygen which act as a heat sink. This was more vividly clear for the case with 0% CO_2 addition, where the increase in flame length due to decrease in equivalence ratio, was insignificant, as shown in Figure 4.30-b.

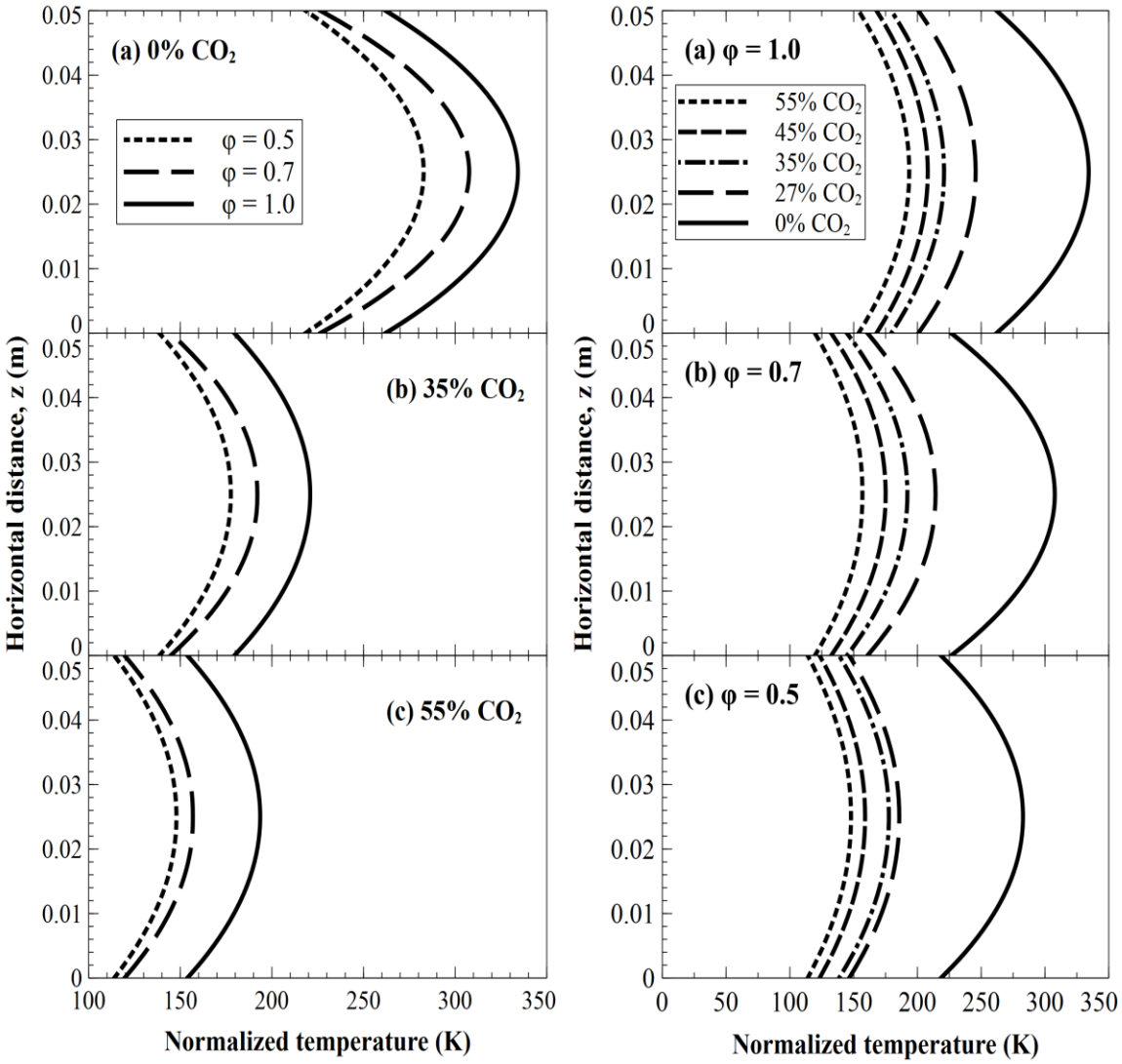

(a) Effect of equivalence ratios (b) Effect of % CO_2

Figure 4.30: Effect of equivalence ratios and percentage of CO_2 addition on the normalized horizontal temperature distribution at the exhaust.

($x = 0.26$, $y = 0$, $-0.025 \leq z \leq 0.025$)

4.4.4.3 Longitudinal temperature distributions

The normalized longitudinal temperature variations along x-axis, starting from the origin to the exhaust of the combustor at the centerline are shown in Figure 4.31 for both the effects of change in equivalence ratios and percentage of CO_2 addition. Note that the longitudinal centerline temperatures do not represents the maximum flame temperature since the two flame sheets were situated away from the center as shown in Figure 4.25 with their tips meeting at the centerline. Hence maximum temperature locations shown in Figure 4.31 were the locations the tips coincidence. All the results elucidated higher temperatures at higher equivalence ratios. The addition of CO_2 decreases the centerline temperatures due the decrease in flame temperatures as seen in the previous sections. The higher the percentage of CO_2 added to the fuel stream, the lower the temperature downstream of the combustor due to the thermal dilution effect of the CO_2. Addition of the CO_2 in the mixture elongated the reaction zone due to increase in Reynolds number of the fuel stream and hence resulted in the increase in the maximum temperature locations. At the stoichiometric equivalence ratios (Figure 4.31-b) the temperature rises suddenly due to the initiation of the combustion reaction and reached it maximum due to the flame temperature rise and drops downstream of the combustor polynomially, irrespective of the % of CO_2 in the mixture. As the amount of oxygen was increased to the lean conditions the temperature decrease reduces to approximately linear.

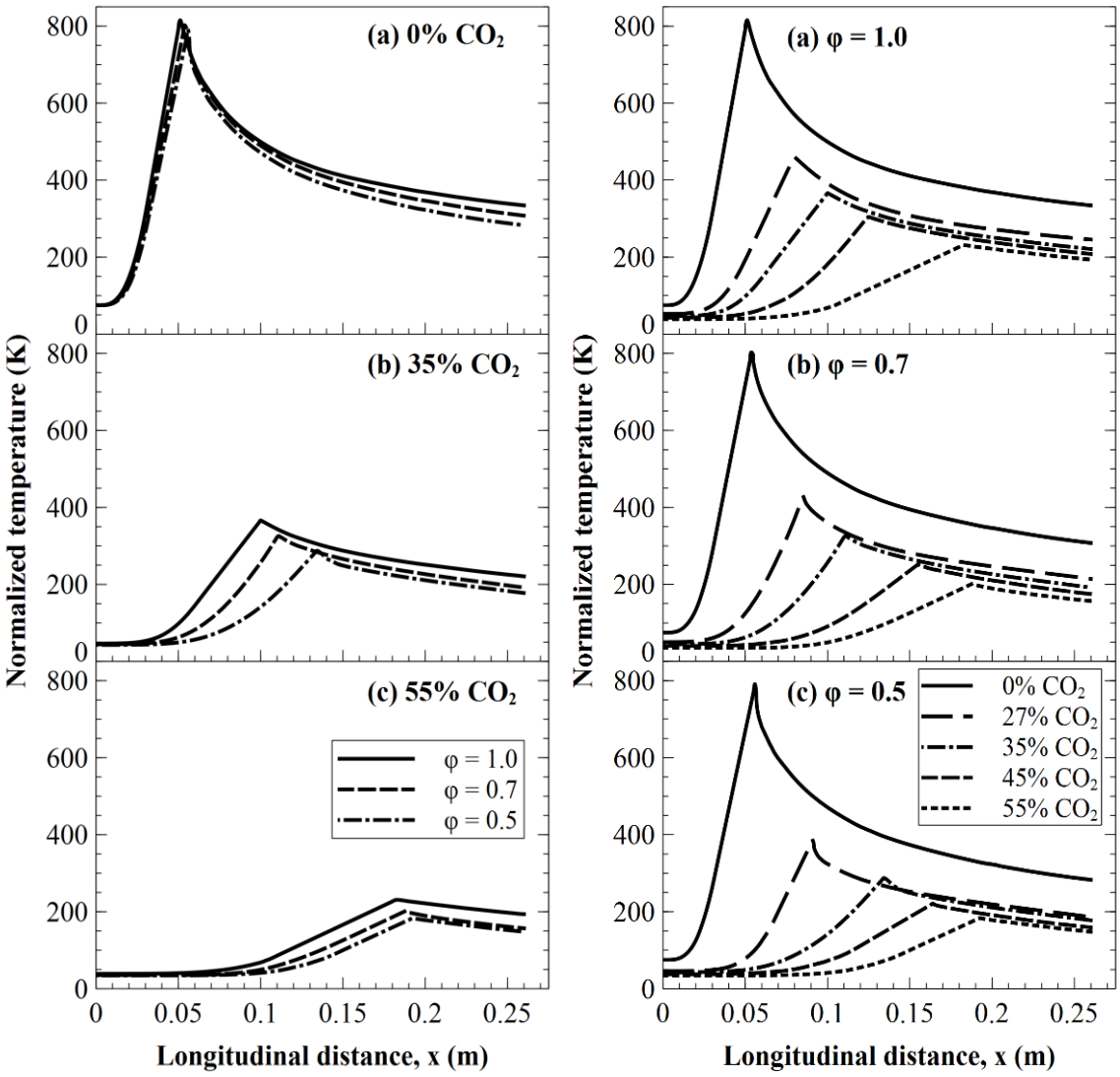

(a) Effect of equivalence ratios (b) Effect of CO_2 %

Figure 4.31: Effect of equivalence ratios and percentage of CO_2 addition on the normalized longitudinal temperature distribution at the centerline.

$(0 \leq x \leq 0.26, y = 0, z = 0)$

4.4.5 Exhaust gas concentration

The exhaust gases are composed of five species, mainly CO_2, H_2O, CO, CH_4 and O_2 which are the dominant species in the reduces chemical reaction kinetics model applied for the combustion modeling. The species mass fractions were averaged at the combustor outlet for every combustion condition using mass-weighted averaging. Mass-weighted averaging involves the ratio of the summation of the value of a specie mass fraction multiplied by the product of the outlet area and momentum vectors to the summation of the value of the product of the outlet area and momentum vectors [133]. The effect of percentage of CO_2 addition on the averaged exhaust gas species mass fractions were presented in Figure 4.32. At lower equivalence ratio ($\varphi = 0.5$), without CO_2 addition, the mass fractions of the fuel components (CH_4 and CO) reduced to almost zero at the outlet due to complete combustion of the fuel at lean equivalence ratio. The combustion products were mainly CO_2 and H_2O with the excess O_2. The averaged mass fractions of the CO_2 at the outlet was increased from about 30% without addition of CO_2 in the fuel stream to about 82% when the CO_2 added was 55%. This indicated that addition of the CO_2 lowered the combustion temperature which in turn slightly decreases the rate of reactivity. This can be seen more evidently from the increase in unburned CH_4 and the decrease in H_2O production as the percentage of CO_2 addition increases (Figure 4.32-a). The decrease in excess O_2 mass fractions were attributed to the overwhelming CO_2 addition.

Figure 4.32-b which presents the gas species mass fractions at equivalence ratio of 0.7 showed similar trends with the leaner equivalence ratio for all the combustion conditions considered. But there was decrease in excess O_2 from about 45% to 25% when no CO_2 was added due to the increase in equivalence ratio. The CO_2 mass fractions increases due to the decrease in O_2 mass fraction at higher equivalence ratio as well as the inlet CO_2 addition. There was also increase in H_2O mass fractions due to lower O_2 mass fractions. The CO concentration at 0% CO_2 addition increases to about 200ppm in comparison to the leaner counterpart that was less than 50ppm. This increase in CO is attributed to the lower oxygen availability for complete combustion. The amount of unburned CH_4 slightly increased to about 0.4% (although still negligible) when the CO_2 addition reached 55%. This was due to the dilution effect of the CO_2 which lowered the combustion temperature and elongated the reaction zone. At stoichiometric equivalence ratio, the trends of CO_2, H_2O and CH_4 mass fractions were similar to those at equivalence ratio of 0.7 at all the conditions but with higher magnitude due to increase in reactivity, combustion temperature and the decrease in excess O_2 to almost zero as shown in Figure 4.32-c. There was slight increase in O_2 mass fraction at the outlet as the CO_2 addition increases due to increase in unburned CH_4 and CO that should have reacted with the available O_2. The CO concentration increased slightly when CO_2 addition increases up to 35% and then increases more rapidly when the CO_2 was further added beyond 35%.

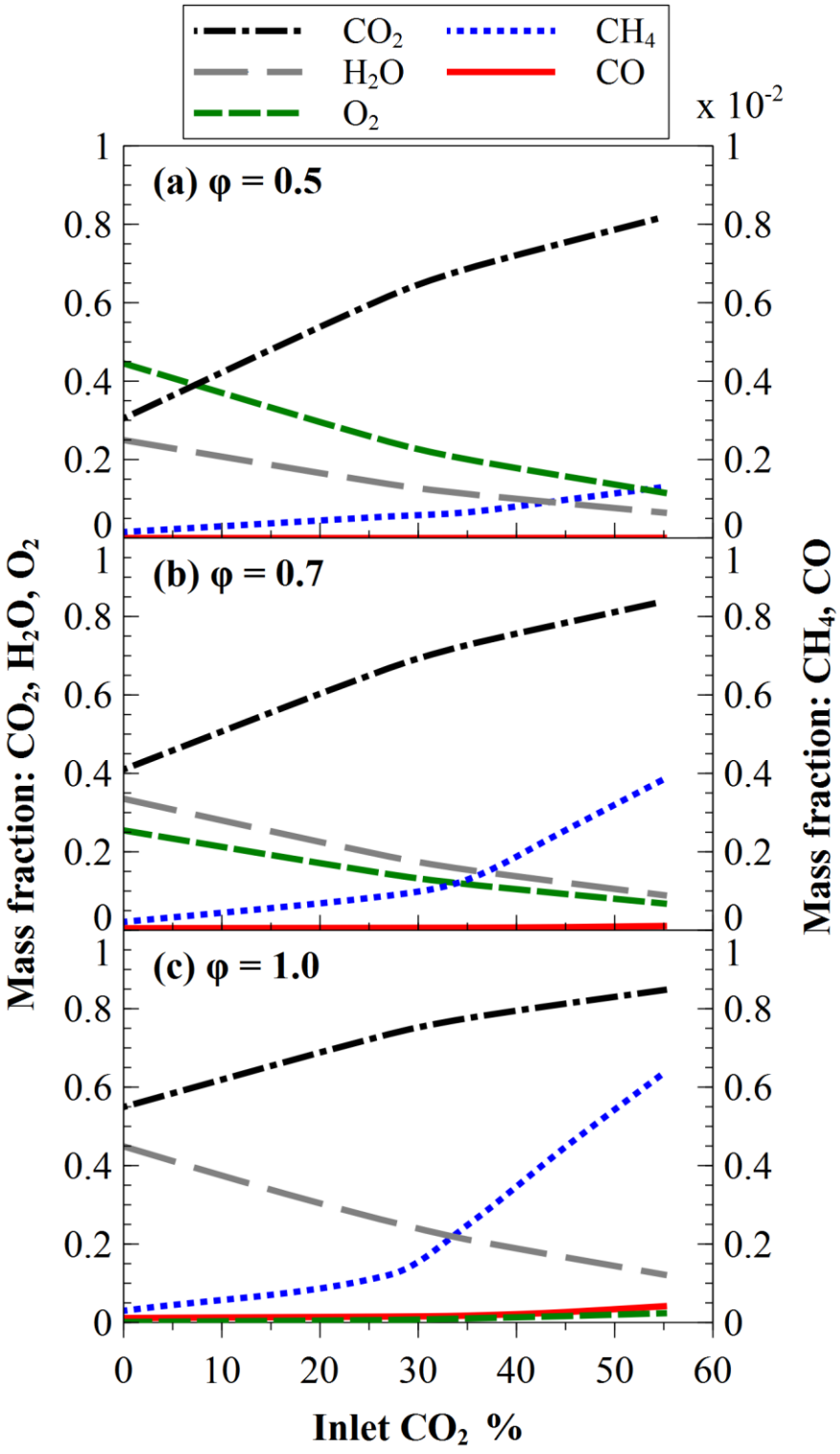

Figure 4.32: Effect of percentage of CO_2 addition on the averaged exhaust gas species concentrations.

The effects of equivalence ratio on the averaged exhaust gas species concentrations are shown in Figure 4.33. For the two fuel lean equivalence ratios (φ=0.5 and φ=0.7) the O_2 mass fractions at the outlet decreases with increase in the percentage of CO_2 addition as shown in Figure 4.33-a. This is due to the overwhelming increase in CO_2 concentrations. The most leaner equivalence ratio, φ=0.5, was having higher values of O_2 mass fraction compared to φ=0.7 due to decrease in the inlet O_2 mass flow rates for the same amount of fuel. At stoichiometric equivalence ratio, the O_2 was mostly consumed during combustion prior to the outlet at lower percentages of CO_2 additions due to higher reactivity at elevated temperatures. There was about 2% of un reacted O_2 mass fraction when the percentage inlet CO_2 addition reached 55% due to very low combustion temperature, elongation of the reaction zone to near the outlet as shown in Figure 4.25-e. The averaged mass fractions of CO_2 at the outlet for the three equivalence ratios investigated were presented in Figure 4.33-b. The results showed that the higher the equivalence ratio the higher the CO_2 mass fraction due to the decrease in the excess oxygen concentrations. Also, the influence in the inlet CO_2 addition was reciprocal to the increase in CO_2 mass fractions at the outlet. For the H_2O mass fractions, as shown in Figure 4.33-c, the effect of increase in equivalence ratio form lean conditions up to the stoichiometric condition was similar to that of CO_2. The higher the equivalence ratio the higher the mass faction of H_2O due to the decrease in excess oxygen concentration relative to the increase in H_2O concentration due to complete combustion at lower equivalence ratio. The inlet addition of CO_2 resulted in the decrease in H_2O mass fractions due to the offsetting increase in CO_2 concentration by the CO_2 addition at the inlet.

The operating equivalence ratio played important role in the fuel consumption during the combustion reaction. As shown in Figure 4.33-d, increase in equivalence ratio reduces CH_4 reactivity due to decrease in oxygen availability for the combustion reaction. Hence, resulted in increase in unburned CH_4 at the outlet, irrespective of the percentage of CO_2 added at the combustor inlet. Up to 27% inlet CO_2 addition, the effect of the CO_2 addition on the CH_4 availability was very lower but heightened afterwards due to low reactivity as the result of low temperatures caused by CO_2 thermal dilution effect. The mass fraction of the CH_4 at the outlet increased by a factor of 5 from equivalence ratio of 0.5 to 1.0 due to decrease in O_2 availability and flame stretching to the outlet which were susceptible to incomplete combustion at the outlet, even though the maximum CH_4 mass fraction was less than 0.7% even at the stoichiometric condition. As for Figure 4.33-e, the effect of equivalence ratio on the unreacted CO availability at the combustor outlet was similar to that of CH_4 due to the same reasons.

CHAPTER 5

RESULTS AND DISCUSSIONS FOR THE OTM REACTOR MODELING

This part of the results and discussion presents the numerical modeling studies of a two-pass oxygen transport membrane reactor for oxygen permeation and oxy-fuel combustion characteristics analyses for the purpose of its application to fire tube boilers. This will involve the replacement of the fire box (burner) with bundles of OTM combustors that will supply the required power range, from 1 to 5 MWe. The development and validation of numerical models for oxygen separation and oxy-methane combustion in the two-pass oxygen transport reactors are presented under several sub-sections: geometry optimization for optimum performance, oxy-methane characteristics analyses, and the effects of the key reactor controlling parameters such as effect of inlet gases temperatures and flow rates on the combustion heat transfer to the saturated water and steam as the load in a fire-tube boiler, the effect of saturated water and steam condition on the OTR unit heat transfer performance and the effects of thermal and radiative properties of some of the reactor materials in order to obtain optimum operating conditions and parameters. The adopted reactor geometry as described in section 3.4 and Figure 3.7, is of cylindrical configuration with several concentric tubular OTRs. A single unit of the OTRs was considered for the analyses which was elaborated in more details in section 3.4.1. The geometry was

represented using a 2D-axissymetry to reduce the intense computational requirements for the solution. The sets of operating and boundary conditions used to achieve the set objectives were presented in Tables 3.11 - 3.18.

5.1 2D Model Validation

To ensure the accuracy of the numerical results, the developed mesh was tested to ensure grid independence and the models were validated using available experimental data from open literature. It consists of the mesh size dependency test, oxygen permeation model validation as well as the methane consumption under oxy-fuel reaction.

5.1.1 Mesh size independence

The mesh grid independence test was performed to ensure the accuracy of the numerical solutions. The test consisted of four different discretized geometries with the number of cells ranges from 6,375 to 51,000 cells (0.6375x104, 1.275x104, 2.55x104, 5.1x104 cells for mesh-1, mesh-2, mesh-3 and mesh-4, respectively). The mass flow rates of oxygen permeated across the OTM and the total heat received by the outer-pipe were computed under the same conditions using the four grid meshes and plotted in Figure 5.1. The maximum variation in O2 mass flow rate between mesh-1 and mesh-4 was found to be 2.84%, between mesh-2 and mesh-4 was 0.16%, and between mesh-3 and mesh-4 was 0.01%. Similarly, the maximum variation between the total heat received by the outer-pipe between mesh-1 and mesh-4 was found to be 0.61%, between mesh-2 and mesh-4 was

0.11%, and between mesh-3 and mesh-4 was 0.0002%. Figure 5.1 elaborated these variations graphically. Both the O2 total mass flow rates and the heat transferred were over predicted by the low-quality meshing with lower grids and the variables remains relatively constant from mesh-3 to mesh-4. From the above analysis, the variation of results of mesh-3 with respect to mesh-4 were insignificant. Hence mesh-3 was choosing for the subsequent analyses. The mesh orthogonal quality usually is in the ranges of 0 - 1, with values approaching 0 corresponding to low quality mesh. The maximum orthogonal skew of mesh-3 was 0 while the minimum orthogonal quality was 1 and the maximum aspect ratio was 2.23. The mesh contained 25,500 cells, having 53,086 faces and 27,583 nodes.

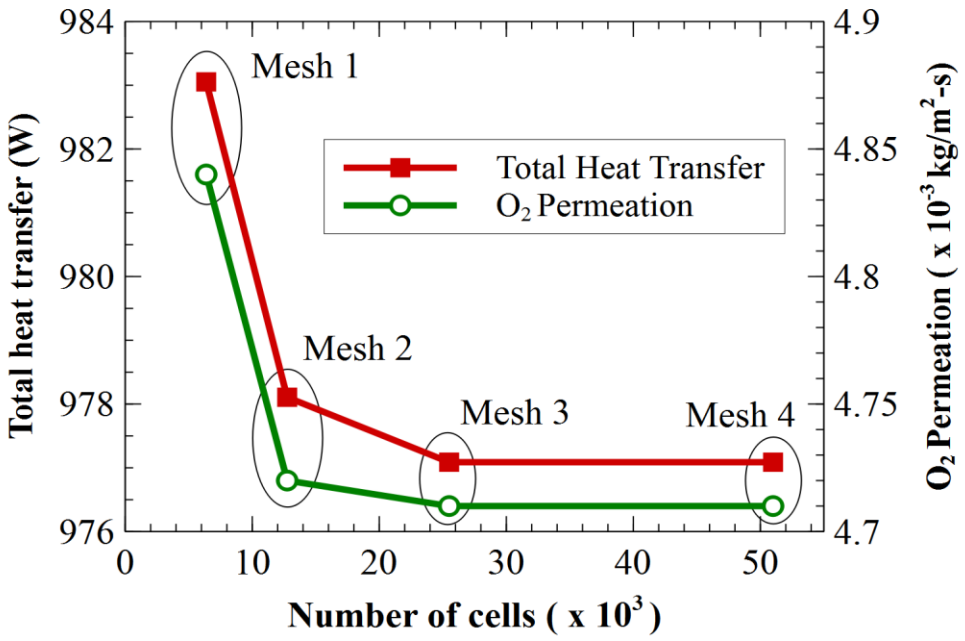

Figure 5.1: Mesh independence analysis

5.1.2 Model Validation

The OTM permeation model presented in Equations 2.28 – 2.31of section 2.4.5 were applied to the experimental work conducted by Behrouzifar *et al.*, [182] and Mezghani and Hamza [197]. In the former experiment [182], O_2 permeation flux was measured across a 1 cm diameter disk-shaped BSCF OTM at various values of thickness under different elevated temperature conditions without reaction under steady laminar flow. They supplied synthetic air (nitrogen + oxygen mixture) at a volume flow rate of 150 cm^3/min in the feed side and pure helium at volume flow rate of 60 cm^3/min in the permeate (sweep) side at atmospheric pressure. The experimental results at varied temperatures and membrane thickness were shown in Figure 5.2 (symbols). The same conditions were modeled in this work and the comparison with the experimental data as shown in the Figure 5.2 (solid lines) indicated the same trend of increase in O_2 permeation flux with increase in temperature and the inverse with increase in membrane thickness with reasonable degree of accuracy. The later experimental data of Mezghani and Hamza [197] was conducted using a 2.5 cm diameter disk-shaped BSCF OTM having thickness of 1 mm over a period of 100 hrs. They supplied helium at constant volume flow rate of 5.0E-7 m^3/s in the sweep side and air at constant volume flow rate of 3.3E-7 m^3/s in the feed side, at 920 ^oC. They achieved constant oxygen permeation flux of 0.0126 mol/m^2-s over the100 hrs period. They also obtained O_2 flux of 0.0091mol/m^2-s when they replaced the inert helium gas with 1.083E-8 m^3/s of gaseous methane as fuel to enable oxy-methane combustion. They reported complete combustion of methane with excess O_2 flow rate of 20 ml/min. These two experimental conditions were modeled using the current model and the results obtained were reasonably compared within an error of less than 6% as shown in Figure 5.3.

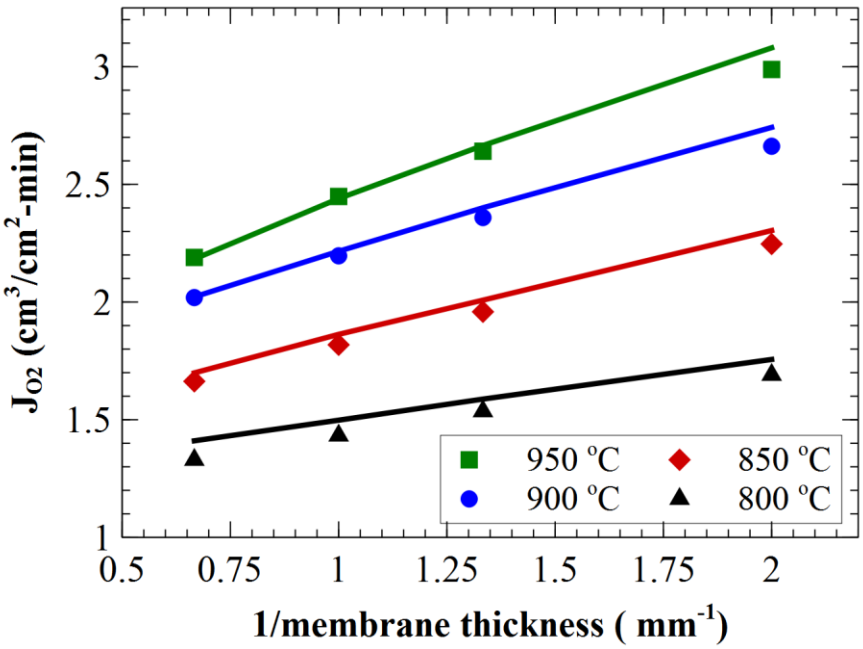

Figure 5.2: Comparison of O_2 permeation flux between numerical and experimental data (solid lines from this numerical model and symbols from experimental work of Behrouzifar et al., [182])

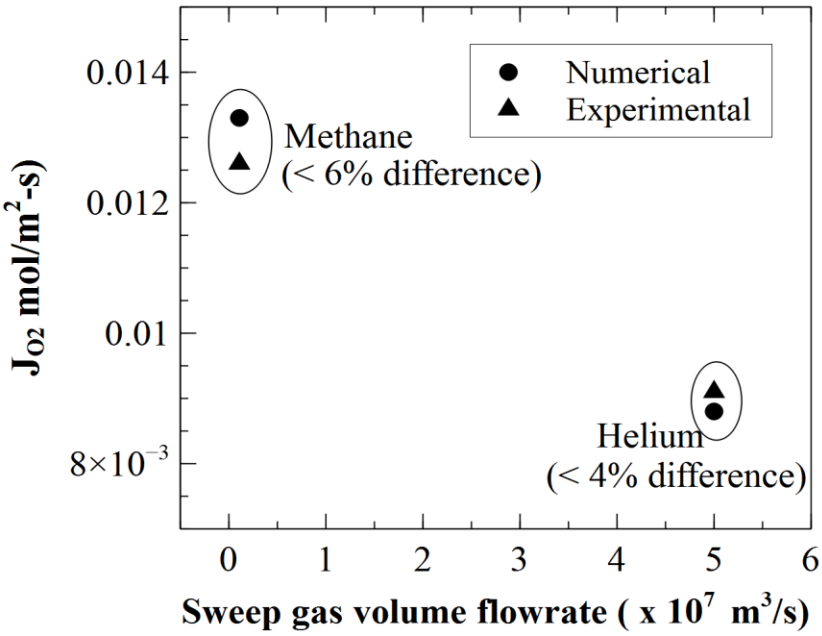

Figure 5.3: Comparison of O_2 permeation flux between numerical and experimental data (circular symbols from this numerical model and triangular symbols from experimental work of Mezghani and Hamza [197])

5.2 OTR Geometry Development

The two-pass OTR geometry shown in Figure 3.7 was optimized to support the combustion of methane with enough oxygen from the OTM for application in fire tube boilers. The geometric parameters that were optimized include: length of the OTM, surface area of the OTM, volume of the combustion annulus, thickness of inner-pipe and outer-pipe surface area. The lengths of the OTM studied ranges from 100mm to 2000mm. It was found that the oxygen permeation was insignificant after 500mm. Hence the length of 500mm of the OTM was considered. The outer surface area of the OTM was determined by the diameter at the fixed length. To obtain enough oxygen for the combustion, the membrane surface area should be reasonably large. Hence the diameter of the membrane was optimized to 200mm based on the laminar velocity requirement due to typical membrane physical strength limitations as well as the higher oxygen partial pressure requirement for effective permeation from feed side to the sweep side. The volume of the combustion zone was determine based on the fuel flow rates as well as adequate residence time within the length of the OTM. It was found that a cross-sectional area of about 600mm^2 is adequate for the 500mm long OTM. This corresponds to the inner-pipe internal diameter of 34mm. The thickness of the inner-pipe was also optimized to provide adequate heat transfer resistance to protect the low temperature combustion reaction from quenching. The thickness of 3mm was adopted based on the thermal properties of the selected material for the inner pipe from the results of preliminary simulations. The outer-pipe surface area was determined based of the heat transfer rate requirements. This was related to the velocity of the exit gases that transferred their heat through convection as well as the outer-pipe temperature (load). The detailed parameters of the geometry were presented in Appendix N.

5.3 Oxygen Permeation Flux

The oxygen permeation across the BSCF membrane was modeled by considering the fuel stream (CO_2) as sweep gas to convey the permeate and (CH_4+CO_2) as sweep to react with the permeate, this was categorized into non-reactive and reactive conditions, respectively. In the non-reactive conditions, the fuel stream acted as a sweep gas only, in order to investigate the OTM permeation capabilities under several operating conditions. In the reactive conditions, the volumetric reaction model was used to simulate the species combustion reaction at the sweep zone. The oxygen permeation due to the two categories were presented in Figures 5.4 to 5.8, under different conditions. The dependence of oxygen permeation flux on the membrane temperature has been fully established by many researchers where they fixed the membrane temperatures at elevated levels to improve permeation. But in practical applications, supplying the gases at elevated temperatures is more realistic. Hence, the inlet temperatures of the gases were varied to obtain an optimum temperature matrix for effective applications in both non-reactive and reactive conditions. Similarly, the effects of sweep and feed inlet mass flow rates as well as the diluent mass fractions were parametrized for the reactor optimization. These effects were presented in the subsequent sections.

5.3.1 Effect of gases inlet temperature on O_2 permeation flux

The influence of feed and sweep inlet temperatures on the oxygen permeation flux across the OTM are shown in Figure 5.4 for both the non-reactive and reactive conditions. As for the non-reactive conditions shown in Figure 5.4-i, the effect of inlet temperature was considered for the fixed gases inlet mass flow rates of 5E-4 kg/s based on an optimized near stoichiometric mixture condition. In Figure 5.4-i(a), the sweep gas inlet temperature was fixed also at 900^{o}C, while the feed gas (air) temperatures were varied from 800-1000^{o}C. The oxygen permeation along the length of the membrane varied exponentially at all the feed inlet temperature conditions. The maximum permeations were observed at the sweep inlet due to the maximum oxygen partial pressure difference since there was no oxygen in the sweep stream, resulting the maximum driving force that led to maximum oxygen permeations. The oxygen permeation drops drastically near the inlets, along the membrane due to the increase in oxygen partial pressure at the sweep side which decreases the driving force. The oxygen partial pressure differences became nearly constant toward the trailing edge of the membrane. The higher the feed inlet temperature the higher the oxygen permeation flux, despite the little variations. This was attributed to the increase in partial pressure difference of oxygen at elevated temperatures. This trend was observed when the feed inlet temperature was fixed at 900^{o}C while varying the sweep inlet temperatures as shown in Figure 5.4-i(b). The effect of the sweep inlet temperature resulted in slightly lower permeation in comparison to the feed effect. Even when both the feed and sweep gases inlet temperatures were varied sequentially (kept at the same value in each case), the oxygen permeation flux profiles along the OTM were similar. But the variations in permeation due to effect of temperature changes were more prominent.

The effect of inlet gases temperature on the oxygen permeation flux across the OTM for the reactive conditions are presented in Figure 5.4-ii. The oxygen permeation trend near the sweep inlet started with the maximum value due to the maximum oxygen partial pressure difference between the feed and sweep sides and decreases sharply within the first 10mm along the length of the OTM at all the inlet gas temperature conditions for the reactive cases. The oxygen permeation flux then suddenly shoots up after 10mm to another maximum value as the result of the initiation of the combustion reaction which caused high temperature release. The temperature elevation due to oxy-methane reaction reduces the membrane surface exchange resistance thereby increasing the oxygen permeation. The increase in temperature has been reported to be responsible for higher oxygen vacancies disorder [218-220]. The surge in the oxygen permeation was also attributed to the oxygen consumption during the reaction near the membrane surface in the permeate side thereby reducing the partial pressure of the oxygen which consequentially increases the oxygen permeation driving force across the OTM. These phenomena were observed when the inlet gas temperature was more than 850^{o}C for the feed, sweep and both, as shown in Figure 5.4-ii (a), (b) and (c), respectively. When the inlet gases were supplied at temperature range of 800-850^{o}C, the combustion reaction was quenched due to the low temperature within the combustion zone caused by the low temperature at the outer pipe. Hence the permeation profiles at lower temperature were similar to those discussed in the non-reactive conditions.

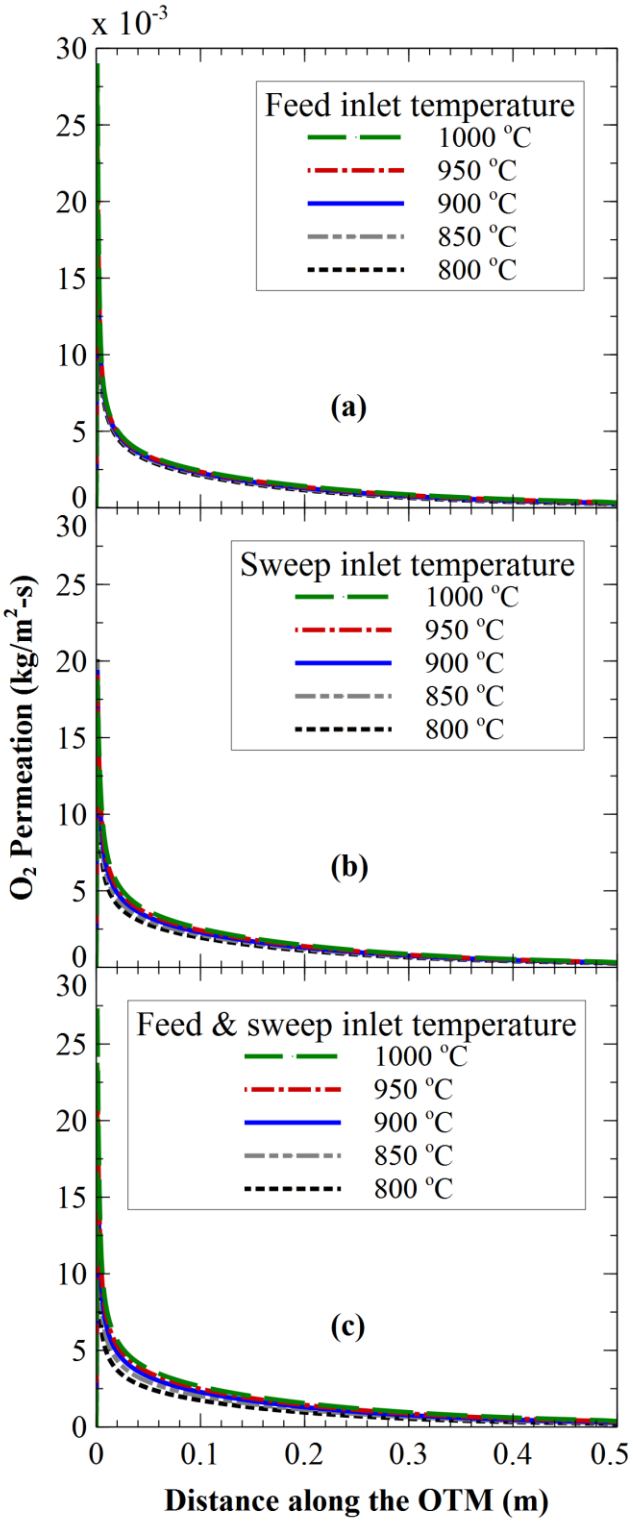

(i) Non-reactive case

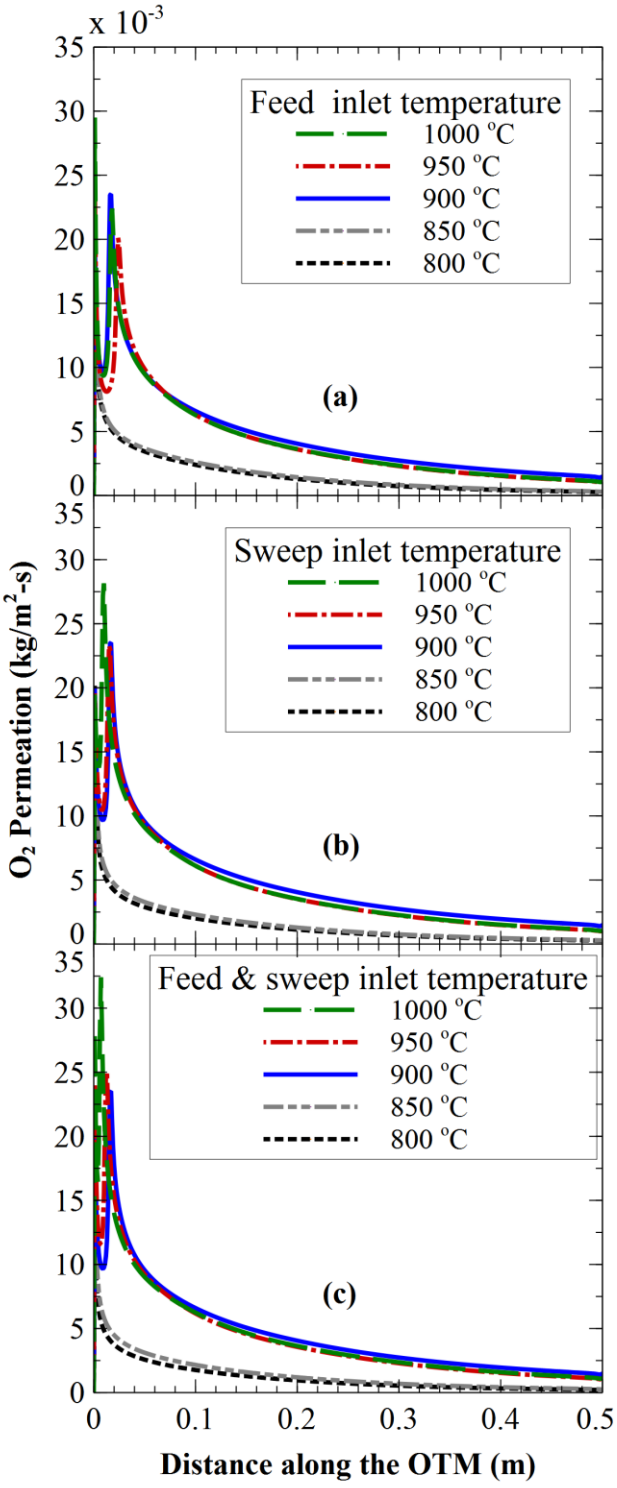

(ii) Reactive case

Figure 5.4: Effect of gas inlet temperature on the rate of O2 permeation flux across the OTM at an inlet gases flow rate of 5E-4 kg/s.

When the total oxygen permeation flux where computed for both the non-reactive and reactive conditions, as shown in Figure 5.5, the effect of gases inlet temperature were more distinct. The higher the gases inlet temperature the more the oxygen permeation rate for all the inlet conditions. As for the non-reactive case, at lower gas inlet temperatures (below 900^{o}C), there was slight increase in oxygen permeation rate for the case of feed inlet conditions compared to the sweep due to the higher constant temperature of the sweep side (900^{o}C) for the feed case which led to the increase in oxygen vacancies disorder. While at higher gas inlet temperatures (above 900^{o}C) the reverse was the case, the feed temperature effect became lower than that of the sweep due to the same oxygen vacancies disorder. When both the feed and sweep gases inlet temperatures were the same, there was lower oxygen permeation at temperatures below 900^{o}C and higher permeation above 900^{o}C due to the double effect. The same trends were observed as for the case of reactive conditions with the feed case providing higher oxygen permeation at lower temperatures and slightly lower permeations at higher temperatures. As shown earlier in Figure 5.4-ii, there was no combustion reaction influence at lower temperatures (below 900^{o}C) due to the low temperature effect.

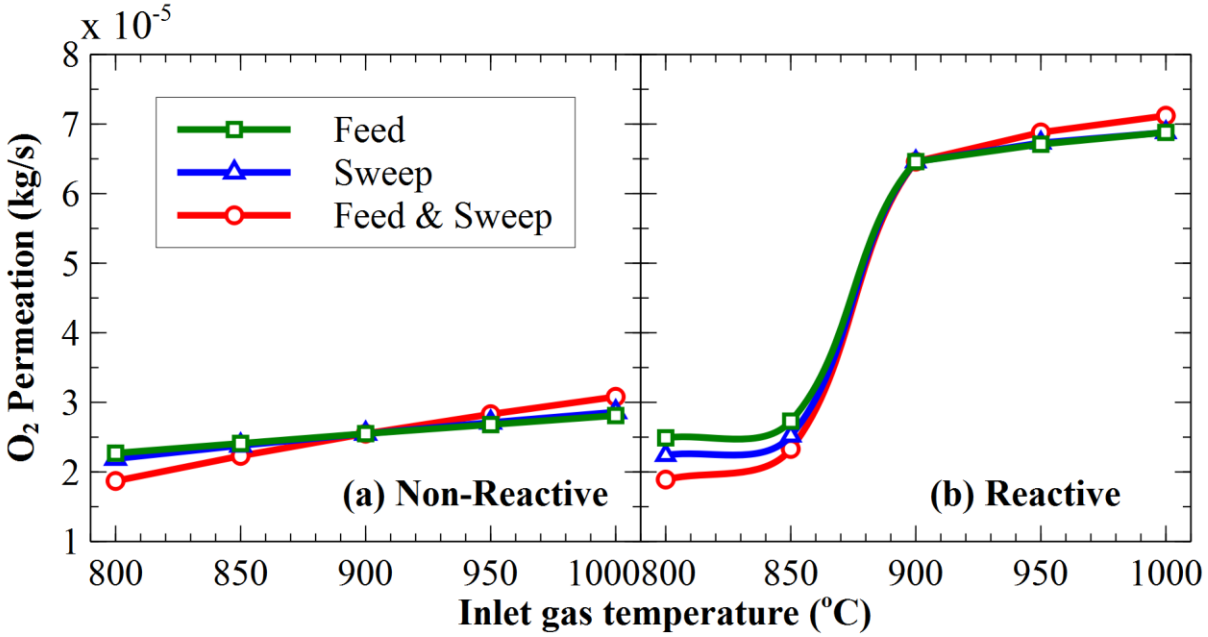

Figure 5.5: Effect of gases inlet temperature on the rate of O_2 permeation across the OTM at inlet gases flow rate of 5E-4 kg/s.

5.3.2 Effect of gases inlet mass flow rate on O_2 permeation flux

The trend of the O_2 permeation flux profiles for the effect of gas inlet mass flow rate across the OTM at an inlet gases temperature of 900°C are presented in Figure 5.6 for both the non-reactive and reactive conditions. The mass flow rates were varied from 1E-5 kg/s to 1E-3 kg/s in all cases. As for the non-reactive conditions as shown in Figure 5.6-i, the higher the gases inlet mass flow rates the higher the oxygen permeation flux in all the cases. Increasing the feed inlet mass flow rates resulted in lower value of the maximum oxygen flux at the beginning of the OTM as compared to increase in sweep gas flow rates. This due to the increase in oxygen vacancies at the membrane surface in the sweep side as the

result of higher sweep flow rates. The oxygen permeation flux drops drastically for all the non-reactive condition along the length of the OTM due to the increase in oxygen concentration in the sweep zone which reduces the magnitude of the driving force by increasing the oxygen partial pressure at the sweep side.

As for the reactive conditions as shown in Figure 5.6-ii, the effect of gas inlet mass flow rate on the oxygen permeation flux across the OTM were similar to the trends of the non-reactive cases at lower flow rates. When the feed gas inlet mass flow rate was considered the variable (Figure 5.6-ii(a)), while the sweep gas was kept at a fixed flow rate of 5E-4 kg/s and the inlet temperature of both inlet streams at 900^{o}C, there were increase in the oxygen permeation flux as the feed gas inlet mass flow rate increases at all the range of flow rates considered. The oxygen permeation at feed flow rates lower than 5E-4 kg/s resulted in insufficient oxygen fluence to support steady combustion due to high sweep flow rate and thermal dilution effect of the 95% CO_2 in the 5E-4 kg/s sweep flow rate. Hence, the combustion reaction was not sustained, leading to the permeation profiles becoming similar to the non-reactive counter-parts. The combustion reaction was sustained when the feed gas inlet flow rates reached 5E-4 kg/s with distinct oxygen permeation flux peak at the reaction zone as shown in Figure 5.6-ii(a). This was attributed to the increase in oxygen consumption at the reaction zone which generated more oxygen vacancies on the permeate side of the membrane that consequently derived more oxygen across the OTM. The temperature raise due to oxy-methane reaction also decreases the membrane surface exchange resistance thereby increasing the oxygen permeation. When the sweep gas inlet mass flow rate was made the variable by fixing the feed gas inlet mass flow rate

at 5E-4 kg/s, the oxygen permeation trends were similar to the feed case as shown in Figure 5.6-ii (b), but with highest combustion reaction intensity occurring at sweep gas inlet flow rate of 5E-4 kg/s. When the sweep gas inlet mass flow rate exceeded 5E-4 kg/s, its high velocity decreases the mixture residence time within the thermal protection zone (reaction zone) as well as further cooling the reaction zone due to the high content of the diluent thereby cooling the flame. This was also observed when both the feed and sweep inlet streams were kept at the same mass flow rates as shown in Figure 5.6-ii (c), but with lowest permeation at lower inlet mass flow rates due to the double effect.

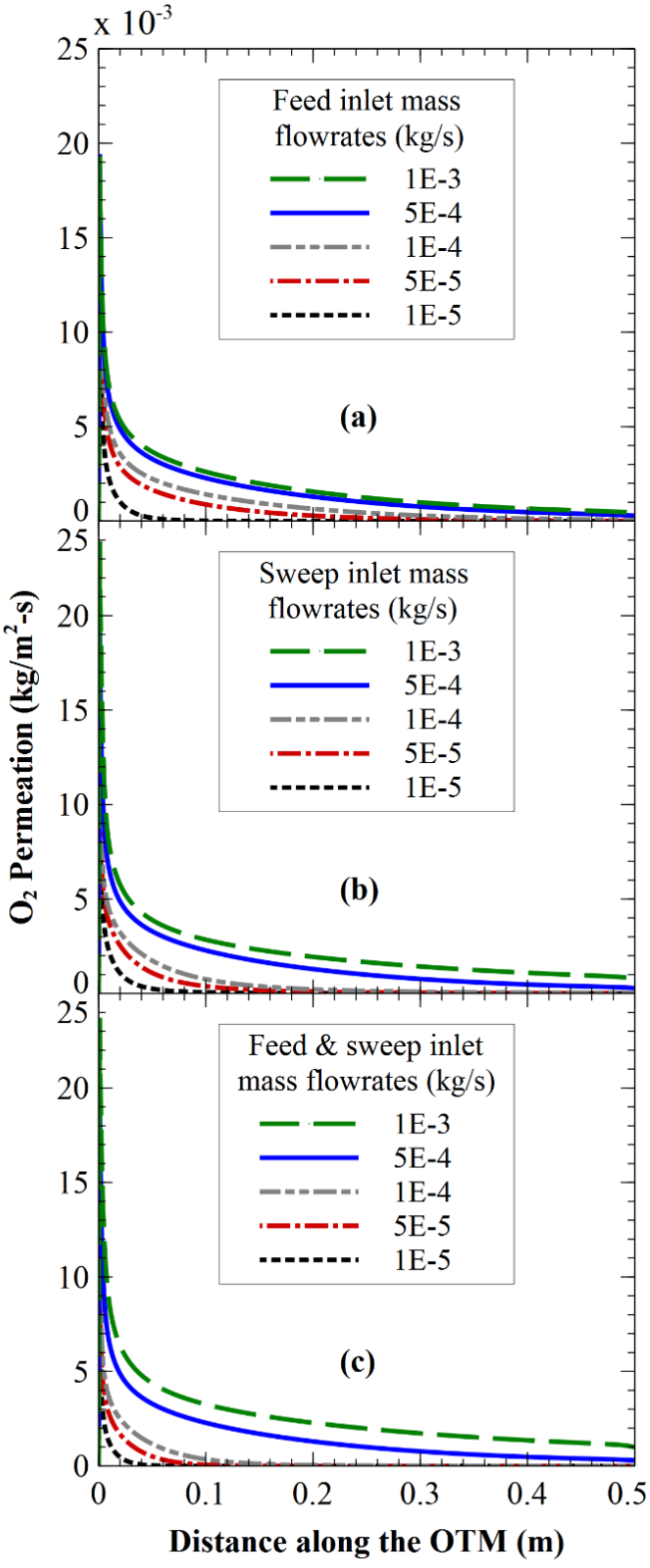

(i) Non-reactive case

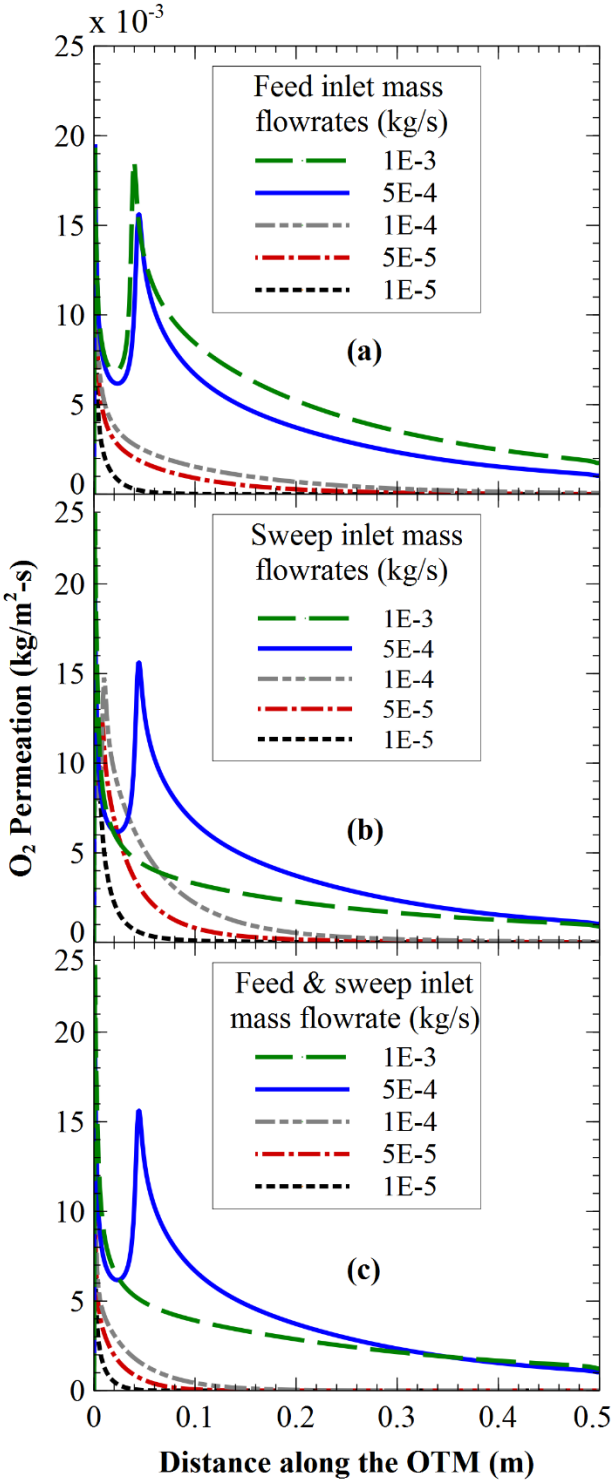

(ii) Reactive case

Figure 5.6: Effect of gas inlet mass flow rate on the rate of O_2 permeation flux across the OTM at an inlet gases temperature of 900 °C.

The effect of gases inlet mass flow rates on the total oxygen permeation flux for both the non-reactive and reactive conditions, were presented in Figure 5.7, for the three-inlet mass flow rate conditions. There was increase in the oxygen permeation rate due to increase in the inlet mass flow rate for all the inlet conditions when there was no reaction, as shown in Figure 5.7-a. This was due to the simultaneous decrease in oxygen partial pressure at the sweep side. At higher gases inlet mass flow rate, beyond 5E-4 kg/s, the effect of feed gas inlet temperatures provided higher oxygen flow rates due to the sustained combustion reaction. The higher sweep inlet mass flow rates exceeding 5E-4 kg/s resulted in lower oxygen permeation flux due to overwhelming sweep Reynolds number which lower the reaction zone temperature that quenched the flame. The oxygen permeation slightly increased when both the feed and sweep gases temperature were increased beyond 5E-4 kg/s.

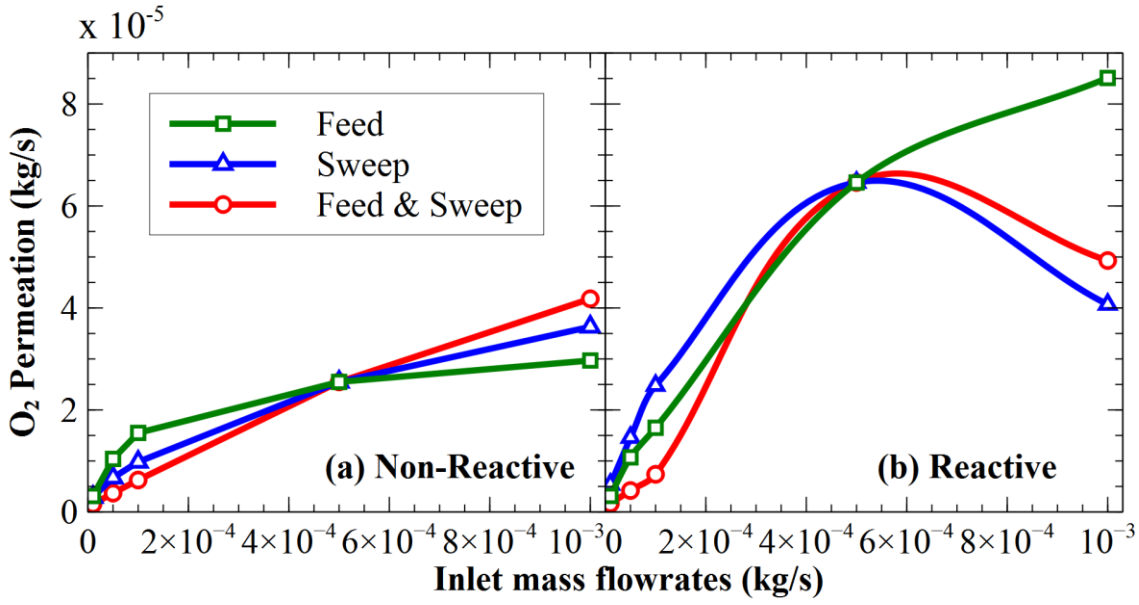

Figure 5.7: Effect of gases inlet mass flow rate on the rate of O_2 permeation across the OTM at inlet gases temperature of 900°C.

5.3.3 Effect of OTM thickness on O_2 permeation flux

The membrane thickness plays important role in the oxygen bulk diffusion resistance across it. Among the techniques of improving oxygen permeation of membranes is reducing the thickness thereby decreasing the diffusion resistance. Despite the selection of OTM thickness of 1 mm as the base case in this work due to its potential with respect to mechanical strength and sufficient oxygen fluence, in this section, the thickness of the OTM was varied from 0.8 to 1.2 mm to determine its influence on O_2 permeation at fixed inlet gases temperature and mass flow rate of 900^{o}C and 5E-4 kg/s, respectively. The results were obtained under both non-reactive and reactive conditions as presented in Figure 5.8. There was decrease in oxygen permeation with increase in OTM thickness as expected due to the increase in oxygen bulk diffusion resistance at larger thickness under both non-reactive and reactive conditions. The effect of the combustions reaction resulted in the increase in oxygen permeation by more than 150% as compared to the non-reactive counterparts due to the increase in the temperature at the sweep side. The decrease in the rate oxygen permeation at membrane thickness of 1mm as compared to 0.8mm was less than 2% under reactive condition and less than 3% under non-reactive condition.

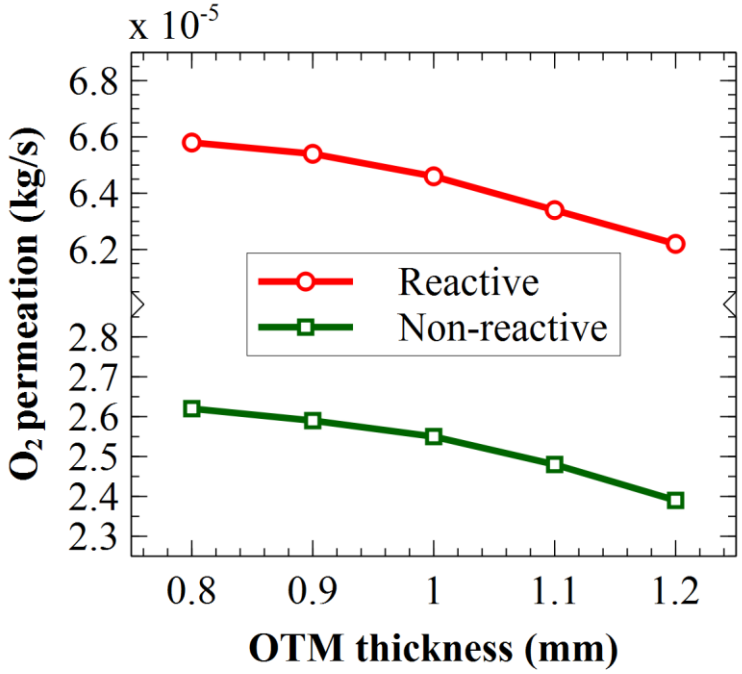

Figure 5.8: Effect of OTM thickness on oxygen permeation at fixed gases inlet temperature and mass flow rates of 900ºC and 5E-4 kg/s, respectively.

5.4 OTR Heat Transfer Characteristics

5.4.1 Effect of gas inlet temperature on heat transfer

The oxy-methane combustion effects on the heat transfer to the outer-pipe (load) are presented in this section with focus on the effects of inlet gas temperature for constant feed and sweep inlet gases mass flow rate of 5E-4 kg/s. These include both the convection and radiation components to evaluate the total heat transfer to the load. Figure 5.9 shows the effect of gas inlet temperatures on heat transfer to the load at fixed inlet gases mass flow rate of 5E-4 kg/s for (a) feed, (b) sweep and (c) combined feed and sweep. The dash-dot line represents the convection component of the heat transferred to the load, the dash line represents the radiation component while the solid line is the total heat transferred to the load. As for Figure 5.9-a, the sweep gas inlet temperature was kept constant at 900^{o}C while the feed gas inlet temperatures were varied from 800 – 1000^{o}C. The convection, radiation and the total heat transfers were found to increase with increase in the feed gas inlet temperature. At lower feed inlet temperatures (800 – 850^{o}C) the convective heat transfer rates was less than 180W, which swiftly increase to about 310 W at 900^{o}C. This heat transfer surge was as the result of the combustion reaction that was sustained at 900^{o}C below which there was no significant reactions. The same heat transfer behavior was observed for the case of radiation heat transfer but the increase in the heat transfer rate was more than that of the convection heat transfer due to the high radiative emissivity of both the outer surface of the inner-pipe and the inner surface of the outer-pipe. The total heat transferred to the load was also replicated the same trend since it is the summation of the

two. Hence the radiative heat transfer accounted for about 67-69% of the total heat transferred to the load while convection component was about 31-33%.

When the feed gas inlet temperature was maintained at 900^{o}C while the sweep gas inlet temperature was parameterized from 800 – 1000^{o}C, the heat transfer profiles were shown in Figure 5.9-b. The heat transfer profiles were similar to the case of variable feed gas inlet temperatures discussed earlier. In comparison to the feed gas inlet temperature conditions, the convective heat transfer values were higher at lower sweep gas inlet temperatures due to and lower heat transfer values at higher sweep temperatures in. Likewise, the radiation heat transfer values were lower at lower sweep gas inlet temperatures and higher at higher sweep gas temperatures as compared to the feed counterparts. The lower heat transfer at lower sweep temperatures were attributed to the lower thermal energy content of the reaction zone mixture as compared with the feed case since there were no reaction. The higher heat transfer at higher sweep inlet gas temperatures was ascribed to the thermal energy release during the combustion reaction. The convective heat transfer at lower sweep inlet temperatures were slightly higher than that of the feed case due to the sweep gas temperature effect and lower at high sweep gas inlet temperatures due to the lower feed gas temperature. Nevertheless, the increase in the rate of heat transfer due to the gas inlet temperature effects were barely trivial (~ 1 W) for both non-reactive and reactive situations. The effect of maintaining the feed and sweep gases at the inlet temperatures as shown in Figure 5.9-c, were almost the same as the effect sweep gas (Figure 5.9-b). This indicated that the heat transfer rates were merely dictated by the sweep gas inlet temperatures.

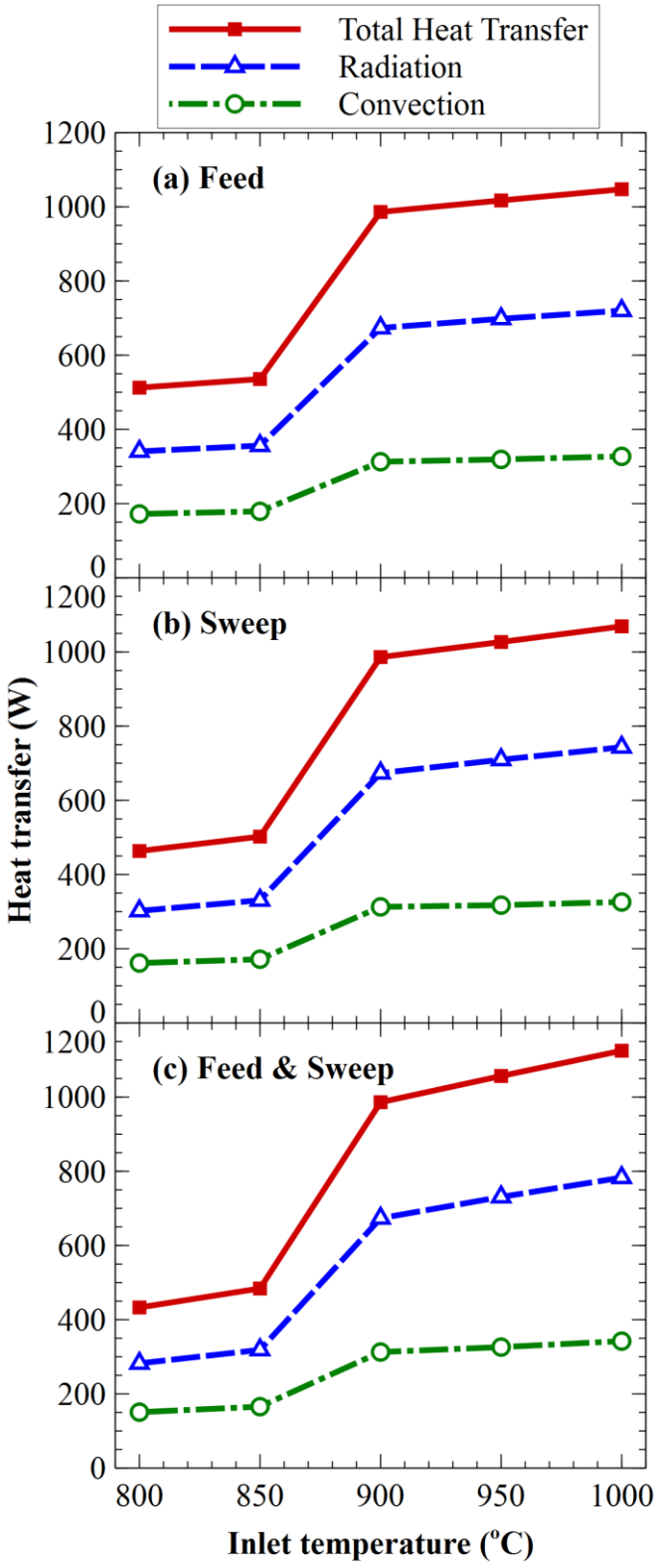

Figure 5.9: Effect of gas inlet temperatures on heat transfer to the outer-pipe (load) at inlet gases mass flow rate of 5E-4 kg/s.

5.4.2 Effect of gas inlet temperature on combustion heat transfer

The contribution of the combustion heat released, and the gases initial inlet thermal heat were shown in Figure 5.10 for the three gas inlet temperature conditions. These were evaluated based on the energy balance across the OTR boundaries. The heat transfers were assumed to be at steady state conditions thereby neglecting the heat required to preheat the inner-pipes. This enabled the assessment of combustion component of the overall heat transferred to the load. In all the three conditions examined in this part (Figure 5.10, a-c), the combustion heat contribution at inlet gas temperatures below 900^{o}C was insignificant due to the flame quenching at steady state. Hence, all the heat transferred to the load were mainly via the inlet gases heat contents. This can be seen in Figure 5.10 were the inlet gas component overlapped with the total heat transferred to the load while the combustion heat transferred was merely zero. There were roughly equal contributions between the combustion heat transferred and the gas inlet thermal heat transferred when all the gases were supplied at 900^{o}C. This was depicted by the coincidence of both the heat transfer components at the same values, as shown in Figure 5.10. When the gases inlet temperatures were beyond 900^{o}C, the combustion component of the heat transferred to the load increases with increase in gas temperatures due to the increase in the overall combustor energy level while the inlet contribution decreases at all the three conditions.

At feed inlet gas temperatures beyond 900^{o}C, while the sweep gas inlet temperature was kept constant at 900^{o}C (Figure 5.10-a), the amount of combustion heat transferred to the load was lower than the heat transferred for the sweep gas cases (Figure 5.10-b). This was

due to the fact that increasing sweep gas inlet temperature led to more heat transfer attributable to the increase in both convection and radiation. When both the feed and sweep gas inlet temperatures where varied, as shown in Figure 5.10-c, there were much higher increase in the amount of heat transferred to the load as compared to the individual streams, beyond 900^{o}C. This was correlated to the increase in both convection and radiation heat transferred as the result of higher energy level of the OTR. As for the gases inlet heat contributions, the sweep gas effect contributed the most as compared to the feed effect, this was due to direct contact of the sweep gas with the outer-pipe which aided the heat transfer.

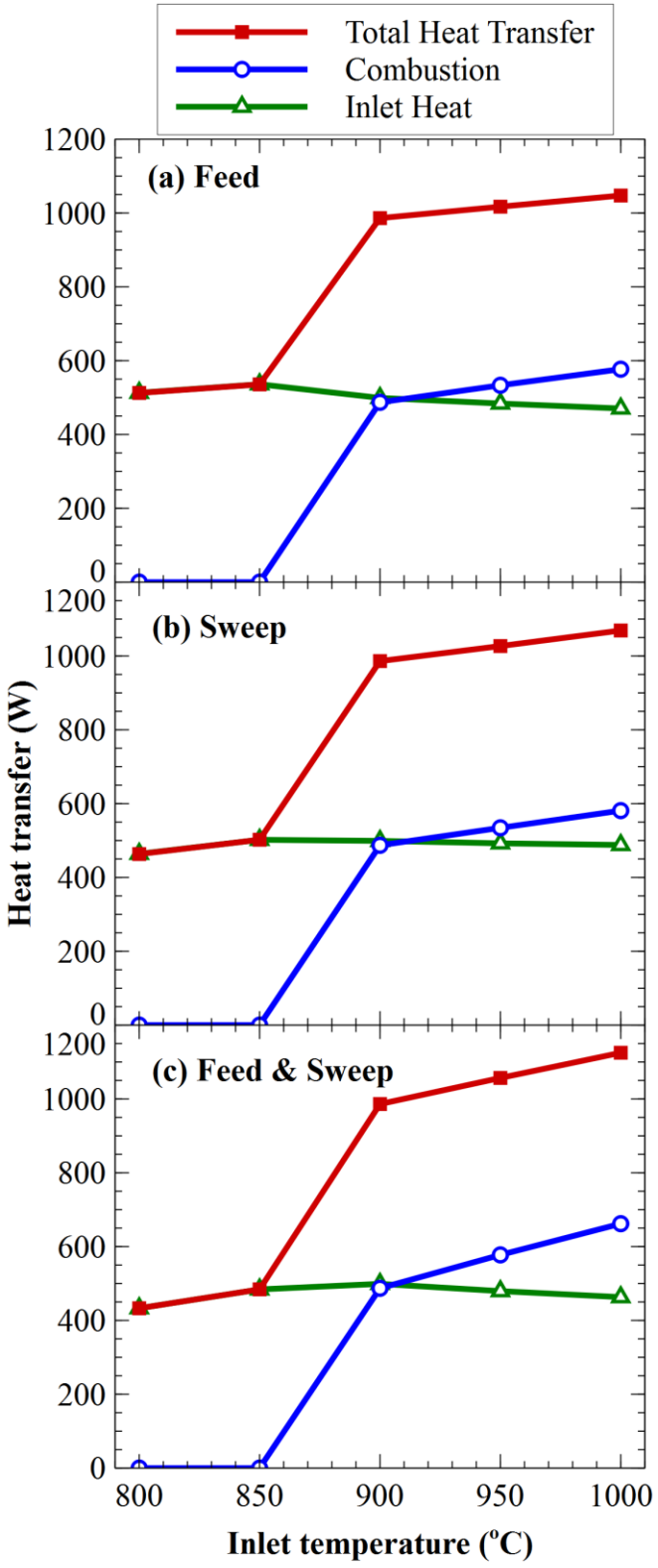

Figure 5.10: Effect of gas inlet temperatures on combustion heat transfer to the outer-pipe at inlet gases mass flow rate of 5E-4 kg/s.

5.4.3 Effect of gas inlet mass flow rate on heat transfer

The effect of gas inlet mass flow rates on heat transfer to the outer-pipe (load) at fixed inlet gases temperature of 900^{o}C while varying the mass flow rates from 1E-5 to 1E-3 kg/s for (a) feed, (b) sweep and (c) feed and sweep conditions were studied in this section and the results were presented in Figure 5.11. As for the condition whereby, the feed gas inlet mass flow rate was varied from 1E-5 to 1E-3 kg/s while keeping the sweep gas inlet mass flow rate constant at 5E-4 kg/s indicated increase in both convection and radiation heat transferred to the load consequently increased the total heat transferred as the feed gas mass flow rate was increased, as shown in Figure 5.11-a. This increase was meager at low feed flow rates (1E-5 to 1E-4 kg/s) due to lack of combustion reaction but surged afterwards as the result of the chemical energy released during combustion reaction. In a similar fashion with the effect of feed gas inlet temperatures, the radiation component of the total heat transferred was twice that of convection heat transferred at all the feed gas inlet flow rates. This is due to the radiative properties of the CO_2-rich exhaust gas mixture as well as the high emissivity of the inner radiating surfaces in contrast to the convective heat transfer coefficient of the same mixture. At feed gas inlet mass flow rate of 5E-4 kg/s, the total heat transferred was about 1000W out of which 68% was by radiation. This increased to about 1150 W at feed gas inlet flow rate of 1E-3 kg/s.

The effect of sweep gas inlet mass flow rates on the heat transfer to the load at fixed feed gas inlet mass flow rate of 5E-4 kg/s, were presented in Figure 5.11-b. Under this condition, the rate of heat transfer at low sweep flow rates were less than that of the feed case with

convection component being below 80 W, radiative component below 270 W and the total heat transferred was below 340 W, even at sweep gas inlet mass flow rate of 1E-4 kg/s. This was due to the low thermal energy content of the sweep gas at low flow rates (< 5E-4 kg/s) since there was no combustion reaction at these conditions. It was interesting to note that the maximum radiative and total heat transferred to the load occurred at sweep gas inlet mass flow rates of 5E-4 kg/s, as shown in Figure 5.11-b, beyond which the they decreased. Meanwhile the convection heat transferred continued to increase with increase in the sweep gas inlet mass flow rates. The decrease in the radiative heat transfer when the sweep gas inlet mass flow rate exceeded 5E-4 kg/s, was attributed to the low reactivity of the mixture due to low residence time within the thermal protection zone (reaction zone) as well as further cooling the reaction zone due to the high content of the diluent. This phenomenon was also observed when both the feed and sweep inlet streams were kept at the same mass flow rates as shown in Figure 5.11-c, but with slight improvement in the radiative heat transferred at higher sweep gas flow rate due to the feed effect. This indicated that the sweep gas inlet mass flow rate is among the most decisive controlling parameters in the total heat transfer to the load.

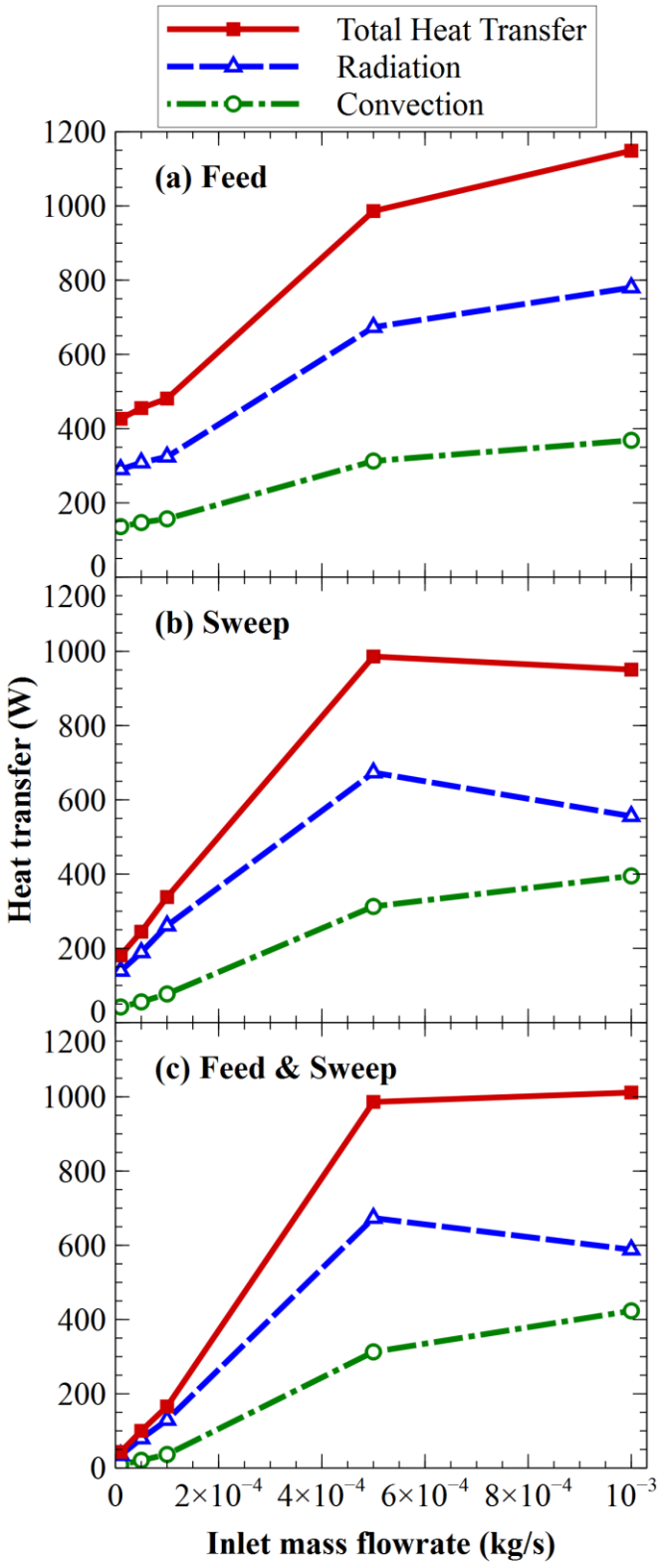

Figure 5.11: Effect of gas inlet mass flow rates on heat transfer to the outer-pipe (load) at inlet gases temperature of 900 ºC.

5.4.4 Effect of gas inlet mass flow rate on combustion heat transfer

Figure 5.12 shows the effect of gas inlet mass flow rates on combustion heat transfer and the gases inlet thermal heat transferred to the load at constant inlet gases temperature of 900 ^{o}C while varying the mass flow rates from 1E-5 to 1E-3 kg/s for (a) feed, (b) sweep and (c) feed and sweep conditions. As we have seen in the previous discussions, the contributions of the chemical heat released during combustion was negligible at low flow rate feed gas inlet mass flow rates between 1E-5 to 1E-4 kg/s as shown in Figure 5.12-a. The inlet thermal heat contributed to all the heat transferred (426 to 455 W) to the load. Although there was slight increase in the inlet gas thermal heat transferred of about 30 W when the feed gas inlet mass flow rate was increased to 5E-4 kg/s, the combustion reaction contributed almost equivalent rate of heat transfer at steady state. Hence the total heat transfer was elevated to about 1000 W as the result of the double effect. There was increase in the combustion heat transfer due to increase in the feed gas inlet mass flow rate beyond 5E-4 kg/s due to the increase in the oxygen permeation resulting in increased oxy-fuel reaction which raised the OTR overall thermal energy. The inlet gas thermal heat contribution slightly decreased but remained relatively constant despite the increase in the feed gas flow rate.

Figure 5.12-b depicted the effect of sweep gas inlet mass flow rate variations at fixed feed gas inlet mass flow rate of 5E-4 kg/s on the combustion heat transfer to the load. From the results, there were limited combustion reactions at low sweep gas inlet mass flow rates as indicated by low combustion heat transfer contributions which increases with increase in

the sweep gas flow rate to the maximum at 5E-4 kg/s. It was affirmed that there was no combustion reaction at sweep gas inlet mass flow rate of 1E-3 kg/s due to zero combustion contribution. The gases inlet heat transferred to the load was proportional to the increase in the sweep gas flow rate due to the increase in the rate specific energy of the sweep gas. There was almost no combustion reaction when both the feed and sweep gases flow rates were fixed between 1E-5 to 1E-4 kg/s due to insufficient oxygen permeation flux to sustain steady reaction, as shown in Figure 5.12-c. The only mass flow rate condition that sustained steady combustion was when both the gas streams were at 5E-4 kg/s. The combustion reaction was extinguished at 1E-3 kg/s of both the streams due to the flow speed overwhelming the laminar flame speed.

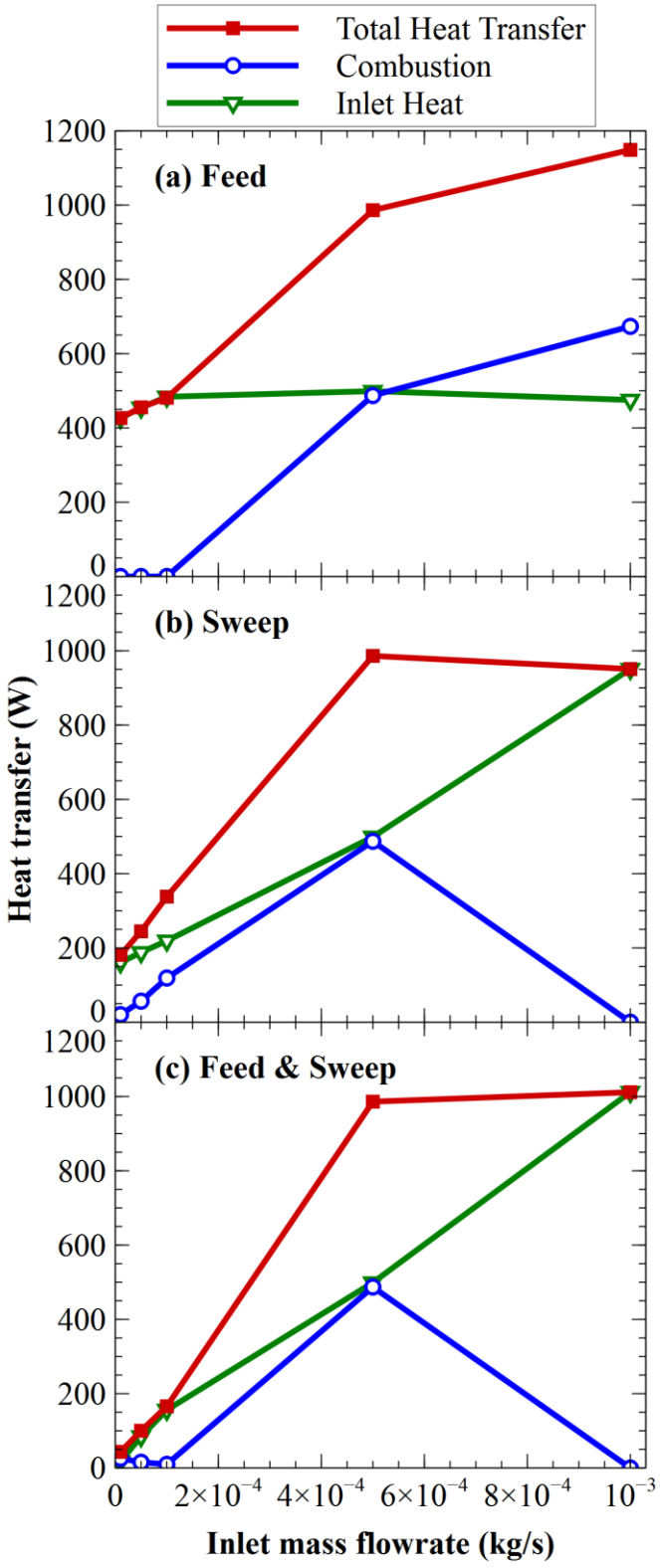

Figure 5.12: Effect of gas inlet mass flow rates on combustion heat transfer to the load at inlet gases temperature of 900 ºC.

5.4.5 Effect of outer-pipe surface condition on heat transfer

The proposed OTR fire tube boiler was intended to deliver saturated steam at pressure and temperature typical to the conventional fire-tube boilers. This saturation condition at the outer-pipe of the OTR is the load expected to be delivered at steady state operation. Hence, the saturation pressure range of 10-50 bars (corresponding to saturation temperatures of 453-537 K) were studied to determine the effect of oxy-fuel combustion characteristics on the deliverability of the expected load. To isolate the effect of the load on the combustion characteristics, a base case was considered in which both the feed and sweep gases were maintained at fixed inlet mass flow rate and temperature of 5E-4 kg/s and 900^{o}C. This set of conditions (base case) was demonstrated to be the most promising optimum condition to deliver the load at 10 bar and 453 K, based on the previous analyses. Hence, the load was increase from 10 to 50 bar and the heat transferred to the load at these conditions were studied as presented in Figure 5.13. There was slight increase in heat transferred through radiation and more decrease in convection heat transfer due to the increase on the outer-pipe surface temperature at fixed reactor firing rate. Apparently, the total heat transferred to the load decreases by only about 2% at 50 bar. Therefore, the load has insignificant effect on the heat transfer at fixed fuel firing rate.

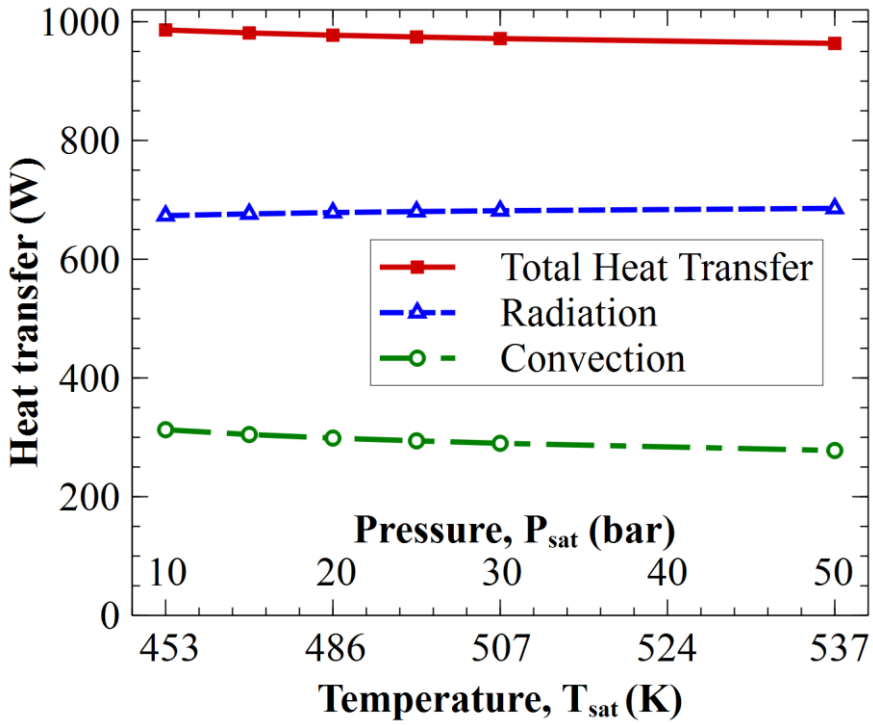

Figure 5.13: Effect of outer-pipe surface condition (saturation temperature and pressure of steam) on heat transfer at base case condition.

5.4.6 Effect of outer-pipe surface condition on combustion heat transfer

The combustion contribution of the total heat transferred to the load while varying the load at the base case condition were evaluated as shown in Figure 5.14. The dotted-line represents the oxygen permeation at the varying load conditions. There was equivalent contribution between the combustion heat transferred and the gas inlet heat transferred at 10 bar beyond which the combustion component decreases at higher loads. The decrease in combustion heat transferred was about 16% at 50 bar attributed to the increase in oxygen

permeation which consequentially acted as diluent that lower the reaction zone temperature. This excess oxygen was also responsible for increase in the inlet heat transfer at higher load up to about 11% at 50 bar. Effectively, the thermal energy level of the outer-pipe (load) affects the rate of combustion heat transferred to the load due to increase in oxygen permeation.

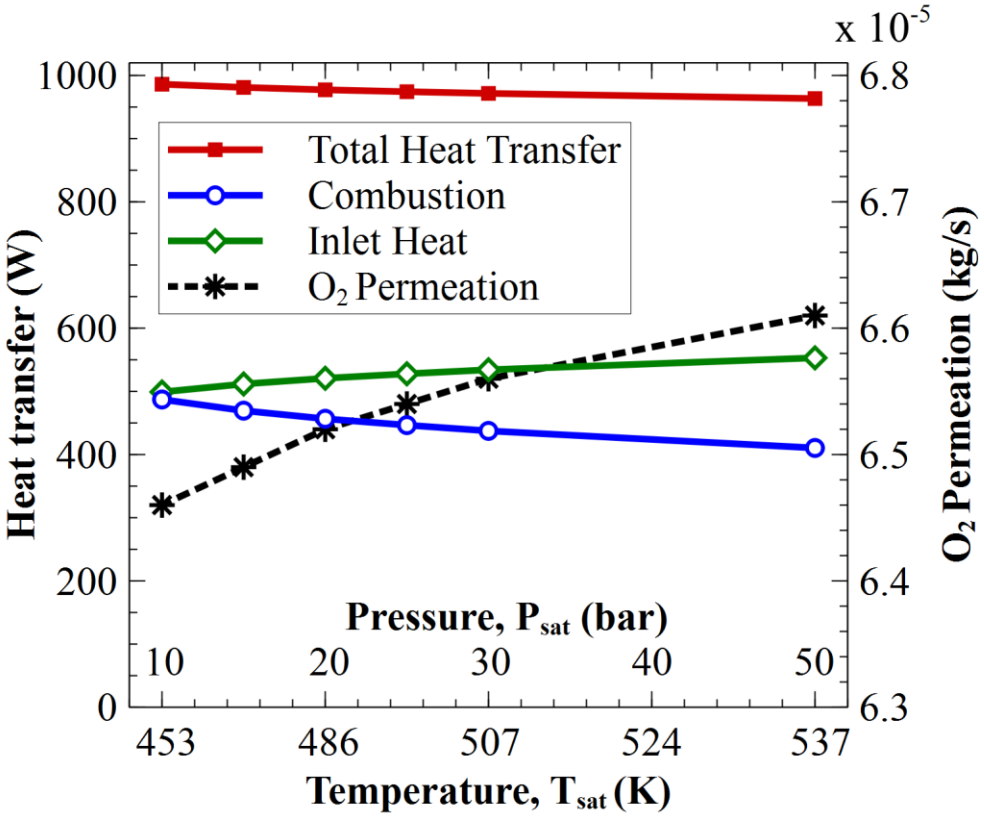

Figure 5.14: Effect of outer-pipe surface condition on combustion heat transfer at base case condition.

5.4.7 Effect of inner-pipe emissivity on heat transfer

The dominant heat transfer mode to the load of this OTR design was principally by radiation from the outer surface of the inner-pipe as well as the flue gas mixture to the inner surface of the outer-pipe. Hence, optimization of the radiative properties of the OTR tubes to maximize the heat transfer to the load was worthwhile. In this section, the effects of inner-pipe surface emissivity on the heat transfer to the load with the outer-pipe fixed at emissivity of 0.95 were presented in Figure 5.15. The inner-pipe emissivity was varied from 0.1 to 1 under fixed feed and sweep inlet gases temperature and mass flow rates of 900^{o}C and 5E-4 kg/s respectively and constant load corresponding to 10 bar. The total heat transferred to the load slightly decreases as the emissivity of the inner-pipe increases up to the emissivity of 0.95 after which the heat transferred decreased drastically at emissivity of 1, as shown in Figure 5.15. There was maximum heat exchange between the low temperature outer-pipe and the reaction zone via the inner-pipe which resulted in lowering the flame zone temperature that extinguished the combustion reaction at steady state. Meanwhile, the maximum decrease in total heat transferred to the load up to inner-pipe emissivity of 0.95 was less than 3%. The radiation heat transferred increases with increase in emissivity up to the point of sustained combustion reaction (up to emissivity of 0.95), while the convection heat transfer decreases with increase in the emissivity to the flame limit.

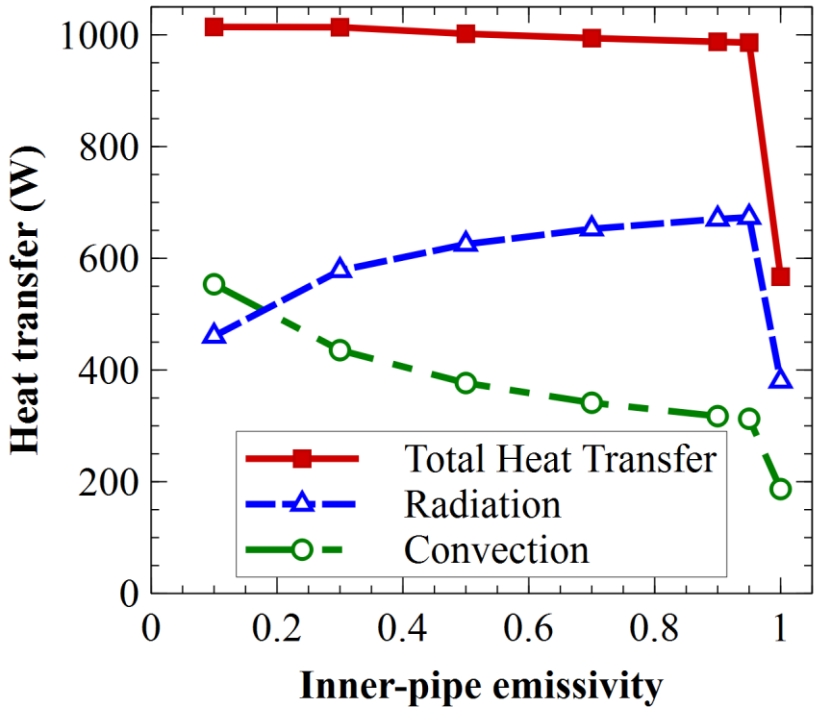

Figure 5.15: Effect of inner-pipe surface emissivity on heat transfer at base case condition.

5.4.8 Effect of inner-pipe emissivity on combustion heat transfer

Figure 5.16 shows the effect of inner-pipe surface condition on combustion heat transfer at the base case condition. The combustion contribution was highest at the lowest inner-pipe emissivity and decreases with the increase in emissivity. This was due the low heat exchange across the inner-pipe at low emissivity which protects the combustion zone from the low temperature of the outer-pipe. At higher emissivity, the rate of heat transfer across the inner-pipe increases which consequently lower the combustion zone temperature which resulted in decrease in the heat transfer to the load. This can also be substantiated by considering the trend of oxygen permeation with respect to the increase in emissivity of

the inner-pipe. The oxygen permeation decreases in a similar fashion with the combustion heat transfer. This indicates that the OTM was experienced higher temperature at lower emissivities which derived more oxygen as compared to higher emissivity cases with lower combustion temperatures. The inlet heat contribution increases with increase in the pipe emissivity which compensate for the decrease in combustion to maintain the total heat transferred to be relatively constant. Also, at inner-pipe emissivity of 1, the combustion heat transfer was zero, the inlet heat contribution upsurge and the oxygen permeation dropped significantly which affirmed the quenching of the flame at steady state condition.

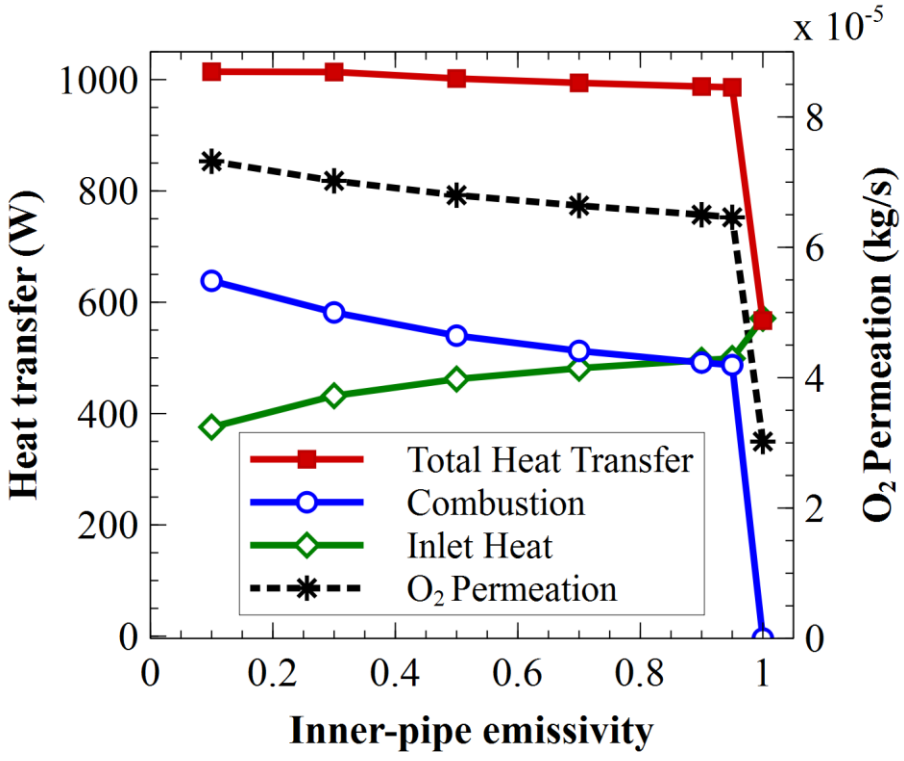

Figure 5.16: Effect of inner-pipe surface emissivity on combustion heat transfer at base case condition.

5.4.9 Effect of outer-pipe emissivity on heat transfer

The emissivity of the outer pipe also plays an important role in the amount of heat transfer to the load. To evaluate the influence of the outer-pipe emissivity on the heat transfer, the inner-pipe was fixed at emissivity of 0.95 and at base case conditions (feed and sweep inlet gases temperature and mass flow rates of 900 ^{o}C and 5E-4 kg/s respectively and constant load corresponding to 10 bar). The total heat transferred to the load remained relatively constant as the emissivity of the outer-pipe was varied from 0.1 to 0.95, beyond which the heat transferred reduced drastically at emissivity of 1, as shown in Figure 5.17. The decrease in the total heat transfer was attributed to the flame extinguishing at outer-pipe emissivity of 1 due to the excessive heat loss from the reaction zone to the outer-pipe which led to the cooling of the reaction zone at steady state. The radiation heat transferred increases with increase in the outer-pipe up to emissivity of 0.95, while the convection heat transfer decreases with increase in the emissivity to the flame limit and further dropped due to flame quenching at emissivity of 1. In general, the trend of the influence of the outer-pipe emissivity at base case condition on the heat transferred to the load was similar to that of the inner-pipe emissivity as described in section 5.4.7.

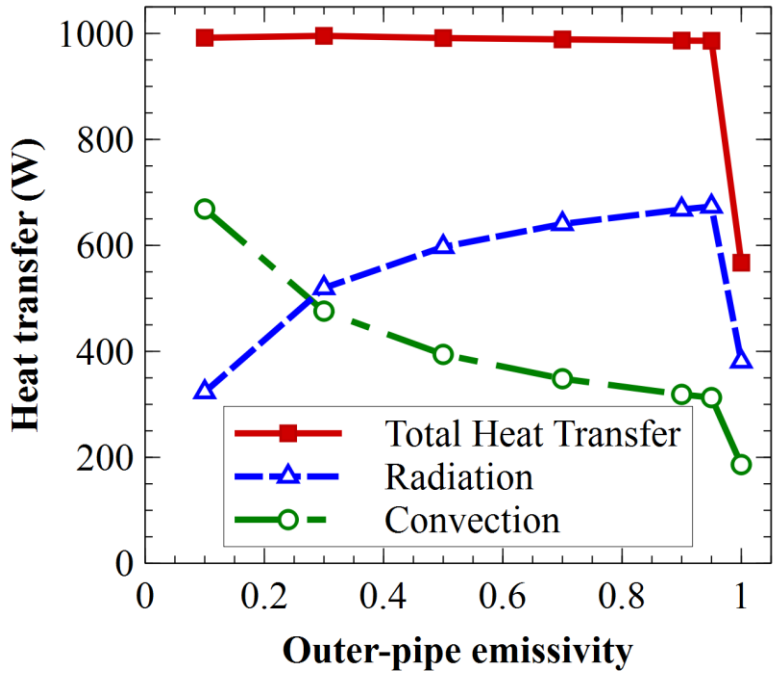

Figure 5.17: Effect of outer-pipe surface condition on heat transfer at base case condition.

5.4.10 Effect of outer-pipe emissivity on combustion heat transfer

The effect of outer-pipe surface emissivity on combustion heat transfer at the base case condition is shown in Figure 5.18. The trends were similar to those of the inner-pipe emissivity as described in section 5.4.8 with the combustion contribution being higher at the lower outer-pipe emissivity and decreases with the increase in the emissivity. The oxygen permeation as a function of the outer-pipe emissivity corroborated the effect of combustion heat transferred. There was no combustion contribution at outer-pipe emissivity of 1 due to the flame extinguishing. The inlet heat contribution also increases with increase in the outer-pipe emissivity. There was upsurge inlet heat contribution at inner-pipe emissivity of 1 due to lack of combustion reaction which also led to sudden decrease in oxygen permeation at steady state.

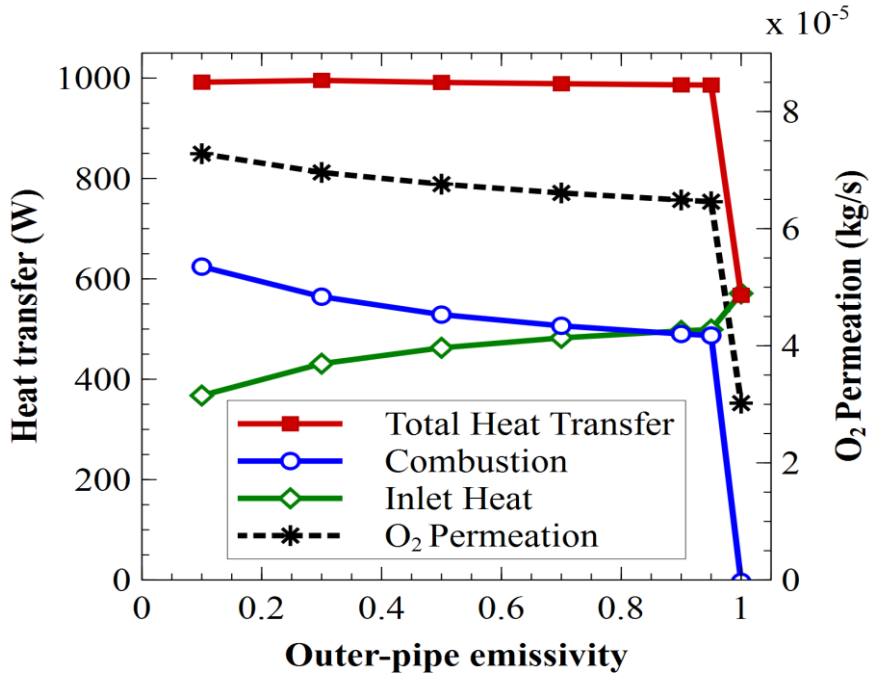

Figure 5.18: Effect of outer-pipe surface condition on combustion heat transfer at base case condition.

5.5 Number of OTR Units for Fire-Tube Boiler Application

The results of the total heat transfer to the load at base condition of the current design, a single unit of the OTR supplies about 1,000 W (1 kW), with combustion heat transfer contributing 50% of the total heat. To supply 1-5 MWe, there should be 1,000-5,000 units of the OTRs based on the total heat supply. By considering only the combustion component, there should be 2000-10,000 units of the OTRs. The current design of the OTR has an outer diameter of 0.05m and a nominal longitudinal distance of 0.505m. Hence, the total surface area of the 1mm membrane required will be 63.5-317 m^2 to deliver the required power output based on first law thermodynamic efficiency.

CHAPTER 6

CONCLUSIONS AND RECOMMENDATIONS

The present research study focused on experimental testing and numerical simulations of oxy-fuel combustion characteristics in a porous-plate reactor as well as numerical modeling of oxy-fuel combustion in oxygen transport reactor for fire-tube boiler applications. The work has been reported under two major categorizations: the two face-to-face porous plate reactors experimental and numerical analyses and the numerical modeling of the OTR. In the porous-plates reactor analyses, experimental and numerical modeling studies of the flow field and oxy-fuel combustion characteristics were conducted under non-reactive flow-field experimental analysis, 2D numerical modeling of the flow and combustion characteristics, hot experimental testing of oxy-fuel combustion, and 3D numerical modeling of oxy-fuel combustion. The non-reactive flow characteristics were investigated experimentally and numerically to predict the flow mixing behavior and the location of the flame zone. Among the non-reactive flow-field characteristics studied includes the velocity vectors, flow streamlines, velocity profiles, and average velocities at some chosen locations within the mixing zone using particle imaging velocimetry technique. Then, flow field and oxy-combustion characteristics of methane were investigated numerically over wide ranges of operating conditions. The non-reactive flow model was used for further analyses of the flow-field as well as oxy-methane combustion characteristics. The non-reactive flow setup was adjusted based on the previous results to cater for hot oxy-methane combustion.

The temperature distributions downstream of the combustor were measured and the flames shape were captured and analyzed. A 3D model was developed for the reactor and the results from the combustion experiments were used for the model validation. The flame structure, stability, temperature distributions were investigated using both the experimental studies and the numerical modeling while the exhaust emissions were numerically modeled. Methane was used as fuel and premixed with the diluent (CO_2) prior to the combustion zone inlet while pure O_2 was supplied to the combustion zone through the two face-to-face porous plates.

As for the numerical simulations of oxygen transport membrane reactor for application in fire tube boilers, a two-pass oxygen transport membrane reactor was considered for analyses of oxygen permeation and oxy-fuel combustion characteristics in order to replace the existing fire-tube burner with bundles of OTM combustors that will supply the required power range, from 1 to 5 MWe. The work involved geometry development for the required performance, oxy-methane characteristics analyses, and the effects of the key reactor controlling parameters such as effect of inlet gases temperatures and flow rates on the heat transfer to the saturated water and steam as the load in a fire-tube boiler, the effect of saturated water and steam condition on the OTR unit heat transfer and the effects of radiative properties of some of the reactor materials in order to obtain optimum operating conditions and parameters. The adopted reactor geometry was of cylindrical configuration with several concentric tubular OTRs. A single unit of the OTRs was considered for the analyses and model using 2D-axissymetry to reduce the intense computational cost for the solution.

6.1 Conclusions

A low-power porous-plate reactor has been used to study experimentally and numerically the flow field and oxy-fuel combustion characteristics over a range of operating equivalent ratio. The reactor was used to mimic the processes of oxygen permeation and oxy-combustion inside high-temperature membrane reactors (HTMRs). Numerical simulations supported by experiments have been conducted to investigate the flow behavior while oxygen permeation through the porous-plates under non-reactive flow conditions. Particle Imaging Velocimetry technique has been used to measure the average axial velocity of the main stream flow and to study the velocity vectors and the streamlines to visualize the effect of oxygen permeation on the velocity field. The experimental results were in good agreement with the results obtained from numerical simulation under the same conditions with absolute error of less than 4% deviation. It was found that enhanced mixing zone was created near the trailing edge of the porous plate affected by oxygen permeation. It was found that the higher the set equivalence ratio, the shorter the axial position where it is achieved, and the lower the mixture fraction. The set equivalence ratio was achieved locally downstream of the porous plates, which predicted the diffusion flame location downstream of the porous plates in the reactive flow. A linear relationship between the equivalence ratio and the axial position where it occurs was obtained. It was found that the higher the set equivalence ratio the shorter the axial position where it will be achieved and the lower the mixture fraction. Similarly, radial variations of mixture fractions and average equivalence ratio was found to increase towards the centerline of the combustion zone with maximum at the center.

The combustion simulations provided more clear insight of the oxy-combustion characteristics and the location of the flame inside the porous-plate reactor. The non-reactive flow predictions for locations of enhanced mixing zones and flame downstream of the porous plates were confirmed in the reactive flow from the distributions of species and temperature within the reactor. The creation of enhanced flow mixing zone beside the porous plate enhanced flame anchoring and stabilization. Location of the flame downstream of the porous plates helps protecting the membrane against high flame temperature in case of HTMR operation. The predicted temperature beside the porous plate lies within the operating limits of ceramic membranes which proves the applicability of HTMRs. Also, a hot zone was created through the entire length of the porous plate, which helps in keeping high oxygen flux of the membrane when the results are projected on HTMR operation.

The results from experimental studies of non-premixed oxy-fuel combustion characteristics in the porous plates reactor aimed at investigating the combustion characteristics and lean blow-out limits of oxy-methane diffusion flames over wide ranges of mixing conditions and equivalent ratios. Visual flame studies have been conducted to determine the flame shapes, length and luminous intensities at the slated operating conditions. It was found that addition of CO_2 elongates the normalized flame length. The flame luminous intensity was found to be decreasing with increase in CO_2 percentage in the mixture at all the equivalence ratios due to lower flame temperatures as the result of increase in the convection and radiation heat loss from the reaction zone. The temperature distributions measured at the combustor outlet were found to be radially parabolic and

longitudinally flattened at all stated conditions. The concentration of CO_2 in the oxidizer at lean blowout limit was found to be directly proportional to equivalence ratio with maximum percentage of 79% up to stoichiometric condition. Increasing the fuel firing rate at stoichiometric equivalence ratio resulted in the decrease in percentage of CO_2 in the oxidizer to instigate flame blowout.

The porous plates reactor was further studied by developing a 3D model of the reactor and the results from the combustion experiments were used for the model validation. The flame structure, temperature distributions were investigated using the numerical model and compared with the experimental results. There was good agreement between the experimental flame images with the numerical temperature contours. The numerical temperature contours at the center of the combustor depicted two flame sheets anchored to the upper and lower breadths of the fuel stream inlet section and elongated along the longitudinal axis of the combustor forming 'an inverted V' shape with average thickness of about 2mm and tip contact angle of about 15^o based on the current design. In general, there were good agreements between the experimental temperature measurements and the numerical results at all the conditions with the numerical results slightly overpredicting the experimental measurements. The maximum percentage difference between the experimental and numerical results were at pure oxy-methane combustion in which it reached up to about 14% at stoichiometric equivalence ratio, 11% and 13% at equivalence ratios of 0.5 and 0.7 respectively. This deviation might be attributed to imperfection of the temperature probe positioning during the measurements. For all percentages of CO_2 additions, the higher the equivalence ratio the higher the flame temperature due to increase

in the rate of reactivity as the result of increase in fuel percentage in the combustor. The higher the percentage of CO_2 added to the fuel stream, the lower the temperature downstream of the combustor due to the thermal dilution effect of the CO_2. Addition of the CO_2 in the mixture elongated the reaction zone due to increase in Reynolds number of the fuel stream. The exhaust gas was composed of five species, mainly CO_2, H_2O, CO, unburned CH_4 and excess O_2 which are the dominant species in the reduced chemical reaction kinetics model applied for the combustion modeling. While the O_2 mass fractions at the outlet decreases with increase in the percentage of CO_2 addition due to the overwhelming increase in CO_2 concentrations at the inlet, the CO concentration increased with CO_2 addition.

The numerical modeling of the two-pass oxygen transport membrane reactor for oxygen permeation and oxy-fuel combustion characteristics analyses for fire tube boilers application revealed that, for the non-reactive conditions, the effects of gases inlet temperature and mass flow rates on oxygen permeation along the length of the membrane were meager within the scope of this study. The gases inlet conditions dictate the rate of oxygen permeation under reactive conditions. The relationship between the membrane thickness and the O_2 permeations was inversely proportional under both reactive and non-reactive conditions. Also, the gases inlet temperature and mass flow rates control the amount of heat transfer to the load. The sweep gas inlet condition was more critical to the stability of the combustion reaction. The boiler operating condition modeled based on the thermal load has insignificant effect on the heat transfer at fixed fuel firing rate. The radiative properties of the OTR materials plays a major role in the total heat transfer to the load.

6.2 Recommendations

The first part of this work focused on low-power porous-plate reactor by experimentally and numerically studying the flow field and oxy-fuel combustion characteristics over a range of operating conditions. The second part was numerical simulations of a two-pass oxygen transport membrane reactor for fire tube boilers application. The following are some possible areas for future work based on the outcomes of this dissertation:

- The effect of geometric configuration of the porous plate combustor can be studied by considering other geometries such as cylindrical.
- The combustion flow field can be investigated using the particle imaging velocimetry for better understanding of the reaction field.
- There is very limited application of porous plate reactor in the open literatures, hence, more experimental and numerical works are required using different porous materials with different porosity.
- Detailed chemical reaction kinetics of the fuel can be employed to capture more detailed combustion characteristics.
- Other types of fuels can be employed such as LPG, Syngas, Liquid fuels, etc, in case of mobile applications.
- The operating range of the combustors should be expanded to ascertain the most critical operating conditions.
- The development of membrane technology is still progressing and the oxygen permeability as well as mechanical strength of the membranes is always being improved. Hence there is need for continuous research in the development of oxygen permeation model.

References

[1] J. D. Figueroa, T. Fout, S. Plasynski, H. McIlvried, and R. D. Srivastava, "Advances in CO 2 capture technology—the US Department of Energy's Carbon Sequestration Program," *International journal of greenhouse gas control*, vol. 2, pp. 9-20, 2008.

[2] G. Marland, T. Boden, R. Andres, A. Brenkert, and C. Johnston, "Global, regional, and national fossil fuel CO2 emissions," *Trends: A Compendium of Data on Global Change*, pp. 37831-6335, 2007.

[3] I. E. Agency. (2016). *World Energy Outlook*.

[4] D. Cebrucean, V. Cebrucean, and I. Ionel, "CO 2 Capture and Storage from Fossil Fuel Power Plants," *Energy Procedia*, vol. 63, pp. 18-26, 2014.

[5] I. E. Agency. (2016). *Technology Roadmap, Carbon Capture and Storage*.

[6] M. A. González-Salazar, "Recent developments in carbon dioxide capture technologies for gas turbine power generation," *International journal of greenhouse gas control*, vol. 34, pp. 106-116, 2015.

[7] R. M. Cuéllar-Franca and A. Azapagic, "Carbon capture, storage and utilisation technologies: A critical analysis and comparison of their life cycle environmental impacts," *Journal of CO2 Utilization*, vol. 9, pp. 82-102, 2015.

[8] B. Sreenivasulu, D. Gayatri, I. Sreedhar, and K. Raghavan, "A journey into the process and engineering aspects of carbon capture technologies," *Renewable and Sustainable Energy Reviews*, vol. 41, pp. 1324-1350, 2015.

[9] B. Singh, A. H. Strømman, and E. G. Hertwich, "Comparative life cycle environmental assessment of CCS technologies," *International journal of greenhouse gas control*, vol. 5, pp. 911-921, 2011.

[10] G. G. Zaimes and V. Khanna, "Microalgal biomass production pathways: evaluation of life cycle environmental impacts," *Biotechnology for biofuels*, vol. 6, p. 1, 2013.

[11] D. Jansen, M. Gazzani, G. Manzolini, E. van Dijk, and M. Carbo, "Pre-combustion CO 2 capture," *International journal of greenhouse gas control,* vol. 40, pp. 167-187, 2015.

[12] I. E. S. database. (2010, Projections: World Energy Projection System Plus

[13] J. Mletzko, S. Ehlers, and A. Kather, "Comparison of Natural Gas Combined Cycle Power Plants with Post Combustion and Oxyfuel Technology at Different CO 2 Capture Rates," *Energy Procedia,* vol. 86, pp. 2-11, 2016.

[14] R. Stanger, T. Wall, R. Spörl, M. Paneru, S. Grathwohl, M. Weidmann, G. Scheffknecht, D. McDonald, K. Myöhänen, and J. Ritvanen, "Oxyfuel combustion for CO 2 capture in power plants," *International journal of greenhouse gas control,* vol. 40, pp. 55-125, 2015.

[15] W.-Y. Chen, *Handbook of climate change mitigation*: Springer, 2012.

[16] T. Burdyny and H. Struchtrup, "Hybrid membrane/cryogenic separation of oxygen from air for use in the oxy-fuel process," *Energy,* vol. 35, pp. 1884-1897, 2010.

[17] T. Banaszkiewicz, M. Chorowski, and W. Gizicki, "Comparative analysis of oxygen production for oxy-combustion application," *Energy Procedia,* vol. 51, pp. 127-134, 2014.

[18] A. P. Simpson and A. Simon, "Second law comparison of oxy-fuel combustion and post-combustion carbon dioxide separation," *Energy Conversion and Management,* vol. 48, pp. 3034-3045, 2007.

[19] E. Kakaras, A. Koumanakos, A. Doukelis, D. Giannakopoulos, and I. Vorrias, "Oxyfuel boiler design in a lignite-fired power plant," *Fuel,* vol. 86, pp. 2144-2150, 2007.

[20] D. D. Athayde, D. F. Souza, A. M. Silva, D. Vasconcelos, E. H. Nunes, J. C. D. da Costa, and W. L. Vasconcelos, "Review of perovskite ceramic synthesis and membrane preparation methods," *Ceramics International,* vol. 42, pp. 6555-6571, 2016.

[21] R. S. Murali, T. Sankarshana, and S. Sridhar, "Air separation by polymer-based membrane technology," *Separation & Purification Reviews,* vol. 42, pp. 130-186, 2013.

[22] J. Caro and Y. Wei, "Ceramic Membranes with Mixed Ionic and Electronic Conductivity: Oxygen and Hydrogen Transporting Membranes–Synthesis, Characterization, Applications," *Membrane Reactor Engineering: Applications for a Greener Process Industry*, p. 75, 2016.

[23] X. Zhu, Q. Li, Y. He, Y. Cong, and W. Yang, "Oxygen permeation and partial oxidation of methane in dual-phase membrane reactors," *Journal of Membrane Science*, vol. 360, pp. 454-460, 2010.

[24] N. Mancini and A. Mitsos, "Ion transport membrane reactors for oxy-combustion–Part I: intermediate-fidelity modeling," *Energy*, vol. 36, pp. 4701-4720, 2011.

[25] P. N. Dyer, R. E. Richards, S. L. Russek, and D. M. Taylor, "Ion transport membrane technology for oxygen separation and syngas production," *Solid State Ionics*, vol. 134, pp. 21-33, 2000.

[26] L. Cai, W. Li, Z. Cao, X. Zhu, and W. Yang, "Improving oxygen permeation of MIEC membrane reactor by enhancing the electronic conductivity under intermediate-low oxygen partial pressures," *Journal of Membrane Science*, vol. 520, pp. 607-615, 2016.

[27] C. Moure and O. Peña, "Recent advances in perovskites: Processing and properties," *Progress in Solid State Chemistry*, vol. 43, pp. 123-148, 2015.

[28] O. Edenhofer, *Mitigation of climate change*: Cambridge University Press, 2014.

[29] V. Zaretskaya, "International Energy Outlook 2016 with Projections to 2040 (IEO2016). Chapter 3: Natural Gas," U.S. Energy Information Administration2016.

[30] M. Kanniche, R. Gros-Bonnivard, P. Jaud, J. Valle-Marcos, J.-M. Amann, and C. Bouallou, "Pre-combustion, post-combustion and oxy-combustion in thermal power plant for CO 2 capture," *Applied Thermal Engineering*, vol. 30, pp. 53-62, 2010.

[31] F. Lecomte, P. Broutin, and É. Lebas, *CO2 Capture: Technologies to Reduce Greenhouse Gas Emissions*: Editions Technip, 2010.

[32] R. Beavis, "The EU FP6 CACHET project-final results," *Energy Procedia*, vol. 4, pp. 1074-1081, 2011.

[33] R. Beavis, J. Forsyth, E. Roberts, B. Song, G. Combes, J. Abbott, N. Macleod, E. Vass, M. Davies, and I. Barton, "A step-change sour shift process for improving the efficiency of IGCC with CCS," *Energy Procedia*, vol. 37, pp. 2256-2264, 2013.

[34] M. K. Mondal, H. K. Balsora, and P. Varshney, "Progress and trends in CO 2 capture/separation technologies: a review," *Energy*, vol. 46, pp. 431-441, 2012.

[35] A. S. Bhown and B. C. Freeman, "Analysis and status of post-combustion carbon dioxide capture technologies," *Environmental science & technology*, vol. 45, pp. 8624-8632, 2011.

[36] F. Rezazadeh, W. F. Gale, M. Akram, K. J. Hughes, and M. Pourkashanian, "Performance evaluation and optimisation of post combustion CO 2 capture processes for natural gas applications at pilot scale via a verified rate-based model," *International journal of greenhouse gas control*, vol. 53, pp. 243-253, 2016.

[37] R. Steeneveldt, B. Berger, and T. Torp, "CO 2 capture and storage: closing the knowing–doing gap," *Chemical Engineering Research and Design*, vol. 84, pp. 739-763, 2006.

[38] R. Haghpanah, A. Majumder, R. Nilam, A. Rajendran, S. Farooq, I. A. Karimi, and M. Amanullah, "Multiobjective optimization of a four-step adsorption process for postcombustion CO2 capture via finite volume simulation," *Industrial & Engineering Chemistry Research*, vol. 52, pp. 4249-4265, 2013.

[39] S. Sircar and T. Golden, "Purification of hydrogen by pressure swing adsorption," *Separation Science and Technology*, vol. 35, pp. 667-687, 2000.

[40] S. Krishnamurthy, V. R. Rao, S. Guntuka, P. Sharratt, R. Haghpanah, A. Rajendran, M. Amanullah, I. A. Karimi, and S. Farooq, "CO2 capture from dry flue gas by vacuum swing adsorption: a pilot plant study," *AIChE journal*, vol. 60, pp. 1830-1842, 2014.

[41] S. J. Wilson, C. C. Beh, P. A. Webley, and R. S. Todd, "The effects of a readily adsorbed trace component (water) in a bulk separation PSA process: the case of oxygen VSA," *Industrial & Engineering Chemistry Research*, vol. 40, pp. 2702-2713, 2001.

[42] C. A. Grande and A. E. Rodrigues, "Propane/propylene separation by pressure swing adsorption using zeolite 4A," *Industrial & Engineering Chemistry Research,* vol. 44, pp. 8815-8829, 2005.

[43] J. Davison and K. Thambimuthu, "Technologies for capture of carbon dioxide," *Proceedings of GHGT,* vol. 7, pp. 5-9, 2004.

[44] D. Y. Leung, G. Caramanna, and M. M. Maroto-Valer, "An overview of current status of carbon dioxide capture and storage technologies," *Renewable and Sustainable Energy Reviews,* vol. 39, pp. 426-443, 2014.

[45] R. Kikuchi, "CO2 recovery and reuse in the energy sector, energy resource development and others: Economic and technical evaluation of large-scale CO2 recycling," *Energy & Environment,* vol. 14, pp. 383-395, 2003.

[46] S. Anderson and R. Newell, "Prospects for carbon capture and storage technologies," *Annu. Rev. Environ. Resour.,* vol. 29, pp. 109-142, 2004.

[47] J. J. Dooley, C. L. Davidson, and R. T. Dahowski, "An assessment of the commercial availability of carbon dioxide capture and storage technologies as of June 2009," *Pacific Northwest National Laboratory, US DOE,* 2009.

[48] W. Seifritz, "CO2 disposal by means of silicates," *Nature,* vol. 345, p. 486, 1990.

[49] S. C. Roy, O. K. Varghese, M. Paulose, and C. A. Grimes, "Toward solar fuels: photocatalytic conversion of carbon dioxide to hydrocarbons," *Acs Nano,* vol. 4, pp. 1259-1278, 2010.

[50] U. Desideri, L. Arcioni, and M. Tozzi, "Feasibility study for a carbon capture and storage project in northern Italy," *International Journal of Energy Research,* vol. 32, pp. 1175-1183, 2008.

[51] B. Van der Meer, "Carbon dioxide storage in natural gas reservoir," *Oil & Gas Science and Technology,* vol. 60, pp. 527-536, 2005.

[52] F. Gozalpour, S. Ren, and B. Tohidi, "CO2 EOR and storage in oil reservoir," *Oil & Gas Science and Technology,* vol. 60, pp. 537-546, 2005.

[53] C. M. White, B. R. Strazisar, E. J. Granite, J. S. Hoffman, and H. W. Pennline, "Separation and capture of CO2 from large stationary sources and sequestration in geological formations—coalbeds and deep saline aquifers," *Journal of the Air & Waste Management Association,* vol. 53, pp. 645-715, 2003.

[54] K. Sumida, D. L. Rogow, J. A. Mason, T. M. McDonald, E. D. Bloch, Z. R. Herm, T.-H. Bae, and J. R. Long, "Carbon dioxide capture in metal–organic frameworks," *Chemical reviews,* vol. 112, pp. 724-781, 2011.

[55] K. Michael, A. Golab, V. Shulakova, J. Ennis-King, G. Allinson, S. Sharma, and T. Aiken, "Geological storage of CO 2 in saline aquifers—a review of the experience from existing storage operations," *International journal of greenhouse gas control,* vol. 4, pp. 659-667, 2010.

[56] M. Habib, H. Badr, S. Ahmed, R. Ben-Mansour, K. Mezghani, S. Imashuku, Y. Shao-Horn, N. Mancini, A. Mitsos, and P. Kirchen, "A review of recent developments in carbon capture utilizing oxy-fuel combustion in conventional and ion transport membrane systems," *International Journal of Energy Research,* vol. 35, pp. 741-764, 2011.

[57] H. Mathekga, B. Oboirien, and B. North, "A review of oxy-fuel combustion in fluidized bed reactors," *International Journal of Energy Research,* 2016.

[58] B. Buhre, L. Elliott, C. Sheng, R. Gupta, and T. Wall, "Oxy-fuel combustion technology for coal-fired power generation," *Progress in energy and combustion science,* vol. 31, pp. 283-307, 2005.

[59] T. Wall, Y. Liu, C. Spero, L. Elliott, S. Khare, R. Rathnam, F. Zeenathal, B. Moghtaderi, B. Buhre, and C. Sheng, "An overview on oxyfuel coal combustion—state of the art research and technology development," *Chemical Engineering Research and Design,* vol. 87, pp. 1003-1016, 2009.

[60] M. B. Toftegaard, J. Brix, P. A. Jensen, P. Glarborg, and A. D. Jensen, "Oxy-fuel combustion of solid fuels," *Progress in energy and combustion science,* vol. 36, pp. 581-625, 2010.

[61] L. Chen, S. Z. Yong, and A. F. Ghoniem, "Oxy-fuel combustion of pulverized coal: Characterization, fundamentals, stabilization and CFD modeling," *Progress in energy and combustion science,* vol. 38, pp. 156-214, 2012.

[62] T. Kangwanpongpan, F. H. França, R. C. da Silva, P. S. Schneider, and H. J. Krautz, "New correlations for the weighted-sum-of-gray-gases model in oxy-fuel conditions based on HITEMP 2010 database," *International Journal of Heat and Mass Transfer,* vol. 55, pp. 7419-7433, 2012.

[63] G. Krishnamoorthy, "A new weighted-sum-of-gray-gases model for oxy-combustion scenarios," *International Journal of Energy Research,* vol. 37, pp. 1752-1763, 2013.

[64] C. Yin, "On gas and particle radiation in pulverized fuel combustion furnaces," *Applied Energy,* vol. 157, pp. 554-561, 2015.

[65] C. Yin, "Refined weighted sum of gray gases model for air-fuel combustion and its impacts," *Energy & Fuels,* vol. 27, pp. 6287-6294, 2013.

[66] C. Yin, L. A. Rosendahl, and S. K. Kær, "Chemistry and radiation in oxy-fuel combustion: a computational fluid dynamics modeling study," *Fuel,* vol. 90, pp. 2519-2529, 2011.

[67] S. Hjärtstam, R. Johansson, K. Andersson, and F. Johnsson, "Computational fluid dynamics modeling of oxy-fuel flames: The role of soot and gas radiation," *Energy & Fuels,* vol. 26, pp. 2786-2797, 2012.

[68] N. Nikolopoulos, M. Agraniotis, I. Violidakis, E. Karampinis, A. Nikolopoulos, P. Grammelis, C. Papapavlou, S. Tzivenis, and E. Kakaras, "Parametric investigation of a renewable alternative for utilities adopting the co-firing lignite/biomass concept," *Fuel,* vol. 113, pp. 873-897, 2013.

[69] R. Johansson, B. Leckner, K. Andersson, and F. Johnsson, "Influence of particle and gas radiation in oxy-fuel combustion," *International Journal of Heat and Mass Transfer,* vol. 65, pp. 143-152, 2013.

[70] D. Bäckström, R. Johansson, K. Andersson, F. Johnsson, S. Clausen, and A. Fateev, "Measurement and modeling of particle radiation in coal flames," *Energy & Fuels,* vol. 28, pp. 2199-2210, 2014.

[71] R. Jovanović, B. Rašuo, P. Stefanović, D. Cvetinović, and B. Swiatkowski, "Numerical investigation of pulverized coal jet flame characteristics under different oxy-fuel conditions," *International Journal of Heat and Mass Transfer,* vol. 58, pp. 654-662, 2013.

[72] M. Momeni, C. Yin, S. K. Kær, T. B. Hansen, P. A. Jensen, and P. Glarborg, "Experimental study on effects of particle shape and operating conditions on combustion characteristics of single biomass particles," *Energy & Fuels,* vol. 27, pp. 507-514, 2012.

[73] S. Ahn, G. Choi, and D. Kim, "The effect of wood biomass blending with pulverized coal on combustion characteristics under oxy-fuel condition," *Biomass and Bioenergy*, vol. 71, pp. 144-154, 2014.

[74] L. Zhang, F. Jiao, E. Binner, L. Chen, S. Bhattacharya, Y. Ninomiya, and C.-Z. Li, "Evolution of organically bound metals during coal combustion in air and O 2/CO 2 mixtures: A case study of Victorian brown coal," *Proceedings of the Combustion Institute*, vol. 33, pp. 2795-2802, 2011.

[75] G. Li, S. Li, M. Dong, Q. Yao, C. Y. Guo, and R. L. Axelbaum, "Comparison of particulate formation and ash deposition under oxy-fuel and conventional pulverized coal combustions," *Fuel*, vol. 106, pp. 544-551, 2013.

[76] W. Li, L. Wang, Y. Qiao, J.-Y. Lin, M. Wang, and L. Chang, "Effect of atmosphere on the release behavior of alkali and alkaline earth metals during coal oxy-fuel combustion," *Fuel*, vol. 139, pp. 164-170, 2015.

[77] W. J. Morris, D. Yu, and J. O. Wendt, "Soot, unburned carbon and ultrafine particle emissions from air-and oxy-coal flames," *Proceedings of the Combustion Institute*, vol. 33, pp. 3415-3421, 2011.

[78] M. de la Torre, A. A. Chowdhury, N. Love, and A. Choudhuri, "Radiative heat release from premixed oxy-syngas and oxy-methane flames," *Fuel*, vol. 166, pp. 567-573, 2016.

[79] P. Kutne, B. K. Kapadia, W. Meier, and M. Aigner, "Experimental analysis of the combustion behaviour of oxyfuel flames in a gas turbine model combustor," *Proceedings of the Combustion Institute*, vol. 33, pp. 3383-3390, 2011.

[80] M. A. Habib, M. A. Nemitallah, P. Ahmed, M. H. Sharqawy, H. M. Badr, I. Muhammad, and M. Yaqub, "Experimental analysis of oxygen-methane combustion inside a gas turbine reactor under various operating conditions," *Energy*, vol. 86, pp. 105-114, 2015.

[81] M. A. Nemitallah and M. A. Habib, "Experimental and numerical investigations of an atmospheric diffusion oxy-combustion flame in a gas turbine model combustor," *Applied Energy*, vol. 111, pp. 401-415, 2013.

[82] A. Mazas, D. Lacoste, and T. Schuller, "Experimental and numerical investigation on the laminar flame speed of CH4/O2 mixtures diluted with CO2 and H2O," in *ASME Turbo Expo 2010: Power for Land, Sea, and Air*, 2010, pp. 411-421.

[83] Y.-H. Li, G.-B. Chen, Y.-C. Lin, and Y.-C. Chao, "Effects of flue gas recirculation on the premixed oxy-methane flames in atmospheric condition," *Energy,* vol. 89, pp. 845-857, 2015.

[84] Y. Song, C. Zou, Y. He, and C. Zheng, "The chemical mechanism of the effect of CO 2 on the temperature in methane oxy-fuel combustion," *International Journal of Heat and Mass Transfer,* vol. 86, pp. 622-628, 2015.

[85] F. Liu, H. Guo, and G. J. Smallwood, "The chemical effect of CO 2 replacement of N 2 in air on the burning velocity of CH 4 and H 2 premixed flames," *Combustion and Flame,* vol. 133, pp. 495-497, 2003.

[86] T. H. Kim, J. W. Park, H. Y. Park, J. Park, J. H. Park, and I. G. Lim, "Chemical and radiation effects on flame extinction and NOx formation in oxy-methane combustion diluted with CO 2," *Fuel,* vol. 177, pp. 235-243, 2016.

[87] v. d. K. W. Woycenko D., Roberts P, "European Commission Joule II clean coal technology program 1992–1995, vol. II. Powder coal combustion projects final reports," EUROPEAN COMMISSION, Directorate-General XII Science, Research and Development1997.

[88] P. Heil, D. Toporov, H. Stadler, S. Tschunko, M. Förster, and R. Kneer, "Development of an oxycoal swirl burner operating at low O 2 concentrations," *Fuel,* vol. 88, pp. 1269-1274, 2009.

[89] C. Liu, G. Chen, N. Sipöcz, M. Assadi, and X.-S. Bai, "Characteristics of oxy-fuel combustion in gas turbines," *Applied Energy,* vol. 89, pp. 387-394, 2012.

[90] F. Halter, F. Foucher, L. Landry, and C. Mounaïm-Rousselle, "Effect of dilution by nitrogen and/or carbon dioxide on methane and iso-octane air flames," *Combustion Science and Technology,* vol. 181, pp. 813-827, 2009.

[91] Z. Chen, X. Qin, B. Xu, Y. Ju, and F. Liu, "Studies of radiation absorption on flame speed and flammability limit of CO 2 diluted methane flames at elevated pressures," *Proceedings of the Combustion Institute,* vol. 31, pp. 2693-2700, 2007.

[92] K. Maruta, K. Abe, S. Hasegawa, S. Maruyama, and J. i. Sato, "Extinction characteristics of CH 4/CO 2 versus O 2/CO 2 counterflow non-premixed flames at elevated pressures up to 0.7 MPa," *Proceedings of the Combustion Institute,* vol. 31, pp. 1223-1230, 2007.

[93] J. Runyon, R. Marsh, A. Valera-Medina, A. Giles, S. Morris, D. Pugh, Y. Sevcenco, and P. Bowen, "Methane-Oxygen Flame Stability in a Generic Premixed Gas Turbine Swirl Combustor at Varying Thermal Power and Pressure," in *ASME Turbo Expo 2015: Turbine Technical Conference and Exposition*, 2015, pp. V04BT04A043-V04BT04A043.

[94] Y. Xie, J. Wang, M. Zhang, J. Gong, W. Jin, and Z. Huang, "Experimental and numerical study on laminar flame characteristics of methane oxy-fuel mixtures highly diluted with CO2," *Energy & Fuels,* vol. 27, pp. 6231-6237, 2013.

[95] G. Kim, Y. Kim, and Y.-J. Joo, "Conditional moment closure for modeling combustion processes and structure of oxy-natural gas flame," *Energy & Fuels,* vol. 23, pp. 4370-4377, 2009.

[96] P. Glarborg and L. L. Bentzen, "Chemical effects of a high CO2 concentration in oxy-fuel combustion of methane," *Energy & Fuels,* vol. 22, pp. 291-296, 2007.

[97] M. A. Habib, F. Tahir, M. A. Nemitallah, W. H. Ahmed, and H. M. Badr, "Experimental and numerical analysis of oxy-fuel combustion in a porous plate reactor," *International Journal of Energy Research,* vol. 39, pp. 1229-1240, 2015.

[98] G. H. Ko, A. Hamins, M. Bundy, E. L. Johnsson, S. C. Kim, and D. B. Lenhert, "Mixture fraction analysis of combustion products in the upper layer of reduced-scale compartment fires," *Combustion and Flame,* vol. 156, pp. 467-476, 2009.

[99] R. McDermott, K. McGrattan, and S. Hostikka, "Fire dynamics simulator (version 5) technical reference guide," *NIST Special Publication,* vol. 1018, 2008.

[100] M. Dharavath, P. Manna, and D. Chakraborty, "Numerical exploration of mixing and combustion in ethylene fueled scramjet combustor," *Acta Astronautica,* vol. 117, pp. 305-318, 2015.

[101] S. Han, J. Kim, and C. Bae, "Effect of air–fuel mixing quality on characteristics of conventional and low temperature diesel combustion," *Applied Energy,* vol. 119, pp. 454-466, 2014.

[102] N. J. Moore, J. Kribs, and K. M. Lyons, "Investigation of Jet-Flame Blowout With Lean-Limit Considerations," *Flow, turbulence and combustion*, vol. 87, pp. 525-536, 2011.

[103] N. Moore, J. McCraw, and K. Lyons, "Observations on jet-flame blowout," *Journal of Combustion*, vol. 2008, 2008.

[104] M. Karbasi and I. Wierzba, "Prediction and Validation of Blowout Limits of Co-Flowing Jet Diffusion Flames—Effect of Dilution," *Journal of Energy Resources Technology*, vol. 120, pp. 167-171, 1998.

[105] J. E. Broadwell, W. J. Dahm, and M. G. Mungal, "Blowout of turbulent diffusion flames," in *Symposium (International) on Combustion*, 1985, pp. 303-310.

[106] W. J. Dahm and A. G. Mayman, "Blowout limits of turbulent jet diffusion flames for arbitrary source conditions," *AIAA journal*, vol. 28, pp. 1157-1162, 1990.

[107] D. R. Dowling and P. E. Dimotakis, "Similarity of the concentration field of gas-phase turbulent jets," *Journal of Fluid Mechanics*, vol. 218, pp. 109-141, 1990.

[108] S. Kondo, K. Takizawa, A. Takahashi, and K. Tokuhashi, "Extended Le Chatelier's formula and nitrogen dilution effect on the flammability limits," *Fire Safety Journal*, vol. 41, pp. 406-417, 2006.

[109] D. R. Noble, Q. Zhang, A. Shareef, J. Tootle, A. Meyers, and T. Lieuwen, "Syngas mixture composition effects upon flashback and blowout," in *ASME Turbo Expo 2006: Power for Land, Sea, and Air*, 2006, pp. 357-368.

[110] H. K. Versteeg and W. Malalasekera, *An introduction to computational fluid dynamics: the finite volume method*: Pearson Education, 2007.

[111] K. Anderson, S. Londerville, and J. Zink, "Practical Use of Computational Fluid Dynamics to Industrial Combustion Applications," in *Proceedings of the American flame research committee combustion symposium. Sheraton Kauai, Hawaii*, 2013, pp. 1-14.

[112] M. A. Lorra and S. X. Chen, "CFD—Based Combustion Modeling," *The Coen & Hamworthy Combustion Handbook: Fundamentals for Power, Marine & Industrial Applications*, p. 183, 2013.

[113] J. Naser, "Industrial Application of CFD–A Review of Few Examples," in *Seventh International Conference on CFD in the Minerals and Process Industries*, 2009.

[114] K. Singh, J. Mathur, V. Ashok, and D. Chakraborty, "Computational fluid dynamics in aerospace industry in India," *Defence Science Journal*, vol. 60, 2010.

[115] H. Pan, X.-Z. Chen, X.-F. Liang, L.-T. Zhu, and Z.-H. Luo, "CFD simulations of gas–liquid–solid flow in fluidized bed reactors—A review," *Powder Technology*, vol. 299, pp. 235-258, 2016.

[116] J. Andersen, C. L. Rasmussen, T. Giselsson, and P. Glarborg, "Global combustion mechanisms for use in CFD modeling under oxy-fuel conditions," *Energy & Fuels*, vol. 23, pp. 1379-1389, 2009.

[117] Y. Ra, F. Chuahy, and S. Kokjohn, "Development and validation of a reduced reaction mechanism with a focus on diesel fuel/syngas co-oxidation," *Fuel*, vol. 185, pp. 663-683, 2016.

[118] S. Coogan, X. Gao, A. McClung, and W. Sun, "Evaluation of Kinetic Mechanisms for Direct Fired Supercritical Oxy-Combustion of Natural Gas," in *ASME Turbo Expo 2016: Turbomachinery Technical Conference and Exposition*, 2016, pp. V04AT04A037-V04AT04A037.

[119] R. F. Pachler, A. K. Ramalingam, K. A. Heufer, and F. Winter, "Reduction and validation of a chemical kinetic mechanism including necessity analysis and investigation of CH 4/C 3 H 8 oxidation at pressures up to 120 bar using a rapid compression machine," *Fuel*, vol. 172, pp. 139-145, 2016.

[120] L. Acampora, F. Marra, and E. Martelli, "Comparison of Different CH4-Air Combustion Mechanisms in a Perfectly Stirred Reactor with Oscillating Residence Times Close to Extinction," *Combustion Science and Technology*, vol. 188, pp. 707-718, 2016.

[121] X. Hu, Q. Yu, Y. Li, and J. Liu, "A Minimal Skeletal Mechanism for Combustion of CH4/O2/CO2 Mixtures," *Energy & Fuels*, vol. 30, pp. 1407-1414, 2016.

[122] M. Aliyu, Nemitallah, M. A., Said, S. A., & Habib, M. A. , "Characteristics of H2-enriched CH4-O2 diffusion flames in a swirl-stabilized gas turbine combustor: Experimental and numerical study," *International Journal of Hydrogen Energy*, 2016.

[123] M. A. Habib, S. A. Salaudeen, M. A. Nemitallah, R. Ben-Mansour, and E. M. Mokheimer, "Numerical investigation of syngas oxy-combustion inside a LSCF-6428 oxygen transport membrane reactor," *Energy*, vol. 96, pp. 654-665, 2016.

[124] H. Xiao, M. Howard, A. Valera-Medina, S. Dooley, and P. J. Bowen, "Study on Reduced Chemical Mechanisms of Ammonia/Methane Combustion under Gas Turbine Conditions," *Energy & Fuels*, 2016.

[125] J. A. Moríñigo and J. Hermida-Quesada, "Evaluation of reduced-order kinetic models for HTPB-oxygen combustion using LES," *Aerospace Science and Technology*, vol. 58, pp. 358-368, 2016.

[126] A. Abou-Taouk, B. Farcy, P. Domingo, L. Vervisch, S. Sadasivuni, and L.-E. Eriksson, "Optimized Reduced Chemistry and Molecular Transport for Large Eddy Simulation of Partially Premixed Combustion in a Gas Turbine," *Combustion Science and Technology*, vol. 188, pp. 21-39, 2016.

[127] V. Giovannoni, R. N. Sharma, and R. R. Raine, "Premixed combustion of methane–air mixture stabilized over porous medium: A 2D numerical study," *Chemical Engineering Science*, vol. 152, pp. 591-605, 2016.

[128] K. Poorghasemi, R. K. Saray, K. Bahlouli, and A. Zehni, "3D CFD simulation of a natural gas fueled HCCI engine with employing a reduced mechanism," *Fuel*, vol. 182, pp. 816-830, 2016.

[129] A. Frassoldati, A. Cuoci, T. Faravelli, E. Ranzi, C. Candusso, and D. Tolazzi, "Simplified kinetic schemes for oxy-fuel combustion," in *1st International conference on sustainable fossil fuels for future energy*, 2009, pp. 6-10.

[130] S. Hjärtstam, F. Normann, K. Andersson, and F. Johnsson, "Oxy-fuel combustion modeling: performance of global reaction mechanisms," *Industrial & Engineering Chemistry Research*, vol. 51, pp. 10327-10337, 2012.

[131] C. Yin, "Advanced modeling of oxy-fuel combustion of natural gas," Department of Energy Technology, Aalborg University2011.

[132] W. Jones and R. Lindstedt, "Global reaction schemes for hydrocarbon combustion," *Combustion and Flame*, vol. 73, pp. 233-249, 1988.

[133] Fluent. (2013, ANSYS 15.0 Fluent Theory Guide.

[134] M. Habib, P. Ahmed, R. Ben-Mansour, H. M. Badr, P. Kirchen, and A. Ghoniem, "Modeling of a combined ion transport and porous membrane reactor for oxy-combustion," *Journal of Membrane Science,* vol. 446, pp. 230-243, 2013.

[135] C. Ghenai, "Combustion of Syngas Fuel in Gas Turbine Can Combustor," *Advances in Mechanical Engineering,* vol. 2010.

[136] C. Ghenai, "Combustion of syngas fuel in gas turbine can combustor," *Advances in Mechanical Engineering,* vol. 2, p. 342357, 2010.

[137] H. Pitsch, "Title," unpublished|.

[138] W. K. Hong and G. M. Choi, "Oxygen permeation of BSCF membrane with varying thickness and surface coating," *Journal of Membrane Science,* vol. 346, pp. 353-360, 2010.

[139] N. Peters, "Title," unpublished|.

[140] Y. Sivathanu and G. Faeth, "Generalized state relationships for scalar properties in nonpremixed hydrocarbon/air flames," *Combustion and Flame,* vol. 82, pp. 211-230, 1990.

[141] B. Mondal and X. Li, "Effect of volumetric radiation on natural convection in a square cavity using lattice Boltzmann method with non-uniform lattices," *International Journal of Heat and Mass Transfer,* vol. 53, pp. 4935-4948, 2010.

[142] J. R. Howell, M. P. Menguc, and R. Siegel, *Thermal radiation heat transfer*: CRC press, 2010.

[143] A. FLUENT, "15-Theory Guide, ANSYS," *Inc., Canonsburg, PA,* 2013.

[144] S. M. Hashim, A. R. Mohamed, and S. Bhatia, "Current status of ceramic-based membranes for oxygen separation from air," *Advances in Colloid and interface Science,* vol. 160, pp. 88-100, 2010.

[145] H. J. Bouwmeester and A. J. Burggraaf, "DENSE CERAMIC MEMBRANES FOR OXYGEN SEPARATION," *Handbook of Solid State Electrochemistry,* p. 481, 1997.

[146] Z. Wu, B. Wang, and K. Li, "A novel dual-layer ceramic hollow fibre membrane reactor for methane conversion," *Journal of Membrane Science,* vol. 352, pp. 63-70, 2010.

[147] A. Leo, S. Liu, and J. C. D. da Costa, "Development of mixed conducting membranes for clean coal energy delivery," *International journal of greenhouse gas control*, vol. 3, pp. 357-367, 2009.

[148] E. Robinson, "Oxygen transport membranes for ultra-clean fuel production," *Fuel Chemistry Division Reprints*, vol. 48, pp. 347-349, 2003.

[149] R. Kiebach, S. Pirou, S. Ovtar, A. B. Haugen, and P. V. Hendriksen, "Research and Development on Oxygen Transport Membranes at the Technical University of Denmark from Materials to Modules," in *Meeting Abstracts*, 2016, pp. 2971-2971.

[150] M. A. Habib and M. A. Nemitallah, "Design of an ion transport membrane reactor for application in fire tube boilers," *Energy*, vol. 81, pp. 787-801, 2015.

[151] K. Zhang, J. Sunarso, Z. Shao, W. Zhou, C. Sun, S. Wang, and S. Liu, "Research progress and materials selection guidelines on mixed conducting perovskite-type ceramic membranes for oxygen production," *RSC advances*, vol. 1, pp. 1661-1676, 2011.

[152] J. Sunarso, S. Baumann, J. Serra, W. Meulenberg, S. Liu, Y. Lin, and J. D. Da Costa, "Mixed ionic–electronic conducting (MIEC) ceramic-based membranes for oxygen separation," *Journal of Membrane Science*, vol. 320, pp. 13-41, 2008.

[153] P. Lemes-Rachadel, G. S. Garcia, R. A. F. Machado, D. Hotza, and J. C. D. d. Costa, "Current developments of mixed conducting membranes on porous substrates," *Materials Research*, vol. 17, pp. 242-249, 2014.

[154] J. Zhu, G. Liu, Z. Liu, Z. Chu, W. Jin, and N. Xu, "Unprecedented Perovskite Oxyfluoride Membranes with High-Efficiency Oxygen Ion Transport Paths for Low-Temperature Oxygen Permeation," *Advanced Materials*, vol. 28, pp. 3511-3515, 2016.

[155] J. Kim and Y. Lin, "Synthesis and oxygen-permeation properties of thin YSZ/Pd composite membranes," *AIChE journal*, vol. 46, pp. 1521-1529, 2000.

[156] U. Balachandran, M. S. Kleefisch, T. P. Kobylinski, S. L. Morissette, and S. Pei, "Oxygen ion-conducting dense ceramic," ed: US Patent 5,580,497, 1996.

[157] C. C. Chen, R. Prasad, and C. F. Gottzmann, "Solid electrolyte membrane with porous catalytically-enhancing constituents," ed: Google Patents, 1999.

[158] K. Foy and J. McGovern, "Comparison of ion transport membranes," in *Proc. 4th Annual Conference on Carbon Capture and Sequestration*, 2005, pp. 2-5.

[159] K. Partovi, B. Geppert, F. Liang, C. H. Rüscher, and J. r. Caro, "Effect of the B-Site Composition on the Oxygen Permeability and the CO2 Stability of Pr0. 6Sr0. 4Co x Fe1–x O3− δ (0.0≤ x≤ 1.0) Membranes," *Chemistry of Materials,* vol. 27, pp. 2911-2919, 2015.

[160] D. M. Turi, P. Chiesa, E. Macchi, and A. F. Ghoniem, "High fidelity model of the oxygen flux across ion transport membrane reactor: Mechanism characterization using experimental data," *Energy,* vol. 96, pp. 127-141, 2016.

[161] S. Smart, S. Liu, J. Serra, A. Basile, and J. Diniz da Costa, "Perovskite membrane reactors: fundamentals and applications for oxygen production, syngas production and hydrogen processing," 2014.

[162] W. Yang and R. Cai, "Oxygen-Ion Transport Membrane and Its Applications in Selective Oxidation of Light Alkanes," in *Inorganic Membranes for Energy and Environmental Applications*, ed: Springer, 2009, pp. 53-65.

[163] X. Tan and K. Li, "Design of mixed conducting ceramic membranes/reactors for the partial oxidation of methane to syngas," *AIChE journal,* vol. 55, pp. 2675-2685, 2009.

[164] D. J. Apo, "Experimental characterization of an Ion Transport Membrane (ITM) reactor for methane oxyfuel combustion," Massachusetts Institute of Technology, 2012.

[165] J. M. Serra, J. Garcia-Fayos, S. Baumann, F. Schulze-Küppers, and W. Meulenberg, "Oxygen permeation through tape-cast asymmetric all-La 0.6 Sr 0.4 Co 0.2 Fe 0.8 O 3− δ membranes," *Journal of Membrane Science,* vol. 447, pp. 297-305, 2013.

[166] H. Bouwmeester, H. Kruidhof, and A. Burggraaf, "Importance of the surface exchange kinetics as rate limiting step in oxygen permeation through mixed-conducting oxides," *Solid State Ionics,* vol. 72, pp. 185-194, 1994.

[167] B. Wang, J. Song, X. Tan, B. Meng, J. Liu, and S. Liu, "Reinforced perovskite hollow fiber membranes with stainless steel as the reactive sintering aid for oxygen separation," *Journal of Membrane Science,* vol. 502, pp. 151-157, 2016.

[168] Y. Liu, X. Tan, and K. Li, "Mixed conducting ceramics for catalytic membrane processing," *Catalysis Reviews*, vol. 48, pp. 145-198, 2006.

[169] S. J. Xu and W. J. Thomson, "Oxygen permeation rates through ion-conducting perovskite membranes," *Chemical Engineering Science*, vol. 54, pp. 3839-3850, 1999.

[170] C. Chen, B. Boukamp, H. Bouwmeester, G. Cao, H. Kruidhof, A. Winnubst, and A. Burggraaf, "Microstructural development, electrical properties and oxygen permeation of zirconia-palladium composites," *Solid State Ionics*, vol. 76, pp. 23-28, 1995.

[171] S. Liu, X. Tan, Z. Shao, and J. Diniz da Costa, "Ba0. 5Sr0. 5Co0. 8Fe0. 2O3-δ ceramic hollow-fiber membranes for oxygen permeation," *AIChE journal*, vol. 52, pp. 3452-3461, 2006.

[172] X. Tan and K. Li, "Modeling of air separation in a LSCF hollow-fiber membrane module," *AIChE journal*, vol. 48, pp. 1469-1477, 2002.

[173] Z. Shao, G. Xiong, J. Tong, H. Dong, and W. Yang, "Ba effect in doped Sr (Co 0.8 Fe 0.2) O 3-δ on the phase structure and oxygen permeation properties of the dense ceramic membranes," *Separation and Purification Technology*, vol. 25, pp. 419-429, 2001.

[174] H. Wang, R. Wang, D. T. Liang, and W. Yang, "Experimental and modeling studies on Ba 0.5 Sr 0.5 Co 0.8 Fe 0.2 O 3− δ (BSCF) tubular membranes for air separation," *Journal of Membrane Science*, vol. 243, pp. 405-415, 2004.

[175] L. Ge, Z. Shao, K. Zhang, R. Ran, J. Diniz da Costa, and S. Liu, "Evaluation of mixed-conducting lanthanum-strontium-cobaltite ceramic membrane for oxygen separation," *AIChE journal*, vol. 55, pp. 2603-2613, 2009.

[176] T. Lee, Y. Yang, A. Jacobson, B. Abeles, and M. Zhou, "Oxygen permeation in dense SrCo 0.8 Fe 0.2 O 3− δ membranes: surface exchange kinetics versus bulk diffusion," *Solid State Ionics*, vol. 100, pp. 77-85, 1997.

[177] F. Akin and J. Y. Lin, "Oxygen permeation through oxygen ionic or mixed-conducting ceramic membranes with chemical reactions," *Journal of Membrane Science*, vol. 231, pp. 133-146, 2004.

[178] M. A. Nemitallah, "A study of methane oxy-combustion characteristics inside a modified design button-cell membrane reactor utilizing a modified oxygen permeation model for reacting flows," *Journal of Natural Gas Science and Engineering*, vol. 28, pp. 61-73, 2016.

[179] R. Wang, B. Meng, X. Meng, X. Tan, J. Sunarso, L. Liu, and S. Liu, "Highly stable La 0.6 Sr 0.4 Co 0.2 Fe 0.8 O 3− δ hollow fibre membrane for air separation swept by steam or steam mixture," *Journal of Membrane Science*, vol. 479, pp. 232-239, 2015.

[180] M. Nemitallah, M. Habib, and R. B. Mansour, "Investigations of oxy-fuel combustion and oxygen permeation in an ITM reactor using a two-step oxy-combustion reaction kinetics model," *Journal of Membrane Science*, vol. 432, pp. 1-12, 2013.

[181] A. A. Asadi, A. Behrouzifar, M. Iravaninia, T. Mohammadi, and A. Pak, "Preparation and Oxygen Permeation of La0. 6Sr0. 4Co0. 2Fe0. 8O3− δ (LSCF) Perovskite-Type Membranes: Experimental Study and Mathematical Modeling," *Industrial & Engineering Chemistry Research*, vol. 51, pp. 3069-3080, 2012.

[182] A. Behrouzifar, A. A. Asadi, T. Mohammadi, and A. Pak, "Experimental investigation and mathematical modeling of oxygen permeation through dense Ba 0.5Sr 0.5Co 0.8Fe 0.2O 3-δ (BSCF) perovskite-type ceramic membranes," *Ceramics International*, vol. 38, pp. 4797-4811, 2012.

[183] Z. Zhang, T. N. Borhani, and M. H. El-Naas, "Carbon Capture," in *Exergetic, Energetic and Environmental Dimensions*, ed: Elsevier, 2018, pp. 997-1016.

[184] R. Ben-Mansour, M. A. Habib, M. A. Nemitallah, M. Rajhi, and K. A. Suara, "Characteristics of oxyfuel and air–fuel combustion in an industrial water tube boiler," *Heat Transfer Engineering*, vol. 35, pp. 1394-1404, 2014.

[185] M. A. Habib, P. Ahmed, R. Ben-Mansour, K. Mezghani, Z. Alam, Y. Shao-Horn, and A. Ghoniem, "Experimental and numerical investigation of La2NiO4 membranes for oxygen separation: geometry optimization and model validation," *Journal of Energy Resources Technology*, vol. 137, p. 031102, 2015.

[186] J. Sunarso, S. S. Hashim, N. Zhu, and W. Zhou, "Perovskite oxides applications in high temperature oxygen separation, solid oxide fuel cell and membrane reactor: A review," *Progress in energy and combustion science,* vol. 61, pp. 57-77, 2017.

[187] J. Hong, P. Kirchen, and A. F. Ghoniem, "Numerical simulation of ion transport membrane reactors: oxygen permeation and transport and fuel conversion," *Journal of Membrane Science,* vol. 407, pp. 71-85, 2012.

[188] X. Zhu, S. Sun, Y. Cong, and W. Yang, "Operation of perovskite membrane under vacuum and elevated pressures for high-purity oxygen production," *Journal of Membrane Science,* vol. 345, pp. 47-52, 2009.

[189] H. Lu, Y. Cong, and W. S. Yang, "Oxygen permeability and stability of Ba 0.5 Sr 0.5 Co 0.8 Fe 0.2 O 3Àd as an oxygen-permeable membrane at high pressures."

[190] L. Di Felice, V. Middelkoop, V. Anzoletti, F. Snijkers, M. van Sint Annaland, and F. Gallucci, "New high temperature sealing technique and permeability data for hollow fiber BSCF perovskite membranes," *Chemical Engineering and Processing: Process Intensification,* vol. 107, pp. 206-219, 2016.

[191] K. Mezghani, A. Hamza, M. A. Habib, D. Lee, and Y. Shao-Horn, "Effect of microstructure and thickness on oxygen permeation of La2NiO4+δ membranes," *Ceramics International,* vol. 42, pp. 666-672, 2016.

[192] A. Ghadimi, M. A. Alaee, A. Behrouzifar, A. A. Asadi, and T. Mohammadi, "Oxygen permeation of BaxSr1 − xCo0.8Fe0.2O3 − δ perovskite-type membrane: Experimental and modeling," *Desalination,* vol. 270, pp. 64-75, 2011.

[193] J. Sunarso, S. Liu, Y. S. Lin, and J. C. Diniz da Costa, "Oxygen permeation performance of BaBiO3-δ ceramic membranes," *Journal of Membrane Science,* vol. 344, pp. 281-287, 2009.

[194] R. Ben-Mansour, A. A. Adebiyi, and M. A. Habib, "Investigation of performance of fire-tube boilers integrated with ion transport membrane for oxy-fuel combustion," *International Journal of Energy Research,* vol. 40, pp. 1673-1687, 2016.

[195] P. Ahmed, M. A. Habib, R. Ben-Mansour, and A. Jamal, "Investigation of oxygen permeation through disc-shaped BSCF ion transport membrane under reactive

conditions," *International Journal of Energy Research,* vol. 41, pp. 1049-1062, 2017.

[196] M. A. Nemitallah, M. A. Habib, S. A. Salaudeen, and I. Mansir, "Hydrogen production, oxygen separation and syngas oxy-combustion inside a water splitting membrane reactor," *Renewable Energy,* vol. 113, pp. 221-234, 2017.

[197] K. Mezghani and A. Hamza, "Application of Ba0.5Sr0.5Co0.8Fe0.2O3−δ membranes in an oxy-fuel combustion reactor," *Journal of Membrane Science,* vol. 518, pp. 254-262, 2016.

[198] J. Hong, P. Kirchen, and A. F. Ghoniem, "Laminar oxy-fuel diffusion flame supported by an oxygen-permeable-ion-transport membrane," *Combustion and Flame,* vol. 160, pp. 704-717, 2013.

[199] M. Nemitallah, M. A. Habib, and R. Ben-Mansour, "Investigations of an ion transport membrane reactor specially designed for a power cycle," in *Applied Mechanics and Materials*, 2013, pp. 440-446.

[200] M. Raffel, C. E. Willert, S. Wereley, and J. Kompenhans, *Particle image velocimetry: a practical guide*: Springer, 2013.

[201] V. Research. (2012, *Phantom (PCC) Camera Control Help* - AMETEK Material Analysis Division, Software Revision: 2.14.727.0

[202] D. Dynamics. (2012, Dynamic Studio Manual - User's Guide, Dantec Dynamics A/S, 121, Tonsbakken 18, DK–2740.

[203] L. Lu and V. Sick, "High-speed particle image velocimetry near surfaces," *Journal of visualized experiments: JoVE,* 2013.

[204] V. Sick, "High speed imaging in fundamental and applied combustion research," *Proceedings of the Combustion Institute,* vol. 34, pp. 3509-3530, 2013.

[205] L. Anetor, E. Osakue, and C. Odetunde, "Reduced mechanism approach of modeling premixed propane-air mixture using ANSYS Fluent," *Engineering Journal,* vol. 16, pp. 67-86, 2011.

[206] M. A. Nemitallah and M. A. Habib, "Numerical investigation of liquid methanol evaporation and oxy-combustion inside a button-cell ITM reactor," *Applied Thermal Engineering,* vol. 112, pp. 378-391, 2017.

[207] H. A. McGee, *Molecular engineering*: McGraw-Hill, 1991.

[208] R. Ben-Mansour, P. Ahmed, M. A. Habib, and A. Jamal, "Oxy-combustion of liquid fuel in an ion transport membrane reactor," *International Journal of Energy and Environmental Engineering*, pp. 1-17, 2017.

[209] A. E. Farooqui, M. A. Habib, H. M. Badr, and R. Ben-Mansour, "Modeling of ion transport reactor for oxy-fuel combustion," *International Journal of Energy Research*, vol. 37, pp. 1265-1279, 2013.

[210] E. Chui and G. Raithby, "Computation of radiant heat transfer on a nonorthogonal mesh using the finite-volume method," *Numerical Heat Transfer*, vol. 23, pp. 269-288, 1993.

[211] M. Habib, R. Ben-Mansour, H. Badr, S. Ahmed, and A. Ghoniem, "Computational fluid dynamic simulation of oxyfuel combustion in gas-fired water tube boilers," *Computers & Fluids*, vol. 56, pp. 152-165, 2012.

[212] M. Aliyu, M. A. Nemitallah, S. A. Said, and M. A. Habib, "Characteristics of H2-enriched CH4O2 diffusion flames in a swirl-stabilized gas turbine combustor: Experimental and numerical study," *International Journal of Hydrogen Energy*, vol. 41, pp. 20418-20432, 2016.

[213] Y. S. Sanusi, E. M. Mokheimer, M. R. Shakeel, Z. Abubakar, and M. A. Habib, "Oxy-Combustion of Hydrogen-Enriched Methane: Experimental Measurements and Analysis," *Energy & Fuels*, vol. 31, pp. 2007-2016, 2017.

[214] J. Oh and D. Noh, "Lifted flame behavior of a non-premixed oxy-methane jet in a lab-scale slot burner," *Fuel*, vol. 103, pp. 862-868, 2013.

[215] P. Sayad, A. Schönborn, D. Clerini, and J. Klingmann, "Experimental investigation of methane lean blowout limit; effects of dilution, mass flow rate and inlet temperature," in *ASME 2012 Gas Turbine India Conference*, 2012, pp. 815-826.

[216] Y. Chan, M. Zhu, Z. Zhang, P. Liu, and D. Zhang, "The Effect of CO2 dilution on the laminar burning velocity of premixed methane/air flames," *Energy Procedia*, vol. 75, pp. 3048-3053, 2015.

[217] P. Dirrenberger, H. Le Gall, R. Bounaceur, O. Herbinet, P.-A. Glaude, A. Konnov, and F. Battin-Leclerc, "Measurements of laminar flame velocity for components of natural gas," *Energy & Fuels*, vol. 25, pp. 3875-3884, 2011.

[218] H. Kruidhof, H. J. Bouwmeester, R. v. Doorn, and A. Burggraaf, "Influence of order-disorder transitions on oxygen permeability through selected nonstoichiometric perovskite-type oxides," *Solid State Ionics*, vol. 63, pp. 816-822, 1993.

[219] X. Chen, L. Huang, Y. Wei, and H. Wang, "Tantalum stabilized SrCoO3− δ perovskite membrane for oxygen separation," *Journal of Membrane Science*, vol. 368, pp. 159-164, 2011.

[220] J. Yi, J. Brendt, M. Schroeder, and M. Martin, "Oxygen permeation and oxidation states of transition metals in (Fe, Nb)-doped BaCoO3− δ perovskites," *Journal of Membrane Science*, vol. 387, pp. 17-23, 2012.

[221] M. Kim, J. Oh J, Y. Yoon, "Flame length scaling in a non-premixed turbulent diluted hydrogen jet with coaxial air,' *Fuel*, 90.8 (2011): 2624-2629.

Appendices

APPENDIX A: The original WD reduced mechanism with kinetic rate data; with units given in [J], [K], [kmol], [m] and [s], [131]

S/No	Reactions	Rate of Reaction [kmol/(m^{3}s)]	A	b	E
1	$CH_4 + 3/2O_2 \rightarrow CO + 2H_2O$	$\frac{d[CH_4]}{dt} = AT^b e^{-E/(RT)} \cdot [CH_4]^{0.7}[O_2]^{0.8}$	5.012E11	0	2.0E08
2	$CO + 1/2O_2 \rightarrow CO_2$	$\frac{d[CO]}{dt} = AT^b e^{-E/(RT)} \cdot [O_2]^{0.25}[CO][H_2O]^{0.5}$	2.239E12	0	1.7E08
3	$CO_2 \rightarrow CO + 1/2\ O_2$	$\frac{d[CO_2]}{dt} = AT^b e^{-E/(RT)} \cdot [CO_2]$	5.000E08	0	1.7E08

APPENDIX B: The modified Westbrook-Dryer (oxyWD) reduced mechanism for oxyfuel reaction with kinetic rate data. The units are in [J], [K], [kmol], [m], [s] [131]

S/No	Reactions	Rate of Reaction [kmol/(m^{3}s)]	A	b	E
1	$CH_4 + 3/2O_2 \rightarrow CO + 2H_2O$	$\frac{d[CH_4]}{dt} = AT^b e^{-E/(RT)} \cdot [CH_4]^{0.7}[O_2]^{0.8}$	5.03E11	0	2.00E08
2	$CO + 1/2O_2 \rightarrow CO_2$	$\frac{d[CO]}{dt} = AT^b e^{-E/(RT)} \cdot [O_2]^{0.25}[CO][H_2O]^{0.5}$	2.24E06	0	4.18E07
3	$CO_2 \rightarrow CO + 1/2O_2$	$\frac{d[CO_2]}{dt} = AT^b e^{-E/(RT)} \cdot [CO_2][O_2]^{-0.25}[H_2O]^{0.5}$	1.10E13	-0.97	3.28E08

APPENDIX C: Global Multi-Steps Combustion Mechanism for Methane by Westbrook and Dryer with Kinetic Rate Data (units in cal, cm, mol and s) [116]

Mechanism	**Reactions**	$\boldsymbol{A}$	$\boldsymbol{\beta}$	$\boldsymbol{E_a}$	**Orders of reaction**
WD1	$CH_4 + 3/2\ O_2 \rightarrow 2\ H_2O +$	1.59×10^{13}	0	47800	$[CH_4]^{0.7}[O_2]^{0.8}$
WD2	CO	3.98×10^{14}	0	40700	$[CO][O_2]^{0.25}[H_2O]^{0.5}$
*WD2*r	$CO + 1/2\ O_2 \rightarrow CO_2$	5.0×10^{8}	0	40700	$[CO_2]$
	$CO_2 \rightarrow CO + 1/2\ O_2$				

APPENDIX D: Jones Lindstedt Global Multi-Steps Combustion Mechanism for Methane with the Kinetic Rate Data [128]

no.	Reactions	A	β	E_a	Orders of reaction
JL1	$CH_4 + 0.5\ O_2 \rightarrow CO + 2\ H_2$	7.82×10^{13}	0	30000	$[CH_4]^{1/2}[O_2]^{4/3}$
JL2	$CH_4 + H_2O \rightarrow 3\ H_2 + CO$	0.30×10^{12}	0	30000	$[CH_4][H_2O]$
*JL3*a	$H_2 + 1/2\ O_2 \rightarrow H_2O$	4.45×10^{18}	-1	40000	$[H_2]^{1/2}[O_2]^{9/4}[H_2O]^{-1}$
*JL3*b	$H_2 + 1/2\ O_2 \rightarrow H_2O$	1.21×10^{18}	-1	40000	$[H_2]^{1/4}[O_2]^{3/2}$
JL4	$CO + H_2O \rightarrow H_2 + CO_2$	2.75×10^{12}	0	20000	$[CO][H_2O]$

APPENDIX E: Modified Multi Steps Combustion Mechanisms for Methane with Kinetic Rate Data [116]

Reaction no.	Reaction Equation	A	β	E_a	reaction orders
WD1	$CH_4 + 3/2\ O_2 \rightarrow CO + 2\ H_2O$	1.59×10^{13}	0	47800	$[CH_4]^{0.7}[O_2]^{0.8}$
WD2(modified)	$CO + 1/2\ O_2 \rightarrow CO_2$	3.98×10^{8}	0	10000	$[CO][O_2]^{1/4}[H_2O]^{1/2}$
WD3(modified)	$CO_2 \rightarrow CO + 1/2\ O_2$	6.16×10^{13}	-0.97	78400	$[CO_2][H_2O]^{1/2}[O_2]^{-1/4}$
JL1	$CH_4 + 1/2\ O_2 \rightarrow CO + 2\ H_2$	7.82×10^{13}	0	30000	$[CH_4]^{1/2}[O_2]^{1.25}$
JL2	$CH_4 + H_2O \rightarrow CO + 3\ H_2$	3.00×10^{11}	0	30000	$[CH_4][H_2O]$
JL3(modified)	$H_2 + 1/2\ O_2 \rightarrow H_2O$	5.0×10^{20}	-1	30000	$[H_2]^{1/4}[O_2]^{3/2}$
JL3 reverse	$H_2O \rightarrow H_2 + 1/2\ O_2$	2.93×10^{20}	-0.877	97900	$[H_2]^{-3/4}[O_2][H_2O]$
JL4	$CO + H_2O \leftrightarrow CO_2 + H_2$	2.75×10^{12}	0	20000	$[CO][H_2O]$

APPENDIX F: JL 6-steps reaction mechanism for oxy-combustion [130]

	Reaction	Reaction rate
1	$CH_4 + \frac{1}{2}O_2 \longrightarrow CO + 2H_2$	$r_1 = 4.4 \cdot 10^{11} e^{-\frac{30000}{RT}} [CH_4]^{0.50} [O_2]^{1.25}$
2	$CH_4 + H_2O \longrightarrow CO + 3H_2$	$r_2 = 3 \cdot 10^{8} e^{-\frac{30000}{RT}} [CH_4][H_2O]$
3	$CO + H_2O \rightleftharpoons CO_2 + H_2$	$r_3 = 2.75 \cdot 10^{9} e^{-\frac{20000}{RT}} [CO][H_2O]$
4	$H_2 + 0.5O_2 \rightleftharpoons H_2O$	$r_4 = 6.80 \cdot 10^{15} T^{-1} e^{-\frac{40000}{RT}} [H_2]^{0.25} [O_2]^{1.50}$
5	$O_2 \rightleftharpoons 2O$	$r_5 = 1.5 \cdot 10^{9} e^{-\frac{113000}{RT}} [O_2]$
6	$H_2O \rightleftharpoons H + OH$	$r_6 = 2.3 \cdot 10^{22} T^{-3} e^{-\frac{120000}{RT}} [H_2O]$

Units of reaction parameters are: cal, mol, l, s.

APPENDIX G: Optimize JL parameters for oxycombustion application [128]

Reaction	Parameter	Original Value	Optimized Value
1	A	$4.4\cdot10^{9}$	$3.06\cdot10^{10}$
1	υ_{f,O_2}	1.25	1.30
2	A	$3.80\cdot10^{8}$	$3.84\cdot10^{9}$
3	A	$2.75\cdot10^{9}$	$2.01\cdot10^{9}$
4	A	$6.80\cdot10^{15}$	$8.03\cdot10^{16}$
4	υ_{f,H_2}	0.25	0.30
4	υ_{f,O_2}	1.50	1.55

APPENDIX H: The refined JL combustion mechanisms for oxy-combustion of natural gas, with the units of kinetic rate data in form of [m], [s], [kmol], [J], [K] [132]

No.	Reactions	Rate equations [kmol/(m^3-s)]	A	b	E
JL-1: refined JL 4-step global mechanism for MILD combustion of natural gas, by replacing reactions no. (3) & (4)					
1	$CH_4+0.5O_2 \rightarrow CO+2H_2$	$\frac{d[CH_4]}{dt}=AT^b e^{-E/(RT)}\cdot[CH_4]^{0.5}[O_2]^{1.25}$	4.4×10^{11}	0	1.26×10^{8}
2	$CH_4+H_2O \rightarrow CO+3H_2$	$\frac{d[CH_4]}{dt}=AT^b e^{-E/(RT)}\cdot[CH_4][H_2O]$	3.0×10^{8}	0	1.26×10^{8}
3	$H_2+0.5O_2 \rightarrow H_2O$	$\frac{d[H_2]}{dt}=AT^b e^{-E/(RT)}\cdot[H_2][O_2]^{0.5}$	7.9×10^{10}	0	1.465×10^{8}
4	$CO+0.5O_2 \rightarrow CO_2$	$\frac{d[CO]}{dt}=AT^b e^{-E/(RT)}\cdot[CO][O_2]^{0.3}[H_2O]^{0.5}$	2.5×10^{8}	0	6.695×10^{7}
JL-2: refined JL 4-step global mechanism for MILD combustion of natural gas, by replacing reaction no. (3)					
1	$CH_4+0.5O_2 \rightarrow CO+2H_2$	$\frac{d[CH_4]}{dt}=AT^b e^{-E/(RT)}\cdot[CH_4]^{0.5}[O_2]^{1.25}$	4.4×10^{11}	0	1.26×10^{8}
2	$CH_4+H_2O \rightarrow CO+3H_2$	$\frac{d[CH_4]}{dt}=AT^b e^{-E/(RT)}\cdot[CH_4][H_2O]$	3.0×10^{8}	0	1.26×10^{8}
3	$H_2+0.5O_2 \leftrightarrow H_2O$	$\frac{d[H_2]}{dt}=AT^b e^{-E/(RT)}\cdot[H_2][O_2]^{0.5}$ (forward)	5.69×10^{11}	0	1.465×10^{8}
4	$CO+H_2O \leftrightarrow CO_2+H_2$	$\frac{d[CO]}{dt}=AT^b e^{-E/(RT)}\cdot[CO][H_2O]$ (forward)	2.75×10^{9}	0	8.36×10^{7}

APPENDIX I: Comparison between calculated and numerical simulation of Average Velocity of the fuel side before the porous plates.

	Φ = 0.6		Φ = 0.5		Φ = 0.4	
	Measured	Numerical	Measured	Numerical	Measured	Numerical
Average Velocity before the Porous Plate (m/s)	0.100	0.100126	0.116	0.116134	0.140	0.140145
% Error	- 0.13		- 0.12		- 0.10	

APPENDIX J: Comparison between experimental and numerical simulation of average velocity of the reaction zone within the porous plates.

Axial Distance (mm)	**Φ = 0.6**			**Φ = 0.5**			**Φ = 0.4**		
	Exp.	**Num**	**% Error**	**Exp**	**Num**	**% Error**	**Exp**	**Num**	**% Error**
135	0.101782	0.101645	0.13	0.120865	0.117776	2.56	0.142978	0.144712	0.68
160	0.105831	0.104124	1.61	0.122576	0.120450	1.73	0.148294	0.147715	2.42
195	0.105397	0.106593	-1.13	0.122121	0.123150	-0.84	0.151266	0.147931	2.35
205	-	0.107634	-	-	0.124018	-	0.152123	0.148484	2.39
240	-	0.114745	-	-	0.135546	-	0.154424	0.160278	-3.79
265	-	0.132059	-	-	0.158052	-	0.225934	0.219778	2.72

APPENDIX K: Flame Images

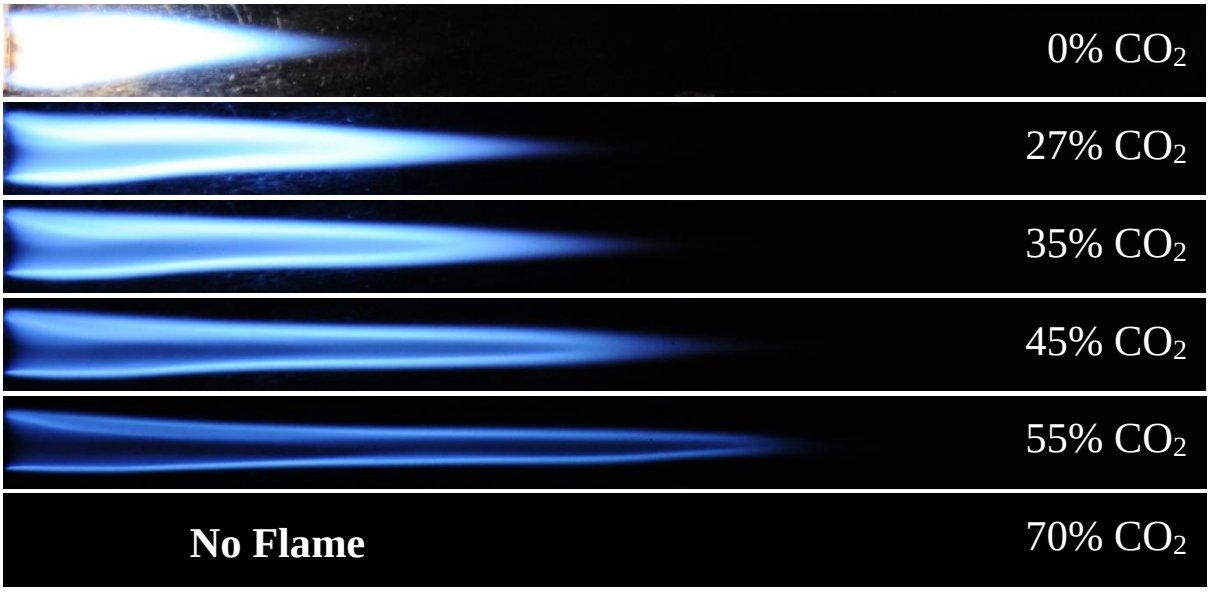

(i) $\Phi = 0.5$

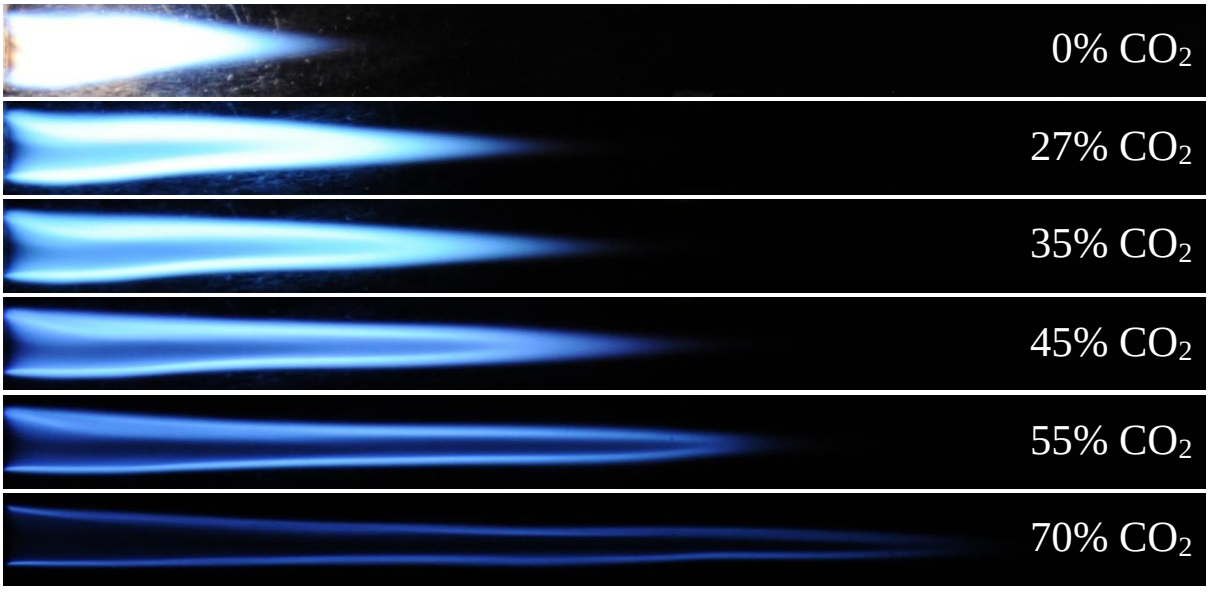

(ii) $\Phi = 0.6$

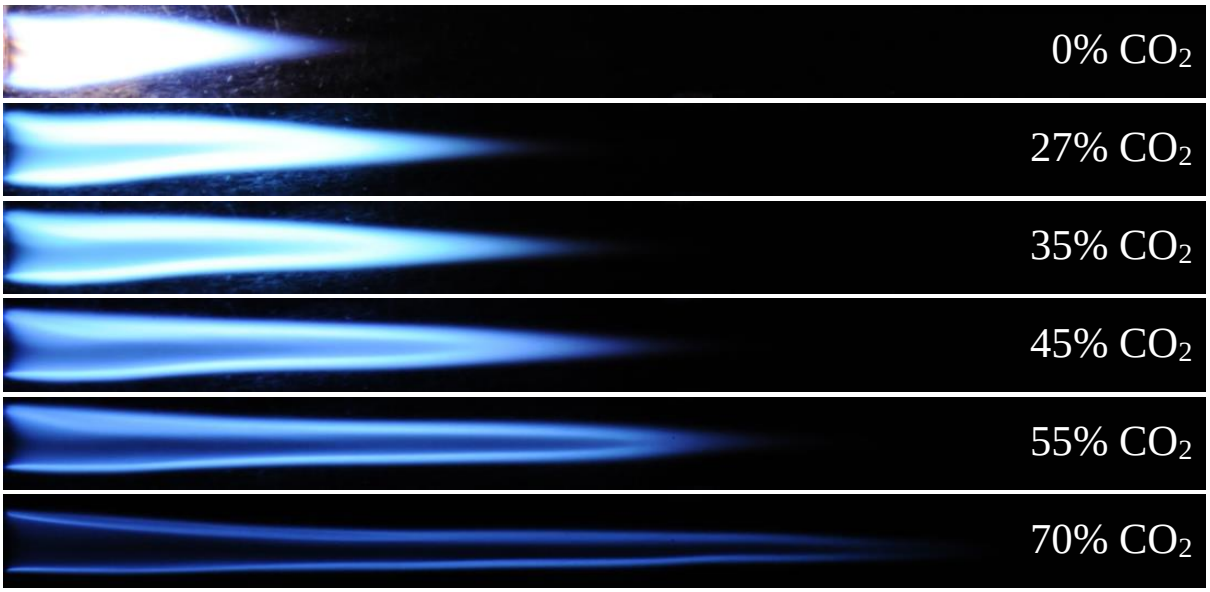

(iii) $\Phi = 0.7$

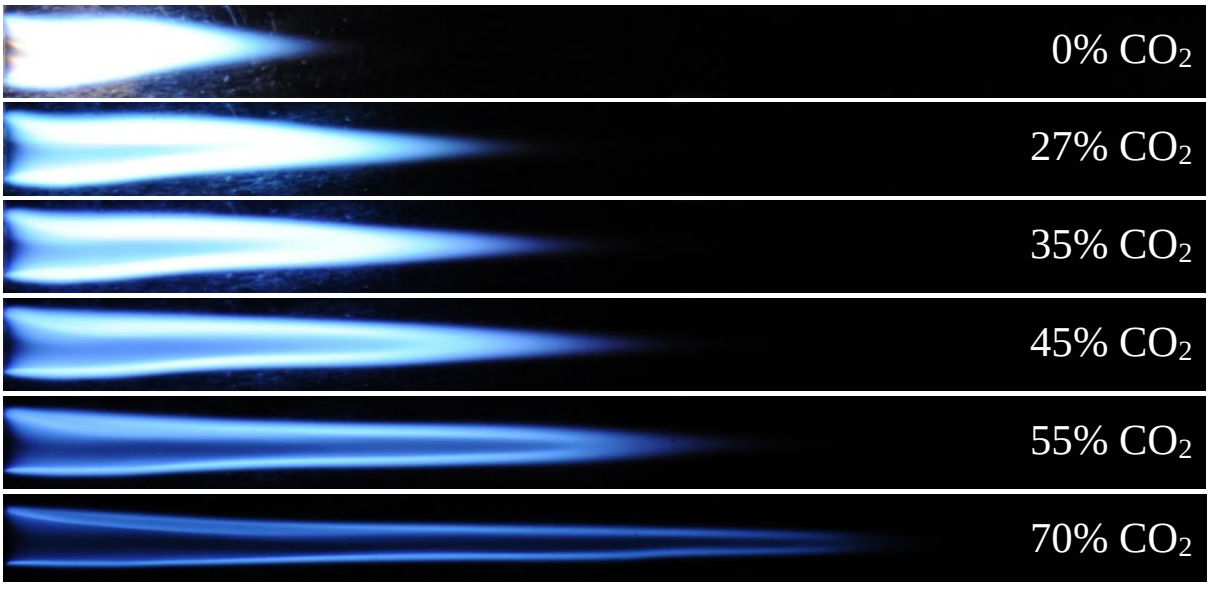

(iv) $\Phi = 0.8$

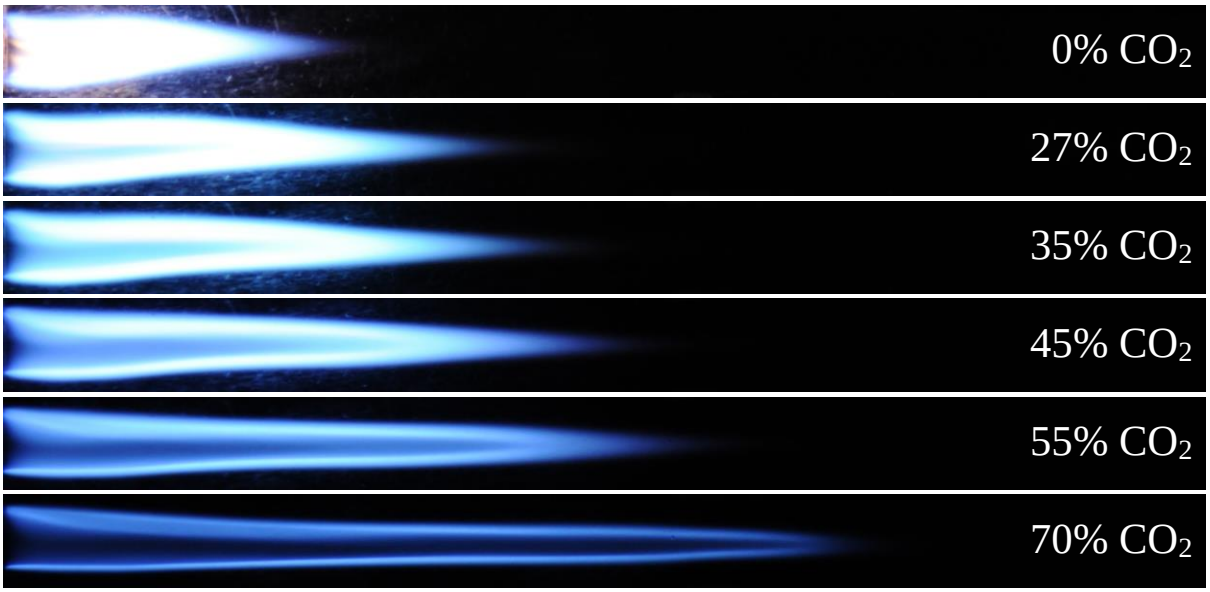
0% CO_2
27% CO_2
35% CO_2
45% CO_2
55% CO_2
70% CO_2

(v) Φ = 0.9

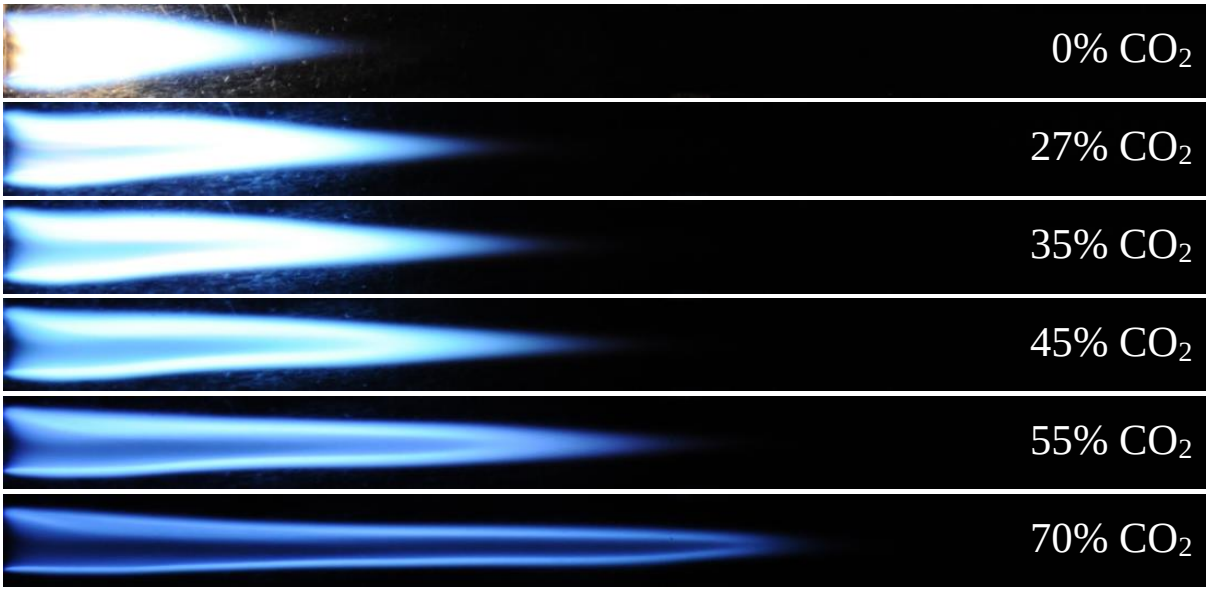
0% CO_2
27% CO_2
35% CO_2
45% CO_2
55% CO_2
70% CO_2

(vi) Φ = 1.0

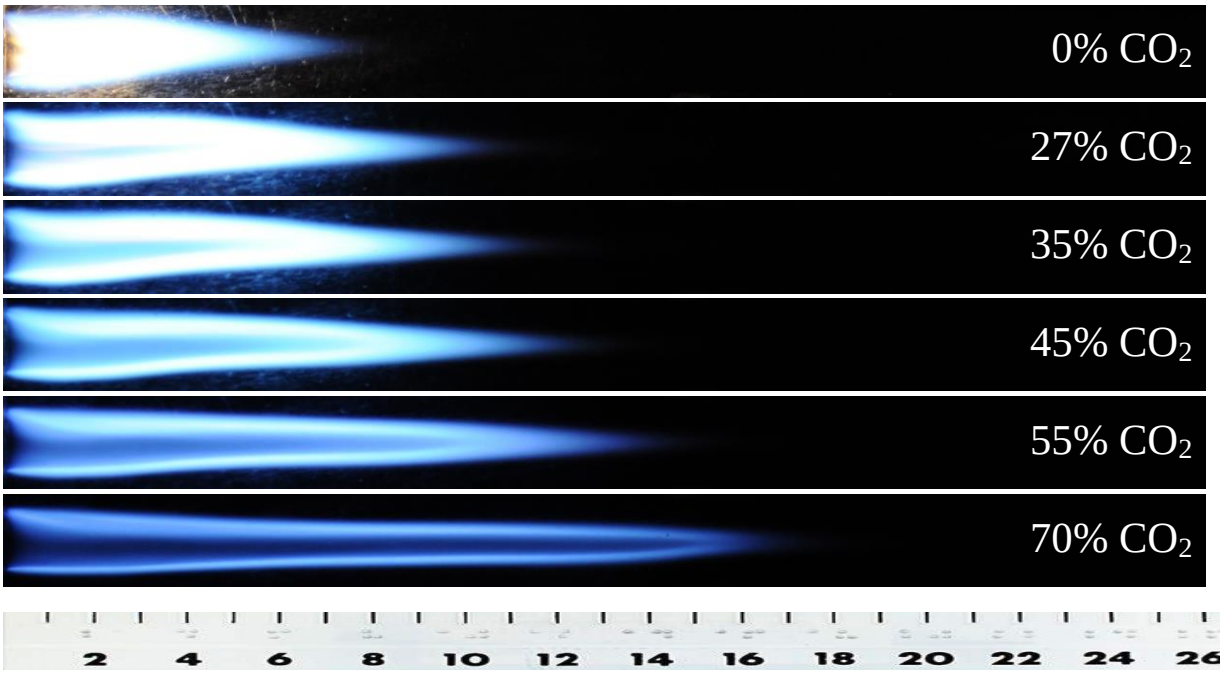

(vii) $\Phi = 1.1$

Figure K1: Effect of CO_2 addition for different equivalence ratios at 1.5kW.

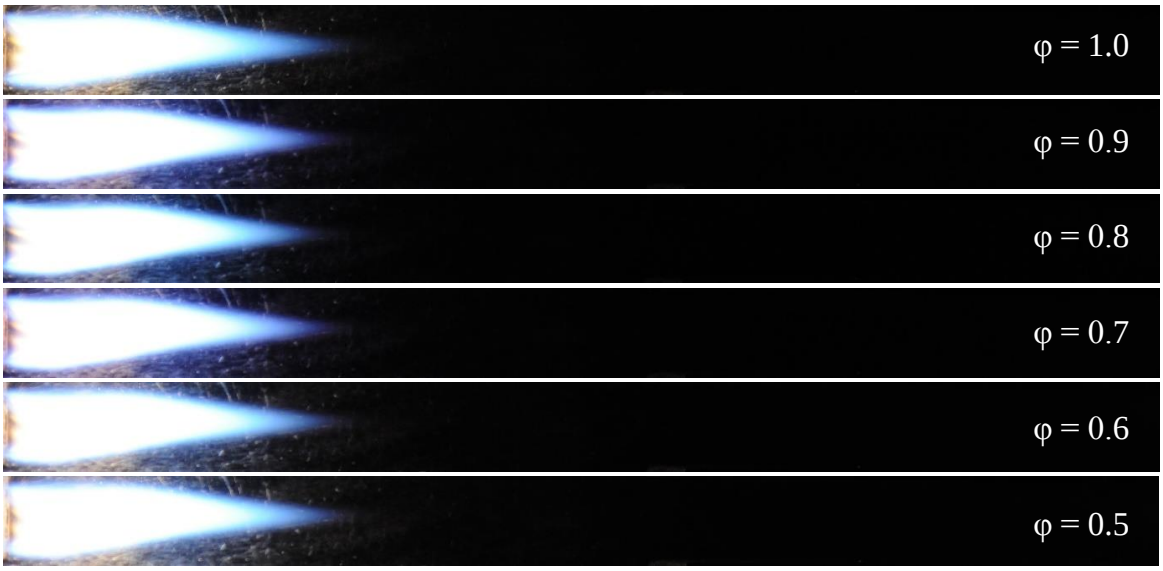

(a) 0% CO_2

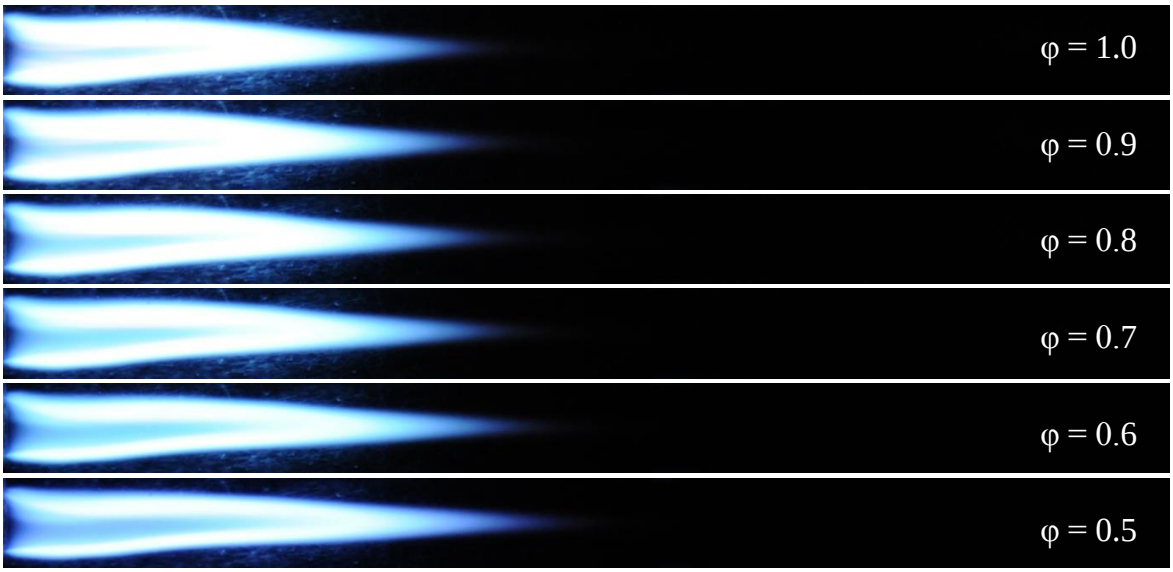

(b) 27% CO_2

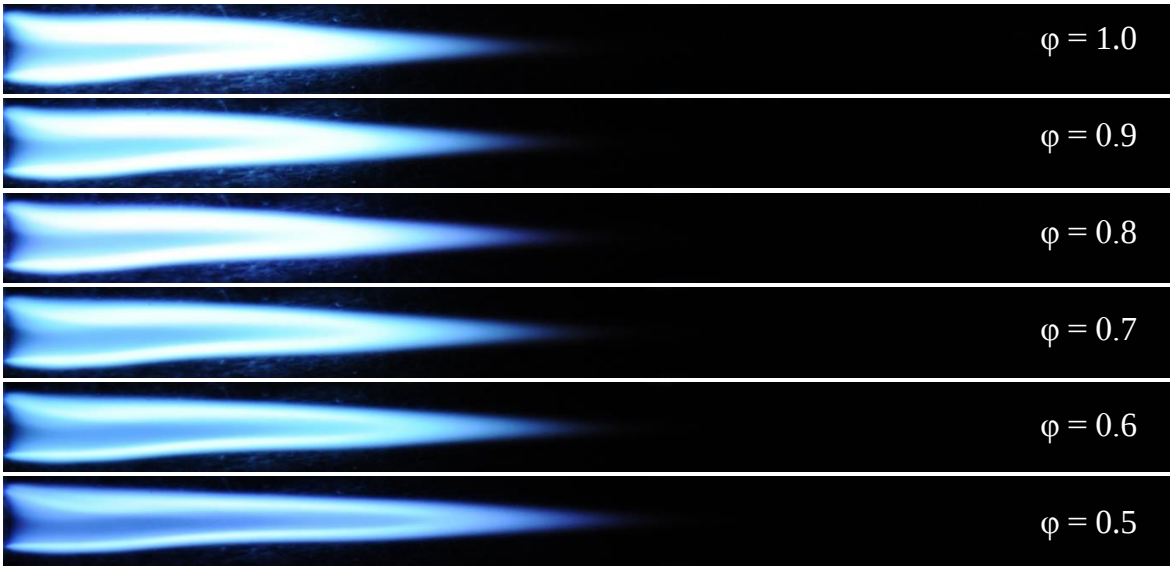

(c) 35% CO_2

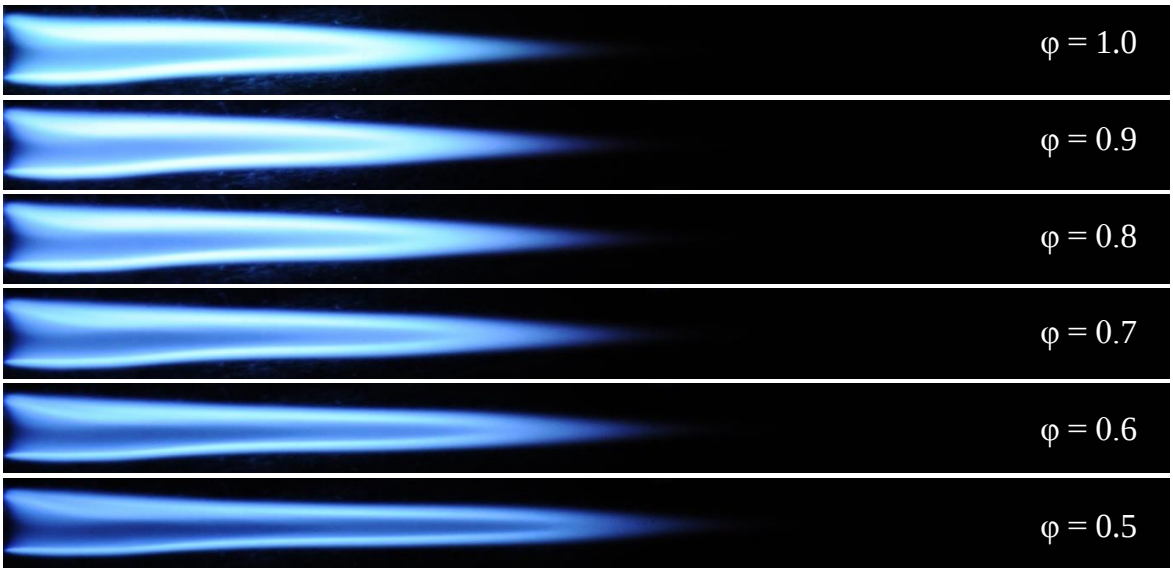

(d) 45% CO_2

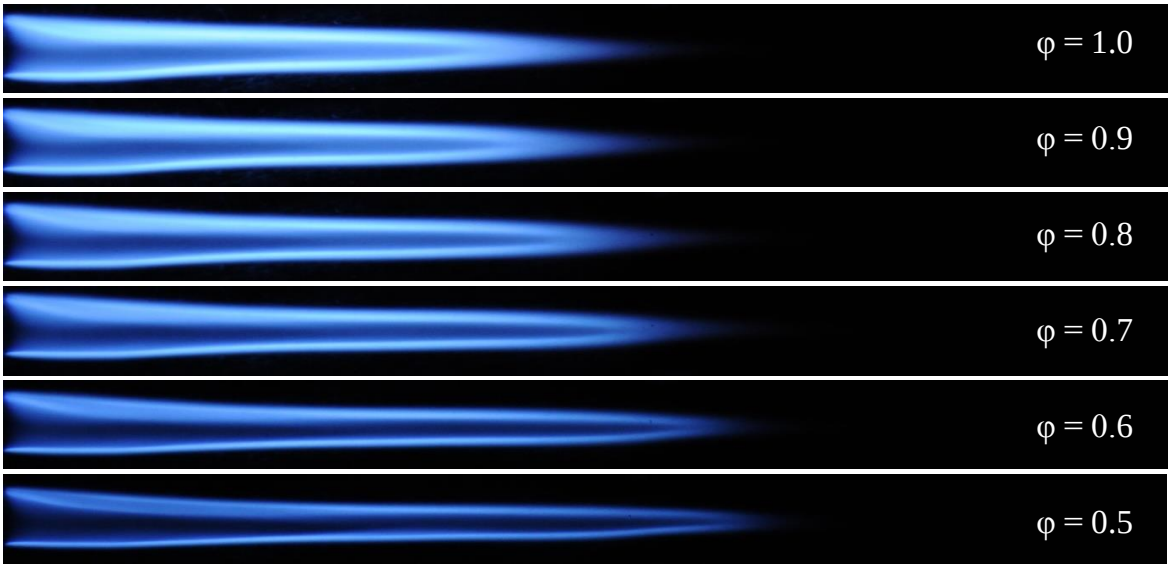

(e) 55% CO_2

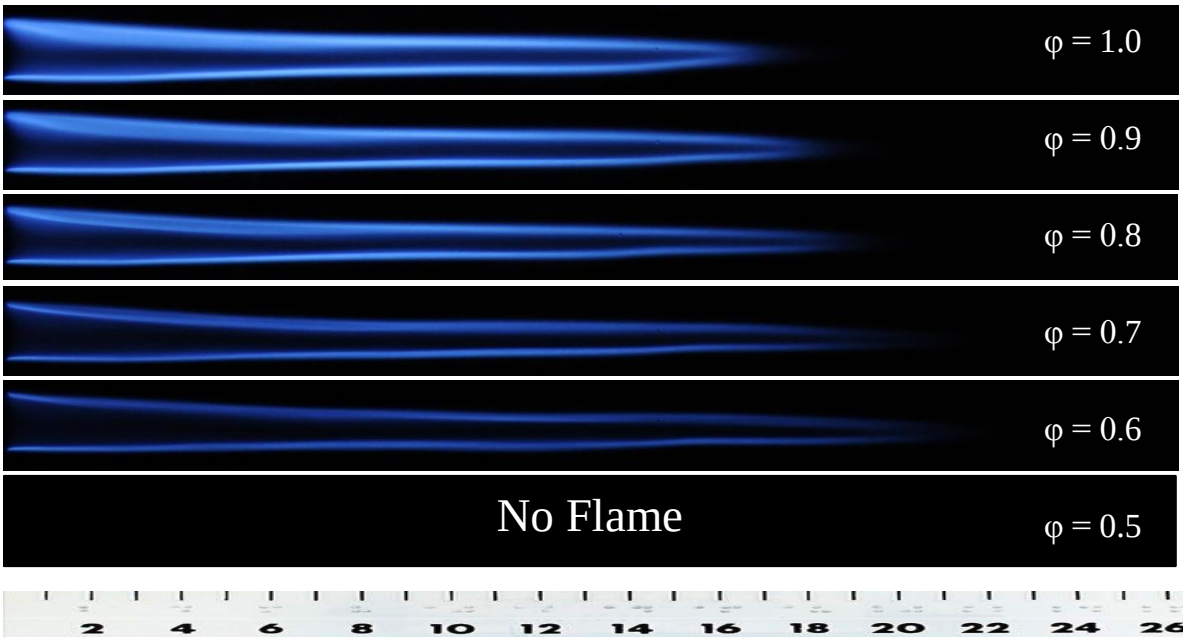

(f) 70% CO_2

Figure K2: Effect of equivalence ratios for different % CO_2 addition at 1.5kW.

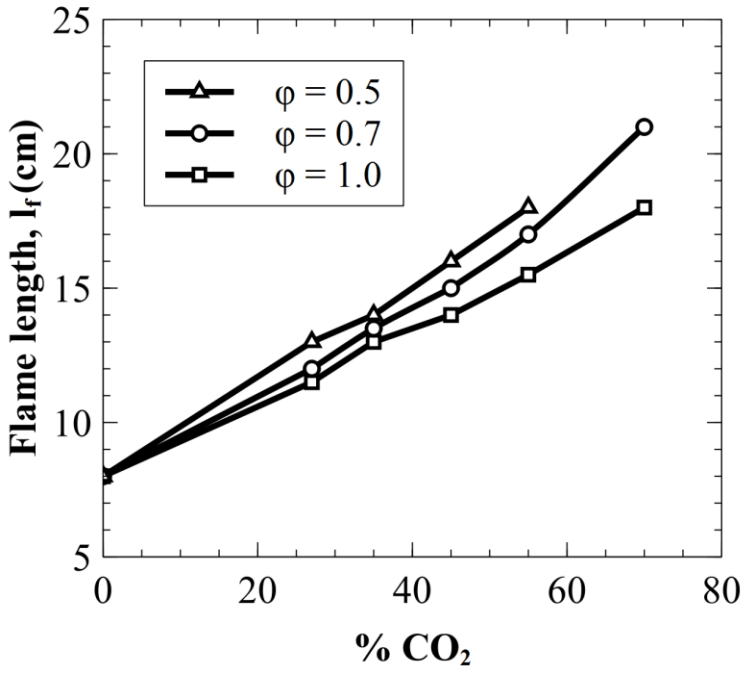

(a)

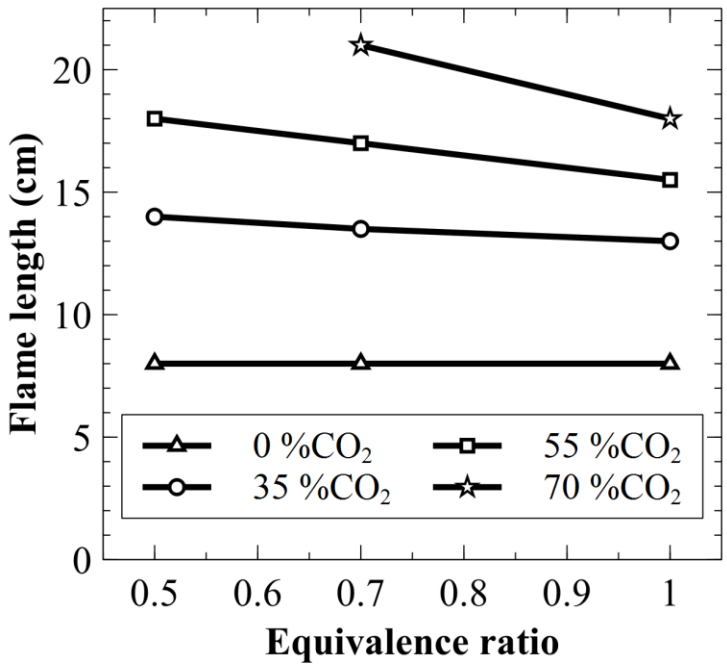

(b)

Figure K3: Effect of operating conditions on the visible flame length. (a) % CO_2 in the oxidizer, (b) equivalence ratio *($l_{f,n} = l_f/w$).*

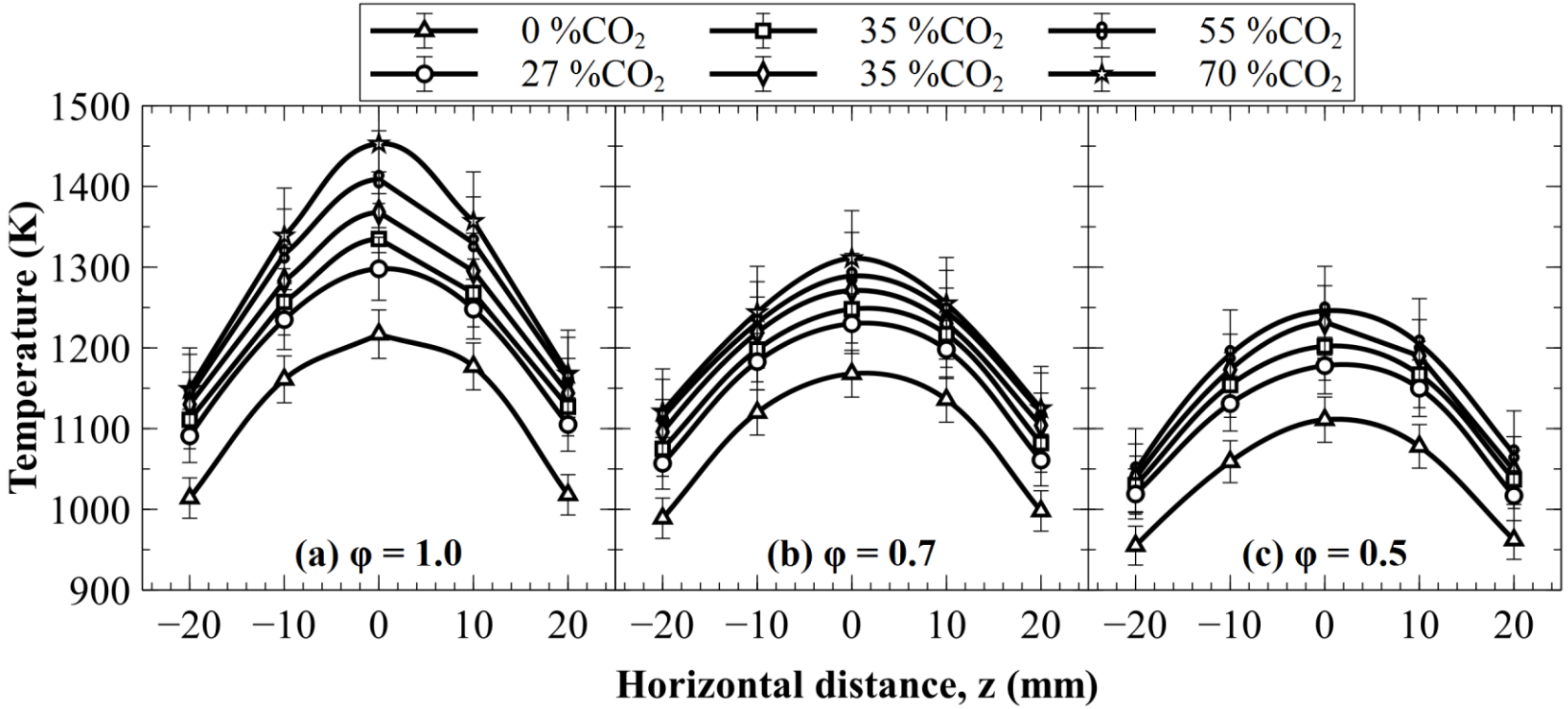

Figure K4: Horizontal temperature variation at the outlet, for fuel firing rate of 1.5kW.

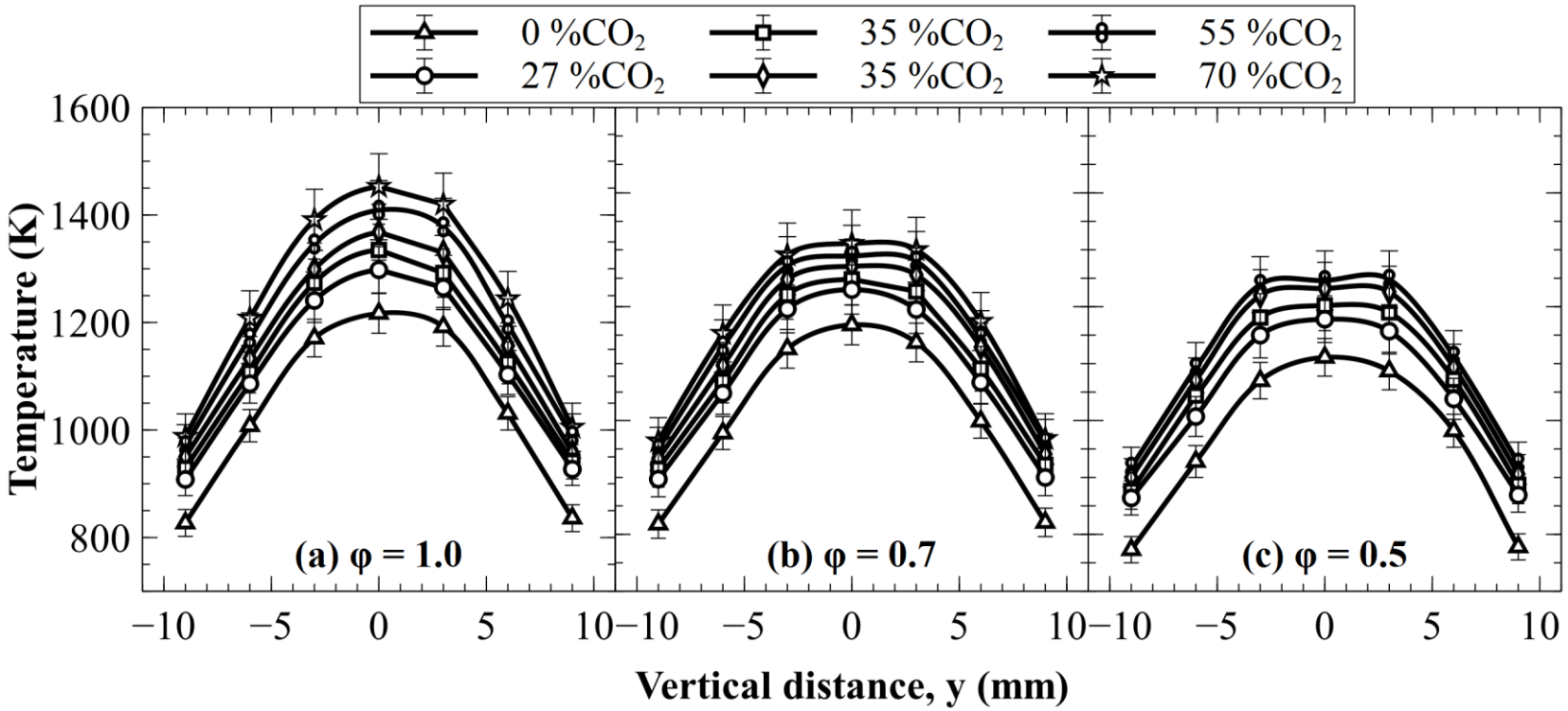

Figure K5: Vertical temperature variation at the outlet, for fuel firing rate of 1.5kW.

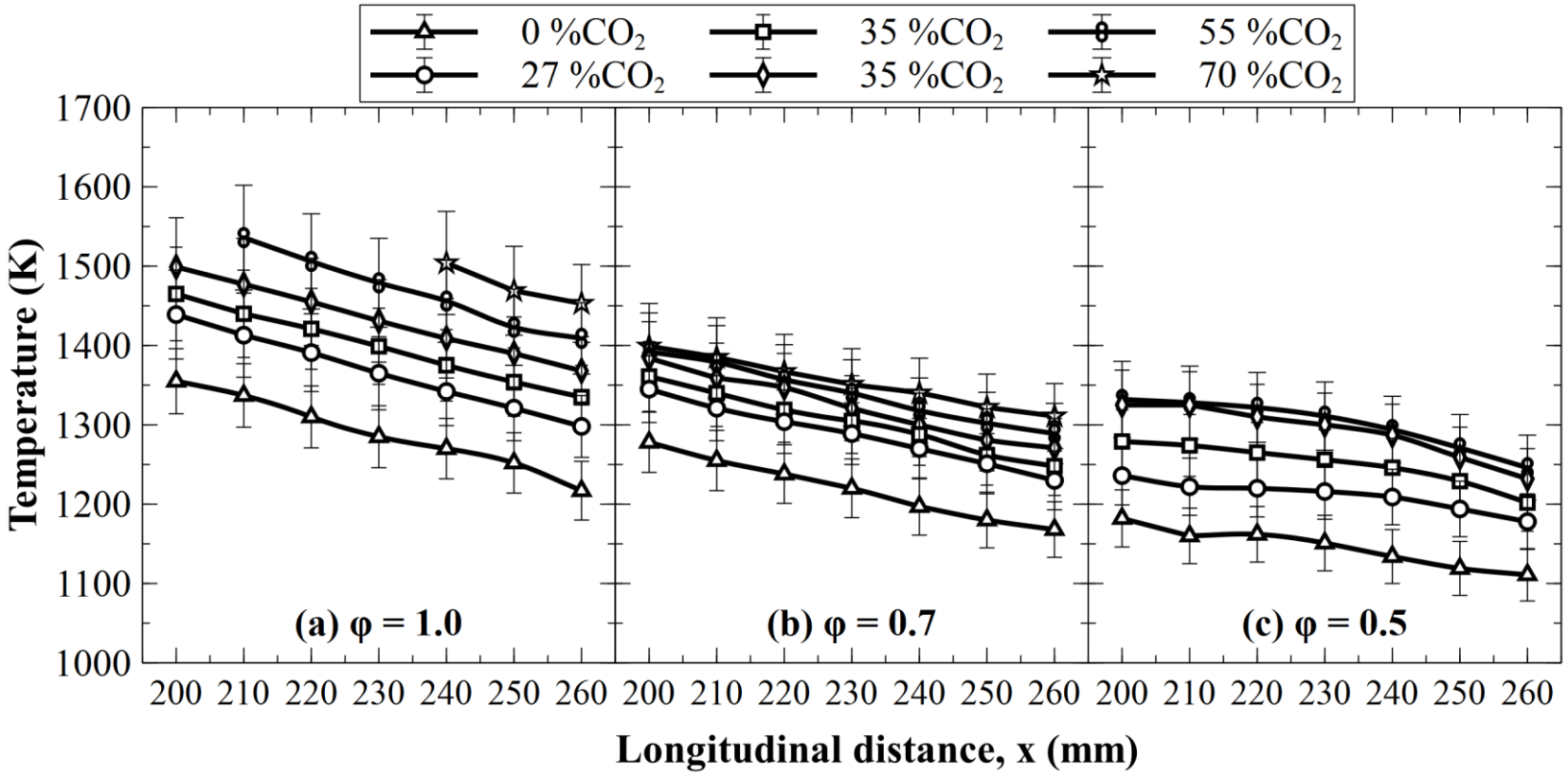

Figure K6: Longitudinal temperature variation towards the exhaust at fuel firing rate of 1.5kW.

APPENDIX L: Experimental and Numerical Comparison of Flame Shapes

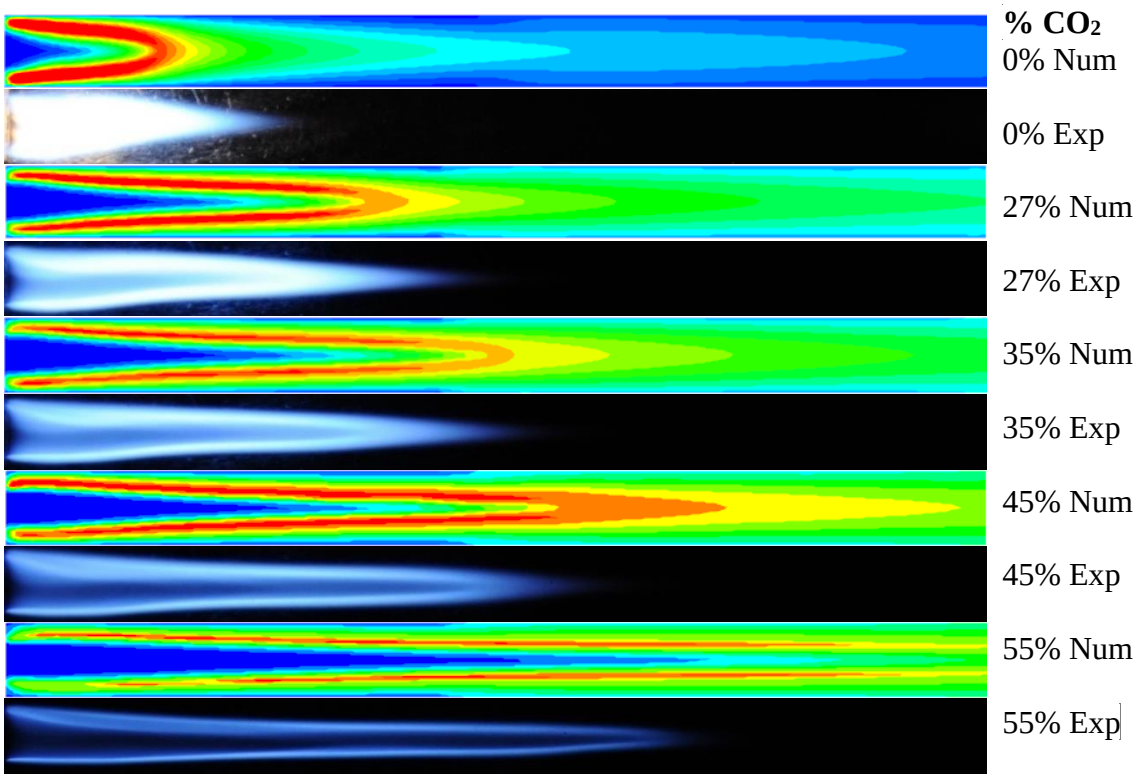

(a) Φ = 0.5

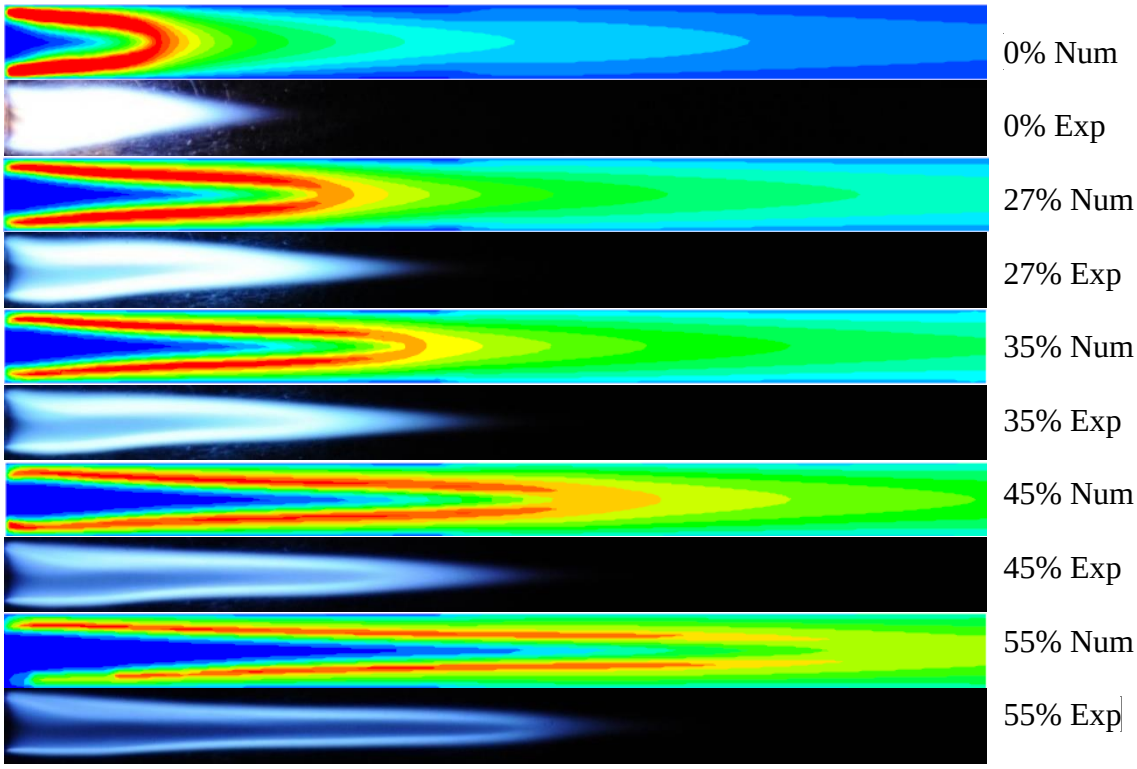

(b) Φ = 0.7

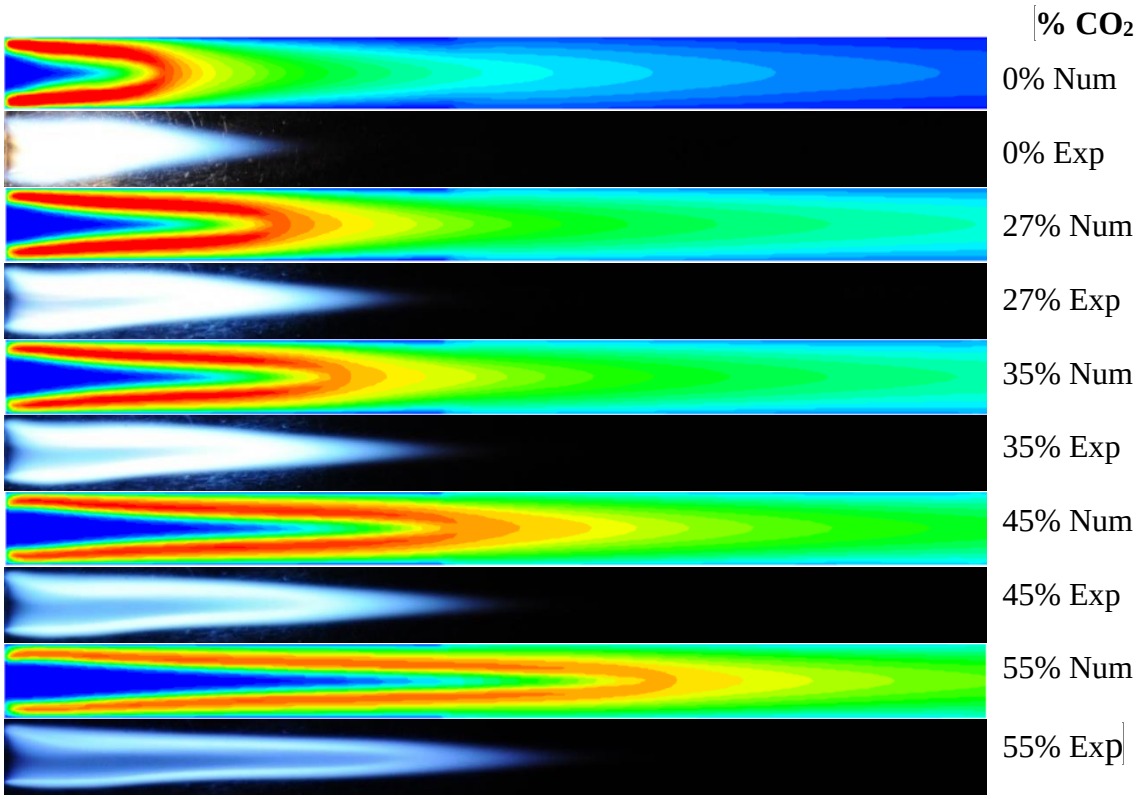

(c) Φ = 1.0

Figure L: Comparison between experimental and numerical flame shapes at different % of CO_2 in the oxidizer mixture for equivalence ratios of (a) Φ = 0.5, (b) Φ = 0.7, (c) Φ = 1.0

APPENDIX M: Maximum Percentage Difference between Experimental and Numerical Combustor Temperatures

% CO_2	Maximum % difference								
	Longitudinal			Horizontal			Vertical		
	ϕ = 0.5	ϕ = 0.7	ϕ = 1.0	ϕ = 0.5	ϕ = 0.7	ϕ = 1.0	ϕ = 0.5	ϕ = 0.7	ϕ = 1.0
0	9.16	8.41	9.87	3.34	5.60	13.29	12.86	10.84	14.07
27	15.03	10.00	8.86	3.55	4.84	14.07	10.41	10.25	13.17
35	15.40	12.37	11.42	4.35	5.39	13.47	12.42	9.45	13.16
45	15.44	14.10	11.55	4.95	4.02	12.72	11.00	9.26	12.15
55	16.92	15.56	9.13	5.10	4.84	13.83	10.77	9.22	11.23

APPENDIX N: OTR Base Case Parameters

Geometry [mm]:

Representation = 2D Axisymmetric

ITM radius = 10

Inner-pipe radius = 17

Inner-pipe thickness = 3

Outer-pipe radius = 25

Length of ITM = 500

Length of Outer-pipe = 500

Length of Inner-pipe = 505

Extension for return = 10

Boundary Conditions:

Air zone:

Air inlet mass flow rate = 5e-4 [kg/s]

Air inlet temperature = 900 [^{o}C] = 1173 [K]

Fuel stream zone:

Fuel stream inlet mass flow rate = 5e-4 [kg/s]

Fuel stream inlet temperature = 900 [^{o}C] = 1173 [K]

Inner-pipe:

Inner surface emissivity = 0.1

Outer surface emissivity = 0.95

Outer-pipe:

Emissivity = 0.95

Temperature = 453 [K] (corresponding to saturation temperature of water and steam @ 10 bar)

Exits = Pressure outlets

APPENDIX O: OTR Oxygen Permeation Flux

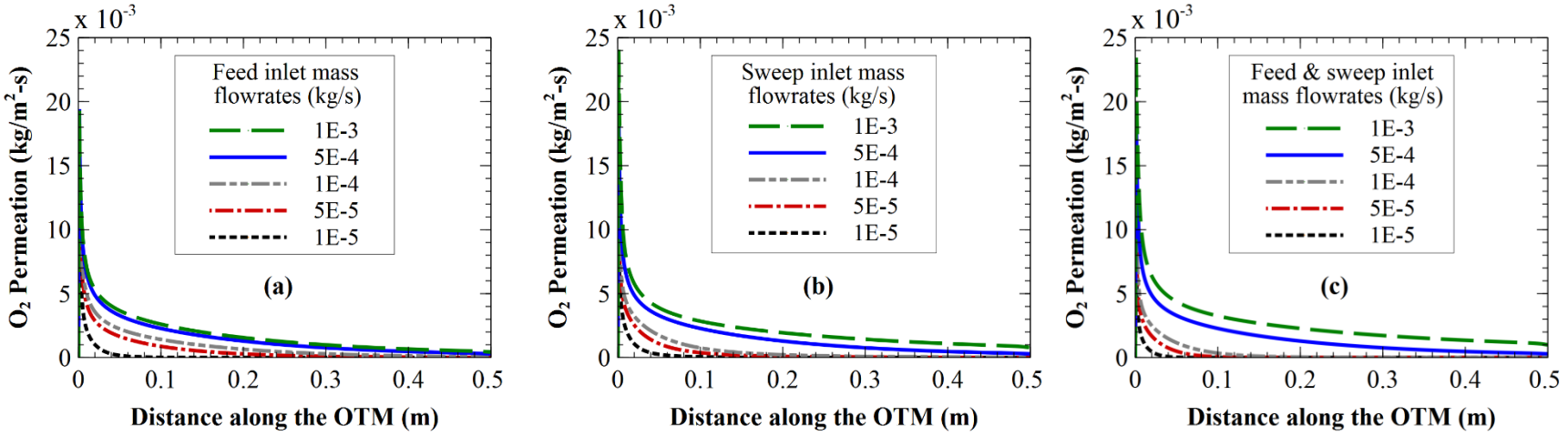

Figure O1: Effect of gas inlet mass flow rate on the rate of O_2 permeation flux across the OTM at an inlet gases temperature of 900 ºC - Non-reactive.

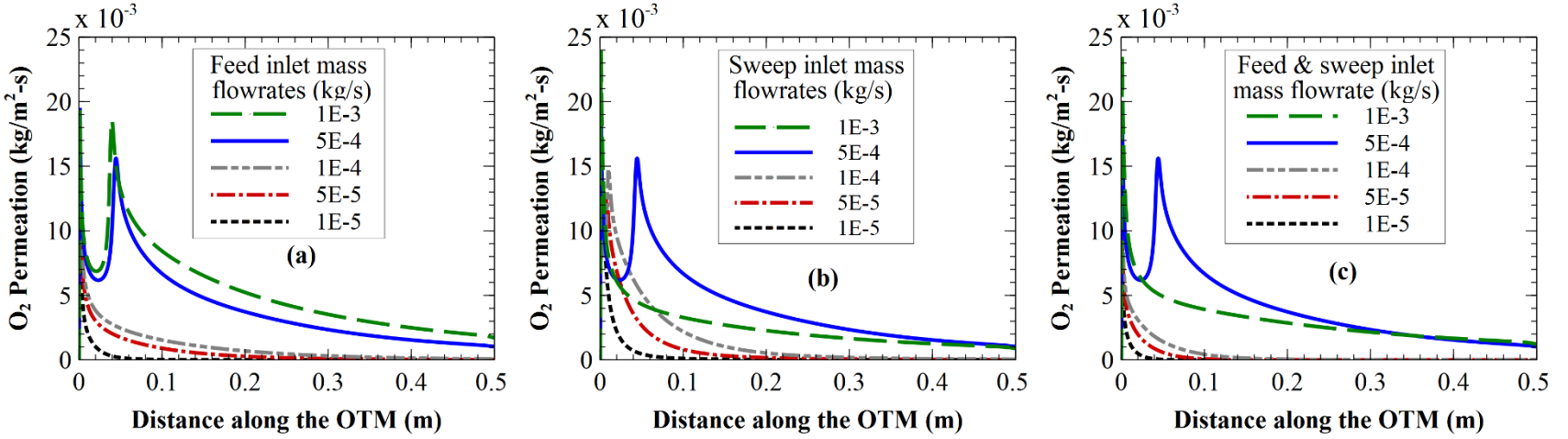

Figure O2: Effect of gas inlet mass flow rate on the rate of O_2 permeation flux across the OTM at an inlet gases temperature of 900 ºC - Reactive.

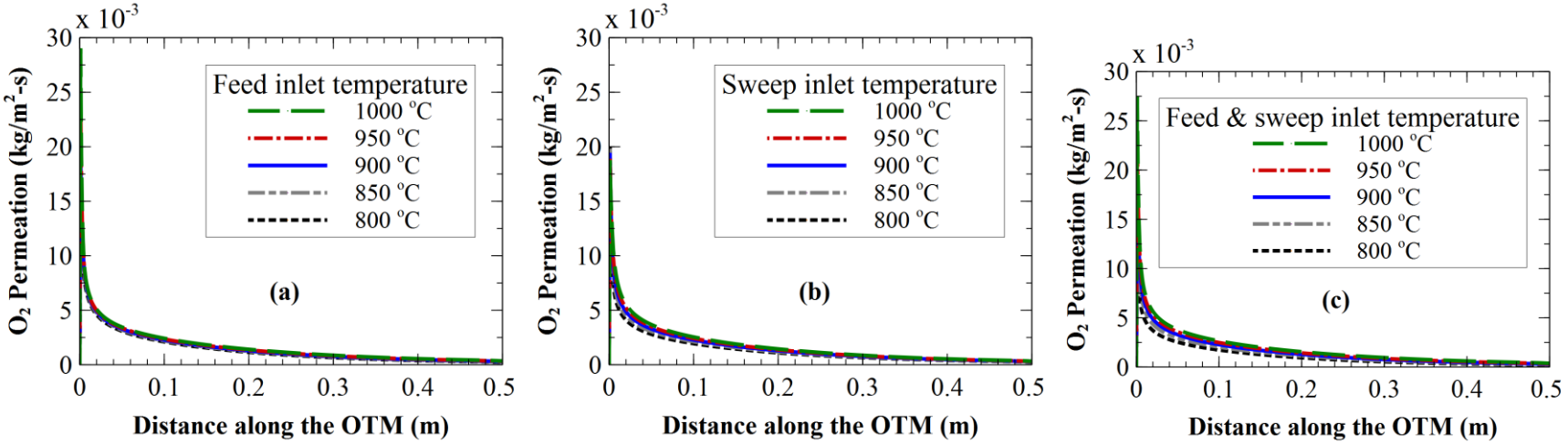

Figure O3: Effect of gas inlet temperature on the rate of O_2 permeation flux across the OTM at an inlet gases flow rate of 5E-4 kg/s - Non-reactive.

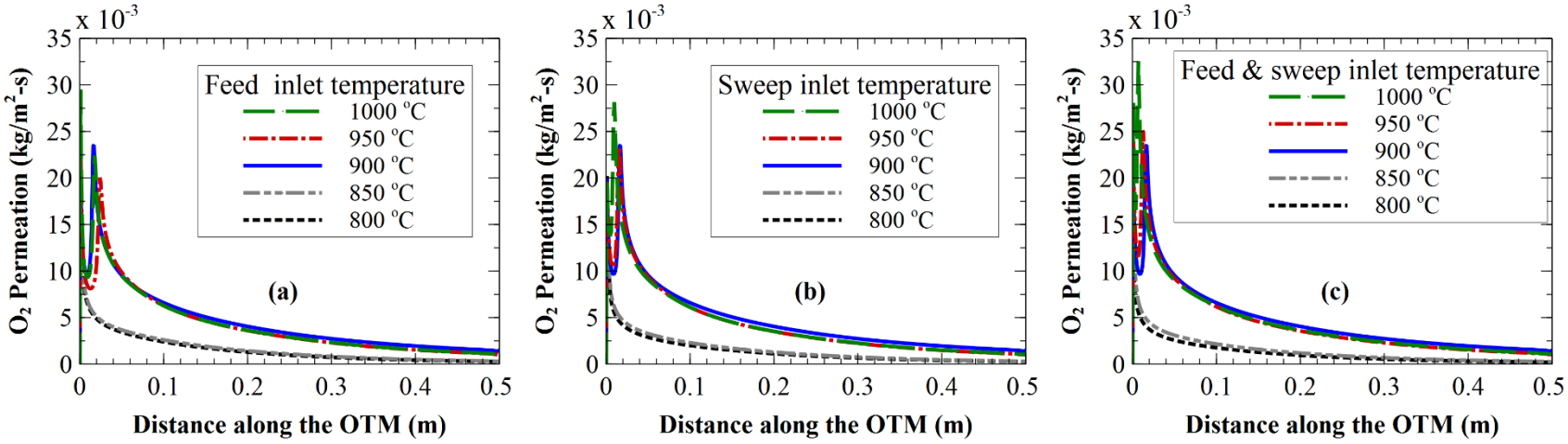

Figure O4: Effect of gas inlet temperature on the rate of O_2 permeation flux across the OTM at an inlet gases flow rate of 5E-4 kg/s - Reactive.

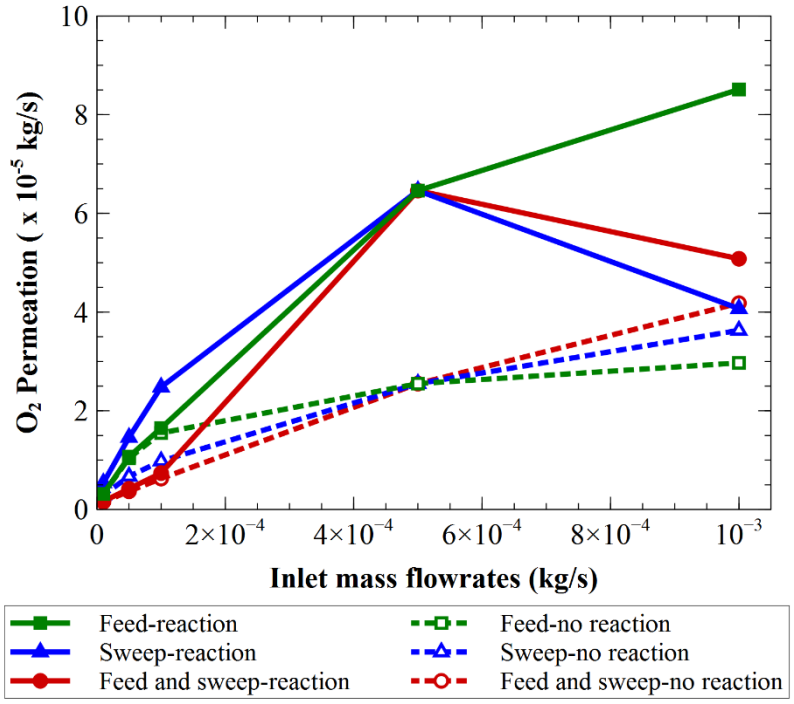

Figure O5: Effect of gas inlet mass flow rates on the rate of O_2 permeation across the OTM at inlet gases temperature of 900 °C under reactive and non-reactive conditions.

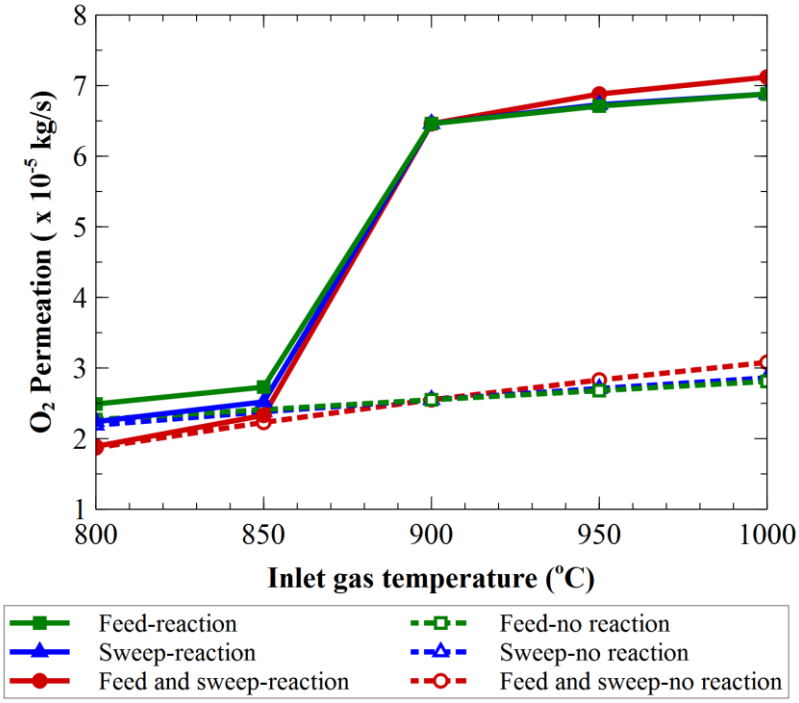

Figure O6: Effect of gas inlet temperatures on the rate of O_2 permeation across the OTM at inlet gases temperature of 900 °C under reactive and non-reactive conditions.

APPENDIX P: OTR Heat Transfer Characteristics

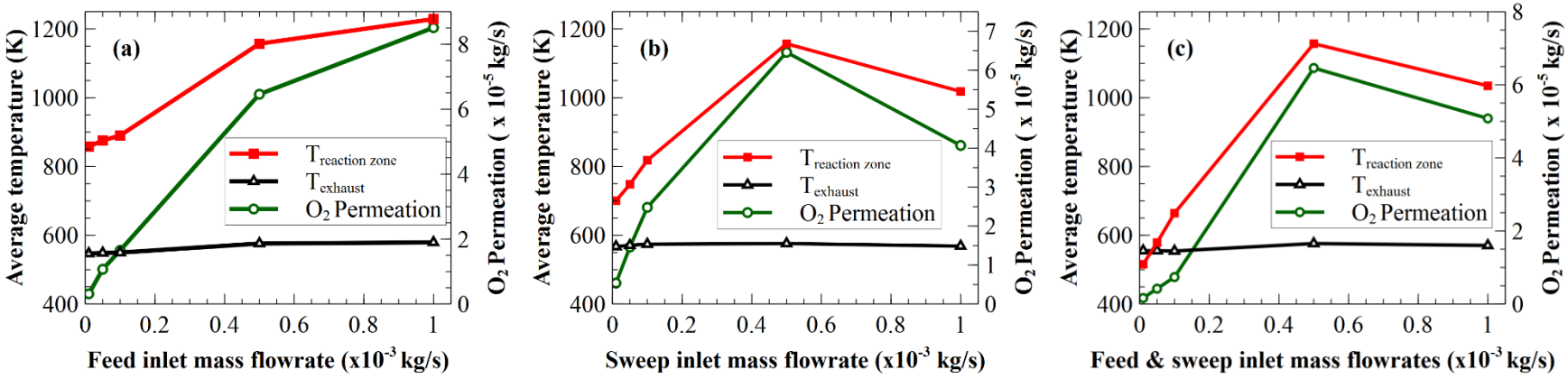

Figure P1: Effect of gas inlet mass flow rates on the average reaction zone and exhaust gas temperatures at inlet gases temperature of 900 ºC.

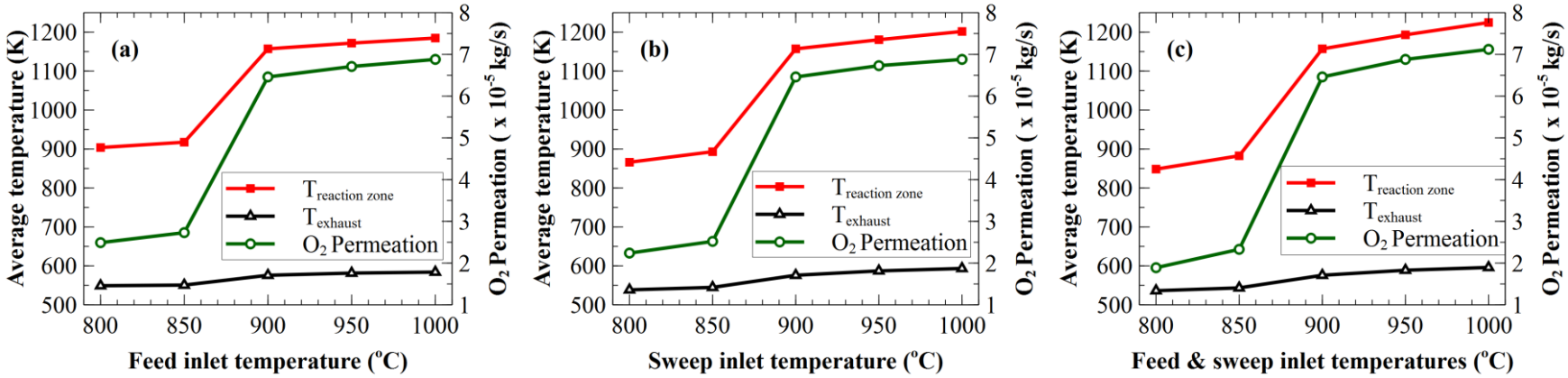

Figure P2: Effect of gas inlet temperatures on the average reaction zone and exhaust gases mass flow rate of 5E-4 kg/s.

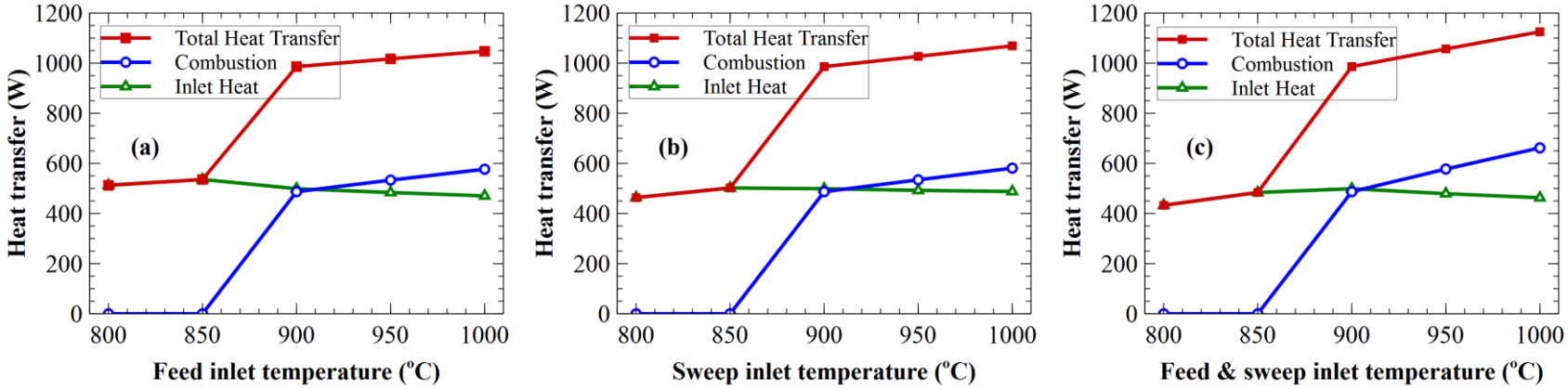

Figure P3: Effect of gas inlet temperatures on combustion heat transfer to the outer-pipe at inlet gases mass flow rate of 5E-4 kg/s.

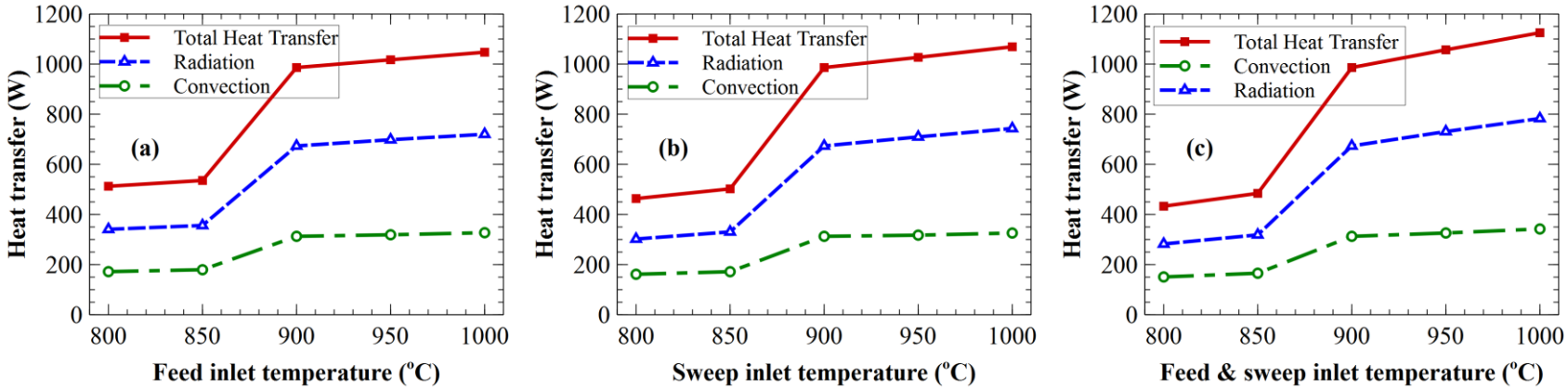

Figure P4: Effect of gas inlet temperatures on heat transfer to the outer-pipe at inlet gases mass flow rate of 5E-4 kg/s.

APPENDIX Q: Effect of outer-pipe surface condition on OTR temperature contours

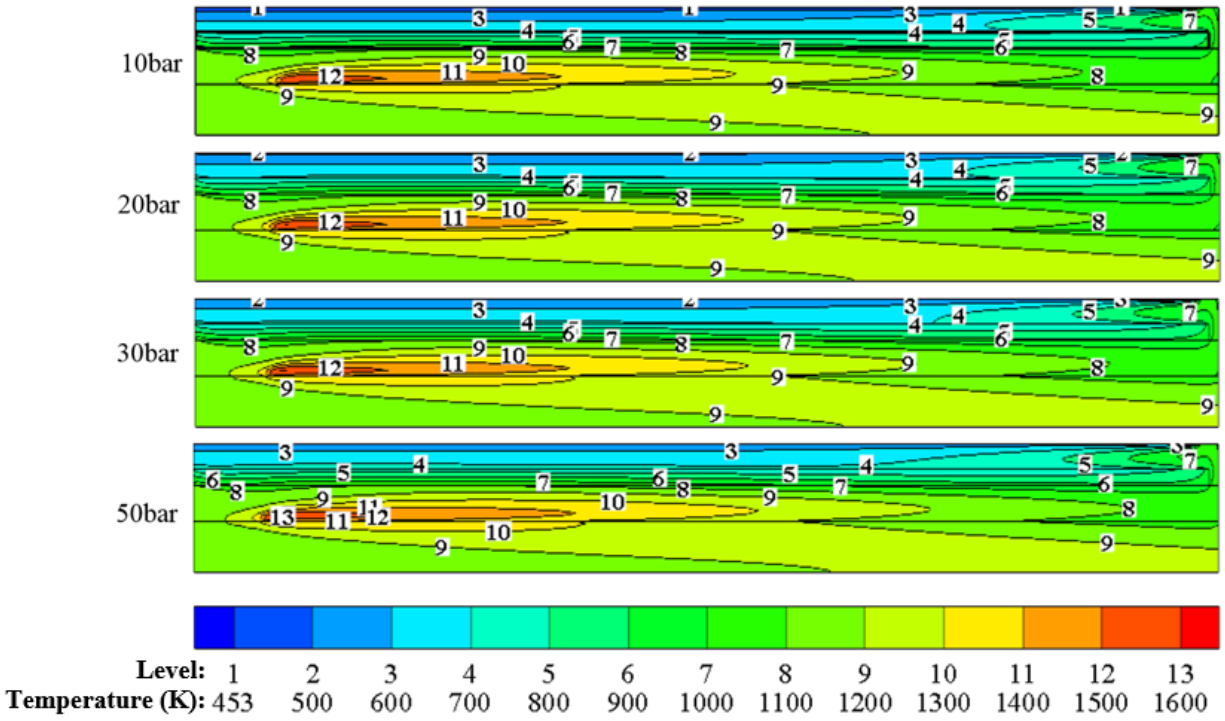

Figure Q1: Effect of outer-pipe surface condition on OTR temperature contours at base case condition.

APPENDIX R: User Defined Function using C++ for O_2 permeation across the OTM

```
/***** UDF for Oxygen permeation *****/

#include "udf.h"
#define WALLSIDE1 11
#define WALLSIDE2 21
#define P_0 101325
#define UDM_NEIGHBOUR_C    0
#define UDM_NEIGHBOUR_TC   1
#define UDM_MASS_SOURCE    2
#define UDM_flux           3
#define UDM_PP             4

#define TOLERANCE 1E-10
#define SPECIES_NUMBER 0

DEFINE_INIT(init_function,d)
{
 Thread *tc1, *tc2;
 Thread *tf1, *tf2;
 cell_t c1, c2;
 face_t f1, f2;
 real   f_c1[2], f_c2[2];
 thread_loop_c(tc1,d)
 {
  begin_c_loop(c1,tc1)
  {
   C_UDMI(c1,tc1,UDM_NEIGHBOUR_C)    = 0.0;
   C_UDMI(c1,tc1,UDM_NEIGHBOUR_TC)   = 0.0;
   C_UDMI(c1,tc1,UDM_MASS_SOURCE)    = 0.0;
  }
  end_c_loop(c1,tc1)
```

```
 }
 tf1 = Lookup_Thread(d,WALLSIDE1);
 tf2 = Lookup_Thread(d,WALLSIDE2);

 begin_f_loop(f1,tf1)
 {
  F_CENTROID(f_c1,f1,tf1);
  c1 = F_C0(f1,tf1);
  tc1 = THREAD_T0(tf1);

  begin_f_loop(f2,tf2)
  {
   F_CENTROID(f_c2,f2,tf2);

    if (fabs(f_c1[0]-f_c2[0]) <= TOLERANCE &&
        fabs(f_c1[1]-f_c2[1]) <= TOLERANCE )
      {
      c2 = F_C0(f2,tf2);
      tc2 = THREAD_T0(tf2);

      C_UDMI(c1,tc1,UDM_NEIGHBOUR_C) = c2 + 0.1;
      C_UDMI(c2,tc2,UDM_NEIGHBOUR_C) = c1 + 0.1;
      C_UDMI(c1,tc1,UDM_NEIGHBOUR_TC) = THREAD_ID(tc2) + 0.1;
      C_UDMI(c2,tc2,UDM_NEIGHBOUR_TC) = THREAD_ID(tc1) + 0.1;
    }
  }
  end_f_loop(f2,tf2)
 }
 end_f_loop(f1,tf1)

Message("\n Membrane initialisation completed.\n"),
}
DEFINE_SOURCE(source_mass,c,t,ds,eqn)
{
```

```
  ds[eqn] = 0.;
  return C_UDMI(c,t,UDM_MASS_SOURCE);
}

DEFINE_ADJUST(adjust_sources, d)
{
  Thread *tc1, *tc2,
  Thread *tf1;
  cell_t c1, c2;
  face_t f1;
  real mass_flux, face_area, face_area_vector[3];
  real massfrac1_CH4, massfrac1_O2, massfrac1_CO2, massfrac1_H2O, massfrac1_CO,
massfrac1_N2, cell_volume1;
  real massfrac2_CH4, massfrac2_O2, massfrac2_CO2, massfrac2_H2O, massfrac2_CO,
massfrac2_N2, cell_volume2;
  real molefrac1_O2, molefrac2_O2;
  real CH4_mwt, O2_mwt, CO2_mwt, H2O_mwt, CO_mwt, N2_mwt,
  real P1, P2, PP1, PP2;
  real L, kr, kf, Dv, T, Told, Tcal;

  CH4_mwt = 16.04;
  O2_mwt = 31.9988;
  CO2_mwt = 44.00995;
  H2O_mwt = 18.01534;
  CO_mwt = 28.00995;
  N2_mwt = 28.0134;

  L = 0.001;

  tf1 = Lookup_Thread(d,WALLSIDE1);
  begin_f_loop(f1,tf1)
  {
    F_AREA(face_area_vector,f1,tf1);
    face_area = NV_MAG(face_area_vector);
```

```
   c1 = F_C0(f1,tf1);
   tc1 = THREAD_T0(tf1);
   cell_volume1 = C_VOLUME(c1,tc1);
   c2  = (int)C_UDMI(c1,tc1,UDM_NEIGHBOUR_C);
   tc2 = Lookup_Thread(d, (int)C_UDMI(c1,tc1,UDM_NEIGHBOUR_TC));
   cell_volume2 = C_VOLUME(c2,tc2);

         massfrac1_CH4 = C_YI(c1,tc1,0);
   massfrac2_CH4 = C_YI(c2,tc2,0);
         massfrac1_O2 = C_YI(c1,tc1,1);
   massfrac2_O2 = C_YI(c2,tc2,1);
         massfrac1_CO2 = C_YI(c1,tc1,2);
   massfrac2_CO2 = C_YI(c2,tc2,2);
         massfrac1_H2O = C_YI(c1,tc1,3);
   massfrac2_H2O = C_YI(c2,tc2,3);
         massfrac1_CO = C_YI(c1,tc1,4);
   massfrac2_CO = C_YI(c2,tc2,4);
         massfrac1_N2 = C_YI(c1,tc1,5);
   massfrac2_N2 = C_YI(c2,tc2,5);

molefrac1_O2 =
(massfrac1_O2/O2_mwt)/((massfrac1_O2/O2_mwt)+(massfrac1_CH4/CH4_mwt)+(massfrac1_CO
2/CO2_mwt)+(massfrac1_H2O/H2O_mwt)+(massfrac1_CO/CO_mwt)+(massfrac1_N2/N2_mwt));

molefrac2_O2 =
(massfrac2_O2/O2_mwt)/((massfrac2_O2/O2_mwt)+(massfrac2_CH4/CH4_mwt)+(massfrac2_CO
2/CO2_mwt)+(massfrac2_H2O/H2O_mwt)+(massfrac2_CO/CO_mwt)+(massfrac2_N2/N2_mwt));

   P1 = molefrac1_O2*((C_P(c1,tc1)+P_0)/P_0);
   P2 = molefrac2_O2*((C_P(c2,tc2)+P_0)/P_0);

   PP1=P1;
   PP2=P2;
```

```
    Told = C_T(c1,tc1);

            kf = 41.688 * exp(-146680/(8.31446 * C_T(c1,tc1)));
            kr = 11660 * exp(-102910/(8.31446 * C_T(c2,tc2)));
            Dv = 0.000059807 * exp(-92709/(8.31446 * C_T(c1,tc1)));

mass_flux = O2_mwt/1000 *face_area * ((kr * Dv * (pow(PP1,0.25)-pow(PP2,0.25)))/(((2 * L * kf
* pow(PP2,0.25) * pow(PP1,0.25))+((pow(PP1,0.25) + pow(PP2,0.25)) * Dv))));

    C_UDMI(c1,tc1,UDM_MASS_SOURCE) = -mass_flux / cell_volume1;
    C_UDMI(c2,tc2,UDM_MASS_SOURCE) = +mass_flux / cell_volume2;
    C_UDMI(c2,tc2,UDM_flux) = mass_flux;
    C_UDMI(c1,tc1,UDM_PP) = PP1;
    C_UDMI(c2,tc2,UDM_PP) = PP2;

            Tcal = C_T(c1,tc1);
            C_T(c1,tc1) = (0.1 * Tcal) + ((1-0.1)* Told);
  }
  end_f_loop(f1,tf1)
}
```

Vitae

Name: - - - Ibrahim Balarabe Mansir

Department: - - - Thermo-Fluid Science Section, Mechanical Engineering Department, King Fahd University of Petroleum & Minerals, Saudi Arabia

Date of Birth: -- - 4th April, 1981

Nationality: - - - Nigerian

Marital Status: - - Married

Current Contact Address: - - Thermo-Fluid Science Section, Mechanical Engineering Department, King University of Petroleum & Minerals, P.O.Box 677, Dhahran 31261, Saudi Arabia (+966553641479, ibrahimmb@kfupm.edu.sa)

Home Address: - - Flat H, Catering Flats, Ahmadu Bello University, P.M.B. 1014, Samaru, Zaria, Nigeria, ibrahimmbalarabe@yahoo.com

Qualifications, Educational Institutions from where obtained and Dates:

- PhD. Mech. Eng. (Thermal Fluid), King Fahd University of Petroleum & Minerals (KFUPM), Saudi Arabia 2018
- M.Sc. Mech. Eng. (Energy), Ahmadu Bello University, Zaria, Nigeria 2012
- B.Eng. Mech. Eng. Bayero University, Kano, Nigeria 2006

Working Experience with Dates

- Lecturer-B, Mechanical Engineering Department, KFUPM 2014 – 2018
- Visiting Lecturer, Mechanical Engineering Department, ABU (Nigeria) 2012 – 2014
- Research Fellow-I, Center for Energy Research and Training (Nigeria) 2008 – 2014
- Reactor Operation and Maintenance of Nigeria Research Reactor (NIRR-1) 2008 – 2014
- De-ionized water production and water purification of NIRR-1 2008 – 2014
- Instrumental Neutron Activation Analysis (INAA) using NIRR-1 2008 – 2014
- Lecturer at Yobe State Business and Engineering Skills Training Centre (BEST Centre), Nigeria 2007 – 2008
- Services Engineer, Mechanical Engineering Design for Building Services at Alim and Associates Consultancy Firm, Kaduna, Nigeria (IT) 2005

Project Experience with Dates

- Design and modelling of Oxygen Transport Reactor for application in a two-pass fire tube boiler, Mechanical Engineering Department, KFUPM, Saudi Arabia 2016 – 2018
- Fatigue Crack Analysis on V-Notch Specimen using X-Ray Tomography 2017 – 2018
- Effect of wind load on solar PV panels support structure at Dhahran, KFUPM, Saudi Arabia 2017 – 2018
- Design and development of a parallel plates porous combustor for Oxy-Fuel combustion, Mechanical Engineering Department, KFUPM, Saudi Arabia 2015 – 2017
- Newtonian Telescope Development at FABLAB, Dhahran, Saudi Arabia 2017
- Development of Nuclear Simulation Code for MNSR, at CERT, Nigeria 2009 – 2012
- Installation of permanent cadmium-lined channel for increasing epithermal NAA capabilities of the Nigerian miniature neutron source reactors 2011 – 2012
- Design and Development of a 100kW Wind Turbine generator BUK, Nigeria 2005 – 2006

Teaching Experience with Dates:

- ME 316: Thermo-Fluid lab, Mechanical Engineering Department, (KFUPM), Saudi Arabia 2015 – 2018
- MEEN 411: Heat Transfer, Mechanical Engineering Department, (A.B.U, Zaria) Nigeria 2012 – 2014
- MEEN 208: Basic Thermodynamics, Mechanical Engineering Department, (A.B.U, Zaria) Nigeria 2012 – 2013
- MEEN 510: Thermal Power Generation, Mechanical Engineering Department, (A.B.U, Zaria) Nigeria 2012 – 2013

Resource Person:

- IAEA Workshop/Meeting on Inter-Comparison Feedback of NAA and other Analytical Techniques Proficiency Tests Performed in 2012 - 2013, International Centre, Vienna, Austria (RAF4022), May 2013
- Stakeholders Workshop on the Draft Regulations on Safety of Research Reactors, REIZ Continental Hotel, Abuja, Nigeria, 2013
- IAEA National Consultants' Meeting on Inter-Comparison Feedback of NAA and other Analytical Techniques Proficiency Tests Performed in 2010, Antananarivo, Madagascar (RAF4022), May 2011

Professional Services:

COREN Registered Mechanical Engineer**:**	Registration Number: **R.22,853,**
	Registration Date: **28th June 2012**
Certified Nuclear Security Professional:	The World Institute for Nuclear Security Academy
	Certificate Number: **000-586**
	Certification Date: **9th July 2017**

International Trainings/Workshops Attended:

1 KAUST Combustion Institute Summer School, KAUST Clean Combustion Research Center (CCRC), Saudi Arabia, April 2018.

2 Joint ICTP-IAEA School on Nuclear Energy Management, Abdus Salam International Centre for Theoretical Physics (ICTP), Trieste, Italy, August 2017.

3 RELAP/SCDAPSIM Novice Training Workshop by Innovative Systems Software, Idaho, USA, Jordan University of Science & Technology (JUST), Irbid, Jordan, July 2016.

4 Tsinghua - Princeton Summer School on Combustion, Beijing, China, July 2015.

5 The IAEA Training Course on Natural Circulation Phenomena and Passive Safety Systems in Advanced Water-Cooled Reactors, *School of Advanced Nuclear Energy System studies (SANESS), Global Centre for Nuclear Energy Partnership (GCNEP),* India, 29 September - 03 October 2014.

6 The 3rd Training Course on Science and Technology of Super-Critical Water-Cooled Reactors, Shanghai Jiao Tong University, Shanghai, China, August 2013

7 Training on Miniature Neutron Source Reactor Operator, China Institute of Atomic Energy, Beijing, China, August 2010

8 Training on Nuclear Power Plant Simulator (VVER-1000 Reactor Department) at SSL, Obninsk, Russia, 2010

9 Workshop on Computer Codes for Nuclear Reaction Cross-Section Determination and Data Retrieval Exercises, National Mathematical Centre, Abuja, Nigeria, May 2013

10 National Training Course on State Systems of Accounting for and Control of Nuclear Material, Abuja, Nigeria, November 2010.

11 Training on NIRR-1 Operation, Utilization and Safety, Centre for Energy Research and Training, Ahmadu Bello University, Zaria, Nigeria, July 2009.

Publication in Peer Reviewed Journals:

Published Papers:

1. Said, Syed A., Mansur Aliyu, Medhat A. Nemitallah, Mohamed A. Habib, **Ibrahim B. Mansir** (2018). Experimental Investigation of the stability of a turbulent diffusion flame in a gas turbine combustor. *Energy*, 157 (2018) 904-913, https://doi.org/10.1016/j.energy.2018.05.177.

2. Nemitallah, M.A., Rashwan, S.S., **Mansir, I.B**., Abdelhafez, A.A. and Habib, M.A., (2018). Review of novel combustion techniques for clean power production in gas turbines. *Energy & Fuels*, 2018, 32, 979−1004, DOI: 10.1021/acs.energyfuels.7b03607

3. Medhat Nemitallah, Mohamed Habib, Shakiruddin Salahuddin, **Ibrahim Mansir**, "Hydrogen production, oxygen separation and syngas oxy-combustion inside a water splitting membrane reactor", *Renewable Energy*, 113 (2017) 221-234.

4. Y. A. Ahmed, **I. B. Mansir**, B. B. M. Dewu, (2013). "Installation of permanent cadmium-lined channel as a Means for increasing epithermal NAA capabilities of miniature neutron source reactors", *Nuclear Engineering and Design* 263 (2013) 70–76.

5. Y. A. Ahmed, **I. B. Mansir,** I. Yusuf, G. I. Balogun, S. A. Jonah, (2011). "Effects of Core Excess Reactivity and Coolant Average Temperature on Maximum Operable Time of NIRR-1 Miniature Neutron Source Reactor". *Nuclear Engineering and Design*, 241, Issue 5 (2011) 1559–1564.

6. **I. B. Mansir,** G. Y. Pam, C. O. Folayan, (2013). "Development of a Steady State Temperature Distribution Code (STD 1.0) for Predicting Thermal-Hydraulics Parameter of MNSR". *Journal of Nuclear Engineering & Technology, STM Journals*, Vol.3 Issue 2 (2013) 1-13.

7. **Mansir I. B**., Pam G. Y., Folayan C. O., (2012). "Effects of Density Variation on the Cooling of the Nigeria Research Reactor-1 (NIRR-1)". *Advances in Applied Science Research*, 2012, 3 (1):110-116.

8. S. A. Arabi, B. B. M. Dewu, A. M. Muhammad, **M. B. Ibrahim** and J. D. Abafoni, (2010). "Determination of Weathered and Fractured Zones in Part of the Basement Complex of North-Eastern Nigeria". *Journal of Engineering and Technology Research*, Vol. 2(11), pp. 213-218

9. G. Y. Pam, **I. B. Mansir**, M. I. Borok, Y. B. Kolo, (2013). "Efficiency and Hydraulic Power of Poldaw Windpump Systems at some Locations in Northern Nigeria", *The International Journal of Engineering and Science*, Vol. 2(8), 80-85.

Papers in progress:

1. **Ibrahim B. Mansir**, Rached Ben-Mansour, Mohamed A. Habib (2018). "Oxy-fuel combustion investigation in a two-pass oxygen transport reactor for fire tube boiler application", *Applied Energy*, Manuscript No.: APEN-D-18-04165 (Under review).

2. **Ibrahim B. Mansir**, Mohamed A. Habib, Medhat A. Nemitallah and Atia E. Khalifa (2018). "Experimental and numerical investigation of flow field and oxy-methane combustion

characteristics in a low-power porous-plate reactor", *Energy*, Manuscript No.: EGY-D-17-06417 (Under review).

3. **Ibrahim B. Mansir**, Mohamed A. Habib, Medhat A. Nemitallah and Atia E. Khalifa (2018). Experimental study on combustion characteristics and lean blow-out limits of non-premixed oxy-methane flames in a porous-plate reactor, *Proceedings of The Combustion Institute*", Manuscript Ref. No.: PROCI-D-17-00109 (Under review).

Conference Papers:

1. **Ibrahim B. Mansir**, Medhat A. Nemitallah, Mohamed A. Habib, Atia E. Khalifa. Experimental study on combustion characteristics and lean blow-out limits of non-premixed oxy-methane flames in a porous-plate reactor. The 37th International Symposium on Combustion, (PROCI-D-17-00109), Dublin, Ireland, 29 July - 3 August 2018. (ACCEPTED)

2. J. Albinmousa, **I. B. Mansir,** S.H. Iftikhar, M. Basha, J. Jose, "Fatigue Crack Imaging of V-Notch Specimen using X-Ray Tomography", The 6th International Conference on Crack Paths (CP 2018), Verona, Italy, 19 - 21 September 2018. (ACCEPTED)

3. **Mansir Ibrahim Balarabe**, Mohamed A. Habib; Medhat A. Nemitallah; Atia E. Khalifa (2016). "Flow Characteristics in a Porous Plate Reactor for Oxy-fuel Combustion", 6th Saudi Arabian Section of the Combustion Institute Annual Meeting, Saudi Aramco Technical Exchange Center, Dhahran, Kingdom of Saudi Arabia, May 1 – 2.

4. Y. A. Ahmed, **I. B. Mansir**, (2012). "Increasing Epithermal Neutron Activation Analysis Capabilities of a Miniature Neutron Source Reactor Using a Permanent Cadmium Lined Channel" The 7th African Conference on Research Reactor Utilization and Safety 14-15 October 2012, Cairo, Egypt

5. I. Yusuf, **I. B. Mansir**, B. B. M. Dewu, (2011). "Maintenance As a Tool for the Enhancement of Safety in the Operation of Nigeria Research Reactor", International Conference on Research Reactors: Safe Management and Effective Utilization, 14-18 November 2011, Rabat, Morocco. IAEA-CN-188/B18, http://www.hub.iaea.org/MTCD/publications/PDF/P1575_CD_web/datasets/foreword.html

Hobbies:

Reading, sharing ideas and traveling.